Title

Atmospheric Boundary Layer Modeling for Wind Energy: Assessing the Impacts of Complex Terrain and Thermally Stratified Turbulence on Wind Turbine Performance

Permalink

https://escholarship.org/uc/item/2v39s2g5

Author

Wise, Adam

Publication Date

2024

Peer reviewed|Thesis/dissertation

Atmospheric Boundary Layer Modeling for Wind Energy: Assessing the Impacts of Complex Terrain and Thermally Stratified Turbulence on Wind Turbine Performance

By

Adam Wise

A dissertation submitted in partial satisfaction of the

requirements for the degree of

Doctor of Philosophy

in

Engineering - Civil and Environmental Engineering

in the

Graduate Division

of the

University of California, Berkeley

Committee in charge:

Professor Fotini Katopodes Chow, Chair
Professor Robert Harley
Professor Alexis Kaminski
Professor Julie K. Lundquist

Summer 2024

Atmospheric Boundary Layer Modeling for Wind Energy: Assessing the Impacts of Complex Terrain and Thermally Stratified Turbulence on Wind Turbine Performance

Abstract

Atmospheric Boundary Layer Modeling for Wind Energy: Assessing the Impacts of Complex Terrain and Thermally Stratified Turbulence on Wind Turbine Performance

by

Adam Wise

Doctor of Philosophy in Engineering - Civil and Environmental Engineering

University of California, Berkeley

Professor Fotini Katopodes Chow, Chair

Wind energy is the leading renewable technology in the U.S., generating over 10% of utility-scale electricity in recent years. Rapid growth in wind energy installations has made modeling and prediction of atmospheric boundary layer (ABL) wind speeds and the associated turbulence critical for wind turbine siting, resource assessment, and operational power forecasting. A number of modeling challenges currently exist, such as representing the impact of terrain on wind turbine wakes and capturing small-scale turbulence in stably-stratified conditions. Many low-fidelity wind turbine simulation methods fail to incorporate topography and struggle to account for dynamic flow behavior. In this dissertation, results are presented using high-fidelity large-eddy simulation (LES), which captures the dynamic and turbulent behavior of ABL winds, providing a framework to simulate a wide variety of turbulent atmospheric phenomena with a wind turbine parameterization to understand turbine-airflow interactions.

First, high-resolution simulations of the 2017 Perdigão field campaign in Portugal are conducted. The Perdigão site consists of two parallel ridges with a wind turbine located on top of one of the ridges. Both convective and stable atmospheric conditions are simulated to understand how the wind turbine wake behaves in complex terrain in two representative flow regimes. For the convective case study, flow recirculation in the lee of the ridge occurred, thus deflecting the wake upwards. For the stable case study, the wake deflected downwards following the terrain due to a mountain wave that occurred. The vertical behavior of the wind turbine wake can be detrimental to downwind turbines; however, this vertical behavior is not accounted for in current wind farm design wake models. These case studies demonstrate the dependence of the wind turbine wake behavior on terrain-induced flow phenomena, which, in-turn, depend on the thermal stratification of the atmosphere.

The stable case study from Perdigão is then studied in more depth to better understand both the ambient and wind turbine wake turbulence characteristics. Novel derived measurements of the turbulence dissipation rate are available from the field campaign, providing an

opportunity to further examine the spatial structure of turbulence predicted by the model. Additionally, in this study, the dynamic reconstruction model (DRM) LES turbulence closure is used to better represent smaller-scale turbulence. The DRM closure more accurately predicts turbulence metrics, including the turbulence dissipation rate, most notably upwind of the major topographic features. After the flow passes over the first ridge, the differences between the DRM and a standard eddy-viscosity closure are small close to the surface, although the DRM closure does better predict the turbulence dissipation rate in the upper atmosphere in this region. Because the DRM closure is not a standard eddy-viscosity closure, negative turbulence dissipation rate or the backscatter of energy from smaller scales to larger scales is predicted; however, backscatter cannot be derived from Perdigão measurements due to the experimental setup and analysis methods used, thus leaving validation of this aspect for future work.

Next, a range of idealized stable boundary layer (SBL) conditions are modeled in support of the American Wake Experiment (AWAKEN) field campaign to address: (1) the effect of wind turbines on SBL development, and (2) the effect of intermittent turbulence on wind farm performance. In weak SBL conditions, turbulence is continuous and easier to simulate. With the intermittent turbulence that occurs in strongly stable conditions, only the DRM closure can resolve realistic turbulence. For all SBL conditions simulated, the wind farm significantly impacts wind speeds and thermal structure well downwind ($> 30D$ or 2.4 km) of the farm. Wind speeds in the wakes are reduced, and the increased mixing as a result of the wakes weakens the stable stratification in the boundary layer.

Finally, simulations are performed of a real case study of intermittent turbulence observed during the AWAKEN field campaign. The intermittent turbulence event is determined to be driven by a nocturnal mesoscale convective system (MCS). The MCS results in a cold pool, which radiates outwards as a density current. This density current perturbs the SBL, thus inducing gravity waves. The structure of the simulated gravity waves is found to be especially sensitive to the parameterization of cloud and precipitation processes (microphysics). The gravity waves have very strong effects on the flow in the upper atmosphere; however, closer to the surface where there is additional ambient turbulence and turbulence generated by wakes, the effect of the waves is more nuanced. Notably, the waves induce local wind direction variation, which leads to fluctuations in the power output as various turbines within the farm are subjected to the wakes of nearby turbines.

The findings presented in this dissertation provide insight into wind farm performance in a broad range of atmospheric conditions by incorporating both terrain effects and thermal stratification. Specifically, these conditions include dynamic turbulent phenomena that current wind farm design tools are unable to capture. The advances in this dissertation related to high-resolution LES reveal novel and complex relationships between wind turbines and the atmosphere that can significantly improve wind farm power predictions at large.

To Boogie

Contents

List of Figures

List of Tables

Acknowledgments

First and foremost, I am thankful for the support from my family. My life partner, Elissa Gray, has been incredibly patient especially when I have been overly consumed by research. She has stood by my side though some incredibly high highs and some really tough lows, which I appreciate more than can be said. I am grateful for the support of my parents who have always ensured that I can pursue what I am passionate about.

I am thankful to my advisor, Tina Chow, for all of the time she has dedicated to me. She has been an inspiration with respect to teaching, mentoring, and as a person. I would like to acknowledge my additional committee members Julie Lundquist, Alexis Kaminski, and Rob Harley. Julie has provided an immense amount of knowledge in the field of wind energy that I am incredibly grateful for. She has grounded my research in a direction that I really appreciate. I feel fortunate that Alexis started as a professor during my time as a PhD student. I appreciate her expertise in stably stratified flow and really appreciate her mentorship.

There are a number of researchers who I have worked closely with throughout my PhD. These researchers include: Bobby Arthur, Jeff Mirocha, Sonia Wharton, Miguel Sanchez-Gomez, and William Corrêa Radünz. The folks at Livermore, especially Bobby, have provided me with endless feedback on my research endeavors and their collaboration have greatly improved my science communication. I am grateful for the countless number of meetings regarding WRF discussion with Miguel and William. When the Chow group thinned out to just me for a time, collaboration with Miguel and William helped me feel less alone in my research and provided me with invaluable feedback.

I would also like to acknowledge Erin Bachynski-Polić and Irene Rivera-Arreba from the Norwegian University of Science and Technology. I really appreciate that I was able to continue collaborations with my former research group in Norway, which allowed me to continue working in offshore wind and provided me with incredible breadth in the wind energy field. Additionally, Sam Kanner and Bingbin Yu from Aikido Technologies gave me an opportunity to work directly in the floating wind industry. Their mentorship gave me real-world experience in wind energy, which was immensely valuable.

I would like to acknowledge the (largely past) members of the Chow group who includes Megnjuan Liu, Alex Connolly, Jason Simon, James Neher, Bowen Zhou, Xioaming Shi, Sienna White, and Mohit Dubey. Even though my time with Alex, Jason, and James was short-lived, they provided me with mentorship and research tools that I continue to use to this day. The additional institutional knowledge provided by Bowen and Xioaming was incredibly helpful. Lastly, I would like to shout out the Environmental Fluid Mechanics & Hydrology research group for fruitful weekly presentations and discussions as well as mentorship and friendship.

Chapter 1

Introduction

1.1 Motivation

Electrical power production from wind energy has grown rapidly over the past two decades. In the year 2000, wind energy accounted for less than 0.15% of electricity generation in the United States (U.S.); as of 2023, wind energy accounts for 10.2% of U.S. electricity generation (U.S. Energy Information Administration, 2024). The levelized cost of energy of wind energy is now on par with conventional gas cycle power plants (and have been for nearly a decade) (U.S. Energy Information Administration, 2022), indicating that wind energy will become an increasingly important part of domestic power production. Additionally, as we face the consequences of the global climate crisis, governments worldwide will continue turning to wind energy as a source of clean, renewable energy in adapting to climate change.

Electrical power generation from wind energy is directly dependent on wind speed. Wind turbines convert the kinetic energy in the wind into usable electrical energy fed back into the grid. This process is a result of wind turbine aerodynamics. Wind turbines (most commonly designed as a three-bladed horizontal axis-type) have blades which generate lift and drag, which rotate the wind turbine rotor in a certain direction. The rotation of the rotor spins a generator to supply electrical energy. As a result of a wind turbine extracting energy from the wind, the wind speed is reduced and turbulence levels are enhanced downwind of the rotor and this is known as a wind turbine wake. Characteristics of the wind turbine wake are slower wind speeds and increased turbulence levels that can be detrimental to neighboring wind turbines when located within a wind farm.

Wind turbines are relatively close to the Earth's surface and thus depend on the wind in the atmospheric boundary layer (ABL). Wind speeds in the ABL are strongly influenced by a number of factors such as synoptic weather patterns, the time of day, topographic features, and other factors discussed later. Prediction of wind speeds is critical for both deciding the location of individual wind turbines and for forecasting power production from existing wind turbines.

Power production from wind farms is difficult to predict due to wake losses among other factors. Wakes result in lower than expected power output and increased structural loading in downstream turbines (Lissaman, 1979; Taylor, 1990; Thomsen and Sørensen, 1999; Frandsen and Christensen, 1994; Frandsen and Thomsen, 1997; Dahlberg et al., 1992). These wakes are highly dependent on the thermal stratification of the ABL; wakes diffuse rapidly and meander due to large-scale eddies that are present in convective conditions, while wakes persist for much greater downstream distances in stable conditions (Hirth and Schroeder, 2013). In addition to the wakes themselves, the background or ambient turbulence is also highly dependent on thermal stratification, with energetic eddies being much smaller during stable conditions. The thermal stratification also plays a significant role for flow over complex terrain where wind turbines are commonly sited to take advantage of accelerating flow over ridgelines. In addition to topographic acceleration, other turbulent flow phenomena that commonly occur in the ABL are mountain waves, low-level jets (LLJs), intermittent turbulence during stably stratified conditions, and recirculation during convective conditions (Stull, 1988). These flow phenomena influence the wind speed a wind turbine sees and also interact with wind turbine wakes which can influence downstream turbines.

The work in this dissertation aims to better understand wind turbine performance in a broad range of atmospheric conditions, especially in stably stratified conditions. The thermal stratification and terrain play a significant role in the type of winds a wind turbine experiences. Many low-cost engineering models only account for the steady behavior of a wind turbine wake and rarely account for terrain effects. Additionally, low-fidelity models largely only account for turbulence in a statistical sense to inform power predictions while failing to account for dynamic flow phenomena, such as intermittent turbulence, that can impact power output. Both how the wind turbine itself interacts with turbulent flow as well as how the subsequent wakes interact with the turbulence is incredibly dynamic and critical for accurate power predictions. The goal in this work is to combine all the necessary physics to accurately simulate wind farm performance in the atmospheric boundary layer while incorporating, critically, the effects of terrain and thermal stratification.

1.2 Atmospheric boundary layer dynamics

Wind turbines sit in the ABL and are thus highly influenced by ABL winds. Over land, the ABL is largely governed by the diurnal cycle as illustrated in Fig. 1.1. As the sun rises, the ABL is heated from the Earth's surface below, generating turbulent mixing or convection, and is thus commonly referred to as the mixed-layer (ML) or convective boundary layer (CBL). The ML grows during the day, and convection results in large-scale turbulent structures that are on the order of the ABL height. The ABL height during day-time, or the ML height, is typically 1 to 2 km.

As the sun sets, the air near the surface is no longer heated but cooled. The stable boundary layer (SBL) develops, which exhibits very different properties compared to the ML. The SBL height is much shallower compared to the ML and is on the order of a few hundred meters. As a result of the surface cooling, the temperature profile is positively

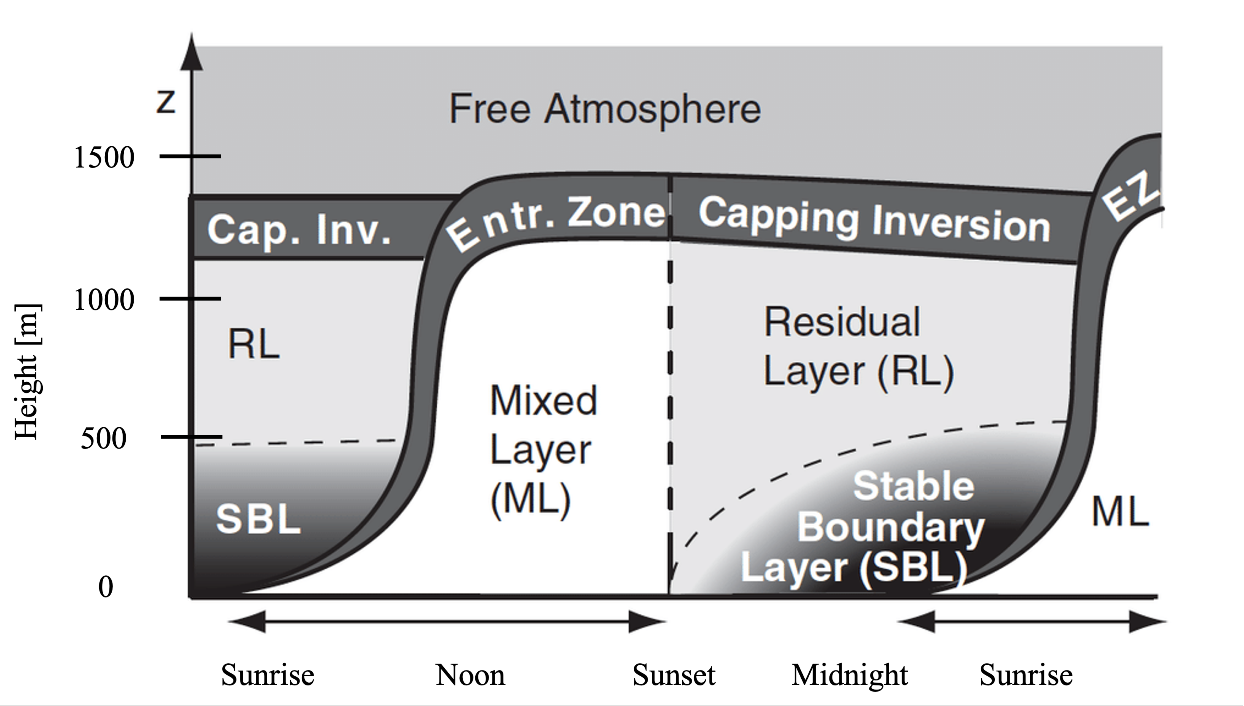

Figure 1.1: Schematic of the diurnal cycle of the atmospheric boundary layer. Image from Stull (2005).

thermally stratified which inhibits mixing. The dominant turbulent structures are on the order of tens of meters, much smaller than in the ML. Additionally, a common feature of the SBL is the nocturnal low-level jet (LLJ). While the LLJ forms due to a number of factors, the overarching reason is due to momentum sinking in the residual layer (RL) above the SBL. As the boundary layer collapses at sunset, higher wind speeds aloft sink to the top of the SBL. The momentum at the top of the SBL forms a balance with Coriolis forcing within the SBL with the added momentum at the top of the SBL considered super-geostrophic. LLJs are a significant reason for increased wind power production at night.

1.3 Complex terrain flow phenomena

The ABL interacts with terrain in a number of complex ways. Figure 1.2 highlights a number of terrain-induced flow phenomena for the site of the Perdigão field campaign, which is a subject of this dissertation. The terrain in Fig. 1.2 is characterized by two parallel ridges. As the flow approaches a ridge, topographic acceleration is observed (which is the main driver for why many wind turbines are located on hilltops). Other terrain-induced phenomena can be highly dependent on the thermal stratification of the ABL. During CBL

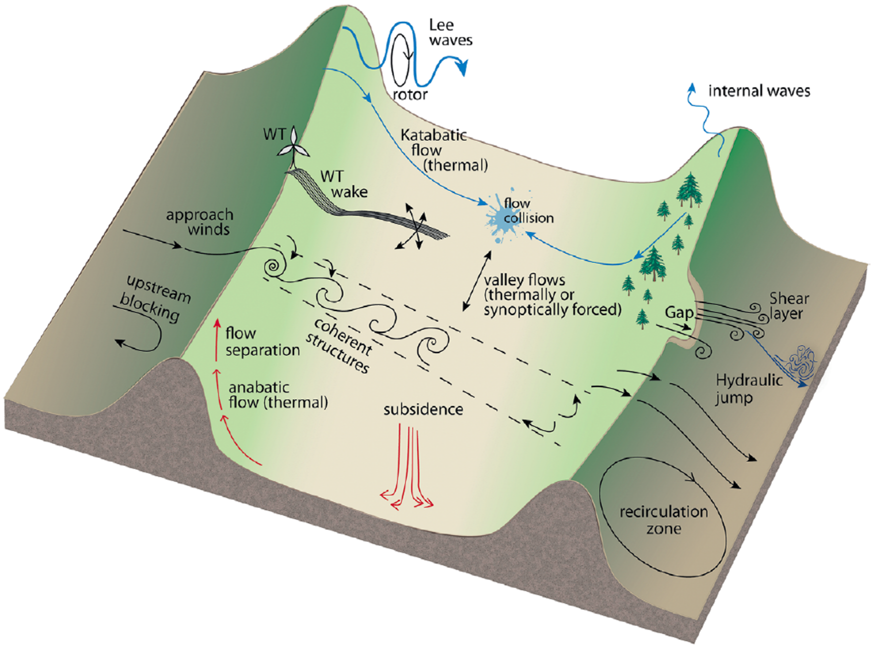

Figure 1.2: Various types of flow phenomena that can occur in complex terrain. Image from Fernando et al. (2019).

conditions, anabatic up-slope flows can occur, while katabatic or down-slope flows can occur during SBL conditions. Additionally during CBL or neutrally stratified boundary layer conditions, flow recirculation can occur in the lee of ridges (Menke et al., 2019). Whether flow recirculation occurs can depend on the wind speed, wind direction, and the surface roughness. In SBL conditions, the positive thermal stratification is conducive to wave-like turbulence. A common feature over topography are mountain or lee waves where the flow deforms into standing waves. Underneath mountain waves, hydraulic jumps and rotors are common turbulent features. Lastly, flow is highly three-dimension in complex terrain. While the wind speeds higher in the atmosphere are largely a result of synoptic forcing, closer to the surface, valley topography can result in phenomena such along-valley or drainage flows.

When considering flow in complex terrain, it is useful to classify the flow behavior as it relates to the Froude number (Stull, 2017). There are various types and definitions of the Froude number, but they exhibit similar properties related to stratified flow approaching a mountain or ridge. When the flow is unstably stratified, the Froude number is undefined and turbulence in the lee of the topographic feature is observed (akin to the recirculation zone previously described). When the flow is stably stratified, lee waves occur with various wavelengths depending on the geometry of the ridge, the depth of the boundary layer, and the speed of the flow. Faster wind speeds result in longer wavelengths, while slower wind speed result in shorter wavelengths. Importantly, when the Froude number is close to unity, a resonance is achieved between the natural wavelength of the wind and the wavelength of the ridge, which results in intense lee waves that can exhibit hydraulic jumps and rotors underneath troughs.

1.4 Intermittent turbulence

The nocturnal SBL is host to a number of unique turbulent phenomena. As mentioned in the previous section, there are a large variety of terrain-induced flow phenomena that occur only in SBL conditions, namely various types of wavy turbulent structures. Wavy turbulence occurs in SBL conditions because of the positive thermal stratification. Buoyancy forces suppress turbulent mixing and as a result, when a fluid parcel is displaced to a higher altitude, the parcel oscillates in a wave-like motion to reach its equilibrium state (Stull, 1988). A fluid parcel can be displaced either due to physical mechanisms such as topography or due to internal mechanisms related to the shear production of turbulence.

The two competing turbulent terms in SBL conditions are shear production and buoyancy suppression. In weaker stability conditions, shear production overcomes buoyancy suppression, which results in continuous turbulence. As stability strengthens and buoyancy suppression becomes harder to overcome by shear, a balance in the forces is reached where turbulence is no longer continuous but intermittent. The Richardson number is one quantity used to define turbulence intermittency and is defined as the buoyancy term divided by the shear term. The balance in shear and buoyancy occurs when the Richardson number Ri is approximately 0.25 (Stull, 1988). When the Richardson number is less than 0, the flow is statically unstable, which describes the CBL. For Richardson numbers greater than 0, the flow is statically stable, but can be broken down into two categories. The flow is dynamically stable and laminar for Richardson numbers greater than 0.25 while the flow is dynamically unstable or turbulent for Richardson numbers between 0 and 0.25. For Richardson numbers between 0 and 0.25, the flow exhibits strong enough shear, inducing shear instabilities of which, perhaps, the most well-known type is the Kelvin-Helmholtz instability. However, these values of the Richardson number assume invsiscid, steady, parallel, non-diffusive stratified shear flows. While the critical Richardson number value (Ri_c) of 0.25 is useful in practice, Ri_c has been observed anywhere between 0.2 and 1.0.

While the Richardson number describes the dynamic stability and formation of turbulence, as previously discussed, there are a number of other physical mechanisms associated with intermittent turbulence Other mechanisms which trigger SBL intermittency include breaking gravity waves, bores, Kelvin-Helmholtz billows, terrain-induced flows, propagating density currents, and more (Rottman and Simpson, 1989; Sun et al., 2002; Banta, 2008), which are often referred to as submeso motions (see Mahrt (2014) and Sun et al. (2015) for thorough reviews on SBL intermittency). Many of these mechanisms were observed to cause SBL intermittency during the the Cooperative Atmosphere–Surface Exchange Study-1999 (CASES-99) (Poulos et al., 2002). For example, Sun et al. (2002) observed three distinct intermittent turbulent events caused by three different phenomena on a single night. Their analysis focused on an event associated with a density current, which induced secondary circulation and generated a shear instability; however, they also determined that solitary waves and downward propagating waves from a LLJ caused the other intermittent turbulent events. Banta (2008) categorically analyzed LLJ properties for CASES-99 and found that at intermediate wind speeds and transitional stabilities (from very stable to less stable), the boundary layer exhibited upside-down structure (Mahrt, 1999) in which the highest turbulence levels are aloft. The upside-down structure was due to downward bursts of turbulence from aloft, as similarly observed by Sun et al. (2002). Traditional boundary layer structure is where turbulence is greatest near the surface and decreases higher in the atmosphere. Coulter and Doran (2002) analyzed the spatial heterogeneity of intermittent turbulent events. They frequently observed events at sites 1 km apart but rarely for sites 20 km in distance implying that intermittent turbulent events tend to be triggered more often locally.

The mechanisms for generating intermittent turbulent events examined in this dissertation are largely physical mechanisms that can perturb a statically stable fluid flow inducing wave-like intermittent turbulence. The most obvious physical mechanism is topography where a ridge-top, for example, can push a fluid parcel upwards thus inducing wavy flow (as seen in Chapters 2 and 3). Another example relevant to the work in this dissertation is a density current in already stably-stratified flow. A real-world example would be a cold pool outflow due to a nocturnal thunderstorm downburst. The colder airmass as a result of the thunderstorm down burst must radiate outwards when it reaches the surface, which then perturbs the existing nighttime SBL and induces waves (see Chapter 5).

1.5 The Weather Research and Forecasting model

To simulate fluid flow in the atmosphere, this dissertation uses the Weather Research and Forecasting (WRF) model as its workhorse. The WRF model is a numerical weather prediction tool and is ubiquitous in atmospheric science research. The WRF model is an open source tool developed by the National Center for Atmospheric Research (NCAR) (Skamarock et al., 2021). The equations that govern fluid flow are numerically solved with a number of input parameters to represent various physical processes that are relevant to atmospheric dynamics.

The fundamental numerical differencing schemes typically used with WRF include a third-order Runge-Kutta scheme in time with fifth-order horizontal and third-order vertical advection schemes in space. The WRF model uses an Arakawa C-staggered grid with a Cartesian coordinate system in the horizontal dimensions and a terrain-following coordinate system in the vertical dimension. WRF uses a multi-scale grid nesting framework to capture a wide range of scales in fluid flow relevant to a wide range of problems. Grids are simulated concurrently with the nesting framework, meaning that lateral boundary conditions are provided by a parent or coarser domain (for the standard one-way nesting approach). For the coarsest domain, lateral and initial boundary conditions are provided by different methods depending on whether WRF is run in an “ideal” or “real” configuration. In an idealized setup, the lateral boundary conditions are periodic with initial conditions provided by an input sounding with vertical profiles of the geostrophic wind speed, potential temperature, and moisture. Real setups are more complex with initial and lateral boundary conditions provided by analysis data, which can come from global or regional models. Some examples of models typically used to force real WRF simulations are the Global Forecasting System (GFS), the European Centre for Medium-range Forecasting (ECMWF) Reanalysis v5 (ERA5), or the High-Resolution Rapid Refresh (HRRR) v4, to name a few.

While the standard WRF modeler is concerned with weather systems that are referred to as mesoscale, this work is also concerned with micro-scale winds, which the WRF modeling framework is well-suited for. The grid nesting native in WRF can capture a range of turbulent scales from larger-scale synoptic and meso-scales all the way down to micro-scale ambient turbulence. On mesoscale grids $\mathcal{O}(1-10)$ km, turbulence is parameterized using a single-column planetary boundary layer (PBL) scheme. Considering the coarse resolution of mesoscale grids, the WRF model solves the Reynolds-Averaged Navier Stokes (RANS) equations of motion since smaller-scale turbulence cannot be resolved on such a grid. As a result, the quantities smaller than the grid resolution, which also tend to be the most energetic in the atmosphere, must be parameterized. PBL schemes parameterize the vertical diffusion or turbulence, with various PBL schemes employing different methods. For example, the Mellor-Yamada-Janjić (MYJ) PBL scheme determines eddy diffusion coefficients by predicting local turbulent kinetic energy (Janjić, 1994). Whereas the Yonsei University (YSU) PBL scheme uses non-local eddy diffusivity with an explicit treatment of entrainment processes at the top of the PBL (Hong et al., 2006). There are many other PBL schemes available in WRF, which are described in Skamarock et al. (2021). On microscale $\mathcal{O}(< 300)$ m grids, a RANS approach with a PBL scheme is no longer appropriate, as the most energetic scales can be resolved on the grid itself (Wyngaard, 2004). At these scales, the technique used to simulate the fluid flow is large-eddy simulation (LES), which explicitly solves for the most energetic turbulent motions (eddies) while parameterizing the smaller-scale effects on the fluid flow. This method is most relevant to the work in this dissertation and described in more detail in the following section.

It is worth briefly mentioning the *Terra Incognita* or “gray zone” and its relevance to modeling the wide range of scales in the atmosphere (Wyngaard, 2004; Shin and Hong, 2015; Chow et al., 2019; Honnert et al., 2020). There exists a range of scales from roughly 300 to 1000 m where neither a PBL scheme nor LES is appropriate (although this range can depend on the thermal stratification of the atmosphere (Zhou and Chow, 2014)). Within the scope of this dissertation, the “gray zone” is largely navigated by skipping those grid resolutions. Many of the methods used in the present work could be used within the gray zone, but this is left to future work.

1.6 Large-eddy simulation

Large-eddy simulation (LES) is a robust method for simulating and resolving turbulent scales in the atmospheric boundary layer (Smagorinsky, 1963; Deardorff, 1970). The multi-scale grid nesting framework in WRF provides for a seamless transition from larger meso-scale grids where turbulence is parameterized using a PBL scheme to micro-scale grids where LES is used. LES explicitly solves for the most energetic eddies in the flow while parameterizing the effect of the smaller-scale motions on the resolved flow. The governing equations in LES are as follows:

$$\frac{\partial \overline{u_i}}{\partial t} = -\overline{u_j}\frac{\partial \overline{u_i}}{\partial x_j} - \frac{1}{\bar{\rho}}\frac{\partial \bar{P}}{\partial x_i} - \frac{\partial \tau_{ij}}{\partial x_j} + F_i \tag{1.1}$$

where u_i is the fluid velocity in the corresponding direction, P is fluid pressure, ρ is the fluid density, τ_{ij} is the turbulent stress, and F_i represents a body force (which represents the wind turbine parameterization in this study). From left to right, the terms represent the local flow acceleration, advection, pressure gradient, turbulent diffusion, and forces imparted on the flow. The overbar represents the spatial filter used in LES. The spatial filter is implicitly defined by the grid resolution LES with filtered quantities being explicitly resolved and other quantities being parameterized. Other methods for filtering Equation 1.1 such as defining an explicit filter are used in this study and are described in detail in the relevant chapters of work.

The turbulent stress term represents the turbulence closure problem in computational fluid dynamics and is commonly defined in its most basic form using an eddy-viscosity model:

$$\tau_{ij} = -2\nu_T \left(\frac{\partial \overline{u_i}}{\partial x_j} + \frac{\partial \overline{u_j}}{\partial x_i} \right) \tag{1.2}$$

where ν_T is the turbulent viscosity. The turbulent stress term is referred to as the subfilter stress in LES as it represents motions smaller than the spatial filter scale (which is typically defined by the grid). The eddy-viscosity relation defined in Equation 1.2 represents a gradient diffusion approach which is an analog to molecular Fickian diffusion.

Three LES turbulence closures are explored in the present work. The first is the turbulent kinetic energy 1.5-order (TKE-1.5) model of Deardorff (1980). The TKE-1.5 closure is one of the standard closures available in WRF and uses an eddy-viscosity formulation as described above. The turbulent viscosity is defined using a characteristic velocity scale determined by solving the prognostic turbulent kinetic energy equation. The turbulent length scale is proportional to the grid spacing. The next two closures both define an explicit filter in addition to the implicitly defined spatial filter in Equation 1.1. The Dynamic Wong Lilly (DWL) (Wong and Lilly, 1994) closure is also an eddy-viscosity model but the explicit filter is used to help determine the turbulent viscosity dynamically using the least-squares method of Lilly (Lilly, 1992). The final method used in this work is the Dynamic Reconstruction Model (DRM) closure of Chow et al. (2005). The DRM closure utilizes the DWL closure for the eddy-viscosity but also includes a resolvable subfilter-scale (RSFS) stress which represents the range of eddy motions between the implicit and explicit filters. More details on the specific methods used in each closure can be found in Chapter 3.

Turbulence closures are a focus in this dissertation because of the difficulty in modeling SBL conditions when using LES. The most energetic turbulent eddies in SBL conditions are on the order of tens of meters, and thus a very small grid spacing is required to resolve these structures, which becomes computationally intensive. There are various methods used to spur turbulence in SBL conditions, such as the Cell Perturbation Method (CPM) (Muñoz-Esparza et al., 2014; Muñoz-Esparza et al., 2015; Muñoz-Esparza and Kosović, 2018) used in this work, but in general dynamic turbulence closures have been shown to outperform conventional closures at coarser grid resolutions (Zhou and Chow, 2011; Zhou and Chow, 2014). Additionally, the DRM closure is able to physically represent negative turbulent dissipation rates or what is known as backscatter, which is the phenomena of smaller turbulent eddies combining into larger turbulent eddies. The backscatter of energy has been observed to be especially important in SBL conditions (Sullivan et al., 2003). This work explores the performance of the TKE-1.5, DWL, and DRM in the context of flow through wind turbines in terrain.

Lastly, the body force defined in Equation 1.1 is used to represent the wind turbine rotor parameterization used in the present work. The generalized actuator disk (GAD) of Mirocha et al. (2014a) is used, which uses properties of a wind turbine model to determine how the turbine affects the fluid flow. The GAD parameterization requires wind turbine power and thrust curves as well as airfoil lift and drag coefficients along the spanwise distance of the blades. These properties are used in conjunction with blade element momentum theory (Mikkelsen, 2003; Wu and Porté-Agel, 2011; Sørensen and Mikkelsen, 2001; Sørensen et al., 1998; Aagaard Madsen, 1997; Glauert, 1963) to determine the normal and tangential forces the wind turbine imparts on the flow within each grid cell as power is converted from the kinetic energy in the wind to electrical energy.

1.7 Summary of chapters

This dissertation focuses on a variety of turbulent atmospheric phenomena with a wind turbine parameterization to understand turbine-airflow interactions. The focus of Chapters 2 and 3 is on modeling the Perdigão field campaign which consisted of a single wind turbine located on top of a ridge. Chapter 2 focuses on the wind turbine wake interaction with two different terrain-induced flow phenomena: a recirculation zone during a CBL case study and a mountain wave during an SBL case study. Chapter 3 more closely examines the SBL case study from Chapter 2 with a special focus on turbulence characteristics both in the ambient flow as well as in the wind turbine wake. Chapters 4 and 5 are done as part of the American Wake Experiment (AWAKEN) field campaign, where the focus is on SBL interactions with a wind farm. Chapter 4 is an idealized study with a nine-turbine wind farm from weak to strong SBL conditions to understand the two-way interaction between wind farms and SBL evolution. In the most strongly stratified SBL conditions, intermittent turbulence is resolved. Chapter 5 is a real study for the eastern half of the King Plains Wind Farm in North-Central Oklahoma. A case study is identified where a thunderstorm outflow perturbs the SBL generating intermittent turbulence (gravity waves) and a model is used to understand how the gravity waves affect wind farm performance. A brief summary of each chapter is provided below.

In Chapter 2, we build a multi-scale nested WRF setup of the site from the Perdigão field campaign with an aim at understanding the vertical behavior of wind turbine wakes as this is not typically accounted for in simple wake models used in wind farm design. The Perdigão site has two parallel ridges with a wind turbine on top of one of the ridges. The complex terrain from the Perdigão site was rigorously instrumented with a number of measurement sites, which are used for model validation. From observations, there was conflicting data on how the wind turbine deflects in the vertical direction. Two case studies are identified as representative flow conditions to examine this question. The first case study is during CBL conditions where a recirculation zone in the lee of the ridge was observed. Flow recirculation was observed to occur over 50% of the time when the flow was oriented perpendicular to the ridge. The second case study is during SBL conditions when a LLJ is modulated by the topography and deforms into a mountain wave. Mountain waves were found to happen on 50% of the nights during the field campaign. The vertical wake behavior is found to be distinct in each of the two case studies, deflecting down along with the mountain wave for the stable case study and upwards above the recirculation zone for the convective case study.

Chapter 3 takes a step further to focus on the turbulence statistics from the stable case study in Chapter 2, with a goal of improving the representation of small-scale turbulence during SBL conditions. With an aim to improve the representation of small-scale turbulence, we use the DRM closure on the micro-scale domains of the multi-scale nested WRF setup. The DRM closure has not yet been rigorously tested in complex terrain and, additionally, this is one of the first studies (along with the work in Chapters 4, 5, and 6) to use the DRM closure with a wind turbine parameterization. The nested setup is also simulated with the TKE-1.5 closure on the micro-scale domains to serve as a reference or the standard. A novel focus of this study is on comparing model predictions of the turbulence dissipation rate, which were derived from observations, including, recently, from a scanning lidar in complex terrain for the first time. The DRM closure captures more small-scale turbulence on the same grid as the TKE-1.5 closure most notably in the upwind blockage region of the first; however, downwind of the first ridge where the flow is significantly affected by the terrain, the difference between the closures is minor. The turbulent dissipation rates predicted by the two closures are similar and match observations in the near-surface region but with weaker agreement in the upper atmosphere. However, it is important to remark that the uncertainty in the observed turbulent dissipation rate increases drastically in the upper atmosphere where turbulence levels are low. Nonetheless, the DRM closures does offer improved predictions compared to the TKE-1.5 closure in the upper atmosphere. The DRM closure also shows negative turbulent dissipation rates or the backscatter of turbulence from smaller scales to larger scales, which the TKE-1.5 closure is unable to capture; however, additional measurements and observational analysis methods are needed to validate the model predictions of backscatter.

In Chapter 4, the focus shifts to modeling work for the AWAKEN field campaign. Two of the major research questions of the field campaign are: (1) how the phenomenon of turbulence intermittency affects wind farm power production and (2) how wind farms impact boundary layer development. An idealized study is conducted where the surface is cooled at different rates to represent, weak, moderate, and strong SBL conditions. The model setup uses a unique grid nesting approach with doubly periodic lateral boundary conditions on the parent domain used to spin up turbulence with a child domain at the same grid resolution with a number of individual wind turbine rotor parameterizations. This setup ensures turbulent structures are developed on the parent domain and passed into the child domain with the wind turbines where the wakes are contained within the child domain and not recirculated. The child domain contains 9 wind turbines located in a 3 × 3 grid to represent a wind farm. Again, the TKE-1.5 and DRM turbulence closures are compared with the DRM closure showing improved turbulence representation, especially in strong SBL conditions where intermittent turbulence is resolved solely with the DRM closure. The effect of intermittent turbulence on wind farm performance increases power output variability and but not average power production. In all SBL conditions analyzed (including strong SBL conditions with intermittent turbulence), the wind farms have a significant impact on the SBL evolution, which includes the wind speeds and thermal structure of the boundary layer well downwind of the farm.

In Chapter 5, a real case study is performed with WRF for a wind farm from the AWAKEN field campaign, with the goal of understanding the generation mechanism for gravity waves in the Southern Great Plains and the subsequent gravity wave-wind farm interaction. Gravity wave-wind farm interaction is a major focus for the AWAKEN field campaign. While gravity wave-wind farm interaction is a highly active research area (Allaerts and Meyers, 2018; Stipa et al., 2024; Devesse et al., 2022; Lanzilao and Meyers, 2022), it is important to note that this study focuses on gravity waves generated independently of wind farms (naturally, in the atmosphere) as is common in the Southern Great Plains. A novel grid nesting setup is designed in WRF, using 3-km HRRR v4 data to force domains at 300 m and 20 m horizontal grid spacing. The domain sizes are quite large (360 km × 360 km and and 13.2 km × 17.4 km for the 300 m and 20 m domains, respectively) to allow mesoscale flow features and their interactions with the wind farm to be captured by the model. On the coarser, 300 m domain, a mesoscale convective structure is resolved and results in a downdraft of colder temperatures. These temperatures form a density current that perturbs the SBL, thus inducing gravity waves. The structure of these waves are found to be especially sensitive to how cloud processes are parameterized with various microphysics schemes. On the 20 m turbine-resolving grid, the effect of the turbulence closure is also examined. As expected, the dynamic closures better resolve the smaller-scale turbulent structures, which provides for more realistic wind turbine wake representation. While the gravity waves are well-defined higher in the atmosphere, their effect closer to the surface and at wind turbine rotor heights is less defined; however, there is a strong dependence on the local wind direction to the waves which results in power losses from waking. This study represents the first

LES study modeling observed gravity waves, including the physical generation mechanism, and their subsequent effect on a wind farm.

In the concluding chapter, a summary of the dissertation is provided along with recommendations for future work.

1.8 Summary of contributions

Listed below are the major contributions of this dissertation work for each of the four major research chapters.

Chapter 2 - Wind turbine wake behavior in complex terrain. This study is published in *Wind Energy Science*.

- Simulations with a wind turbine parameterization and highly complex terrain in non-neutral stability conditions for the first time using high-resolution multi-scale LES.
- The first model validation of the Perdigão field campaign site comparing results from LES with a multitude of measurement devices. Some novel comparisons between model results and measurement devices including a tethered lifting system which collects in-situ data as it moves upwards and downwards as well as four scanning Doppler lidars forming a nearly 8 km long transect.
- Modeling results and analysis contributed to the research question on the vertical behavior of the wind turbine wake in representative flow conditions. Previous literature based on observations of vertical wake behavior at the Perdigão site was conflicting.

Chapter 3 - Small-scale and wind turbine wake turbulence in complex terrain. This study is to be submitted to the *Journal of the Atmospheric Sciences*.

- First study combining the DRM closure, a wind turbine parameterization, and highly complex terrain using high-resolution multi-scale LES.
- Analyze modeled wind turbine wake turbulence characteristics in complex terrain for the first time using high-resolution multi-scale LES.
- Comparisons of modeling results with measurements included a number of novel methods such as the first retrieval of turbulence dissipation rate from a scanning lidar in complex terrain.

Chapter 4 - Wind farm performance in a range of stable atmospheric conditions. This study is in review for the AWAKEN Special Issue in the *Journal of Renewable and Sustainable Energy*.

- First LES study parameterizing wind turbines in such a broad range of stably stratified atmospheric conditions (from cooling rates of -0.2 to -2.0 K hr^{-1}).

- Demonstrate the merits of using the DRM closure for simulating stably stratified atmospheric conditions at coarser resolutions compared to conventional closures, thus decreasing computational cost and increasing efficiency.
- First study to combine intermittent turbulence with a wind turbine parameterization. Implement a novel method for quantifying intermittent turbulence and demonstrate how the power output of a wind farm could be affected by intermittent turbulence.

Chapter 5 - Effect of an atmospheric bore and associated gravity waves on wind farm performance. This study is to be submitted to *Wind Energy Science*.

- Simulations with a unique high-resolution multi-scale LES nested setup by incorporating the HRRR model v4 as forcing for the coarsest domain. Demonstrate how a nested setup should be designed when simulating an atmospheric bore and associated gravity waves generated as a result of a mesoscale convective system.
- Decouple the DWL implementation in WRF from the DRM implementation thus providing for an additional dynamic LES turbulence closure but with reduced computational cost compared to the DRM closure. This study is computationally feasibly due to the unique nested setup and, in part, due to using dynamic turbulence closures at relatively coarse (20 m) horizontal grid spacing, increasing computational efficiency.
- First study simulating an observed intermittent (wavy) turbulence phenomena and its effect on a real wind farm's performance using high-resolution multi-scale LES. Furthermore, the first study simulating the generation of gravity waves due to nocturnal mesoscale convection while also nesting down capturing smaller-scale turbulence necessary to incorporate a wind turbine parameterization.
- Demonstrate gravity wave effects at heights relevant to wind turbines. Novel analysis for how wind direction and pressure are correlated and how that can affect wind farm power output.

In addition to the publications associated with the four major research chapters in this dissertation, the present work supported two co-author publications in *Wind Energy*:

- "Effect of atmospheric stability on the dynamic wake meandering model applied to two 12 MW floating wind turbines" by Irene Rivera-Arreba, Adam S. Wise, Lene V. Eliassen, Erin E. Bachynski-Polić, Sep 2023. (Rivera-Arreba et al., 2023)
- "Effects of atmospheric stability on the structural response of a 12 MW semisubmersible floating wind turbine" by Irene Rivera-Arreba, Adam S. Wise, Mahé Hermile, Fotini K. Chow, and Erin E. Bachynski-Polić, July 2022. (Rivera-Arreba et al., 2022)

Chapter 2

Wind turbine wake behavior in complex terrain[1]

2.1 Introduction

Wind turbines are commonly sited in complex terrain to take advantage of topographic flow enhancement, such as the acceleration of flow over ridge lines and hill tops. In addition to topographic acceleration, other terrain-induced flow phenomena in the atmospheric boundary layer (ABL) affect wind turbine performance and wake propagation and characteristics (Xia et al., 2021; Draxl et al., 2021). These microscale processes include mountain/lee waves (and associated rotors), hydraulic jumps, valley flows, and flow separation/recirculation (Fernando et al., 2019; Baines, 1998).

The dynamics of terrain-induced flow phenomena vary based on the time of the day, with lee waves only occurring during stably stratified conditions, typical at night, and flow separation or recirculation often occurring during daytime convective (or unstably stratified) conditions. Interactions of the terrain with different stability conditions thus impact both the background flow and the resulting turbine performance. The difficulty of capturing the interaction between wind turbine wakes and complex terrain has historically limited research studies to wind tunnel experiments and numerical simulations with simple Gaussian and sinusoidal hills (see Porté-Agel et al. (2020) for a recent review on wind farm flows and topography). Additionally, turbine wake models used for designing wind farms typically do not account for terrain-induced flow phenomena and their effects on turbine wake behavior. Increased knowledge of wind flows in complex terrain is therefore critical to improve predictions to support growing wind energy resources (Veers et al., 2019).

---

[1] This chapter is a modified reproduction of the article “Meso-to micro-scale modeling of atmospheric stability effects on wind turbine wake behavior in complex terrain” by Adam S. Wise (the principal author), James M. T. Neher, Robert S. Arthur, Jeffrey D. Mirocha, Julie K. Lundquist, and Fotini K. Chow, first published in *Wind Energy Science*, Feb 2022, Volume 7, pages 367-386 (Wise et al., 2020), © 2022 Copernicus.

In the present work, we use large-eddy simulation (LES) to examine the wake behavior of a wind turbine situated in complex terrain. LES explicitly solves for the most energetic eddies while parameterizing the effects of the smaller turbulent length scales on the resolved-scale flow. LES can therefore capture transient turbulent flow structures, which are important features of the ABL that interact with turbine wakes. While LES is computationally expensive, and thus requires the use of substantial high-performance computing resources, LES is increasingly complementing and in some cases replacing lower-fidelity techniques as a means to investigate wind turbine wake effects (see Stevens and Meneveau (2017) for a recent review). Specifically, we utilize the LES capability of the Weather Research and Forecasting (WRF) model (Skamarock et al., 2008; Powers et al., 2017) for our simulations.

The multi-scale framework in WRF dynamically downscales mesoscale forcing to microscale LES using a grid nesting approach, with lateral boundary conditions provided from each parent domain. Such setups can provide LES with realistic time-varying inflow conditions directly from the mesoscale simulations.

Implementation of a wind turbine actuator disk parameterization within the nested LES domain provides a unique turbulence-resolving simulation framework for wind turbine wake prediction in turbulent flow settings under more realistic environmental and atmospheric forcing conditions. This study utilizes a generalized actuator disk (GAD) wind turbine parameterization on the finest domain following Mirocha et al. (2014a) and Wu and Porté-Agel (2011). In the GAD parameterization, thrust and rotational forces computed at the turbine's blades are averaged over a discretized two-dimensional disk formed by their rotation. These forces are then applied to the flow surrounding the turbine, capturing both the velocity deficit and rotation of the wake, which simpler parameterizations (such as the Fitch et al. (2013) wind farm parameterization) neglect. The GAD tool has been previously validated and shown to capture turbine-airflow interactions and wake behavior at grid resolutions of 10 m in simple terrain (Mirocha et al., 2015; Aitken et al., 2014; Marjanovic et al., 2017; Arthur et al., 2020). However, the multiscale WRF-LES-GAD framework (hereinafter used to denote the model in its entirety) has yet to be evaluated in complex terrain where the combination of terrain and thermal stratification directly affects the flow and impacts operating turbines.

The test location chosen in this study is that of the Perdigão field campaign (Fernando et al., 2019), which took place in 2017 in Portugal. The Perdigão experiment characterized the flow over two parallel ridges with a wind turbine located on the southwest ridge and provided valuable data for characterizing wind turbine wakes in complex terrain (Menke et al., 2018; Barthelmie and Pryor, 2019; Wildmann et al., 2018; Wildmann et al., 2019). Menke et al. (2018) classified wind turbine wake behavior based on atmospheric stability using scanning Doppler lidars at Perdigão, identifying four different cases based on the stratification: a “stable + mountain wave” case where the wake deflected downwards following the terrain, “stable” and “neutral” cases where the wake remained at a constant height above sea level, and “unstable” cases where the wake deflected upwards. Barthelmie and Pryor (2019) similarly characterized wake behavior at Perdigão based on atmospheric stability. Using measurements averaged over longer time periods (10 minutes compared to 24 seconds in Menke et al. (2018)), they inferred that all wakes were initially lofted and then strongly influenced by stability, with wake centers moving downwards in unstable conditions and also generally moving downwards but remaining at greater heights during stable conditions. The different findings in these two studies motivate the need to further study wind turbine wakes in complex terrain.

Two fine-scale ($\Delta x = 10$ m) LES modeling studies of the Perdigão campaign have been conducted with a wind turbine parameterization, both in idealized conditions with neutral stability. Berg et al. (2017) performed idealized LES of the Perdigão site in neutral atmospheric stability conditions and showed that the steep terrain in Perdigão resulted in the formation of a recirculation zone with which the wake did not interact. Instead, the wake advected at a constant height above sea level like the "neutral" case characterized by Menke et al. (2018). Dar et al. (2019) also simulated the Perdigão site using idealized LES to examine the self-similarity of wind turbine wake behavior as a function of varying terrain complexity under neutral stratification. They found that self-similarity is preserved for a shorter distance compared to what is observed in flat terrain and that the wake propagation was similar to that seen by Berg et al. (2017). There have also been been two relatively coarse nested LES studies of the Perdigão campaign by Connolly et al. (2021) and Wagner et al. (2019a), where grid resolutions of 150 m and 200 m were used, respectively, with both utilizing the LES capability of WRF. The findings from these studies have provided guidance for the setup used in this study (as discussed in Section 2.3) but their setups are too coarse to resolve a utility-scale wind turbine with a rotor diameter of 80 m.

The goal of this work is to examine the ability of the WRF-LES-GAD framework to capture terrain-induced flows and their interaction with an operating wind turbine at the Perdigão site (described further in Sect. 2.2), to thereby demonstrate the efficacy of mesoscale-to-microscale coupled simulations to improve wind plant simulations in complex terrain. We focus on two distinct but representative case studies with different atmospheric stability regimes, convective and stable, both of which were commonly observed during the field experiment. We validate the predicted flow structure and turbine wake behavior during each case study using comparisons with observations from meteorological towers, scanning lidars, and a tethered lifting system (Sect. 2.4). Furthermore, we present a detailed analysis of the turbine wake in both stability regimes in order to comment on the discrepancy in the observational studies discussed above.

2.2 Case Study

Overview of the Perdigão campaign

The Perdigão field campaign was a European Union - United States collaboration of over 70 scientists, engineers, and support personnel. The Perdigão site, named for a village located near the Vale do Cobrão in eastern Portugal, consists of two parallel ridges with a 2 megawatt (MW) wind turbine located on the southwest ridge (see Fig. 2.1). This site was selected

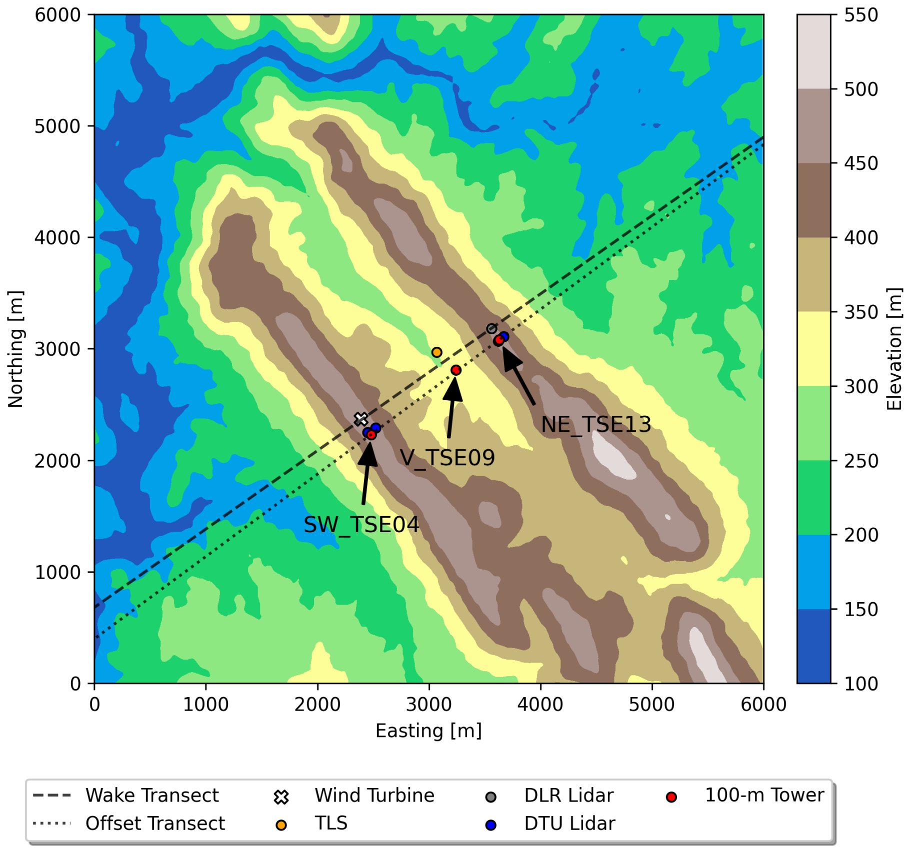

Figure 2.1: Terrain and layout of the Perdigão site showing the location of relevant instrumentation. The Wake and Offset Transects are used for analysis later in this chapter. Each of the three 100 m meteorological towers is labeled following the naming convention in the publicly available dataset corresponding to their geographic location.

because the straight valley extends over 2 km in distance, suggesting that the flow could be representative of an idealized two-dimensional valley flow in nature. Additionally, the annual climatology showed that common wind directions measured at ridge-top are perpendicular to the ridges (Fernando et al., 2019).

During the intensive operation period from 1 May 2017 to 15 June 2017, a comprehensive, high-resolution dataset was collected. Instrumentation included 100-m meteorological towers (hereinafter referred to as met towers), lidars, a tethered lifting system (TLS), and numerous shorter meteorological towers and radiometers. The instrumentation of interest is discussed here, and the layout of the Perdigão field site is shown in Fig. 2.1.

Three 100-m met towers were placed along a transect roughly perpendicular to the ridges (see Fig. 2.1). SW_TSE04, located approximately 150 m southeast of the wind turbine laterally along the ridgeline, is representative of inflow conditions. V_TSE09 is located in the valley, and NE_TSE13 is on the northeast ridge. These three towers have booms angled at 135° from north located at heights of 10, 20, 40, 60, 80, and 100 m with sonic anemometers sampling three-dimensional velocity at 20 Hz. In this paper, data representative of near surface winds (10 m) and at hub-height (80 m) are examined. Temperature sensors available at 10 m and 100 m are used to characterize atmospheric stability using a simple temperature gradient similar to Menke et al. (2019).

A tethered lifting system (TLS) from the University of Colorado, Boulder, was also launched from the valley. The TLS is a unique device that is able to obtain in-situ measurements of wind speed, wind direction, and temperature aloft at 1 kHz (Balsley, 2008). GPS measurements of latitude, longitude, and altitude are sampled at 5 s. When in profiling mode, the TLS ascends and descends at $\sim$0.3 m s^{-1} and covers a vertical range of $\sim$400 m. The capabilities of the TLS have been demonstrated in several field campaigns, including a previous wind turbine wake investigation (Lundquist and Bariteau, 2015).

Simulation results are also compared with scanning Doppler lidar data. The first is a scanning lidar operated by the German Aerospace Center (DLR) located on the northeast ridge (Wildmann et al., 2018). This lidar's scanning trajectory is perpendicular to the wind turbine rotor allowing for the wake to be captured in addition to relevant flow features in the valley. The second set of scanning lidars used here were operated by the Danish Technical University (DTU) (Menke et al., 2020). Four lidars, two on each ridge, scanned a transect perpendicular to the valley. Because of how the lidars are arranged, a multi-Doppler lidar scan of the valley, the two ridges, and the surrounding area can be formed. This multi-Doppler lidar scan does not capture the wind turbine wake but does show microscale features that interact with the wind turbine wake (as seen later in Figure 2.4).

Case Studies and Phenomena of Interest

Two terrain-induced flow features characteristic of the field site are of interest for the present work: (a) mountain waves and (b) recirculation zones, which occur frequently at the Perdigão site depending on the time of day (Menke et al., 2019; Fernando et al., 2019; Wagner et al., 2019a). Fernando et al. (2019) found that mountain waves occurred for almost 50% of the nights during the intensive operation period while Menke et al. (2019) found that recirculation occurred over 50% of the time when the wind direction was perpendicular to the ridges. To help select appropriate time periods representing mountain waves and recirculation zones, we examine a few stability parameters.

Mountain waves can occur when stably stratified flow approaches a topographic disturbance, such as a mountain ridge. These waves can be described using a ratio of inertial to buoyant forces represented by the internal Froude number (Stull, 1988),

$$Fr = \frac{\pi U}{WN}, \tag{2.1}$$

where W is the mountain ridge width (defined for the southwest ridge of Perdigão to be 586.5 m on average according to Palma et al. (2020)), U is the free stream wind speed, and N is the Brunt-Väisälä frequency, defined as:

$$N = \sqrt{\frac{g}{\theta}\frac{d\theta}{dz}}. \tag{2.2}$$

Here g is the gravitational constant, θ is the potential temperature of the environment, and $\frac{d\theta}{dz}$ is the lapse rate or vertical gradient in potential temperature. The internal Froude number can also be defined as the ratio of the natural wavelength of the air ($\lambda = 2\pi U N^{-1}$) to the effective wavelength of the mountain ridge ($2W$).

For subcritical flow ($Fr < 1$), when wind speeds are low or the stability is very strong, λ is much shorter than $2W$ resulting in weak mountain waves. Mountain waves resonate when $Fr \sim 1$, resulting in strong up and downdrafts where rotors (and potentially hydraulic jumps) are present (Jackson et al., 2013). When wind speeds are strong and stability is weak, $Fr > 1$ and flow is supercritical resulting in long wavelengths with the potential for reverse flow in the lee of the mountain.

Neutral and convective conditions represent the theoretical case of $\mathrm{Fr} \sim \infty$, when a turbulent mountain wake with recirculation forms instead of mountain waves. Relevant to this study are $\mathrm{Fr} \approx 1$ during stable conditions and $\mathrm{Fr} \approx \infty$ during convective conditions. For more information regarding mountain waves, the reader is referred to Stull (1988), Baines (1998) and Jackson et al. (2013).

Quantifying atmospheric stability in complex terrain is an active research area. Using a gradient Richardson number is difficult because of the effect of terrain-induced flow-speedup over the ridge affecting the shear terms (Menke et al., 2019). Bodini et al. (2020) calculated the Obukhov length for Perdigão and found that it was not very powerful in predicting dissipation rate. Despite this, the Obukhov length is still useful for selecting stable and unstable case studies. The Obukhov length, L, is defined as

$$L = \frac{-u_*^3\theta}{\kappa g \overline{w'\theta'}}, \tag{2.3}$$

where u_* is the friction velocity, κ is the von Kármán constant (taken as 0.4), w is the vertical velocity, and $w'\theta'$ is the surface heat flux. The prime denotes fluctuations and the overbar a mean. The friction velocity is defined as

$$u_* = \left(\overline{u'w'}^2 + \overline{v'w'}^2\right)^{1/4} \tag{2.4}$$

The Obukhov length and friction velocity, valid for the surface layer, are calculated at SW_TSE04 using 5 minute statistics from the lowest sensors available at 10 m. Obukhov lengths between 0 and 500 are considered stable and 0 to -500 unstable.

In addition to the Obukhov length, the potential temperature gradient between 10 m and 100 m at SW_TSE04 is used as a proxy for atmospheric stability throughout this study and when comparing observations with the model. Note that SW_TSE04 was not outfitted with any pressure sensors; therefore, the potential temperature is approximated by $\theta \approx T + (g/C_p) \cdot z$ where $(g/C_p) = 0.0098$ K m^{-1} as was done by Menke et al. (2019). Fig. 2.2 shows wind speed, direction, temperature gradient, and Obukhov length for two different dates during the field campaign, and representative time periods are selected from these for the stable and convective case studies. The met tower measured periods of counter-gradient heat fluxes during both stable and convective conditions but not during the time periods selected for this tower location.

Case 1: Stable Conditions

The early morning of 14 June 2017 shows typical stably-stratified conditions as indicated by a positive temperature gradient and Obukhov length in Fig. 2.2(e) and Fig. 2.2(g), respectively. From 04:00 to 06:00 UTC (05:00 to 07:00 local time, with sunrise at 06:02 local time), the hub-height wind direction is relatively constant between 200° and 220° (Fig. 2.2(c)). These wind directions are close to a southwesterly wind of 215°, perpendicular to the ridges. The average wind speed is 6.3 m s^{-1}, a speed in which the turbine will operate and generate wake effects. Using the average wind speed (6.3 m s^{-1}), temperature gradient or lapse-rate (0.031 K m^{-1}), potential temperature of the environment (296.7 K), and width of the southwestern ridge of Perdigão (586.5 m), the average internal Froude number during the period of interest is calculated to be 1.05. With a Froude number close to one, we expect a resonant mountain wave to occur.

Case 2: Convective Conditions

Typical daytime convective conditions on 13 May 2017 are indicated by the negative temperature gradient and Obukhov length in Figs. 2.2(f) and 2.2(h), respectively. For much of the day (08:00-16:00 UTC, 09:00-17:00 local time), the temperature gradient is approximately -0.005 K m^{-1}. During the period of interest (13:00-14:00 UTC) a wind speed of 7 m s^{-1} causes the wind turbine to operate and generate wake effects. The negative lapse rate results in an infinite internal Froude number and with wind perpendicular to the ridge a turbulent mountain wake with recirculation should form.

2.3 Methods

WRF-LES-GAD

The present work utilizes the large-eddy simulation capability of the WRF model, version 3.7.1, with modifications including vertical grid nesting (Daniels et al., 2016), the generalized actuator disk (GAD) (Mirocha et al., 2014a), and a turbine yawing capability (Arthur et al., 2020). The GAD requires specifications for the turbine's airfoil lift and drag coefficients. The turbine located at the Perdigão site is a 2.0-MW E-82 Enercon turbine; however, the

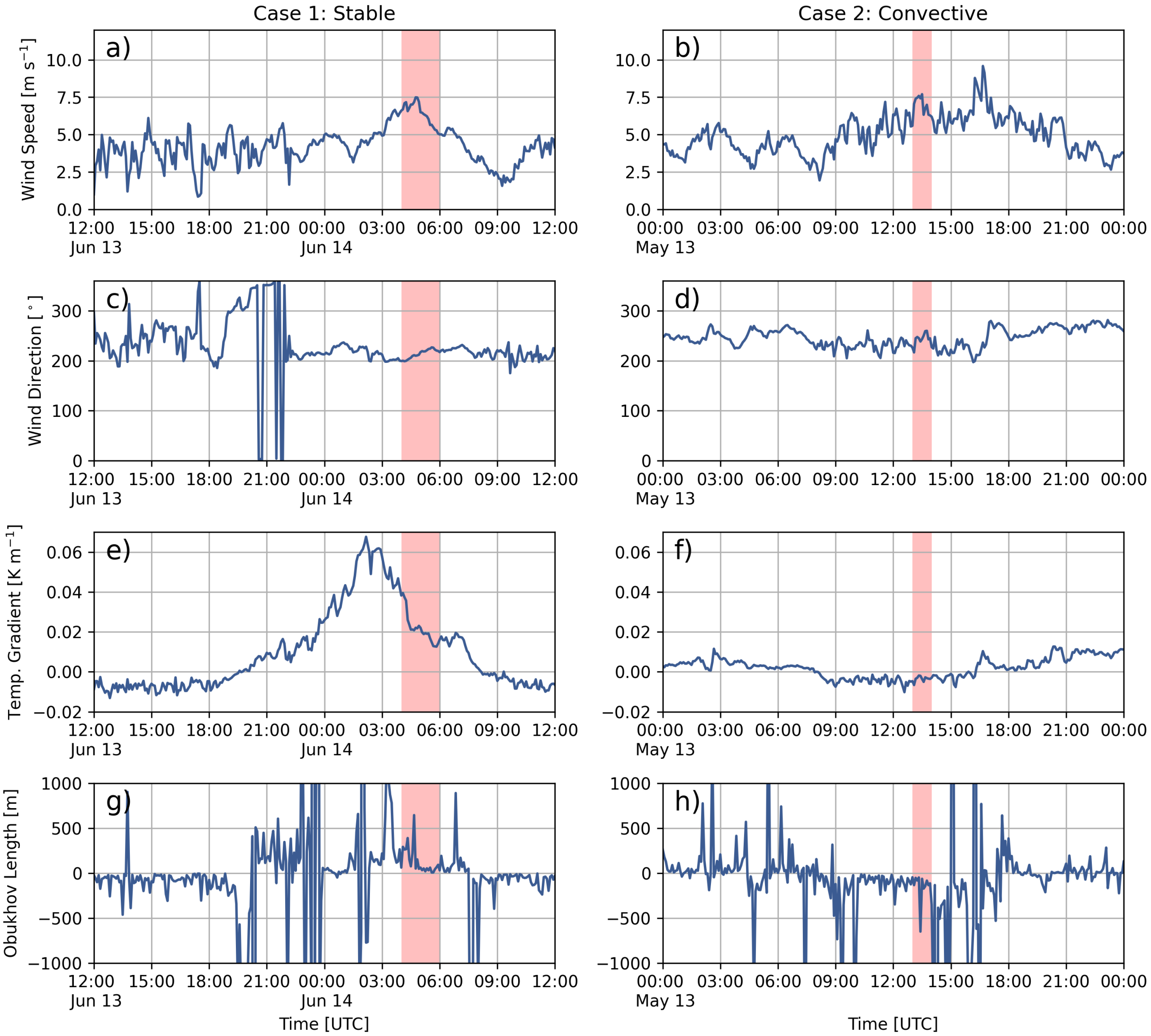

Figure 2.2: Hub-height (80 m) wind speed, wind direction, 100 m - 10 m potential temperature gradient, and Obukhov length for the stable case and for the convective case. Data are from SW_TSE04 and the periods of interest are highlighted in red. Data have been subsampled to five minute intervals.

required lift and drag parameters are not publicly available. We therefore use the wind turbine parameterization from Arthur et al. (2020), which is similar but not identical to the turbine at Perdigão. Both turbine types have a roughly 80-m hub-height and rotor diameter, and are therefore expected to create similar wake effects. Minor differences between the two turbines are not expected to be critical to the conclusions of this study.

Multi-Scale Simulation Setup

The 5-domain nested multi-scale setup for WRF-LES-GAD is shown in Fig. 2.3, with details in Table 5.2. The outermost domain, d01, captures mesoscale forcing and has a horizontal grid resolution of 6.75 km; the innermost domain, d05, uses 10 m spacing and captures microscale flow features. The two coarsest domains are mesoscale simulations that use a planetary boundary layer (PBL) scheme, while the three inner domains use a microscale LES turbulence closure. There is a relatively large parent grid ratio of 15 from d02 to d03, intentionally chosen to skip across the gray zone where turbulence is only partially resolved (Wyngaard, 2004; Chow et al., 2019; Haupt et al., 2019; Muñoz-Esparza et al., 2017). The multi-scale setup also makes use of vertical grid nesting (Daniels et al., 2016) to adjust the vertical layers in each domain, with grid spacing as fine as 8 m near the surface for d05 and increasing for the coarser domains, up to roughly 60 m near the surface for d01. The coarser vertical resolution for d01 - d04 has the benefit of reducing computational costs (the current setup takes roughly eight hours of wall-clock time for five minutes of simulation time on 288 cores) while also maintaining an aspect ratio ($\Delta x/\Delta z$) closer to unity on the LES domains d03 and d04 (Daniels et al., 2016). On d05, most of the vertical resolution is devoted to the bottom ~2 km of the atmosphere, above which there is a gradual drop off in resolution all the way to the domain top of ~20 km. Because of the steepness of the terrain, numerical stability requires the use of very small time steps (as small as 1/60 s for d05). Domains d01, d02, and d03 were spun up for 9 hours, prior to starting d04, and d05.

All three LES domains (d03, d04, and d05) use a stochastic inflow perturbation method (the cell perturbation method; CPM) to improve the downscaling of coherent, turbulent structures in the nested approach (Muñoz-Esparza et al., 2014; Muñoz-Esparza et al., 2015) in a range of stability conditions (Muñoz-Esparza and Kosović, 2018). The CPM works by applying small temperature perturbations to the flow on the upwind domain boundaries that accelerate the development of a full range of turbulent scales, at essentially no additional computational cost. While the use of high-resolution terrain data is expected to spur turbulence, Connolly et al. (2021) found that during convective conditions in the Perdigão valley, using the CPM further improved the representation of turbulence and the rate at which smaller-scale turbulence forms, with no known negative impacts on the flow from the perturbations. Similar findings regarding CPM are described by Arthur et al. (2020) for nested WRF-LES-GAD simulations of a wind farm in less complex terrain.

WRF-LES-GAD is run using a third-order Runge-Kutta time advancement scheme, with fifth-order horizontal and third-order vertical advection schemes. Relevant physical parameterizations selected include the Eta (Ferrier) scheme for microphysics (Rogers et al., 2001), the Noah land surface model (Chen and Dudhia, 2001), the Rapid Radiative Transfer Model for longwave radiation (Mlawer et al., 1997), and the Dudhia shortwave radiation model (Dudhia, 1989). The mesoscale simulations, d01 and d02, use the Mellor-Yamada–Nakanishi–Niino (MYNN) level-2.5 PBL scheme (Nakanishi and Niino, 2006; Nakanishi and Niino, 2009), and d03, d04, and d05 use the turbulent kinetic energy (TKE) level-1.5 LES closure (Deardorff, 1980). All domains use the MYNN surface

Table 2.1: Parameters used for the nested multi-scale WRF-LES-GAD setup. For the vertical resolution, Δz_{min} is for the first grid point above the surface and is approximate due to the nature of the terrain-following coordinate system in WRF.

Domain	Δx [m]	Nest ratio	$\sim\Delta z_{min}$ [m]	$N_x \times N_y$	Δt [s]	turb. closure
d01	6750	-	60	141 × 141	30	2.5-level MYNN
d02	2250	3	60	181 × 181	10	2.5-level MYNN
d03	150	15	30	271 × 271	0.5	TKE 1.5
d04	50	3	30	271 × 271	0.0833	TKE 1.5
d05	10	5	8	601 × 601	0.0167	TKE 1.5

layer scheme in which the lower-boundary conditions are determined from Monin–Obukhov similarity theory. Additionally, topographic shading is enabled to account for shading effects on the surface heat flux in the complex Perdigão terrain. For the upper-boundary condition, we use a Rayleigh damping layer for the top 5 km of the domain.

Mesoscale forcing for d01 is provided by Global Forecast System (GFS) data from the National Center for Environmental Protection (National Centers for Environmental Prediction, 2015). In a sensitivity study comparing both GFS and European Centre for Medium-Range Weather Forecasts data for the boundary conditions, the GFS data produced more accurate results near the surface for the dates of interest here (Wendels, 2019).

Land cover data was obtained from the Coordination of Information on the Environment (CORINE) dataset at a resolution of 100 m, much finer than the default land cover data provided in WRF. The CORINE Land Cover 2006 raster dataset (Bossard et al., 2000) is transformed into United States Geological Survey (USGS) land use types to obtain surface roughness lengths for WRF (Pineda et al., 2004). The CORINE dataset seemingly misclassifies the land type in the valley as mixed shrubland/grassland when the vegetation is mostly tall eucalyptus and fir trees. Likewise, Wagner et al. (2019a) concluded that the surface roughness lengths at the Perdigão site based on the CORINE Land Cover data were too small. To account for this, we set the surface roughness length for the mixed shrubland/grassland land use category in the valley to 0.5 m, the same value used in the LES studies of Berg et al. (2017) and Dar et al. (2019). High-resolution terrain data (1-arc-second, approximately 30 m) were obtained from the Shuttle Radar Topography Mission (Farr et al., 2007). This high resolution terrain data is required to resolve flow features within the narrow valley (see Appendix A for more details).

2.4 Results and Discussion

Validation of the Stable Case Study

The stable case is influenced by a mountain wave event. To validate the accuracy of this event in WRF-LES-GAD, we compare the model with multi-Doppler lidar scans obtained by

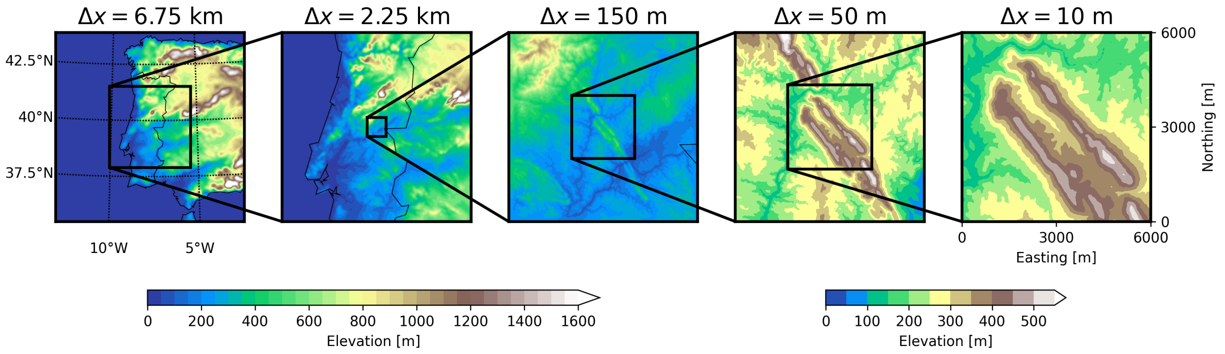

Figure 2.3: Topography of domains used in the multi-scale simulation centered over the Perdigão site. The five domains have resolutions of 6.75 km, 2.25 km, 150 m, 50 m, and 10 m. Dimensions of each domain and other configuration information are included in Table 5.2.

the DTU lidars. The model u- and v-velocities have been projected onto a rotated coordinate system aligned with the Wake Transect in Fig. 2.1 for comparison. For the lidar, the line-of-sight velocities have been converted into horizontal velocity along the Offset Transect in Fig. 2.1. Velocity components perpendicular to the lidar's line-of-sight are not captured, so this conversion results in larger errors at higher elevation angles, but errors are small across the valley near the wind turbine, where the lidar beam is near horizontal. The wavelength of the mountain wave is defined as the distance from the first ridge (where the low-level jet begins to deform) to the first crest of the mountain wave. The model predicts a wavelength of 1220 m (Fig. 2.4(a)), 13% less than the 1410 m wavelength from the DTU lidars, which is almost exactly the ridge-to-ridge distance of 1400 m (Palma et al., 2020). In both the model and multi-Doppler lidar scans, the flow follows the terrain over each ridge, creating a small rotor in the Perdigão valley and a larger rotor beneath the third wave crest downstream of the valley.

Figure 2.5 shows 1 h (from 04:30 to 05:30 UTC) time-averaged along-transect velocities for the stable case from the model and the DLR lidar scan along the Wake Transect (Fig. 2.1). The lidar data are interpolated onto the model grid, and the difference between the model and observations is shown in Fig. 2.5(c). The height of the mountain wave does not extend as high in the model compared to measurements, likely a result of errors in the GFS forcing. This is clear in Fig. 2.5(c), where there are large differences in the along-transect velocity from roughly 800-1200 m a.s.l. The lidar data also show striations of slower and faster wind speeds within the wave, but these striations are not captured by the model. For both the model and the lidar scans, the wake propagates downward following the terrain into the valley. The velocity deficit from the turbine wake dissipates more quickly in the observations compared to the model. The model's resolvable turbulent length scale is limited by the grid

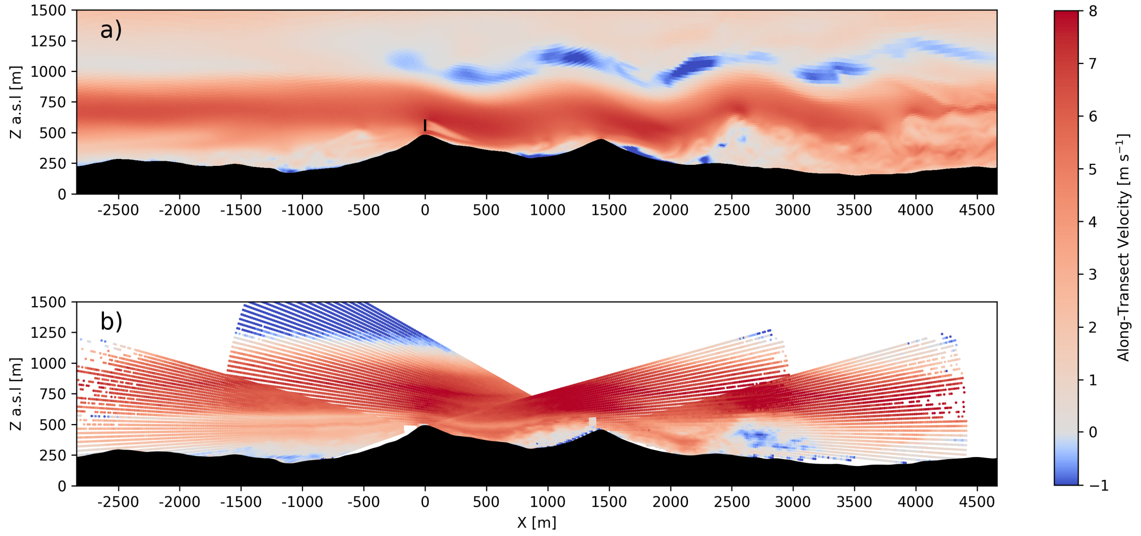

Figure 2.4: Instantaneous along-transect horizontal velocity during the stable case study for (a) the model and (b) the DTU multi-Doppler lidar scan at approximately 04:20 UTC. The output from the model is instantaneous while the multi-Doppler measurements are over the course of a single scan, which takes about 24 s. The model transects are aligned with the Wake Transect and the lidar transects are aligned with the Offset Transect in Fig. 2.1.

resolution, making it possible that the model turbulence dissipation is underpredicted; in addition, this could be due to the different turbine model or errors from a number of other parameterizations.

Figure 2.6 shows instantaneous wind speed from the model overlaid with measurements from the TLS, and met towers V_TSE09 and NE_TSE13, at times when the TLS is near the surface, halfway up, near the top of its ascent, and halfway down its descent (the tower on the southwest ridge is omitted for clarity). Fig. 2.6(e) shows a time series from the model, a virtual TLS, extracted using the GPS position at the corresponding time step of the actual TLS. Comparison of time-dependent turbulent flow fields from a model and a measurement system that moves in three-dimensions over time is difficult because the instantaneous positioning of turbulent flow features will likely not match. To partially account for this and for any uncertainty of the TLS positioning (estimated to be ±30 m), the wind fields in Fig. 2.6(a-d) have also been spatially averaged by ±30 m in the span-wise direction. Additionally, time series with an easting and northing position ±30 m and ±60 m are shown in Fig. 2.6(e) but with a lighter shading. During the two ascents, the virtual TLS and real TLS show good agreement with a root mean squared error (RMSE) under 2.0 m s^{-1}. However, the model slightly underestimates the strength of the jet and there is a negative bias of -0.78 m s^{-1}

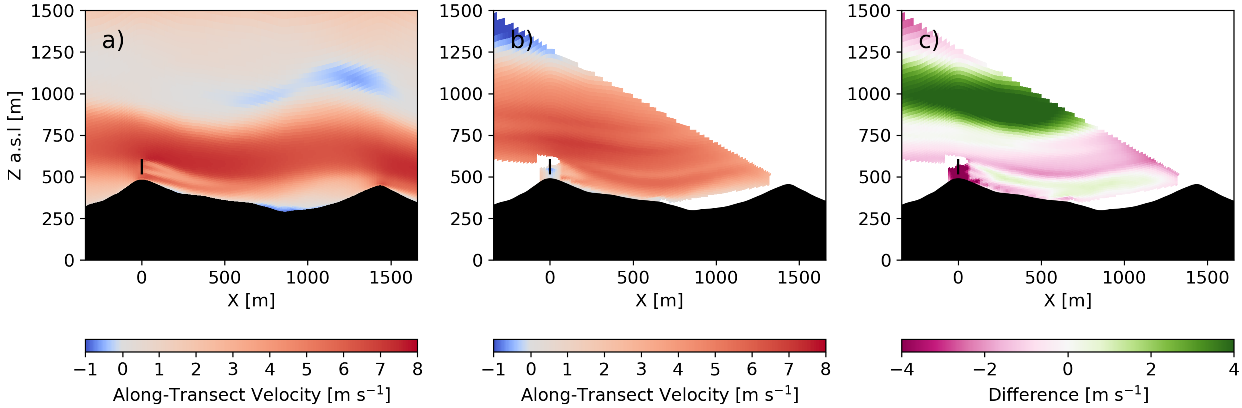

Figure 2.5: Transect of 1 h time-averaged along-transect velocity for the (a) model and (b) DLR lidar during the stable case study with (c) as the difference between the DLR lidar and the model. The transects are aligned with the Wake Transect in Fig. 2.1.

over the course of the two ascents and descents. In Fig. 2.6(e), the predictions for ±30 m and ±60 m are similar because the flow is relatively homogeneous in the spanwise direction (a result of the limited terrain variability in this direction, as seen in Fig. 2.11 and discussed more in Section 2.4).

Wind speed, wind direction, and the potential temperature gradient are also compared with met tower measurements in Fig. 2.7. The modeled wind speed and wind direction generally follow the observations at both hub-height (80 m) and near the surface (10 m), with greater variability in the valley compared to on top of the two ridges. Errors quantified in terms of bias and RMSE are shown in Table 2.2. At hub-height and along the two ridges, wind speed errors are below 1.5 m s^{-1} and wind direction errors are below 12°. Within the valley, hub-height wind speed and wind direction errors are on the order of 2 m s^{-1} and 60°, respectively. Both the wind speed and wind direction fluctuate much more in the valley compared to the ridges, which the model captures reasonably well considering the low wind speeds present. The temperature gradient within the valley in the model is indicative of a well-mixed region whereas the measurements indicate more stable stratification, resulting in an RMSE of 0.017 K m^{-1}, although this stratification does vary significantly over the period of interest. This discrepancy is also evident in Fig 2.6(a-d) where the model predicts that the 10-m and 80-m locations for V_TSE09 are located below the mountain wave and in a region of more well-mixed and coherent turbulence.

Validation of the Convective Case Study

As for the stable case, WRF-LES-GAD is validated for the convective case using comparisons to the multi-Doppler lidar scans (Fig. 2.8). Unstable stratification and increased turbulent

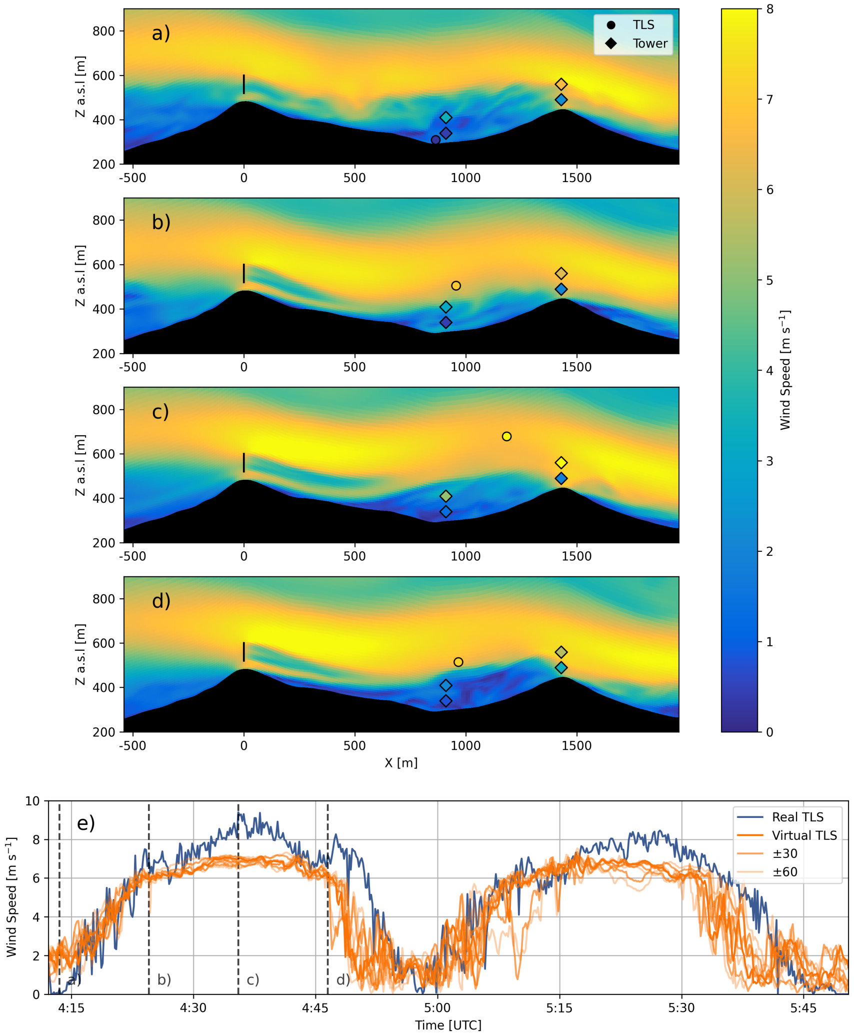

Figure 2.6: Transects of instantaneous wind speed for WRF with measurements from V_TSE09, NE_TSE13, and the TLS overlaid for (a) 04:13:30 UTC, (b) 04:24:30 UTC, (c) 04:35:30 UTC, and (d) 04:46:30 UTC and (e) comparison of wind speed between the TLS data and the virtual TLS in WRF-LES-GAD d05. The transects are aligned with the Wake Transect in Fig. 2.1. Virtual TLSs with an easting and northing position ±30 m and ±60 m are shown with a lighter shading and dashed lines indicate the times shown in the transects.

mixing lead to a turbulent mountain wake in the lee of the first ridge, which forms a recirculation zone as seen in Fig. 2.8. Reverse flow or recirculation near the surface in the lee of the first ridge is both predicted by the model and observed by the multi-Doppler lidar scans. Additionally, turbulent eddies are visible over the entirety of the transects in Fig. 2.8(a) and Fig. 2.8(b).

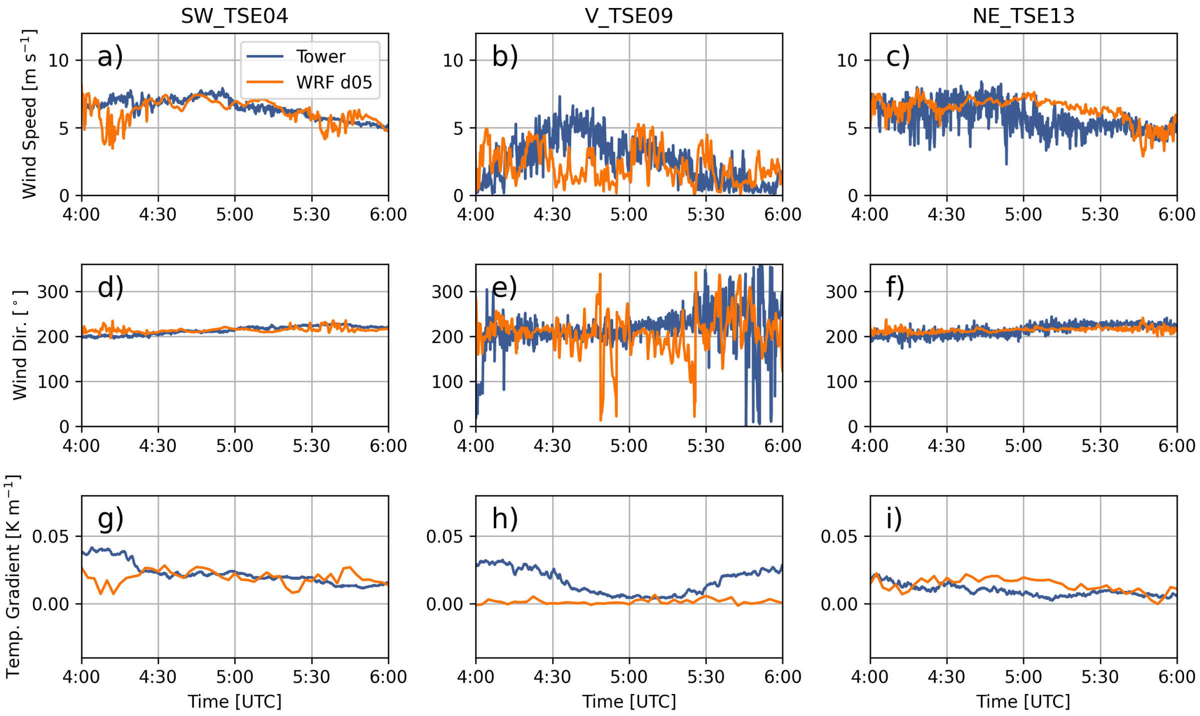

Figure 2.7: Comparison between meteorological tower data and WRF-LES-GAD d05 for 80 m wind speed (a-c), 80 m wind direction (d-f) and 100 m - 10 m temperature gradient (g-i) for the stable case study. SW_TSE04 and NE_TSE13 are located on ridges while V_TSE09 is located in the valley. Note that the model wind speed and direction are output at 10 s intervals while the temperature is output every 150 s.

The wind turbine wake interaction with the recirculation zone is shown in Fig. 2.9 over a 1 h time average (from 13:00 to 14:00 UTC). From Fig. 2.9, the recirculation zone in the lee of the first ridge extends nearly 500 m into the valley for both the model and the lidar measurements as indicated by the small difference in velocities (< 1 m s^{-1}) in Fig. 2.9(c). In both the model and measurements, the wake does not mix with the recirculation zone or mountain wake and deflects upwards; however, the model predicts faster velocities below the wind turbine wake and above the recirculation zone.

A comparison with WRF-LES-GAD and the meteorological towers in Fig. 2.10 during this time period, shows all three parameters (wind speed, wind direction, and temperature gradient) are relatively constant with the greatest variability in the wind speed and wind direction in the valley. Errors between the model and the met tower measurements at both 80 m and 10 m are shown in terms of bias and RMSE in Table 2.3, with wind speed errors less than 2.5 m s^{-1}. Larger errors in the near-surface wind direction within the valley are a result of lower wind speeds and increased turbulence, as compared to the flow on the

Table 2.2: Wind speed, wind direction, and temperature gradient bias and RMSE between WRF-LES-GAD and meteorological tower measurements for the stable case study.

	SW_TSE04		V_TSE09		NE_TSE13	
Parameter	Bias	RMSE	Bias	RMSE	Bias	RMSE
80 m Wind Speed (m s^{-1})	-0.22	0.83	-0.51	2.01	-0.69	1.34
10 m Wind Speed (m s^{-1})	-0.48	0.81	0.98	1.25	2.65	2.90
80 m Wind Direction (°)	-0.4	8.4	-12.7	64.1	0.0	11.3
10 m Wind Direction (°)	-8.1	18.5	-28.9	120.5	-0.2	19.0
Temperature Gradient (K m^{-1})	-0.003	0.011	-0.014	0.017	0.004	0.007

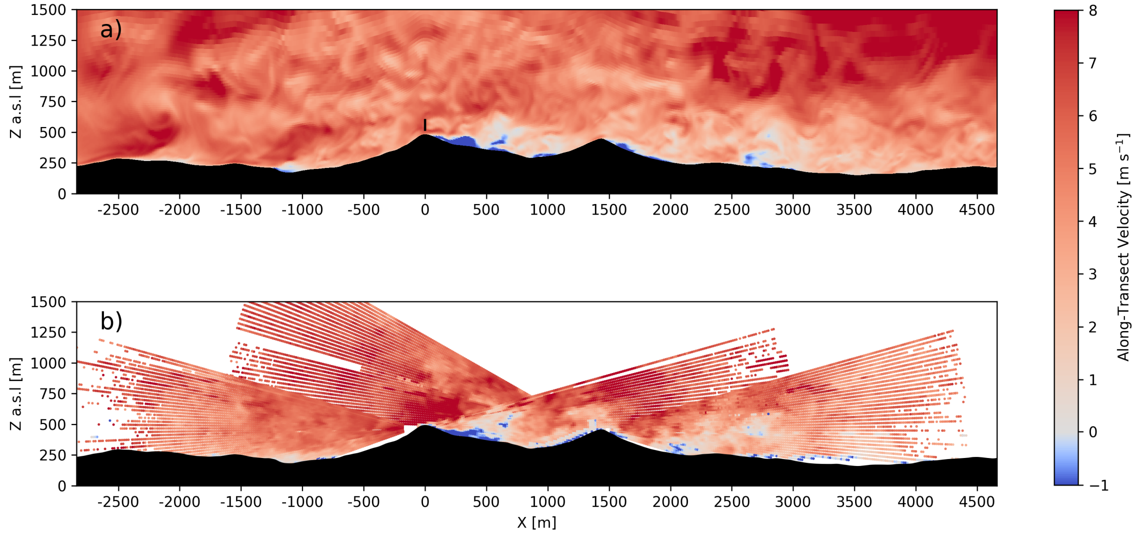

Figure 2.8: Instantaneous along-transect horizontal velocity during the convective case study for the model (a) and DTU multi-Doppler lidar scan (b) at approximately 13:20 UTC. The output from the model is instantaneous while the multi-Doppler measurements are over the course of a single scan, which takes about 24 s. The model transect is aligned with the Wake Transect and the lidar transect is aligned with the Offset Transect in Fig. 2.1.

ridges. Despite the variability in the modeled temperature gradient (Fig. 2.10g-i), the bias and RMSE values are small relative to the magnitude of the gradient itself.

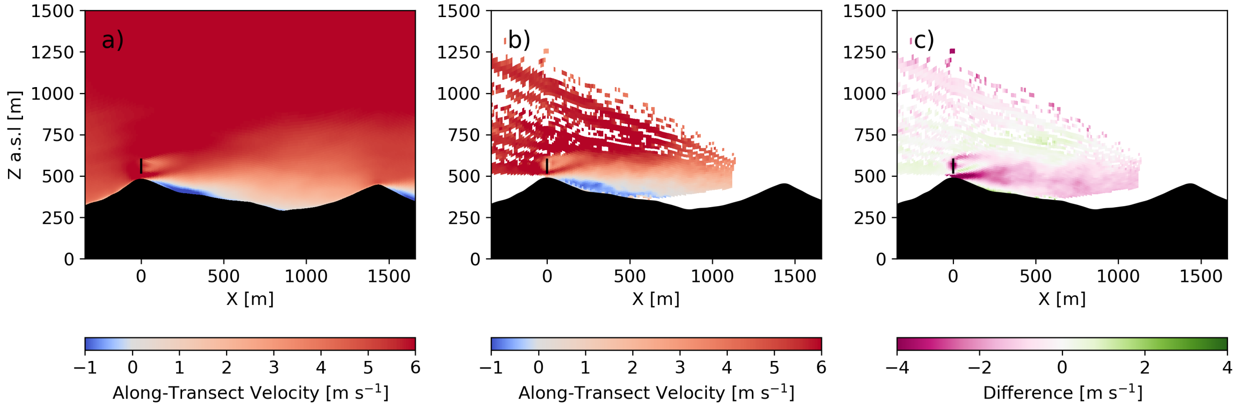

Figure 2.9: Transect of 1 h time-averaged along-transect velocity for the model (a) and DLR lidar (b) during the convective case study with (c) as the difference between the DLR lidar and the model. The transects are aligned with the Wake Transect in Fig. 2.1. The dots represents the vertical location of the maximum velocity deficit.

Table 2.3: Wind speed, wind direction, and temperature gradient bias and RMSE between WRF-LES-GAD and meteorological tower measurements for the convective case study.

	SW_TSE04		V_TSE09		NE_TSE13	
Parameter	Bias	RMSE	Bias	RMSE	Bias	RMSE
80 m Wind Speed (m s^{-1})	-0.20	2.17	0.62	2.38	-0.74	2.04
10 m Wind Speed (m s^{-1})	-0.12	2.25	1.28	2.12	0.35	1.67
80 m Wind Direction (°)	-19.5	31.6	6.4	101.2	-14.5	44.0
10 m Wind Direction (°)	-15.5	23.9	77.1	141.2	-13.3	39.2
Temperature Gradient (K m^{-1})	-0.002	0.005	-0.002	0.005	-0.004	0.007

Wind Turbine Wake Behavior

For the complex Perdigão terrain, Menke et al. (2018) and Wildmann et al. (2019) showed that wind turbine wakes in stable stratification can be observed up to 10 rotor diameters (D) downstream, following the terrain into the valley. Our model agrees with these observations. Figure 2.11 shows 1 h time-averaged wind speed at approximately 80 m above the terrain for the stable case (14 June 2017 04:30-05:30 UTC) and the convective case (13 May 2017 13:00-14:00 UTC). The wake signature in terms of a wind speed deficit persists over 700 m into the valley for the stable case. The wake for the convective case dissipates much more quickly.

Three-dimensional visualizations provide insight into the wind turbine wake advection, meandering, and direction downstream as the flow evolves and develops over the first ridge and through the valley. Figure 2.12(a) and Fig. 2.12(b) show a volume rendering of wind

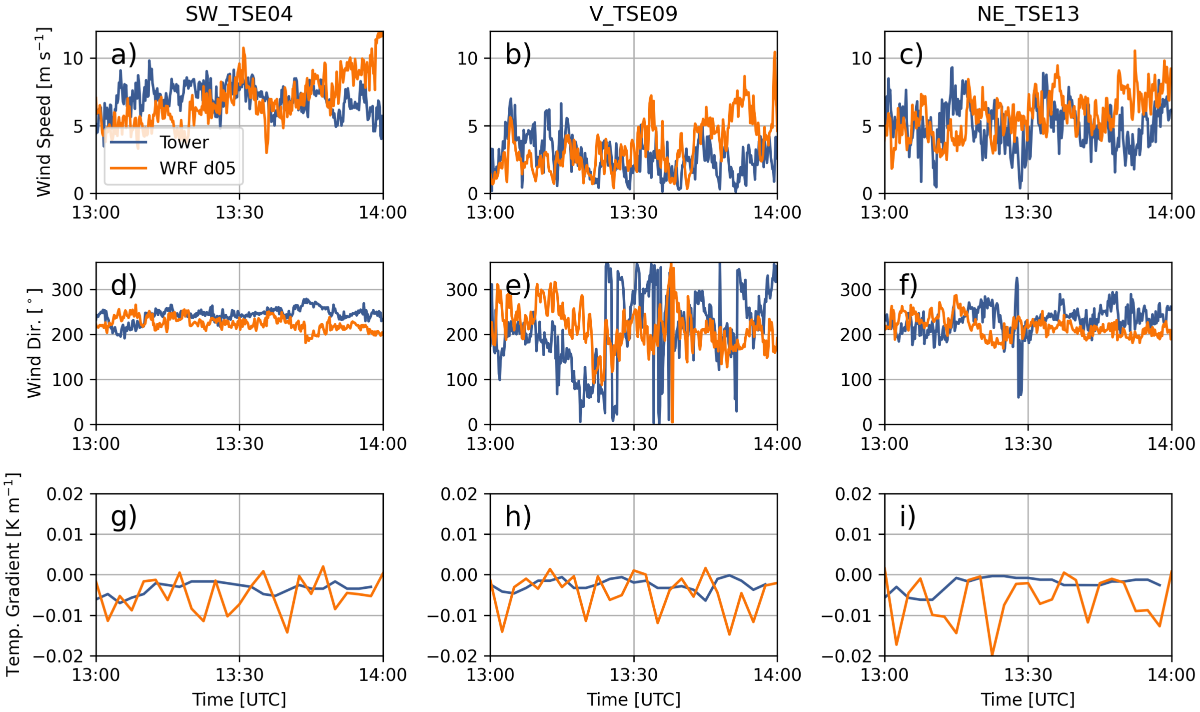

Figure 2.10: Comparison between meteorological tower data and WRF-LES-GAD d05 for 80 m wind speed (a-c), 80 m wind direction (d-f) and 100 m - 10 m temperature gradient (g-i) for the convective case study. SW_TSE04 and NE_TSE13 are located on ridges while V_TSE09 is located in the valley. Note that the model wind speed and direction are output at 10 s intervals while the temperature is output every 150 s.

speed at 04:37:30 UTC for the stable case. Note that the colorbar has been designed to highlight the velocity deficit imparted by the wind turbine rotor. In Fig. 2.12(a), the coherent, tubular structure that is the wind turbine wake propagates downward into the valley following the terrain. At wind speeds highlighted by the volume rendering, the wind turbine wake is the dominant structure compared to any background turbulence in the flow field. In Fig. 2.12(a), the wake persists well into the valley and only begins to dissipate as it reaches the second ridge. Figure 2.12(b) shows how the wake meanders as it propagates into the valley. Wind veer causes the wake to deflect to the north near the second ridge.

Turbulent structures dominate the flow field in the convective case. A volume rendering of wind speed at 13:33:20 UTC for the convective case is shown in Fig. 2.12(c) and Fig. 2.12(d). A similar design of the colorbar that was done for Fig. 2.12(a) and Fig. 2.12(b) is done here for Fig. 2.12(c) and Fig. 2.12(d) except that the visible range of wind speeds is shifted from 3.0-5.0 m s^{-1} to 3.5-5.5 m s^{-1}. Additionally, data to the south and west of the wind turbine have been omitted for clarity. The wake structure is not nearly as coherent and dissipates

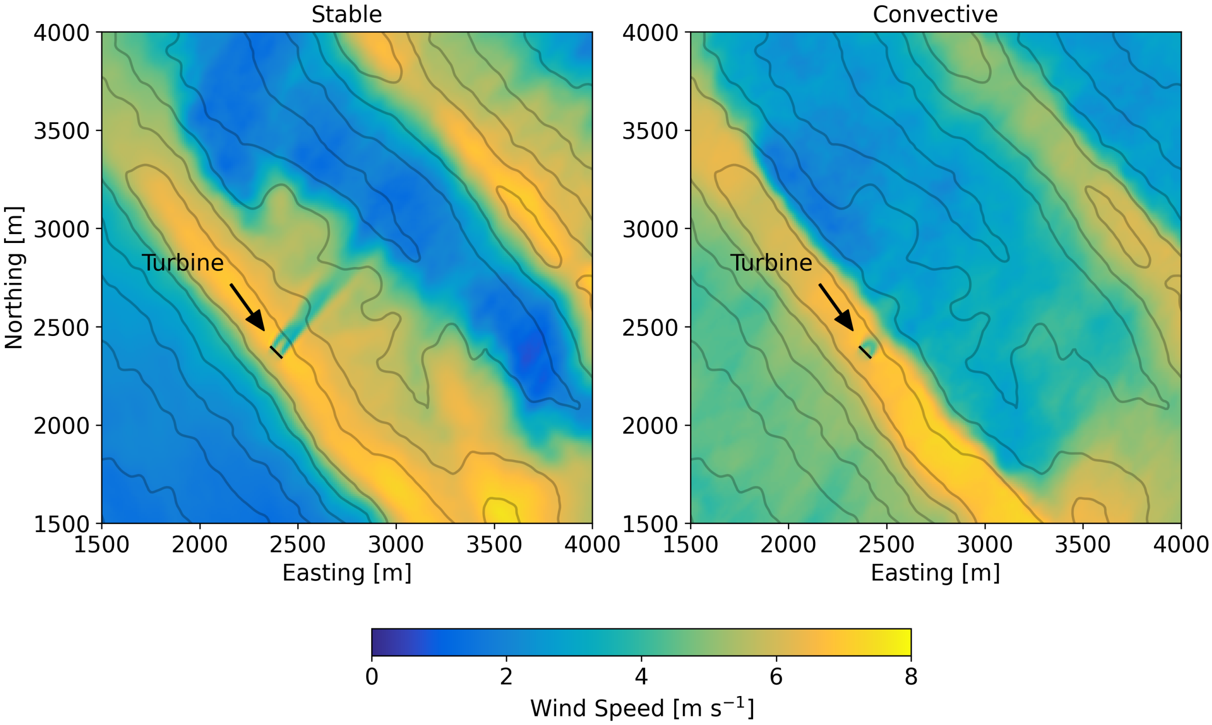

Figure 2.11: 1 h time-averaged wind speed contours at 80 m above the terrain for the stable case study and for the convective case study. Line contours represent 50 m changes in elevation.

much more quickly in the convective case compared to the stable case. Figure 2.12(c) clearly shows the wake as the dominant feature on top of the first ridge. Directly behind the rotor, the wake is level but is then deflected upwards. Background turbulence begins to dominate in the lee of the first ridge and into the valley. The viewing angle used in Fig. 2.12(d) makes it so the wake is difficult to distinguish from any background turbulence except very close to the rotor.

The recirculation zone for the convective case and the mountain wave for the stable case modulate the flow behavior in the valley. The evolution of these phenomena, their interaction with the wind turbine wake, and any spatial heterogeneity in the flow can be visualized using $y-z$ cross sections of the wake at different downstream distances. Figure 2.13 shows 1 h time-averaged wind speed for the two stability cases at distances of 1D, 2D, 3D, and 4D along the Wake Transect (see Fig. 2.1). For the stable case, the wake propagates downward, following the terrain, above the slower near-surface winds. Additionally, the upper half of the wake veers in the positive y-direction leading to an ellipsoid shape for the wake. This stretching of the wake due to the veer in the inflow is characteristic of stable conditions (Lundquist et al., 2015; Abkar et al., 2016; Bromm et al., 2017; Churchfield and Sirnivas, 2018; Englberger and

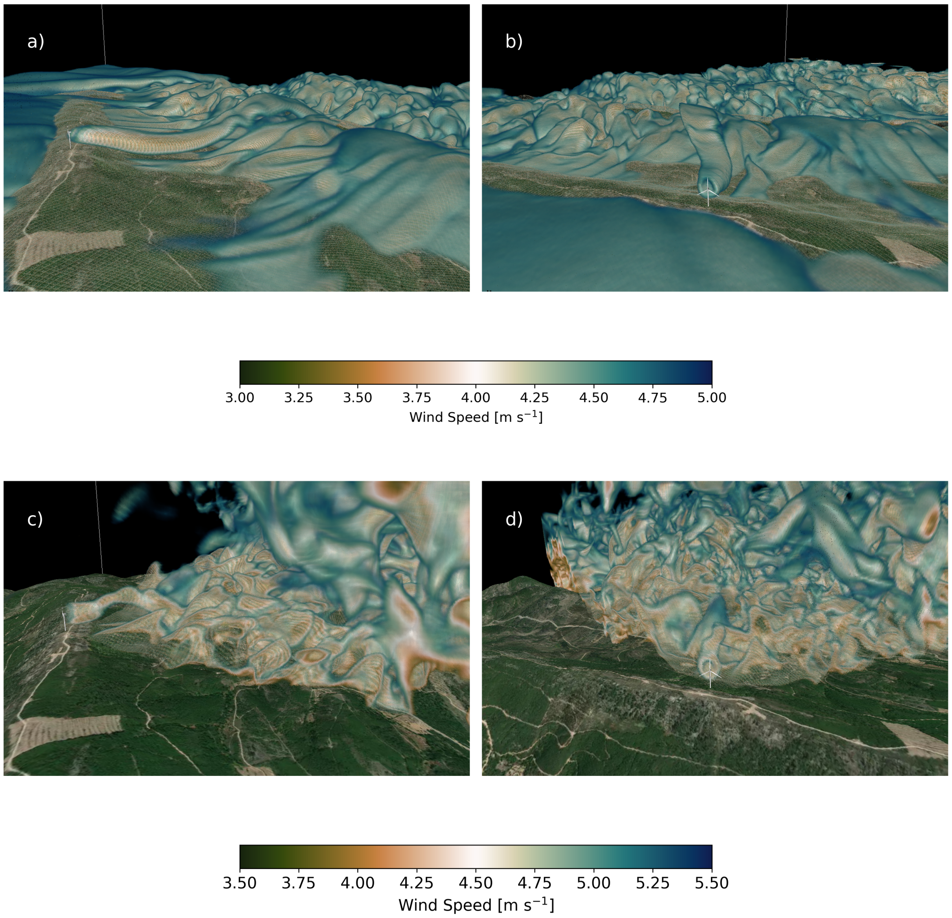

Figure 2.12: Three-dimensional volume rendering of wind speed for the stable case at 04:37:30 UTC (a and b) and for the convective case at 13:33:20 UTC (c and d). For the stable case, only wind speeds between 3.0 and 5.0 m s^{-1} are shown and the wind speeds at the first five vertical levels have been removed for clarity. For the convective case, only wind speeds between 3.5 and 5.5 m s^{-1} are shown and data to the south and west of the turbine have been removed for clarity. The view point in (a) and (c) is from the southeast looking down the valley to the northwest. The view point in (b) and (d) is southwest of the wind turbine looking to the northeast. Visualization made using VAPOR (Clyne et al., 2007).

Dörnbrack, 2018; Bodini et al., 2017), while the amount of veer in the wake depends on the shape and magnitude of the inflow veer (Englberger and Lundquist, 2020). For the convective case, we see that as the flow follows the terrain down into the valley, the recirculation zone and mountain wake rise in height. The wake structure is circular and much more coherent at distances of 1D and 2D compared to further downstream; however, a wind speed deficit

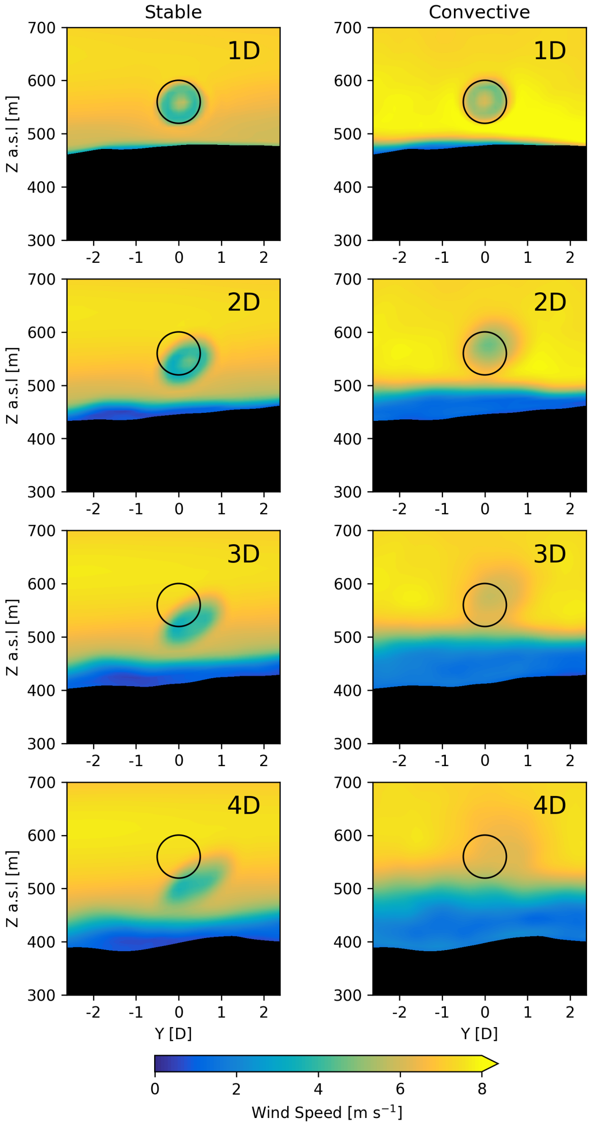

Figure 2.13: 1 h time-averaged wind speed at different downstream distances for the stable and convective case studies taken along the Wake Transect in Fig. 2.1. The black circle represents the circumference of the wind turbine rotor at a constant height a.s.l.

is still clearly visible above the recirculation zone further downstream. The wake also drifts slightly in the positive y-direction, but this is due to the slight misalignment between the Wake Transect and the mean wind direction.

To further quantify wake behavior in the Perdigão terrain, we determine the wake center locations downstream of the wind turbine. Using the model data, we extract 1 h time-averaged velocity profiles at distances of 1D, 2D, 3D, and 4D from the rotor along the Wake Transect. We also extract 1 h time-averaged velocity profiles along the Offset Transect. Since the terrain is similar on the nearly parallel transects, the velocity deficit can be calculated by taking the difference between the profiles along the Offset Transect and the profiles along the Wake Transect. We follow a similar procedure with the observations. The DLR lidar represents the velocity profiles along the Wake Transect while the DTU lidar represents the velocity profiles along the Offset Transect. In these velocity deficit profiles, the vertical wake centers can then be determined by finding the vertical location at which the velocity deficit is greatest.

In Fig. 2.14, the vertical wake centers follow similar patterns between the measurements and model with the wake centers tracking downwards in the stable case and upwards in the convective case. For the stable case, the wake deflects downwards nearly 100 m in the model and 90 m in the measurements at 4D downstream. At the same downstream distance, for the convective case, the wake deflects upwards above the hub-height as high as 54 m in the model and 42 m in the measurements. Additionally, an acceleration occurs in the velocity profiles for both case studies below the wake. This speedup is more apparent for the stable case, but is still clear for the convective case in the near wake. While the speedup could be due to the small differences in terrain between the two transects, it is more likely due to flow being channeled beneath the wake and above the slower near-surface wind speeds; this is consistent with the observation that this near-surface speedup occurs in LES of wakes in flat terrain (Vanderwende et al., 2016).

2.5 Conclusions

The multi-scale WRF-LES-GAD modeling framework has been used here to simulate wind turbine wake propagation in complex terrain under different atmospheric stability conditions, with horizontal grid resolutions ranging from 6750 m on the mesoscale domain to 10 m for the finest LES domain. This setup allows the simulations to capture the interplay between terrain, atmospheric stability, and wind turbine wake dynamics. To the authors' knowledge, this study is the first to combine the effects of highly complex terrain with a wind turbine GAD parameterization for real large-eddy simulations in non-neutral stability conditions. The WRF-LES-GAD framework was applied to a stable case study with a mountain wave and a convective case study with a recirculation zone, and the simulations were compared to field observations from both in situ and remote sensing instrumentation.

In the stable case, the wind turbine wake is deflected downward, following the terrain along with the mountain wave. The general characteristics of the mountain wave were well-captured by the model over the extent of the roughly 8 km domain in comparisons with meteorological towers, a tethered lifting system, and lidar data. The wind speeds within the wave were slightly underestimated, which resulted in under-prediction of the wavelength for the mountain wave. Notably, the mountain wave caused the wake to deflect downwards into the valley. At four rotor diameters downstream of the wind turbine, the wake deflected

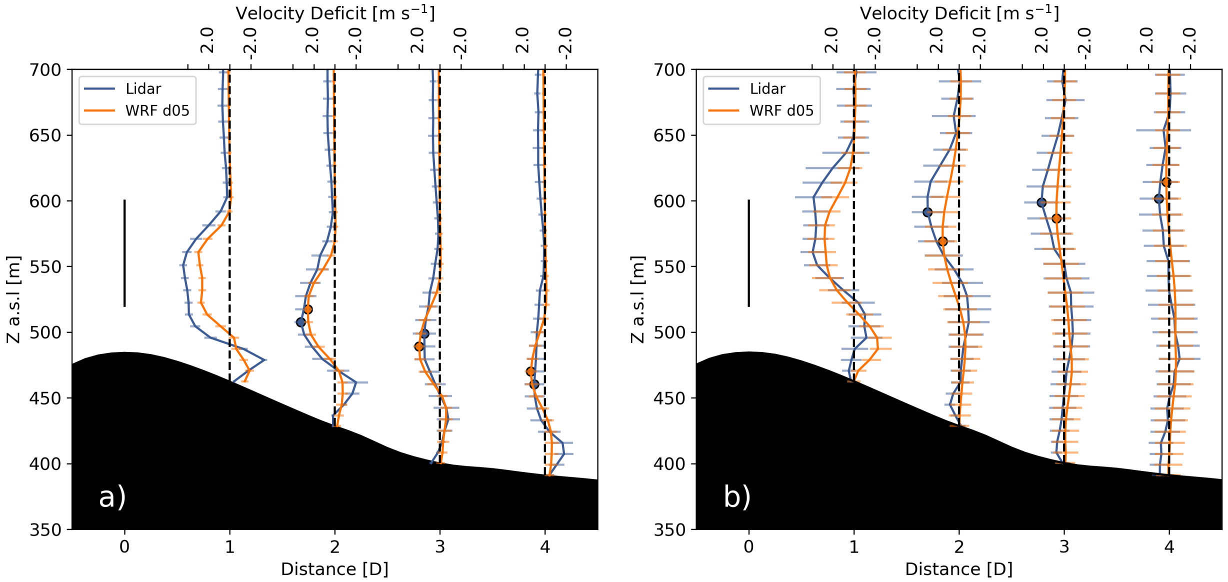

Figure 2.14: 1 h time-averaged profiles of velocity deficit along the Wake Transect based on the lidar measurements and calculated in WRF-LES-GAD d05 for the (a) stable and (b) convective case studies. The error bars correspond to $\pm\sigma$, where σ is the standard deviation during the averaging period. The solid black line represents the diameter of the wind turbine rotor.

downwards on average nearly 100 m below the hub-height, consistent with observations. Further, the stable wake structure stretched from a circular wake into an ellipse due to veer in the wind profile.

In the convective case, the wake was lofted above the terrain and above the original elevation of the wake as a result of the recirculation zone that formed in the lee of the first ridge. With unstable thermal stratification, a mountain wake formed in the lee of the first ridge. Averaged over the hour, we observed a 500 m long recirculation zone in the valley, consistent with observations. The formation of a recirculation zone resulted in the wind turbine wake deflecting upwards. The wake deflected an average of 54 m above hub-height at four rotor diameters downstream, compared to 42 m in the lidar data. In the convective case, the wake maintains a circular structure downwind but diffuses more rapidly than in the stable case due to increased ambient turbulence.

The WRF-LES-GAD framework presented here exhibits good agreement with field observations during the Perdigão field campaign, demonstrating its suitability for examining turbine-airflow interactions and wake evolution in realistic settings involving complex terrain and varying atmospheric stability. The ability of the model to capture different wind turbine wake behavior over complex terrain under stable and convective conditions indicates the model's ability to integrate both mesoscale, i.e., regional winds and stability, and local micro-scale flow phenomena which influence the wake behavior. We expect that the conclusions in terms of the wind turbine wake behavior would hold for most convective and stable atmospheric conditions at the Perdigão site as long as the phenomena of interest (recirculation zones and mountain waves) are present.

Other flow phenomena could be modeled using the multi-scale WRF-LES-GAD framework to examine wind turbine wake behavior under other conditions. Further studies at the Perdigão site may also include comparisons with observed turbulence quantities. Of particular interest is the effect of turbulence closure models (Kirkil et al., 2012; Zhou and Chow, 2012) on the detailed behavior of the background turbulence and its interactions with the wind turbine wake. As more wind turbines are sited in complex terrain, WRF-LES-GAD will be a useful tool for modeling the effects of surface roughness, terrain steepness, and atmospheric forcing on wake dynamics in these environments.

Chapter 3

Small-scale and wind turbine wake turbulence in complex terrain[1]

3.1 Introduction

Wind turbines in complex terrain experience the combined effects of near-surface turbulence and larger-scale turbulent phenomena such as mountain waves (Baines, 1998; Xia et al., 2021; Draxl et al., 2021). The complexities of these interactions are seen in the behavior of the wind turbine wake and its downwind recovery. Chapter 2 showed that the wake of a wind turbine on top of a topographic ridge was deflected upward or downward depending on ambient atmospheric stability. While this behavior was observed in the field, many turbine wake models used in wind farm design do not adequately account for this vertical deflection.

Another aspect not well captured in wake models is the persistence of the wind turbine wake in complex terrain and strong stability conditions. Wind turbines extract the kinetic energy from the wind and convert it into usable electrical energy. This extraction of kinetic energy results in reduced wind speeds downwind, known as a wake. How far wakes persist can depend on the ambient turbulence (Wu and Porté-Agel, 2011; Smalikho et al., 2013; Bodini et al., 2017), which, in-turn, can depend strongly on the thermal stratification of the atmosphere (Abkar and Porté-Agel, 2015) with ambient turbulence typically decreasing with increasing stability. In the field, during stable conditions, and in relatively simple terrain, wind turbine wakes have been observed over 30 rotor diameters in distance downwind (Hirth and Schroeder, 2013). The combination of ambient turbulence and terrain-induced flow phenomena can result in harmful effects to downwind turbines. The slower wind speeds of the wake create a shear layer with the atmospheric boundary layer (ABL) winds, which breaks down into vortices leading to higher turbulence levels downwind. The slower wind speeds and increased turbulence levels of the wake are detrimental to downwind turbines

---

[1] This chapter is being prepared for submission as "Small-scale and wind turbine wake turbulence in complex terrain" by Adam S. Wise (the principal author), Norman Wildmann, Julie K. Lundquist, and Fotini K. Chow to the *Journal of Atmospheric Sciences.*

because they can decrease power output and increase damage, respectively (Magnusson and Smedman, 1994; Barthelmie et al., 2010; Thomsen and Sørensen, 1999; Kelley et al., 2006; Sim et al., 2010; Sathe et al., 2013).

Turbulence metrics such as the turbulence dissipation rate have not been studied extensively for wind turbine wakes. Of the studies that involve measurements of the turbulence dissipation rate and wind turbine wakes, Lundquist and Bariteau (2015) observed dissipation rates one to two orders of magnitude higher in the wake compared to the background flow. In more complex terrain, Wildmann et al. (2019) observed enhanced turbulence due to the wake over 11 rotor diameters downwind of the turbine.

A notable study of the turbulence dissipation rate in the atmosphere is that of Carper and Porte-Agel (2004) who deployed an array of closely spaced sonic anemometers in order to "recreate" the computational method of large-eddy simulation (LES) in the field. Their study is notable as their unique experimental setup meant that they could measure both the forward-scatter of turbulence as it cascades from larger to smaller scales as well as the backscatter of turbulence from smaller scales to larger scales. While the net turbulence dissipation during their analysis periods was positive, they did commonly observe periods of backscatter.

Observations of ABL flow and wind turbine wakes provide insight into turbine-airflow interactions; however, it is helpful to supplement observations with modeling results. Atmospheric models provide a three-dimensional understanding of the fluid flow and wind turbine wake, which is extremely beneficial when the flow itself is highly three-dimensional such as in complex terrain. Therefore, in this study, we turn to LES, which is one of the most widely used methods for simulating the atmospheric boundary layer (Stoll et al., 2020). LES resolves the most energetic eddies while parameterizing the effect of the smaller-scales on the resolved-scale flow due to the implicitly defined spatial filter. While LES can help provide a more complete picture of the flow, the parameterization of the subfilter scales strongly affects the coherent turbulent structures in the resolved flow, which creates a sensitivity of modeling results to the turbulence closure. The role of the turbulence closure in LES is exacerbated in SBL conditions as the most energetic eddies are on the order of tens of meters. Previous research in an idealized study with flat terrain have shown that conventional turbulence closures can be overly dissipative, while dynamic turbulence closures have been shown to be less dissipative, which in essence, extends the working range of LES (Zhou and Chow, 2011). Specifically, this study utilizes the Dynamic Reconstruction Model (DRM) turbulence closure of Chow et al. (2005). The methods of the DRM closure are able to incorporate negative turbulence dissipation rates or the physical process of backscatter as was observed by Carper and Porte-Agel (2004). While the DRM closure has been rigorously used and verified in flat or simple terrain (Zhou and Chow, 2012; Zhou and Chow, 2014; Kirkil et al., 2012), it has yet to be studied in highly complex terrain.

The goal of this study is to better understand ambient and wind turbine wake turbulence characteristics in complex terrain during SBL conditions. The case study is a mountain wave event observed during the Perdigão field campaign. The field campaign along with instrumentation and the case study are described in Sect. 3.2. Another goal of this study is to understand the performance of the DRM closure in complex terrain compared to a conventional closure with the methods of the DRM closure described in Sect. 3.3. Also described in Sect. 3.3 are the analysis methods used to obtain turbulence metrics. Section 3.3 briefly describes the multi-scale modeling setup, which is an extension of the work from Chapter 2. Turbulence metrics from the modeling results are compared with observations to gauge model performance (Sect. 3.4). Furthermore, we focus specifically on wind turbine wake turbulence characteristics within the model.

3.2 Field campaign description

Overview of the Perdigão field campaign

The Perdigão field campaign was an international field campaign conducted in June-July 2017 in eastern Portugal in the Vale de Cobrão. The site is characterized by two parallel ridges that extend nearly 2 km in length, with the ridges being oriented northwest to southeast. Long term measurements conducted prior to the campaign demonstrated that the dominant wind directions at the site are southwesterly or northwesterly during some parts of the year, with flow roughly perpendicular to the ridges (Fernando et al., 2019). Considering the meteorology and 2 km spanwise extent of the terrain, the Perdigão site was chosen for its potential to represent an idealized valley flow and wind turbine interactions, with a focus on stable conditions.

An intensive operation period of the campaign was conducted from 1 May to 15 June 2017. During this period, a comprehensive dataset was gathered using 195 sonic anemometers on 49 meteorological (met) towers, 26 lidar systems, and a number of other instruments described in more detail in the following section with relevant instrumentation shown in Fig. 3.1. A single 2-MW Enercon E-82 wind turbine is located on the southwest ridge with an approximately 80-m hub height and rotor diameter. This turbine and its wake were the object of focused scans by lidars and other measurement devices to explore the interaction of the coherent structure of the wake with stable stratification (Robey and Lundquist, 2024).

Instrumentation

This study focuses largely on 80 m (the wind turbine hub height) and 10 m (near surface) quantities. The 80 m quantities are obtained from sonic anemometers placed on the three 100 m towers along a transect roughly perpendicular to the ridges. Following the naming convention in Chapter 2 and from the Perdigão data repository, SW_TSE04 is the 100 m tower on the southwest ridge and represents the inflow conditions given the southwesterly wind direction for the specific case study (described in the following section). V_TSE04 is the 100 m tower in the valley, and NE_TSE13 is the downwind tower on the northeast ridge. These towers have additional sonic anemometers at heights of 10, 20, 40, 60, and 100 m. All available 10 m sonic anemometers from the field campaign are used to examine near

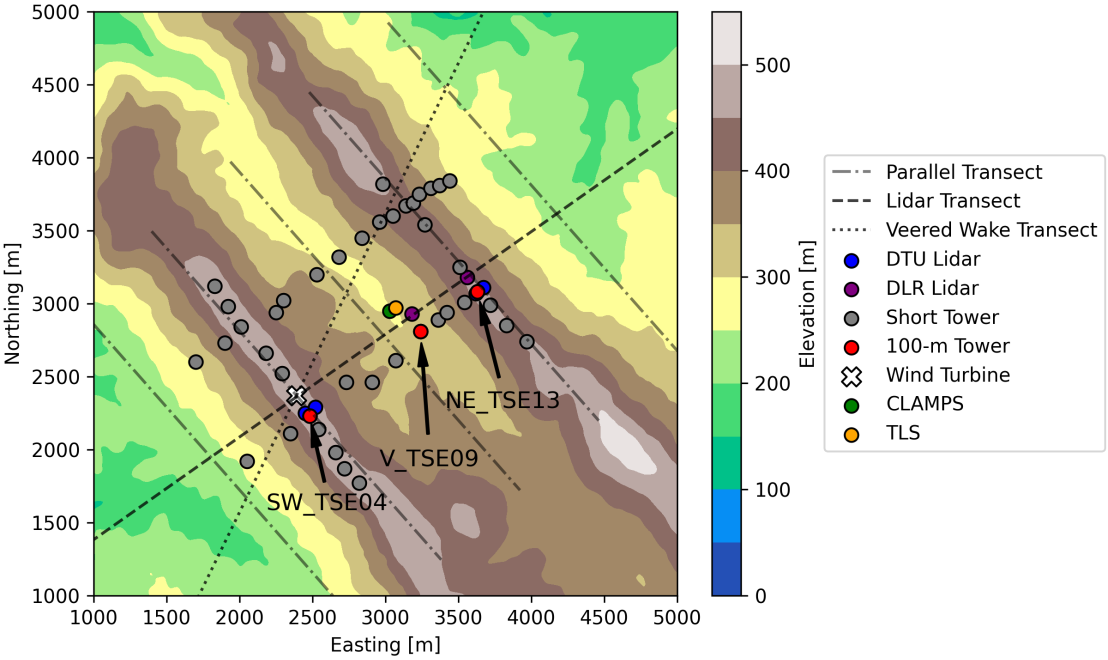

Figure 3.1: Layout of the Perdigão field campaign with the location of various instrumentation including every tower location. Note that the towers vary in height and that transect naming conventions differ from Chapter 2 (Fig. 2.1)

surface wind statistics, comprising measurements from 47 different met towers. These met towers are arranged in four distinct transects denoted in the Perdigão data repository as the northwest transect (tnw), the southeast transect (tse), the southwest ridge transect (risw), and the northeast ridge transect (rine). All sonic anemometers measure three-dimensional wind at a temporal resolution of 20 Hz.

A tethered lifting system (TLS) is also used for comparison in this study. The TLS is a specially designed tethersonde operated by the University of Colorado Boulder (CU) that was launched from the valley floor. The instrumentation package was similar to that of Frehlich et al. (2008) and Lundquist and Bariteau (2015), which notably includes a hot-wire anemometer, thermistors, a pressure sensor, and a global positioning system (GPS). The TLS profiles a vertical range of ∼400 m, providing in-situ measurements of wind speed, wind direction, and temperature at 1 kHz while taking GPS measurements of latitude, longitude, and altitude every 5 s (Balsley, 2008). The TLS travels at approximately 0.3 m s^{-1} and takes just over 45 minutes to conduct an upwards and downwards vertical profile. For the specific case study analyzed here, the TLS conducts two back-to-back profiles from 04:13 to 05:50 UTC. Using the high-rate measurements of wind speed, a time-varying turbulence dissipation rate can be estimated following Fairall et al. (1990).

Lastly, measurements from scanning Doppler lidar data are used to estimate dissipation rates. The scanning lidars used in this study are located along the Lidar Transect in Fig. 3.1 with one lidar in the valley and another on the northeast ridge; these are the RHI#2 and RHI#1 lidars, respectively, from the German Aerospace Center (DLR), described in Wildmann et al. (2019). These lidars are in locations where they could capture and measure effects due to the wind turbine wake using range-height indicator (RHI) scans. In addition to the line-of-sight measurements provided by the lidars, Wildmann et al. (2019) derived a method to determine a 30 minute time-averaged turbulence dissipation rate, which is discussed in more detail in Sect. 3.3. Additional vertical profile measurements from the University of Oklahoma (OU) Collaborative Lower Atmospheric Mobile Profiling System (CLAMPS) (Wagner et al., 2019b) are used. The CLAMPS was at the same location as the TLS on the valley floor. Vertical stare measurements from the CLAMPS are used in this work to obtain turbulence dissipation rates. Lastly, model results are briefly compared with four scanning lidars deployed by the Danish Technical University (DTU) (Menke et al., 2020); two DTU lidars were located on each ridge scanning in opposite directions and forming a nearly 8 km vertical transect across the valley. Additionally, although dissipation rates are usually available from profiling lidars like the CU lidar located near the base of the TLS (Bodini et al., 2018; Bodini et al., 2020; Sanchez Gomez et al., 2021), the lidar visibility was not high enough during this time period to provide useful data.

Case Study

The case study of interest starts in the early morning of 14 June 2017. This case study is the same as the stable boundary layer mountain wave case study from Chapter 2 (Wise et al., 2022) and is summarized as follows. The period of interest is from 04:00 to 06:00 UTC, which corresponds to 05:00 to 07:00 local time (LT) with sunrise at 06:02 LT. The 100 - 10 m potential temperature gradient as measured by SW_TSE04 is 0.031 K m^{-1} on average, indicating a stably stratified atmosphere. Note that given the absence of pressure sensors, the potential temperature is determined using $\theta \approx T + (g/C_p) \cdot z$ as was done by Menke et al. (2019). The Obukhov length at 10 m was also determined to be positive as shown in Chapter 2 indicating stable atmospheric conditions. The average 80 m wind speed and wind direction are 6.3 m s^{-1} and southwesterly at 215°, respectively.

Lastly, the internal Froude number is calculated to be 1.05 during the period of interest given the geometry of the terrain (see Chapter 2 for details). With a Froude number close to 1, a resonant mountain wave forms. In general, mountain waves with various wavelengths were typical during the Perdigão field campaign (Menke et al., 2019; Fernando et al., 2019; Wagner et al., 2019a) with Fernando et al. (2019) determining that mountain waves occurred on 50% of the nights during the IOP.

3.3 Methods

WRF-LES-GAD

This study uses the nested, multi-scale modeling framework of the Weather Research and Forecasting (WRF) model (Skamarock et al., 2021), with a planetary boundary layer (PBL) scheme on the coarser grids and a large eddy simulation (LES) approach on the finer grids. This multi-scale framework captures turbulence across a broad range of scales, from mesoscale and synoptic time-varying forcing to resolved, smaller-scale ambient turbulence on the finest grids. The WRF model v4.4 is used with a number of modifications to the source code that are publicly available. Specifically, we utilize a generalized actuator disk (GAD) parameterization (Mirocha et al., 2014a; Aitken et al., 2014) and turbine yawing capability (Arthur et al., 2020) to represent the wind turbine rotor on the southwest ridge. The wind turbine parameterization used in this study is that of Arthur et al. (2020) and was also used in Chapter 2. The GAD requires airfoil lift and drag coefficients, which are not publicly available for the 2.0 MW Enercon E-82 turbine located at the Perdigão site. We therefore use the wind turbine parameterization from Arthur et al. (2020), which is similar but not identical to the turbine at Perdigão. Both the turbine used by Arthur et al. (2020) and the Enercon E-82 turbine have a roughly 80 m hub-height and rotor diameter and are therefore expected to have a similar impact on the flow. Additionally, we also use the dynamic reconstruction model (DRM) turbulence closure first implemented in WRF by Kirkil et al. (2012).

Turbulence modeling

In stable boundary layer conditions, the resolved LES turbulence is very sensitive to the grid resolution and the choice of turbulence closure. In WRF, the effective resolution is approximately $7\Delta x$ (Skamarock, 2004). Finer scale turbulence can be resolved by increasing the grid resolution, at higher computational cost. For reference, the multi-scale setup takes roughly 6.2 hours of wall-clock time for five minutes of simulation time on 440 cores when using a standard LES closure. Increasing the grid resolution further from the setup used here and in Chapter 2 is computationally prohibitive. The representation of fine scale turbulence in LES also depends on the choice of turbulence closure. Previous work has shown that the DRM closure outperforms TKE-1.5 and other closures in stably stratified conditions (Zhou and Chow, 2011; Zhou and Chow, 2014) largely in flat and simple terrain (also shown in Chapter 4). Additional testing of the DRM's performance in WRF for complex terrain is a focus here, with the TKE-1.5 and DRM closure results compared in detail in the context of integral time and length scales, turbulent kinetic energy, and turbulence dissipation rates.

Dynamic reconstruction model

The dynamic reconstruction model uses a 3D filter applied to the Navier-Stokes equations to separate large and small scales. This filter is twice the grid cell spacing and is applied explicitly in the model; it is thus distinct from the implicit effects of grid discretization. The effect of the implicit grid filter, as well as numerical truncation errors, is to prohibit motions smaller than the grid scale. There is thus a range of scales between the grid scale and the filter scale that can be partially reconstructed in the model.

The governing equations of LES on a discrete grid are:

$$\frac{\partial \overline{\tilde{u}}_i}{\partial t} + \frac{\partial \widetilde{\overline{\tilde{u}}_j \overline{\tilde{u}}_i}}{\partial x_j} = -\frac{1}{\rho}\frac{\partial \overline{\tilde{p}}}{\partial x_i} + \nu \frac{\partial^2 \overline{\tilde{u}}_i}{\partial x_i \partial x_j} - \frac{\partial \tilde{\tau}_{ij}}{\partial x_j} + \tilde{F}_i \tag{3.1}$$

where x_i represents the x, y, and z spatial dimensions, u_i are velocities, p is pressure, ρ is density, τ is the turbulent stress, and $\tilde{F}_i$ represents a body force (such as drag from a wind turbine rotor). The operators are: $\overline{u}_i$ is the filtered velocity field via a smooth spatial filter, $\tilde{u}_i$ is the resolved velocity field, and $\overline{\tilde{u}}_i$ is a resolved, filtered velocity. The larger implicit filter over the advection term represents the effect of the discretization ∂/∂_j which acts as an implicit filter cutting off higher wavenumbers.

The full turbulent stress term is referred to as the subfilter scale stress (τ^{SFS}) which is made up of two components, a resolvable subfilter-stress (RSFS), τ^{RSFS}, and a subgrid scale (SGS) stress, τ^{SGS}:

$$\tau^{SFS} = \tau_{ij} = \tau^{SGS} + \tau^{RSFS} = \left(\overline{u_i u_j} - \overline{\tilde{u}_i \tilde{u}_j}\right) + \left(\overline{\tilde{u}_i \tilde{u}_j} - \overline{\tilde{u}}_i \overline{\tilde{u}}_j\right) \tag{3.2}$$

The RSFS term represents the range of eddy motions between the implicitly defined grid filter (i.e., the Nyquist limit) and the explicit LES filter. When an explicit filter is defined, τ^{RSFS} is resolvable on the grid, but this term is generally ignored in conventional turbulence closures which only parameterize SGS stresses.

For the DRM, the subgrid scale stress, τ^{SGS} is parameterized using the Dynamic Wong-Lilly (DWL) (Wong and Lilly, 1994) eddy-viscosity model:

$$\tau^{SGS} = -2\nu_t \overline{\tilde{S}}_{ij} \tag{3.3}$$

where $\overline{\tilde{S}}_{ij}$ is the filtered and resolved strain rate tensor and $\nu_t = C_\epsilon \Delta^{4/3}$ is the dynamic eddy viscosity. In the dynamic eddy viscosity, Δ is the filter width chosen as 2 and C_ϵ is determined dynamically using the least-squares method of Lilly (1992).

The RSFS stress is determined by reconstructing the velocity field using the approximate deconvolution method (Stolz et al., 2001):

$$\tilde{u}_i \approx \overline{\tilde{u}}_i + (I - G) * \overline{\tilde{u}}_i + (I - G) * \left[(I - G) * \overline{\tilde{u}}_i\right] + \dots \tag{3.4}$$

where I is the identity matrix, G is the explicit filter and $*$ represents the convolution operator. Each additional term in the series adds a level of reconstruction that more accurately represents the RSFS velocities. In this study, level-0 reconstruction is used which includes the first term in the series, and the velocity is approximated as the filtered velocity. This level-0 reconstruction is the same as the scale-similarity model of Bardina et al. (1983). Combined with the eddy viscosity SGS term, this level-0 reconstruction becomes a dynamic mixed model (Zang et al., 1993). We refer to the closure as DRM for simplicity and to indicate the more general implementation in WRF.

Lastly, near-wall stresses are usually under-predicted with dynamic SGS models applied in ABL flows. A near-wall stress model is used to account for this, following Brown et al. (2001), which has improved agreement with similarity theory in previous studies (Chow et al., 2005; Zhou and Chow, 2011; Kirkil et al., 2012). The near-wall stress is defined for $i = 1, 2$ and is added only to the τ_{i3} terms as follows:

$$\tau_{i3}^{\text{near-wall}}(z) = -\int_0^{H_c} C_c a(z) |\bar{\tilde{u}}| \bar{\tilde{u}}_i dz \tag{3.5}$$

where C_c is a strength factor, set to 0.5 due to the grid-aspect ratio in this study (Chow, 2004), and $a(z)$ is a shape function set to smoothly decay the effect of the canopy stress at a specific cutoff height H_c (Chow et al., 2005; Kirkil et al., 2012). H_c is chosen as $2\Delta x$ following Zhou and Chow (2011). The shape function is defined as:

$$a(z) = \cos\left(\frac{\pi z}{2H_c}\right)^2 \tag{3.6}$$

The DWL eddy-viscosity model and the scale-similar RSFS term are combined to create a mixed-model for turbulence. This mixed model along with the added canopy stress result in:

$$\tau_{ij} = \tau^{RSFS} + \tau^{SGS} = \overline{\tilde{u}_i \tilde{u}_j} - \overline{\tilde{u}_i}\,\overline{\tilde{u}_j} - 2C_\epsilon \Delta^{4/3} \bar{\tilde{S}}_{ij} + \tau_{i,\text{near-wall}} \tag{3.7}$$

With the DRM's formulation for RSFS motions, subfilter scale turbulence dissipation $\epsilon = -\tau_{ij}\bar{\tilde{S}}_{ij}$ can vary both positively and negatively representing dissipation and backscatter. It is worth noting that in conventional closures, such as TKE-1.5, the eddy-viscosity form is purely dissipative. This is because the SFS stress does not represent RSFS motions and only encompasses SGS motions, resulting in ϵ being strictly positive.

The SFS scalar fluxes in the DRM follow a similar procedure to momentum. The SFS fluxes are comprised of two terms, the SGS, eddy-diffusivity contribution from the DWL model and the RSFS contribution from the approximate deconvolution method. The SFS potential temperature, θ, flux in the DRM model is:

$$\tau_{\theta j} = \underbrace{\overline{\tilde{\theta} \tilde{u}_j} - \bar{\tilde{\theta}}\,\bar{\tilde{u}}_j}_{\tau_{\theta j}^{RSFS}} \underbrace{- 2\nu_{t,h} \frac{\partial \bar{\tilde{\theta}}}{\partial x_j}}_{\tau_{\theta j}^{SGS}} \tag{3.8}$$

where $\nu_{t,h}$ is the dynamic, scalar eddy diffusivity defined as $\nu_{t,h} = \frac{\nu_t}{\text{Pr}}$ with $Pr = 1/3$ as defined in WRF (Skamarock et al., 2021).

Turbulent kinetic energy 1.5-order model

The TKE-1.5 model is an eddy-viscosity turbulence closure which solves a prognostic turbulent kinetic energy (TKE) equation to obtain a characteristic turbulent velocity scale and uses the grid spacing as the length scale to parameterize the SGS stresses (the RSFS term is not included) (Deardorff, 1980). The TKE equation describes the evolution of TKE and parameterizes sources and sinks from shear production, buoyancy production or suppression, turbulent mixing, and dissipation. The eddy-viscosity is defined as:

$$\nu_t = C_k l_{h,v} e^{1/2} \tag{3.9}$$

where e is the TKE and C_k is a constant (set to 0.15). The length scales are defined anisotropically with the horizontal length scale defined as $l_h = (\Delta x \Delta y)^{1/2}$ with $\Delta x, \Delta y$ representing the grid spacing in the corresponding direction. The vertical length scale depends on the Brunt-Väisälä frequency, N, and is given by:

$$l_v = \begin{cases} \min\left[\Delta z, 0.76\frac{e^{1/2}}{N}\right] & : N^2 > 0 \\ \Delta z & : N^2 \leq 0 \end{cases} \tag{3.10}$$

The scalar eddy diffusivity is defined for TKE-1.5 in the same way as the SGS component of the DRM model above:

$$\tau_{\theta j} = -2\nu_{t,h} \frac{\partial \bar{\tilde{\theta}}}{\partial x_j} \tag{3.11}$$

Turbulence metrics

In addition to standard, measured quantities from the devices at the Perdigão site, this study focuses heavily on three turbulence quantities. We compare modeling results with derived turbulence quantities such as the integral length scale, turbulence dissipation rate, and turbulent kinetic energy (TKE). Note that many of the techniques used to quantify turbulence rely on the assumption of local isotropy and homogeneity in small-scale turbulence, which has found to be valid for high Reynolds number flows (Kolmogorov, 1941). Under these assumptions, energy must cascade from larger scales to smaller scales in the inertial subrange of turbulence. However, there are certain flow regimes, namely strongly stable flow, in which these assumptions may break down.

Integral time and length scale

The integral length scale L is the scale at which turbulence is physically correlated (Kaimal and Finnigan, 1994) and is defined in the same as in Wildmann et al. (2019):

$$L = \frac{1}{\sigma^2} \int_0^\infty dr B(r) \tag{3.12}$$

where $B(r)$ is the correlation function of the wind speed. The integral time scale T can be obtained by invoking Taylor's frozen hypothesis during the analysis period $T = L/U$ where U is the mean wind speed. The variance σ is the integral of the energy spectrum $S(\kappa)$ as a function of wavenumber:

$$\sigma^2 = \int_{-\infty}^{\infty} d\kappa S(\kappa) \tag{3.13}$$

Within the inertial range of subrange of turbulence (Kolmogorov, 1941), the theoretical energy spectrum is defined as:

$$S(\kappa) = \alpha \epsilon^{2/3} \kappa^{-5/3} \tag{3.14}$$

where α is a universal constant, ϵ is the turbulence dissipation rate (discussed in more detail in the following section), and κ is the wave number.

Obtaining variances and integral length scales for time-series data (such as from the sonic anemometers, TLS, or model output) is relatively straightforward; however, it is non-trivial in scanning lidar data. For the lidar data, length scales are necessary to derive the turbulence dissipation rate. The length scale obtained from lidar data is defined as follows:

$$L_l = c_1 \left(\frac{\sigma_t^2}{\sigma_v^2} \right)^{c_2} + c_3 \tag{3.15}$$

where c_1, c_2, and c_3 are coefficients specific to each lidar that depend on the physical resolution of the lidar measurement, which is, in turn, a function of the pulse length. σ_t is the variance in the turbulent broadening of the spectra while σ_v is the total variance in the line-of-sight velocity (which are also non-trivial to obtain in lidar data). For additional details, the reader is referred to the derivations in Wildmann et al. (2019).

Turbulence dissipation rate

The turbulence dissipation rate ϵ represents the transfer of kinetic energy from larger scales to smaller scales (Champagne, 1978; Oncley et al., 1996). ϵ was a major focus of the study by Wildmann et al. (2019), which derived the turbulence dissipation rate from a number of measurement devices including for a scanning lidar in complex terrain. To obtain the turbulence dissipation rate from the sonic anemometers, a second-order structure function $D(\tau)$ for the horizontal velocity is used:

$$D(\tau) = C_{ko} \epsilon^{2/3} \tau^{2/3} \tag{3.16}$$

where $C_{ko} \approx 2$ is the Kolmogorov constant and τ is a separation time determined by using Taylor's hypothesis of frozen turbulence. In this study, ϵ_{sonic} is calculated every 30 s and fit to the Kolmogorov model using separation times between 0.1 s and 2 s (see Bodini et al. (2018)).

For the TLS, ϵ_{TLS} is obtained using the inertial dissipation technique and Corrsin relation (Fairall et al., 1990):

$$\epsilon_{TLS} = \left[0.52 C_u^2\right]^{3/2} \tag{3.17}$$

where C_u is the mean structure function parameter computed over the frequency band 5 to 10 Hz. C_u is obtained after applying a Hamming window over each 1 s of data to get the velocity spectra.

Lastly, the method to obtain ϵ_{lidar} is described in detail in Wildmann et al. (2019) with the turbulence dissipation rate calculated as:

$$\epsilon_{lidar} = \frac{1.972}{C_k^{3/2}} \frac{\sigma_v^3}{L_{lidar}} \tag{3.18}$$

The turbulence dissipation rates estimated by the lidar result in a 30 minute time-average while the TLS and sonic anemometers from the tower can provide estimated over shorter time periods.

The turbulence dissipation rate in LES represents the transfer of kinetic energy between resolved and subfilter scales. Therefore, ϵ is a subfilter scale quantity and defined as $\epsilon = -\tau_{ij}\overline{\tilde{S}}_{ij}$. In the model, the turbulence stresses τ_{ij} and strain rate tensor S_{ij} are output every 10 s at all grid points. For the DRM closure, ϵ can vary both positively and negatively representing dissipation and backscatter. Traditional eddy-viscosity closures, such as TKE-1.5, are known to be overly dissipative with respect to ambient flow (Carper and Porté-Agel, 2004; Sullivan et al., 2003). Additionally, backscatter has been been shown to be important for turbulence resolving LES, especially in stably stratified flows (Mason and Thomson, 1992; Kosović, 1997; Porté-Agel et al., 2011), as is the case in the present study.

Turbulent kinetic energy

TKE is computed as:

$$TKE = \frac{1}{2}\left(u'^2 + v'^2 + w'^2\right) \tag{3.19}$$

where u', v', and w' are the fluctuating components of the velocities using running, centered 300 s bins. Note that the TKE from the model represents the resolved TKE. To calculate TKE in the model, additional outputs at 1 s for heights of 10 m and 80 m above ground level (a.g.l.) were specified at all horizontal grid points.

Model configuration and description

The modeling setup is similar to that of Chapter 2 (Wise et al., 2022), but with various changes to improve model fidelity, numerical stability, computational efficiency, and to function on the 4.4 version of WRF (Chapter 2 used WRF version 3.7.1). Most configuration options are the same between the current setup and Chapter 2, with the major differences summarized as follows. A PBL scheme is used on domain d03 (as opposed to LES) and the PBL scheme chosen is the Bougeault–Lacarrere (BouLac) scheme (Bougeault and Lacarrere,

Table 3.1: Relevant WRF parameters used for the nested multi-scale WRF-LES-GAD setup. For the vertical resolution, Δz_{min} is the height of the first w-grid point above the surface (on the Arakawa C-staggered grid) and is approximate due to the nature of the terrain-following coordinate system in WRF. This setup follows that of Chapter 2 but with a larger domain in x and y for domains d01, d02, and d03 for more efficient parallelization.

Domain	Δx [m]	Nest ratio	$\sim \Delta z_{min}$ [m]	$N_x \times N_y$	Δt [s]	turb. closure
d01	6750	-	60	201 × 201	30	BouLac
d02	2250	3	60	271 × 271	10	BouLac
d03	150	15	30	361 × 361	0.5	BouLac
d04	50	3	30	361 × 361	0.0833	TKE-1.5/DRM
d05	10	5	8	601 × 601	0.0167	TKE-1.5/DRM

1989). The BouLac scheme was chosen for two reasons. First, the BouLac scheme was found to be more numerically stable than the Mellor-Yamada–Nakanishi–Niino (MYNN) level-2.5 PBL scheme (Nakanishi and Niino, 2006; Nakanishi and Niino, 2009). Second, a sensitivity study was done for the turbulence closure on domain d03 and the BouLac scheme was found to have the lowest wind speed errors for this specific case (Appendix B). Chapter 2 used an LES scheme for domain d03; however, in their stable case study, very little turbulence was resolved on the 150 m grid resolution (see Fig. A.3) indicating that there is little merit to using LES at such a coarse grid resolution in such strongly stratified conditions. The next major difference is that the number of grid points for domains d01, d02, d03, and d04 were increased in the downwind directions. The fetch or inflow distance is the same as the setup from Chapter 2 as the southwestern latitude and longitude of each domain was kept constant between the two modeling setups. The domain sizes were increased for more efficient parallelization (WRF decomposition prefers domain sizes of similar number of grid points) and, considering that the fetch distance was kept constant, found to have negligible effects on the simulation results.

Other than the PBL scheme, the modeling setup uses the same physics suite as Chapter 2. The cell perturbation method (CPM) is used to help spur the generation of turbulence at inflow boundaries (Muñoz-Esparza et al., 2014; Muñoz-Esparza et al., 2015; Muñoz-Esparza and Kosović, 2018; Connolly et al., 2021). Mesoscale forcing for domain d01 is provided by Global Forecast System (GFS) data (National Centers for Environmental Prediction, 2015). High-resolution terrain data (1-arc-second, approximately 30 m) are obtained from the Shuttle Radar Topography Mission (Farr et al., 2007) to resolve topographically-induced flow features. Lastly, the CORINE Land Cover 2006 raster dataset (Bossard et al., 2000) is transformed into United States Geological Survey (USGS) land use types to obtain surface roughness lengths for WRF (Pineda et al., 2004). Following the findings of Chapter 2 (Wise et al., 2022) and Wagner et al. (2019a), the surface roughness height for the mixed shrubland/grassland category is increased to 0.5 m to more realistically represent the tall eucalyptus and fir trees that were characteristic of the Perdigão site.

3.4 Results and discussion

Comparisons with observations

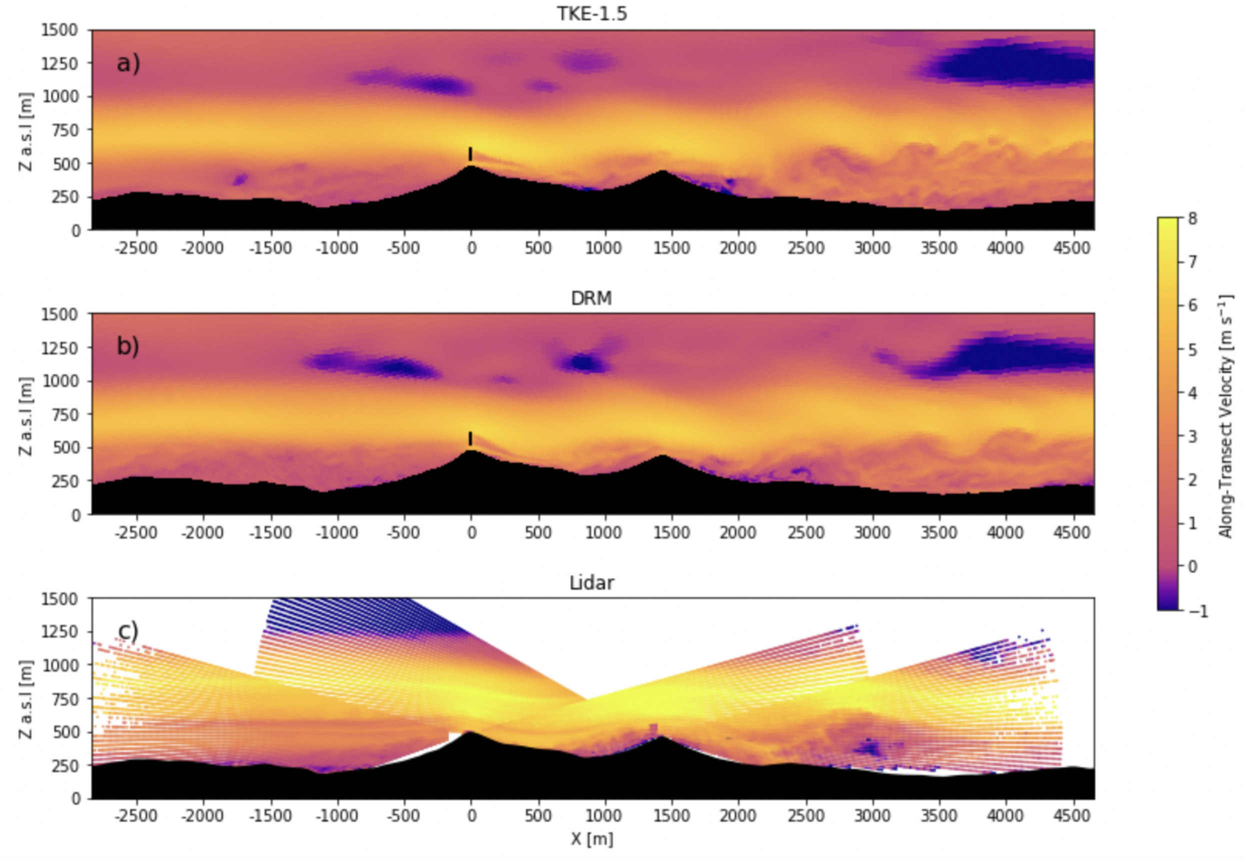

Figure 3.2: Instantaneous vertical slice of horizontal velocity at approximately 05:20 UTC for modeling results using (a) the TKE-1.5 closure, (b) the DRM closure, and (c) observations from the DTU multi-Doppler lidar scan. Note that the DTU multi-Doppler lidar scans are offset by 100 m and do not intersect the wind turbine and its wake.

During the analysis period, the flow is characterized by a low-level jet (LLJ) modified due to topographic effects. Figure 3.2 provides a broad overview of the flow by showing the velocity predictions from the model compared with the multi-Doppler lidar scans from the DTU lidars. The velocities shown are along-transect, with the model $u-$ and $v-$ velocities projected onto a rotated coordinate system aligned with the lidar transect in Fig. 3.1. For the lidar, the line-of-sight velocities are converted to horizontal velocities. As a result of this conversion, there can be larger errors at higher scan angles; however, this study focuses on flow quantities within and below the LLJ where scan angles are closer to horizontal. As discussed in Chapter 2, the horizontal wavelength of the mountain wave is slightly underestimated in the model regardless of turbulence closure due to slower wind speeds predicted within the LLJ itself. As a result, the turbulent rotor downwind of the second ridge is less coherent in the modeling results compared to the observations. The underestimation of the mountain wave wavelength results in the rotor appearing closer ($x \approx 2700$ m) in the model compared to in the lidar scans ($x \approx 3000$ m). However, the large-scale structure of the flow is reasonably well captured with turbulent structures underneath the LLJ upwind of the second ridge followed by near-surface turbulence downwind of the second ridge. Additionally, it is worth noting that in the region upwind of the first ridge, Fig. 3.2(b) demonstrates more turbulence or wind speed variability beneath the LLJ for the DRM closure compared to that of the TKE-1.5 closure.

Comparing the model results with the 100 m met towers aims to further quantify the flow evolution as it approaches and goes over the parallel ridges. Figure 3.3 compares the time-series of wind speed, wind direction, 100 - 10 m potential temperature gradient, TKE, and turbulent length scale from 04:00 to 06:00 UTC for the observations with modeling results using the two different turbulence closures. Figure 3.3 illustrates results at 80 m a.g.l, and Tables 3.2 and 3.3 provide biases and errors at both 80 m a.g.l. and 10 m a.g.l. for the two closures to characterize both the near-surface and higher altitude flow. Overall, the two closures capture flow characteristics similarly. Both closures underestimate the wind speed at the inflow ridge (SW_TSE04) from 04:00 to 05:00 UTC but improve during the final analysis hour. In general, there is more variability in the valley (V_TSE04) and on the downwind ridge (NE_TSE13). While the modeling results are more neutrally stratified compared to the observations, the TKE is underestimated with biases of -0.138 m^2 s^{-2} for the TKE-1.5 closure and -0.247 m^2 s^{-2} for the DRM closure with the observed value as 0.378 m^2 s^{-2}, with both closures having a root-mean-square error (RMSE) close to 0.3 m^2 s^{-2}. Similarly, both closures underestimate turbulence by nearly 0.2 m^2 s^{-2} for the downwind ridge. For the inflow ridge, turbulence is reasonable well-captured, with biases much lower at 0.128 m^2 s^{-2} for the TKE-1.5 closure and 0.040 m^2 s^{-2} for the DRM closure.

Turbulent length scales calculated using Equation 3.12 show that the length scales resolved in the model along the ridgetops and within the LLJ are over-predicted while the length scales are well-predicted in the valley. At the three tower locations shown in Figs. 3.3(m), 3.3(n), and 3.3(o), the resolved turbulent length scales are relatively similar between the two turbulence closures. Overall, both the model-predicted and measured length scales are larger on the ridge-tops compared to the valley due to their faster wind speeds. For the ridge-top locations, the turbulent length scales are overestimated on average by 40 m. For example, at 80 m a.g.l., the observed average length scale at SW_TSE04 is 68.5 m whereas the TKE-1.5 closure predicts 114.5 m and the DRM closure predicts 113.1 m. The towers located on the ridge-tops are within the LLJ; in the valley, where turbulence is driven by surface and topographic effects, the modeled and observed length scales are very similar.

A benefit of the DRM closure is that it can represent the backscatter of energy from sub-filter scales to resolved scales, which is quantified when the SFS dissipation rate $\epsilon = -\tau_{ij}\overline{\widetilde{S}}_{ij}$

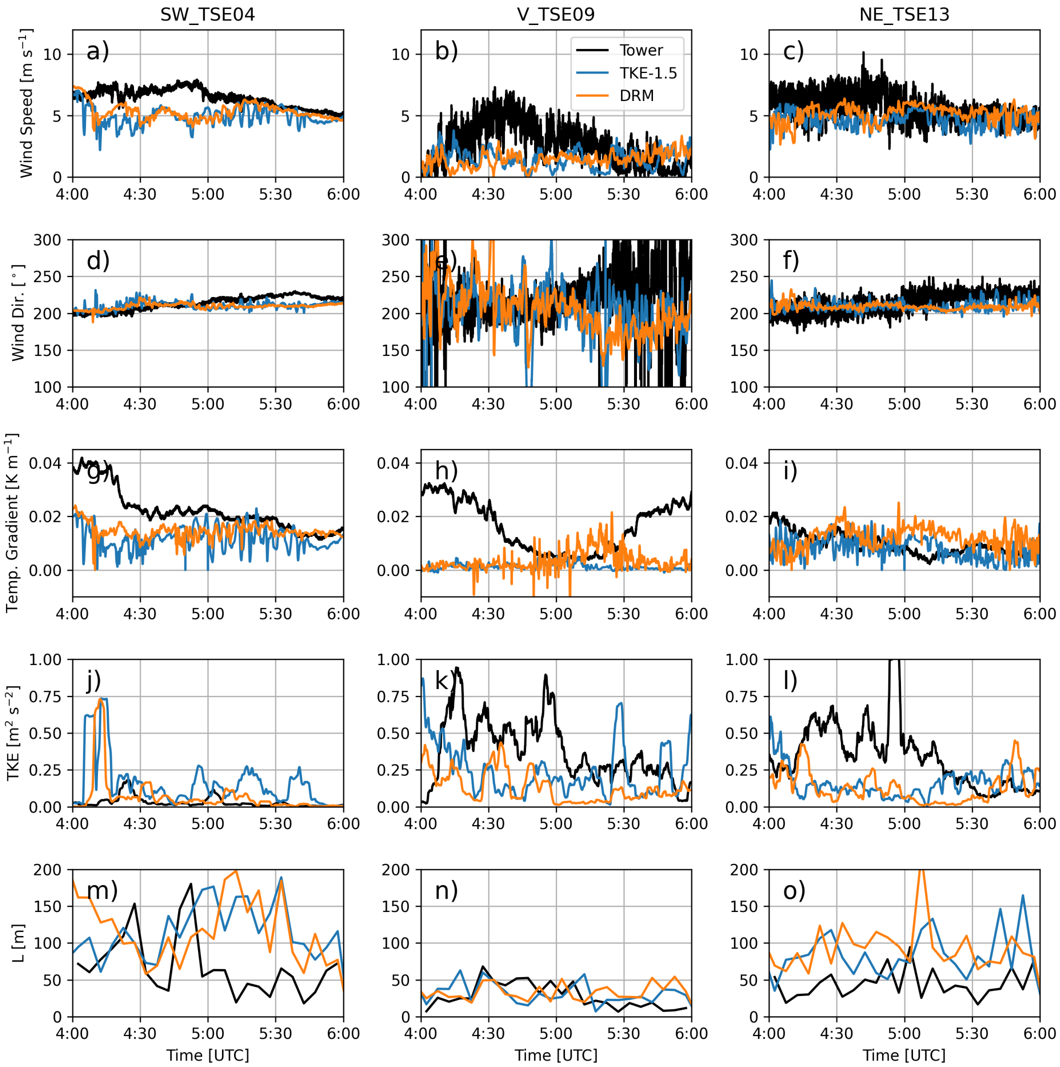

Figure 3.3: Time-series of (a-c) 80 m wind speed, (d-f) 80 m wind direction, (g-i) 100 - 10 m potential temperature gradient, (j-l) TKE, and (m-o) integral length scale from measurements and from the model with the two different closures. Towers SW_TSE04 and NE_TSE13 are located on ridge tops while tower V_TSE09 is located in the valley. Note that the length scale is calculated using a non-overlapping 5 minute window.

is negative. While for this specific experiment, negative dissipation rates cannot be validated, previous work (Carper and Porté-Agel, 2004) has demonstrated the importance of backscatter or, physically, smaller eddies combining into larger eddies. Turbulence dissipation rates for the three tall tower locations are shown in Figs. 3.4(a-c) for the modeling results at 80 m a.g.l. In addition to the time-series of dissipation rate, Figs. 3.4(d-f) show the distribution of

Table 3.2: Biases and errors of wind speed, TKE, and turbulent length scale at 80 m and 10 m a.g.l as well as for the 100 - 10 m potential temperature gradient for the TKE-1.5 closure at towers SW_TSE04, V_TSE09, and NE_TSE13.

	SW_TSE04		V_TSE09		NE_TSE13	
Parameter	Bias	RMSE	Bias	RMSE	Bias	RMSE
80 m Wind Speed (m s^{-1})	-1.505	1.833	-1.154	2.132	-1.011	1.600
10 m Wind Speed (m s^{-1})	-0.948	1.277	0.596	0.808	1.124	1.443
80 m Wind Direction (°)	-3.2	10.0	-17.3	69.9	-4.7	14.6
10 m Wind Direction (°)	-2.5	17.4	24.1	114.8	-4.1	20.3
Temp. Gradient (K m^{-1})	-0.011	0.013	-0.015	0.018	-0.001	0.005
80 m TKE (m^2 s^{-2})	0.128	0.205	-0.138	0.317	-0.182	0.327
10 m TKE (m^2 s^{-2})	0.034	0.104	0.032	0.074	-0.213	0.284
80 m L (m)	45.94	72.01	3.685	19.940	36.885	58.257
10 m L (m)	46.261	56.637	18.755	21.153	45.398	50.633

Table 3.3: As in Table 3.2 but for the DRM closure.

	SW_TSE04		V_TSE09		NE_TSE13	
Parameter	Bias	RMSE	Bias	RMSE	Bias	RMSE
80 m Wind Speed (m s^{-1})	-1.123	1.515	-1.186	2.207	-0.538	1.443
10 m Wind Speed (m s^{-1})	-0.879	1.213	0.590	0.775	0.985	1.401
80 m Wind Direction (°)	-4.3	9.5	-11.6	65.8	-5.5	14.8
10 m Wind Direction (°)	-3.8	20.6	-3.9	116.3	-2.4	20.1
Temp. Gradient (K m^{-1})	-0.008	0.011	-0.013	0.017	0.003	0.007
80 m TKE (m^2 s^{-2})	0.040	0.140	-0.247	0.325	-0.214	0.323
10 m TKE (m^2 s^{-2})	0.002	0.108	0.041	0.136	-0.211	0.295
80 m L (m)	44.594	78.487	5.368	20.648	48.719	62.415
10 m L (m)	64.946	52.296	17.475	20.326	56.273	61.458

ϵ normalized by its standard deviation. The DRM closure indicates backscatter at all three locations, with backscatter more common at the ridgetop locations. For towers SW_TSE04 and NE_TSE13, backscatter occurs roughly 25% of the analysis period, while it only occurs 10% of the time for the tower in the valley. The TKE-1.5 closure cannot represent backscatter, as it is a standard eddy-viscosity closure. While the DRM closure indicates backscatter, additional measurements are required to validate the modeled quantities, as the methods used to derive the turbulence dissipation rate from the sonic anemometers assumes positive dissipation. Even though backscatter cannot be validated with the experimental setup, the positive dissipation rate values from the DRM closure can be compared with the dissipation rates from the TKE-1.5 closure and those derived from the tower.

Similarly, the TLS provides only positive dissipation rates; therefore, we focus solely on dissipation and not backscatter when comparing the TLS results with modeling results

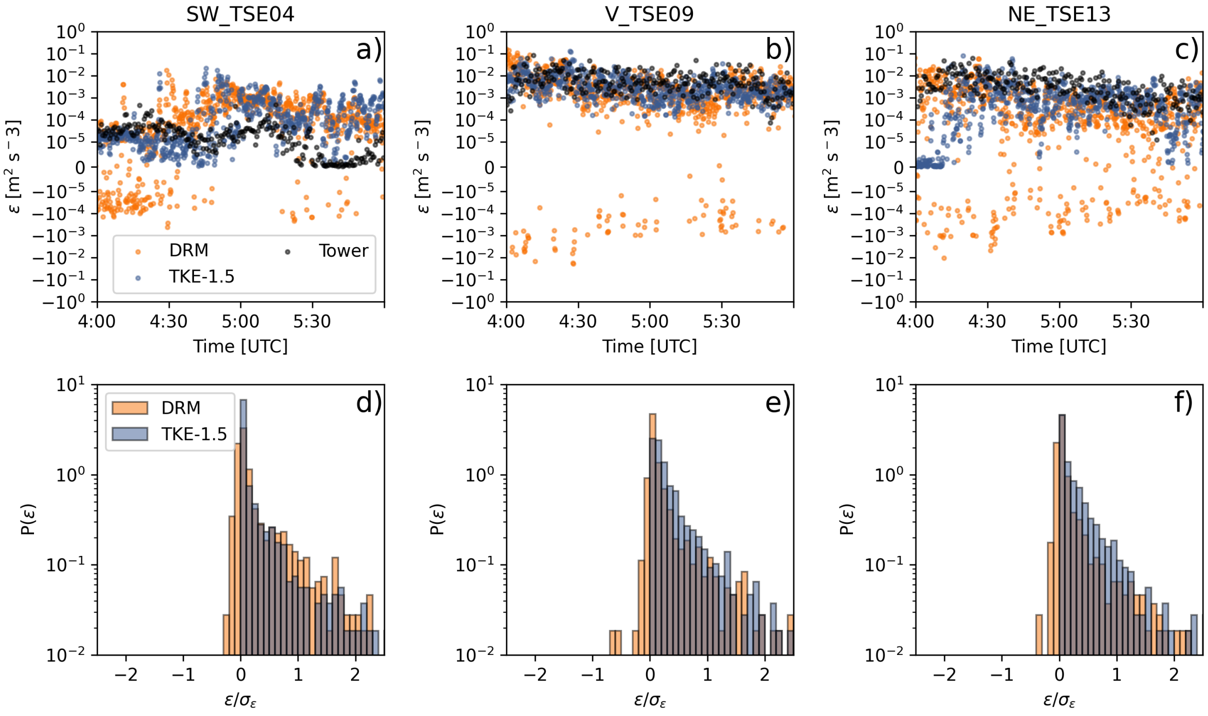

Figure 3.4: Time-series of 80 m turbulence dissipation rates from the model (a-c). Distribution of modeled turbulence dissipation rates (d-f). Towers SW_TSE04 and NE_TSE13 are located on ridge tops while tower V_TSE09 is located in the valley. Note that negative turbulence dissipation rates represent the backscatter from modeled scales to resolved scales. A scatter plot is used in (a-c) for clarity because periods of backscatter and dissipation can occur in quick succession for the DRM closure.

using the two closures. Figure 3.5 shows a time-series of dissipation rates derived for the TLS as well as for modeling results with the two turbulence closures. The TLS outputs GPS coordinates during its profiling, which allow us to extract the modeled dissipation rates at the same location as the TLS. In addition to the dissipation rates, Fig. 3.5 shows the vertical height of the TLS above sea level (a.s.l.). Closer to the surface, the modeled and observed dissipation rates are similar and largely range from 10^{-3} to 10^{-1}. When the TLS is at higher altitudes, the dissipation rates represent those above surface-generated turbulence and from within the LLJ. At the higher altitudes, both models underestimate the dissipation rates. The DRM closure provides slightly better predictions at higher elevations (from 04:25-04:40 UTC and 05:15-05:35 UTC), by over an order of magnitude, compared to the TKE-1.5 closure.

Analyzing flow quantities using a plan view provides context as to how the flow interacts with the terrain. Figures 3.6 and 3.7 show the time-averaged (05:00-06:00 UTC) wind

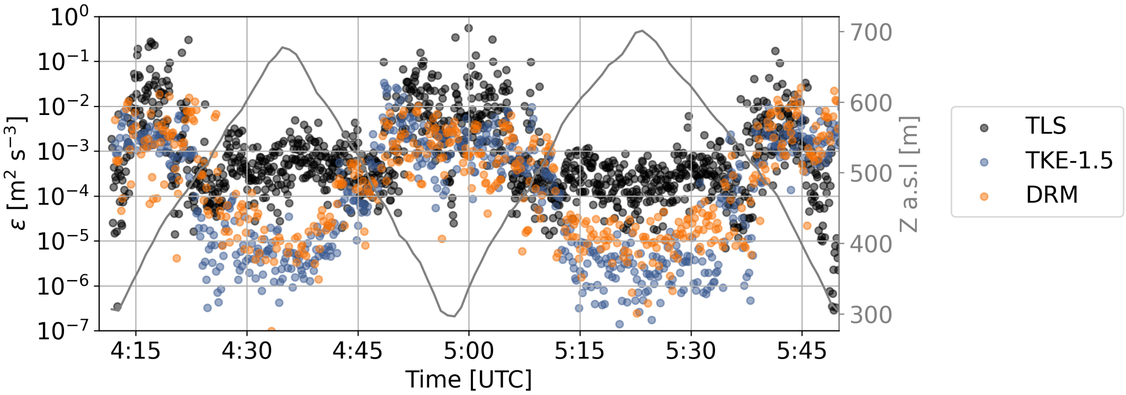

Figure 3.5: Time-series of turbulence dissipation rates from the TLS and the model with the two different closures. The values from the model are extracted based on the measured GPS positioning and altitude measurements from the TLS. The height of the TLS as a function of time is denoted with the secondary axis. Only positive values of turbulence dissipation rates from DRM are shown as the TLS only measures dissipation and not backscatter.

speed, turbulence dissipation rate, TKE, and integral time scale for the two different closures at 80 m a.g.l and 10 m a.g.l., respectively. For both of the figures, observed and derived time-averaged quantities from sonic anemometers are overlaid, which includes 3 tower locations for 80 m a.gl. (Fig. 3.6) and 47 tower locations for 10 m a.g.l. (Fig. 3.7). At 80 m a.g.l. (Fig. 3.6(a) and 3.6(e)), qualitatively, the wind speeds are similar for the two modeling results with the DRM closure predicting slightly faster wind speeds on the ridge tops. Additionally, the wind turbine wake is evident as the slower wind speeds downwind of the wind turbine where wake effects persist to the second ridge on average. At 10 m a.g.l. (Fig. 3.7(a) and 3.7(e)), there are a much larger number of sonic anemometers available for comparison at the met tower locations. For the near-surface winds, the first ridge experiences faster wind speeds compared to the second ridge, which both turbulence closures predict well. Overall, both turbulence closures predict near-surface winds accurately, displaying trends of slower wind speeds outside of the ridge-tops and faster winds on top of the ridges.

Given the good agreement of mean wind speeds from the modeling results and observations for both closures, we now move on to turbulence quantities, starting first with turbulence dissipation rates. For the DRM closure, only positive dissipation rates are included in the time-average. At 80 m a.g.l. (Fig. 3.6(b) and 3.6(e)), the flow is characterized with relatively low turbulence dissipation rates on the ridgetops and upwind of the first ridge, with much higher dissipation rates in the valley and downwind of the second ridge. The DRM closure does a better job of predicting the very low dissipation rates on the first ridge as results are more closely aligned with the observations. The DRM closure also predicts slightly higher dissipation rates upwind of the first ridge and in the valley. For the near-surface dis-

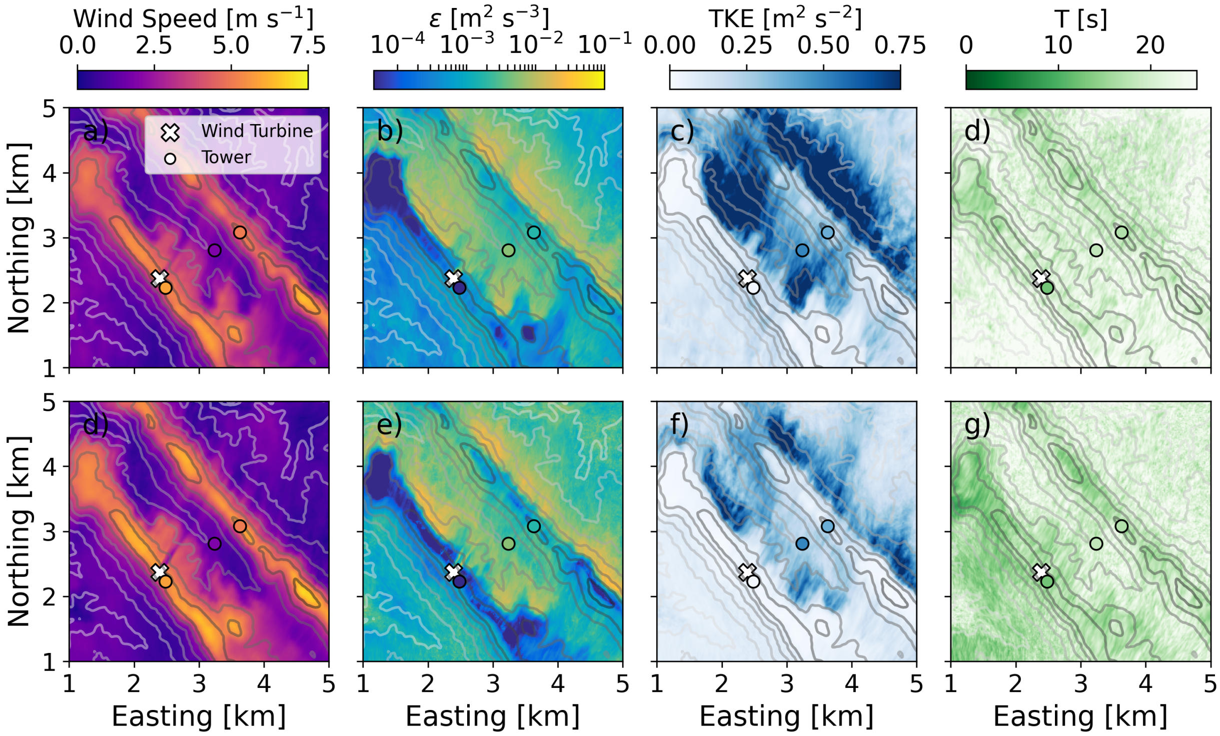

Figure 3.6: 1 h average (from 05:00 to 06:00 UTC) of 80 m wind speed, turbulence dissipation rate, TKE, and integral time scale for (a-d) the TKE-1.5 closure and (e-g) the DRM closure. Measurements from the SW_TSE04, V_TSE09, and NE_TSE13 are overlaid. Note that the integral time scale calculated for the towers has been multiplied by a factor of two for visualization purposes. Line contours represent 50 m changes in elevation.

sipation rates (Fig. 3.7(b) and 3.7(e)), in general, the DRM closure similarly predicts higher dissipation rates upwind of the first ridge; however, the TKE-1.5 closure predicts higher dissipation rates on the ridge-tops, in the valley, and downwind of the second ridge.

There is more TKE predicted by the TKE-1.5 closure compared to the DRM closure as shown at 80 m and 10 m a.g.l. in Figs. 3.6 and 3.7. The TKE, in general, is quite low outside of the regions downwind of the ridges. The TKE-1.5 closure more accurately predicts TKE at both heights, especially in the valley region, which agrees with the lower TKE biases for the TKE-1.5 closure at V_TSE09 indicated Tables 3.2 and 3.3. For the near surface, there is some over-prediction in TKE with the TKE-1.5 closure. The DRM closure underpredicts TKE, especially on the downwind ridge. One possible explanation is because the results with the DRM closure are more stably stratified than observed, as illustrated in Fig. 3.3(i).

The DRM closure resolves shorter integral time scales in the flow overall compared to the TKE-1.5 closure at both 10 m and 80 m a.g.l as shown in Figs. 3.6 and 3.7. Note that in Figs. 3.6 and 3.7, the integral time scales calculated for the towers have been multiplied

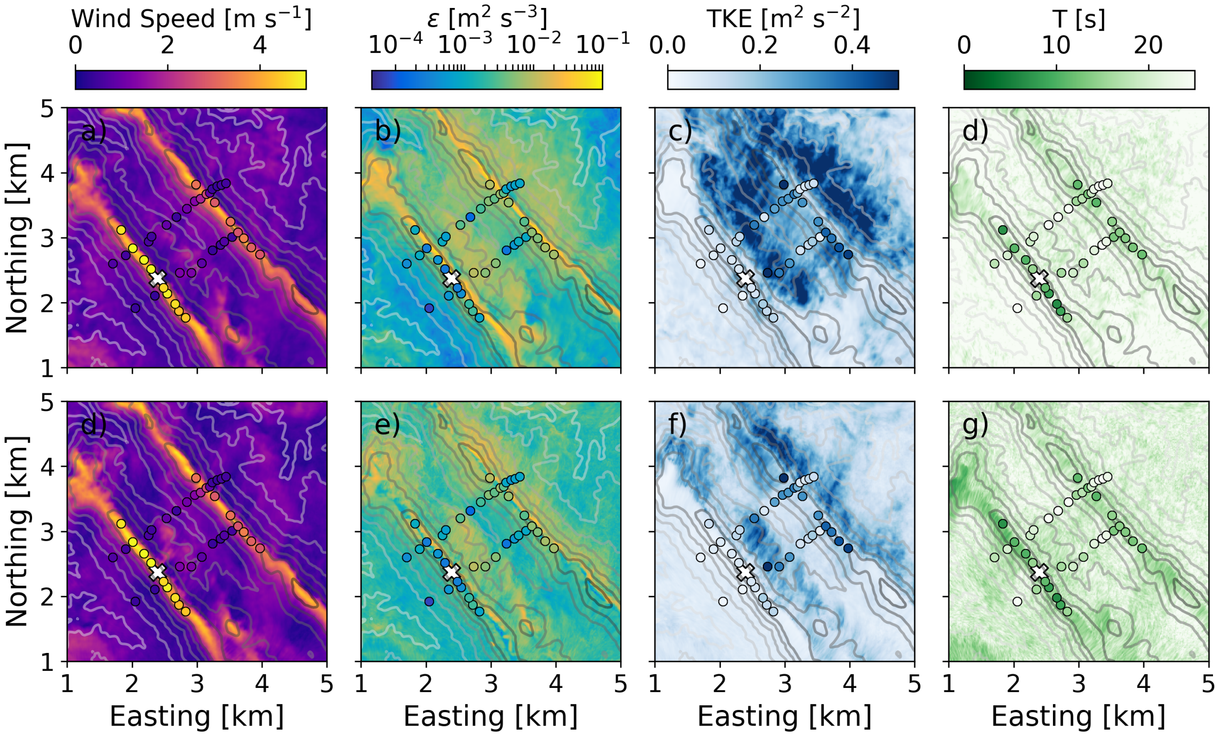

Figure 3.7: As in Fig. 3.6 but at 10 m and including measurements from additional towers of at least 10 m in height. As was done Fig. 3.6, the integral time scale calculated for the towers has been multiplied by a factor of two for visualization purposes.

by a factor of two for easier comparison, since both closures over-predicted the integral length scales by roughly a factor of two. Additionally, we examine the integral time scale as opposed to the integral length scale to reduce the dependency of the visualization on the wind speed itself. At both heights, the two closures over-predict the integral time scales but capture the general trend of shorter (or smaller) turbulent structures on the ridge-tops with much longer (or larger) structures elsewhere. The prediction of integral time-scales would be improved with a finer grid resolution, with significant additional computational expense. With the current modeling setup, the DRM closure demonstrates its skill resolving smaller-scale structures. However, note that the dissipation rates are very small ($\epsilon < 10^{-3}$ m^2 s^{-3}) at higher altitudes within the LLJ where the measurement uncertainty gets very large.

The spectral energy of vertical velocity transects at various locations demonstrates the quality of turbulence at different scales resolved by the model. In Fig. 3.8, $w-$velocity spectra taken along transects shown in Fig. 3.1 are presented for the two turbulence closures. The spectra are obtained following the methods of Durran et al. (2017) and Connolly et al. (2021) and consist of 300 points (3 km) along the transect. Spectra are obtained for each output time-step (1 Hz) between 05:00 and 06:00 UTC and then averaged. Upwind of the first ridge, the DRM closure resolves significantly more smaller-scale turbulent structures. On top of the first ridge, the DRM closure resolves much lower spectral energy for larger-scale structures compared to the TKE-1.5 closure. However, the larger-scale (or lower frequency) structures resolved by TKE-1.5 are not necessarily correct (discussed in the following paragraph). In general, the TKE-1.5 closure is resolving more energy at lower wave numbers for all five locations. For the smallest-scale turbulence, the DRM closure typically contains more energy except on top of the second ridge. Note that the spectral energy is lower in general for the ridge-tops compared to the other locations regardless of closure. Even though the spectral energy decreases rapidly for smaller-scales, which is a characteristic of a finite-difference scheme for LES, the increased energy at smaller wave-numbers for the DRM closure results in the shorter resolved integral time scales in Figs. 3.6 and 3.7.

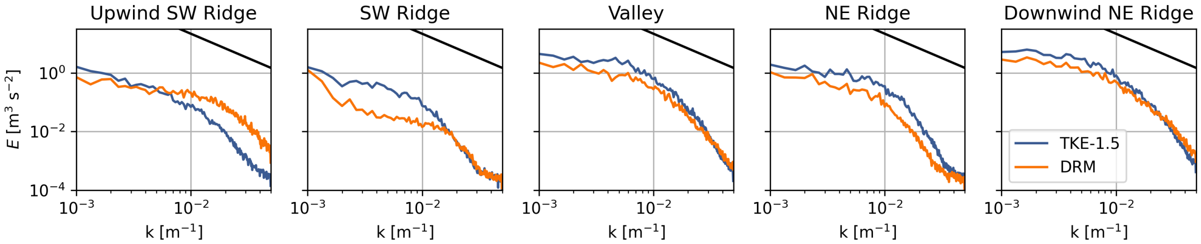

Figure 3.8: Wave-space spectra from 05:00 to 06:00 UTC of the vertical velocity at various locations along the transects shown in Fig. 3.1. The solid black line represents the -5/3 energy cascade in the inertial subrange.

Turbulence spectra in time-space can be compared with measurements from the sonic anemometers. In Figure 3.9, 80 m wind speed spectra is shown at two locations computed via the method of Welch (1967). The first location corresponds to the location of a tower named TSE01, while the second is on the ridgetop at SW_TSE04. Note, however, that the tower TSE01 is only a 20 m tower; therefore, measurements are only included for comparison with SW_TSE04. 10 and 20 m measurements are not used in the analysis because the differences between the resolved spectra for the two closures near the surface is negligible (not shown). At TSE01, upwind of the first ridge, the DRM closure resolves much more turbulent energy at higher-frequencies representing small-scale turbulence. For SW_TSE04, the TKE-1.5 closures contains more turbulent energy across all frequencies. At lower frequencies, both closures contain more energy compared to the measurements, with the TKE-1.5 resolving significantly more larger-scales, which follows Fig. 3.8.

The vertical structure of the flow is significantly modulated by the terrain. Figure 3.10 shows a time-averaged vertical slice (along the lidar transect in Fig. 3.1) of the velocity for the modeling results and DLR lidar. Focusing specifically on the flow downwind of the first ridge, the low-level jet deflects downwards as a result of the mountain wave. The wind turbine wake deflects downward as discussed in Chapter 2. Below the mountain wave, the

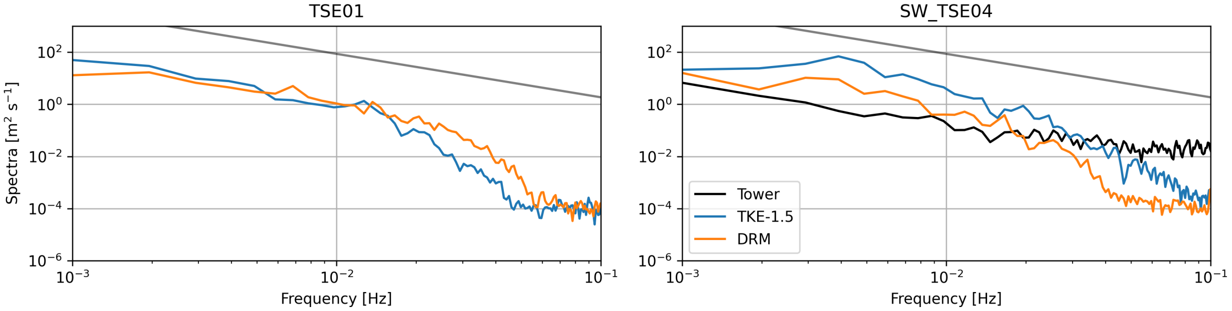

Figure 3.9: Spectra of 80 m wind speed at the locations of TSE_01 and SW_TSE04 for the measurements and model results for 05:00 to 06:00 UTC. The -5/3 inertial subrange energy cascade power law is shown in gray. Note that TSE_01 is only a 10 m tower so no measurements at 80 m are available at this location.

flow is affected by the ground, which results in wind shear and slower wind speeds closer to the surface. The modeling results agree well with the observations with some differences higher in the atmosphere. The two closures display similar characteristics but with the DRM closure having a stronger downward deflection of the wake in the lee of the first ridge similar to the observations. The TKE-1.5 closure predicts slower velocities at the surface in the lee of the first ridge, which elevates the wind turbine wake slightly in comparison to the results from the DRM closure.

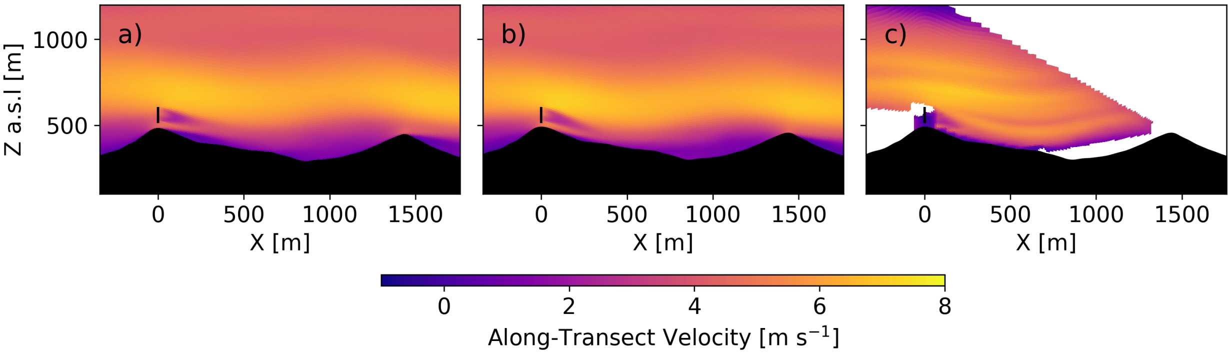

Figure 3.10: Vertical slice of along-transect velocity time-averaged from 05:00 to 06:00 UTC for (a) TKE-1.5, (b) DRM, and (c) the DLR lidar. The transects are aligned with the lidar transect from Fig. 3.1.

The vertical turbulent structure of the flow can be analyzed by looking at the time-averaged (05:00-06:00 UTC) turbulence dissipation rate for the flow in Fig. 3.11. For the results from the DRM closure (Fig. 3.11(a)), only positive dissipation rates are used in the time-average. Figure 3.11 also has the dissipation rates from the CLAMPS lidar overlaid. Both of the turbulence closures have similar turbulence characteristics with higher dissipation rates closer to the surface and in the wind turbine wake. The DLR lidar scan demonstrates this as well; however, with slightly higher values, especially from $X = 750$ - 1500 m. Additionally, the DLR lidar shows higher dissipation rates in the negative shear region of the LLJ in the upper atmosphere that the models largely do not capture. This is likely because there is less shear in the model compared to the observations and because the height of the wave is underestimated (see Fig. 3.10. There is some increased dissipation for the DRM closure in the upper atmosphere, but the rates are still underestimated compared to the observations. Within the LLJ, the modeling results predict lower dissipation rates compared to the DLR lidar scan from $X = 0 - 500$ m; however, it should be noted that in these lower turbulence regions, there is more uncertainty in the lidar returns (Wildmann et al., 2019). Further downwind, there are missing data points from the DLR lidar in very low turbulence regions, but the CLAMPS is available and indicates very low dissipation rates that agree well with the modeling results (discussed in more detail in Fig. 3.13).

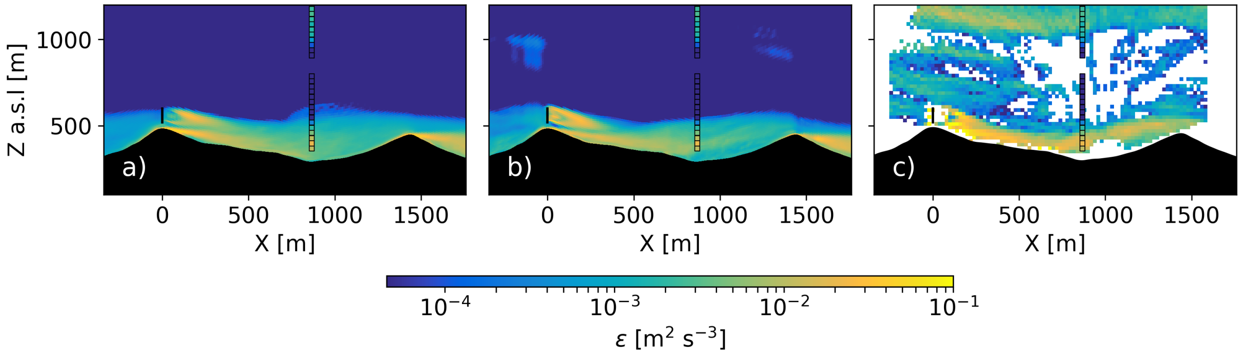

Figure 3.11: As in Fig. 3.10 but for turbulence dissipation rate. Additionally, data from the CLAMPS are overlaid. Note that for DRM, the average only considers positive values or dissipation and not backscatter.

Comparisons between the modeling results and observations have focused on the positive dissipation rate since the measurement devices can only derive positive dissipation. In a model to model comparison, we can compare dissipation rates including the negative backscatter values. Figure 3.12 shows turbulence dissipation rates for the two closures at 04:28:30 UTC. For the TKE-1.5 closure, all dissipation rates are positive since it can only represent positive dissipation whereas for the DRM closure, there are small regions of blue representing backscatter. In Fig. 3.12, there are two pockets of backscatter in the inflow region of the wind turbine that potentially resemble the coherent vortical structures observed by Carper and Porte-Agel (2004). In addition to those pockets of backscatter, there are other regions in the near-surface flow indicating backscatter. Upwind of the first ridge, the

DRM closure also displays much more variability in ϵ compared to the TKE-1.5 closure.

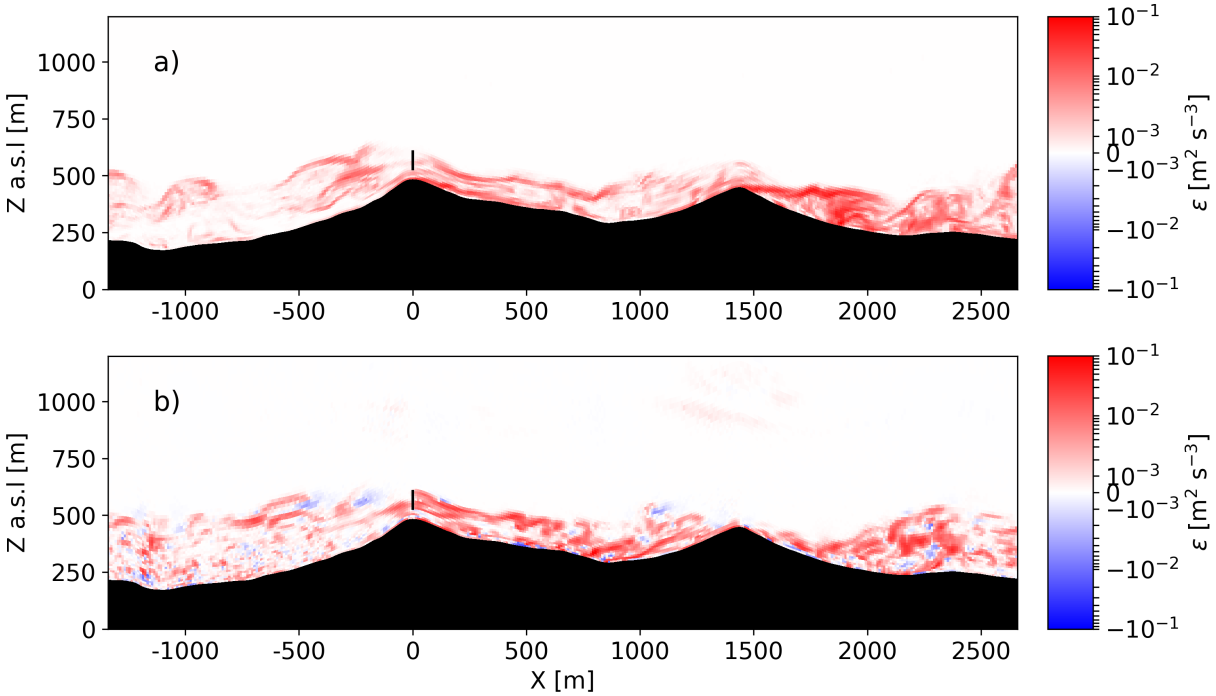

Figure 3.12: Vertical slice of turbulence dissipation rate for (a) TKE-1.5 and (b) DRM at 04:28:30 UTC. Regions in blue highlight backscatter which is only present when using the DRM closure. The transects are aligned with the lidar transect from Fig. 3.1align

The measurements and modeling results can be more quantitatively compared by extracting time-averaged vertical profiles at various streamwise distances in the flow. Figure 3.13 shows vertical profiles for the turbulence dissipation rates at various distances upwind and downwind of the wind turbine. The distances in Fig. 3.13 are normalized by rotor diameter ($D = 80$ m), which is common in many wind studies involving wind turbine wakes. The DLR lidar scans are included at all the distances while the CLAMPS data is only include at $10.84D$, which corresponds to its location in the rotated coordinate system. As previously discussed, the models underestimate the turbulence dissipation rates above the near surface region (greater than 150 m a.g.l.). It should be noted again that the uncertainties in the DLR lidar dissipation rates grow very large when $\epsilon < 10^{-3}$ m^2 s^{-3} (Wildmann et al., 2019). While both turbulence closures underestimate ϵ in the upper atmosphere, the values for the DRM closure can be over an order of magnitude larger and closure to the observations than the TKE closure. At a distance of $10.84D$, there is good agreement between the modeling results and the CLAMPS from the surface and within the LLJ, with slightly better agreement for the DRM closure, especially within the LLJ. Neither closure captures the increased dissipation rates above 600 m a.g.l. because, as previously mentioned, there is less shear in the negative shear region predicted by the model and because the height of the wave is underestimated. In the near-surface region (below 150 m a.g.l.), the modeling results and measurements show strong agreement.

A second suite of simulations was conducted in an aim to extract effects solely due to the wind turbine wake. For both turbulence closures, the additional simulation runs from 05:00 to 06:00 UTC with the same modeling setup but without the wind turbine parameterization. In Fig. 3.13, additional vertical profiles are shown for the simulations conducted without the wind turbine. At distances of $2D$ and $4D$, the added dissipation by the wind turbine wake is evident in the bottom 200 m. Notably, at a distance of $2D$, the wake added dissipation is as much as two orders of magnitude or more higher throughout the rotor plane. At a distance of $4D$, the wake added dissipation is larger in the upper half of the rotor plane with added dissipation rates being roughly one order of magnitude larger. These increases in ϵ are inline with those observed by Lundquist and Bariteau (2015) but with some variability due to differences in the downstream distance of the vertical profiles.

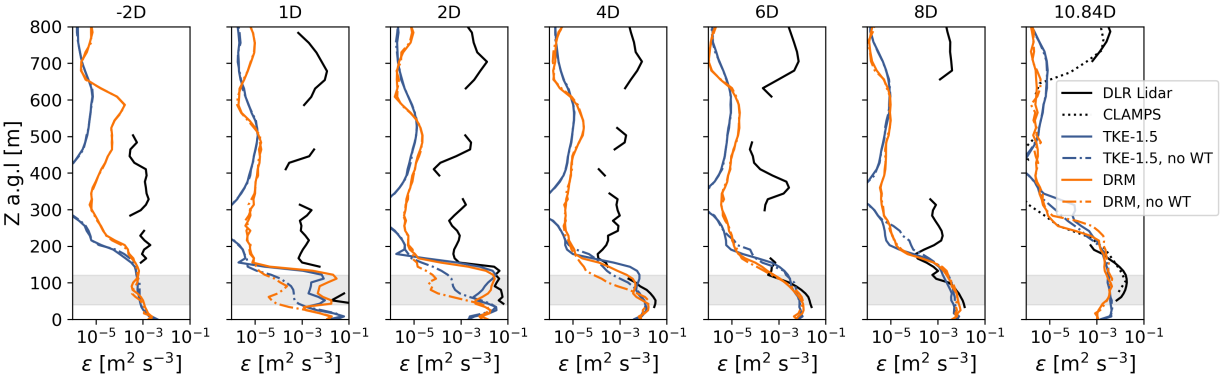

Figure 3.13: Comparison of 1 h averaged (from 05:00 to 06:00 UTC) vertical profiles of measured and modeled turbulence dissipation rates at various distances upwind and downwind of the wind turbine. Note that for DRM, the average only considers positive values or dissipation and not backscatter. The gray region represents with the wind turbine rotor layer.

Wind turbine wake recovery

The simulations without the wind turbine parameterization allow us to analyze the impact of the wind turbine wake on the flow for each turbulence closure. Transects shown in this subsection are along the veered wake transect in Fig. 3.1. While the lidar transect captures the near wake of the wind turbine, the wind direction is misaligned by nearly 20 degrees with this transect and as a result, the wake veers out-of-plane. Figure 3.14 shows the average wind direction as function of height as well as a plan view of the wind speed difference for simulations with and without turbines for the two closures. For Figs. 3.14(b) and 3.14(c), the wind speed difference is vertically averaged for model levels between heights of 40 m and 320 m a.g.l. due to the vertical movement of the wake downwind. The wind speed differences show the velocity deficit as a result of the wind turbine wake with the veered wake transect intersecting the majority of the deficit. However, note that the flow evolves slightly differently as a result of the wind turbine rotor parameterization so not all differences are due to the wake itself. The veered wake transect aims to capture as much of the wake as possible in a two-dimensional visualization, although the wind direction changes with height (wind veer), wake rotation, and wake meandering can still result in the wake moving out of the veered wake transect. In an attempt to capture as much of the wake effects as possible in this subsection, quantities are averaged by the rotor diameter (80 m) in the spanwise direction. Additionally, note that because the analysis in this subsection focuses on the average veered wake transect, no measurement devices are available for comparison.

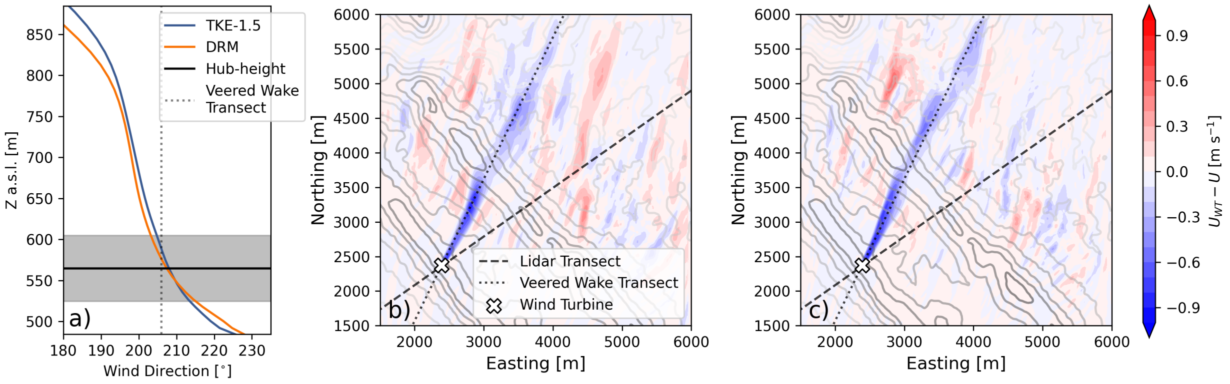

Figure 3.14: (a) 1 h averaged (from 05:00 to 06:00 UTC) wind direction as a function of height in the simulations without the wind turbine at $X = 0$ m as well as a plan view of the wind speed U difference between simulations with and without the wind turbine for (b) TKE-1.5 and (c) DRM. For the (b) and (c), the plan view is vertically averaged for model levels between heights of 40 m and 320 m a.g.l. to capture as much of the wake deficit as possible. Line contours represent 50 m changes in elevation.

.

Figure 3.15 shows the difference in the wind speeds, TKE, and turbulence dissipation rate between the two simulations due to the wind turbine wake for the two turbulence closures. Regardless of closure, the modeling results suggest that the slower wind speeds induced by the wind turbine persists over 3.5 km downwind of the turbine, which is over 40 rotor diameters (Figs. 3.15(a) and 3.15(b)). In Fig. 3.15, the X dimension represents nearly the entire downwind distance until the domain edge. While $40D$ is a long distance for the wind turbine wake to propagate, this is consistent with observations for wind turbine wakes in flat terrain in stable boundary layer conditions (Hirth and Schroeder, 2013). The wind turbine wake largely exists within the LLJ where turbulence levels are low. The average TKE at the inflow location on SW_TSE04 where the tower and turbine sit within the LLJ is just 0.03 $\mathrm{m}^2\ \mathrm{s}^{-2}$. For reference, the TKE in the valley, which represents flow beneath the LLJ is over 12 times greater at nearly 0.33 $\mathrm{m}^2\ \mathrm{s}^{-2}$. Additionally, work from Chapter 2 (Wise et al., 2022) shows that wind turbine wake effects persist for significantly longer (over $30D$) when the rotor is positioned within a LLJ compared to below it. Overall, both turbulence closures display similar trends; however, the TKE-1.5 closure does show slower wind speeds in the wake persisting slightly further in the X-direction most notably between 1000 and 1500 m.

Wake-added turbulence dissipation rates are greatest in the first 1500 m downwind of the turbine with some persistence further downwind. In Figs. 3.15(c) and 3.15(d), the wake-added dissipation follows similar trends between the two closures but the DRM closure indicates higher ϵ within the wind turbine wake which then also persists across the entire domain, as far as the velocity deficit. In contrast, the wake-added ϵ predicted by the TKE-1.5 closure does not persist as far. There are also significant differences in the wake-added ϵ predicted by the two closures in the very near wake region (within 160 m or $2D$). Validating ϵ within the wind turbine wake is difficult due to the misalignment of the wake with any measurements; however, Fig. 3.13 does show that the DRM closure seems to predict ϵ more accurately at distances of $2D$ and $4D$ when the wake is still partially captured by the lidar transect. At distances closer to the rotor (less than $2D$), the lidar is unable to retrieve the turbulence dissipation rate.

While the velocity deficits (and ϵ for the DRM closure) induced by the wake persist over $40D$, the added TKE due to the wind turbine does not persist as far. Figs. 3.15(e) and 3.15(f) show the TKE difference for the simulations with and without the wind turbines for the two closures. The added TKE persists 2.5 to 3.0 km downwind of the turbine for both closures, with slightly more persistence for the DRM closure. Interestingly, for both closures, there is some reduced TKE below the wake and LLJ downwind of the second ridge, which follows trends observed for ϵ. For both closures, the added TKE from the wake is greatest mid-way through the valley ($X \approx 400-640$ m or 4-$8D$), which is characteristic of wind turbines wakes observed in wind tunnels (Crespo and Hernández, 1996) and other modeling studies (Wu and Porté-Agel, 2011). While both closures display similar behavior, the TKE-1.5 closure does show slightly greater added TKE compared to the DRM closure. The added TKE in wind turbine wakes is a result of vortices within the wake breaking down and because of the increased shear as a result of the slower wind speeds of the wake. Sarlak et al. (2015) found that less dissipative turbulence closures had a quicker breakdown of wake contained vortices to smaller structures. This is in line with the results presented in Fig. 3.15 in that the lower wake-added dissipation for the TKE-1.5 closure results in greater TKE (due to the breakdown of vortical structures) within the wind turbine wake.

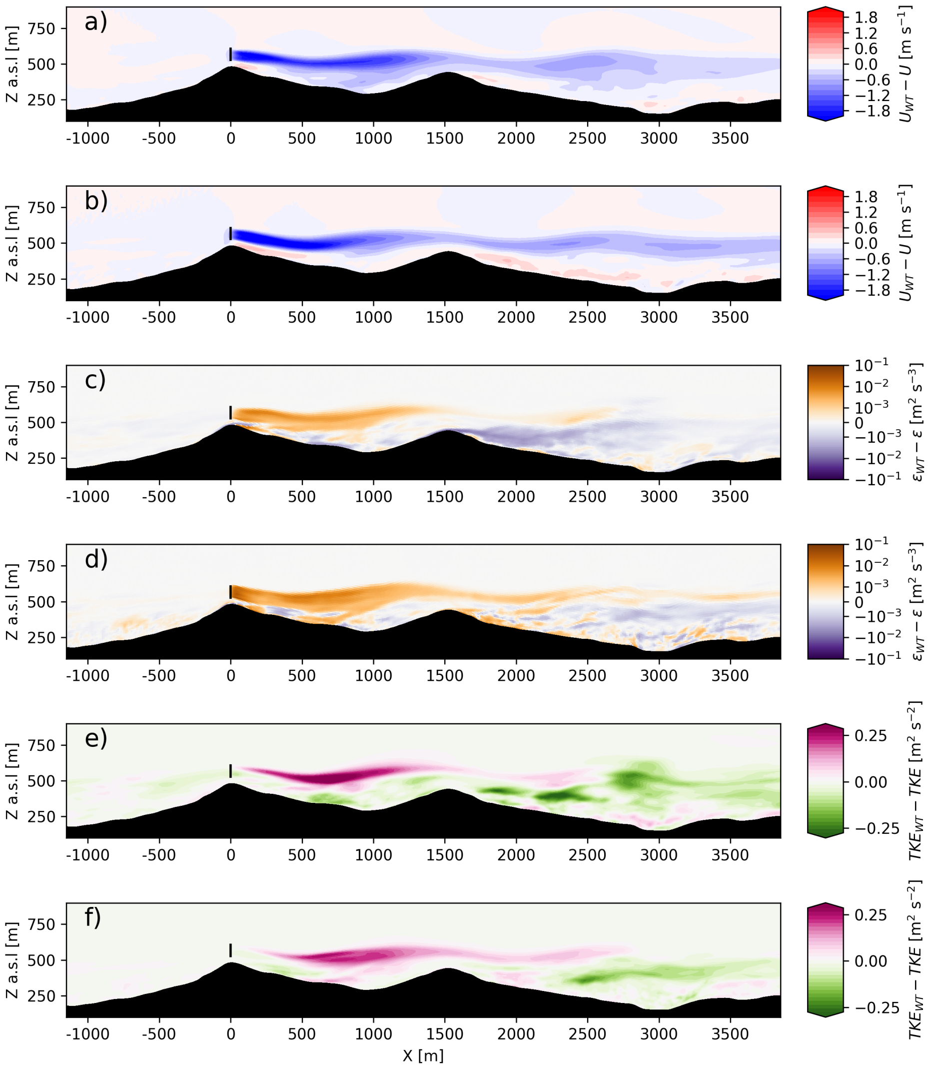

Figure 3.15: Vertical slice of 1 h averaged (from 05:00 to 06:00 UTC) (a,b) wind speed U, (c,d) turbulence dissipation rate ϵ, and (e,f) TKE difference between simulations with and without the wind turbine for (a,c,e) TKE-1.5 and (b,d,f) DRM. The transect is aligned with the veered wake transect in Fig. 3.1.

3.5 Conclusions

In this study, modeling results of a mountain wave in complex terrain are compared with novel measurement techniques with a strong focus on turbulence quantities during a detailed stable boundary layer (SBL) case study. The modeling setup uses the WRF-LES-GAD tool, which captures turbulence from time-varying multi-kilometer mesoscale phenomena to microscale ambient turbulence. All of these scales of turbulence are relevant to understanding the complex interaction between stable boundary layer flows, terrain, and wind turbine wake dynamics. SBL conditions are especially of interest to wind turbine wake flows, as the generally low turbulence levels during these conditions result in wind turbine wake effects propagating very far downstream with the possibility of affecting neighboring wind turbines. This study is the first of its kind to analyze wind turbine wake turbulence characteristics in complex terrain.

This work builds upon the stable boundary layer case study of Chapter 2 (Wise et al., 2022) and Wildmann et al. (2019). For the modeling setup, two different large eddy simulation (LES) closures were used on the micro-scale domains. The first is the standard turbulent kinetic energy 1.5-order (TKE-1.5) model from Deardorff (1980), which is a commonly used closure in LES modeling and represents the standard. The second closure is that of Chow et al. (2005) and utilizes an explicit filtering and reconstruction and velocity reconstruction framework, known as the dynamic reconstruction model (DRM), which has been found to outperform conventional turbulence closures, especially in stably stratified conditions (Zhou and Chow, 2011; Zhou and Chow, 2014) (and is also shown in Chapter 4). Modeling results are compared with numerous measurement devices including sonic anemometers on met towers, lidars, and a tethered lifting system (TLS). This work pays special attention to turbulence quantities such as integral length and time scales, turbulence dissipation rate, and turbulent kinetic energy (TKE), many of which are derived from the measurement devices using novel methods.

Modeling results exhibit good agreement with many of the measurement devices. Both closures underestimate the wind speed within the low-level jet (LLJ), which results in a decrease in the mountain wave wavelength compared to the observations. However, at the ridgetops and when analyzing the flow at the hub-height (80 m a.g.l.) and near the surface (10 m a.g.l.), the wind speeds agree well with measurements, especially in the second half of the simulation period (05:00-06:00 UTC). The TKE at the southwest ridge (which can be considered as inflow for the wind turbine) is very low at 0.14, 0.03, and 0.05 $\mathrm{m}^2\ \mathrm{s}^{-2}$ for the measurements, TKE-1.5 closure, and DRM closure, respectively. The TKE-1.5 closure overestimates turbulence because it resolves structures that are larger than those that were observed (Fig. 3.9). Additionally, the DRM closure was found to resolve smaller-scale turbulence (shorter time-scales) with more energy compared to the TKE-1.5 closure, which was especially true upwind of the southwest ridge (Figs. 3.8 and 3.9). After the flow is significantly modulated by the terrain, however, the differences between the two closures is less pronounced.

One added benefit of using the DRM closure is its ability to capture negative turbulence dissipation rates, which represent the backscatter of energy from smaller-scales combining into larger scales. In comparison, the TKE-1.5 closure is a standard eddy-viscosity model and can only capture positive dissipation rates. The turbulence dissipation rate is visualized for the modeling results and coherent vortical structures of negative dissipation rates akin to those observed in the field by Carper and Porte-Agel (2004). With the experimental setup and methods from the Perdigão campaign, backscatter could not be derived from the measurements. When analyzing only the forward scatter, both closures agreed well with observations, especially in the near-surface and wind turbine wake regions with slightly better predictions from the DRM closure. Within the LLJ, the modeling results underestimate the dissipation rates compared with the scanning lidar and TLS, but with some improvement when using the DRM closure. The dissipation rates within the LLJ are very low ($< 10^{-3}$ m^2 s^{-3}), which is where the measurements have a relatively large uncertainty. The dissipation rates from the vertical profiling lidar show overall very strong agreement with the modeling results except at higher altitudes, highlighting the variability in the dissipation rates within the LLJ. While backscatter could not be validated with the experimental setup, turbulent spectra showed that the DRM closures shows more energy at fine scales due to backscatter and is therefore more realistic.

Wind turbine wake characteristics were isolated by running analogous simulations but without the wind turbine parameterized. While the differences in the flow are largely due to the wind turbine wake, the flow evolved slightly different so not all differences were entirely due to the wake itself. When analyzing wake characteristics along a transect that aims to capture as much of the wake effects as possible, the velocity deficits persist over $40D$ downwind regardless of turbulence closure. The wakes propagate this far because the turbine is within a LLJ with very little ambient turbulence. The wake therefore stays lofted in the lower turbulence levels of the LLJ with little energy to diffuse the wake. While the velocity deficits persist over $40D$, the wake-added TKE and turbulence dissipation rates do not persist as far (except for very weak levels of ϵ for the DRM closure). Both turbulence metrics persist with elevated levels until $30D$ but peak in the mid-wake region (4-$8D$). The turbulence characteristics of the wake themselves vary between the two closures, with the DRM closure indicating higher turbulence dissipation compared to the TKE-1.5 closure. As a result, the resolved TKE is greater for the TKE-1.5 closure as the wake breaks down more quickly compared to the DRM closure.

The results presented here demonstrate the DRM closure's performance in SBL conditions with complex terrain with a wind turbine rotor parameterization. The ability of the DRM closure to represent backscatter and smaller turbulent structures is a benefit; however, differences in the flow structure compared to the TKE-1.5 are small in regions downwind of major topographic features, which is consistent with Connolly et al. (2021) who, for their method, also saw that topography reduces downwind differences in turbulence evolution. Ultimately, the DRM closure should be tested in a broad range of conditions in complex terrain to better understand in what flow regimes the DRM closure is most impactful. Nonetheless, this study demonstrates the efficacy of the DRM closure in cases where small-scale turbulence is especially important.

Chapter 4

Wind farm performance in a range of stable atmospheric conditions[1]

4.1 Introduction

Onshore wind turbines experience the stable atmospheric boundary layer nearly every night. Stably stratified flows occur as the earth's surface cools in the absence of radiation from the sun. The associated buoyancy suppression results in small-scale and sometimes intermittent turbulence, which can be difficult to capture in numerical models. This relatively small-scale and low-amplitude ambient turbulence, especially when compared to daytime convective conditions, results in wind turbine and farm wakes sometimes persisting over 30 rotor diameters (D) in distance (Hirth and Schroeder, 2013), which can be over 4 km downwind, depending on the turbine type. Additionally, turbine fatigue damage is highly correlated with strong vertical wind shear, periods of elevated turbulence, and wavy turbulence, all of which are common in the stable boundary layer (SBL) (Sisterson and Frenzen, 1978). Representation of stably-stratified turbulence is critical when modeling wind farms to characterize and predict performance.

Wind turbine performance during nocturnal stable conditions is highly dependent on many factors, including the strength of stability, presence of waves, intermittency, and characteristics of frequently occurring low-level jets (LLJs), which can increase turbulence intensity and intermittency, as well as mean shear and veer profiles. For weak and moderate stability, shear production overcomes buoyancy and turbulence is continuous in the SBL. For strong stability, buoyancy suppression can overwhelm shear production, resulting in an intermittent regime of turbulence (Stull, 1988). This interaction between mean shear and buoyancy is only one mechanism by which turbulence is intermittent. Other mechanisms which trigger SBL intermittency include breaking gravity waves, bores, Kelvin-Helmholtz

---

[1] This chapter is a modified reproduction of a manuscript "Two-way interactions between wind turbines and atmospheric turbulence under weak to strong stability conditions" by Adam S. Wise (the principal author), Robert S. Arthur, Jeffrey D. Mirocha, Julie K. Lundquist, and Fotini K. Chow, submitted to the *Journal of Renewable and Sustainable Energy*, Apr 2024, (Wise et al., 2024), © 2024 AIP Publishing.

billows, terrain-induced flows, and propagating density currents (Rottman and Simpson, 1989; Sun et al., 2002; Banta, 2008).

Intermittent turbulence in the SBL can affect turbine power production, wake recovery, and structural loading. Among the goals of the American Wake Experiment (AWAKEN) field campaign is to investigate the role of intermittent turbulent bursting events on wind farm power production and the structural loading of wind turbines (Moriarty et al., 2020). The AWAKEN field campaign focuses on nine wind farms in Oklahoma, USA. The terrain is characterized by gentle, hilly ridges with numerous river valleys. This region is known for its abundant wind resource which commonly comes in the form of nocturnal LLJs (Krishnamurthy et al., 2021). The predominant wind direction of these LLJs is from the south, and several of the wind farms are located north of east-west river valleys leading to the potential for terrain-generated production and augmentation of intermittent turbulence.

Intermittent turbulence was observed on numerous nights with strongly stable conditions during the Cooperative Atmospheric Surface Exchange Study (CASES-99) (Poulos et al., 2002; Coulter and Doran, 2002). CASES-99 took place nearby in Kansas in October 1999, with terrain similar to AWAKEN. Zhou and Chow successfully modeled intermittent turbulence observed during the CASES-99 field campaign (Zhou and Chow, 2014). They used the Advanced Regional Prediction System model in a multi-scale nested setup with large-eddy simulation (LES) at a horizontal grid spacing of 25 m on the finest domain. Their study found that intermittent turbulence could be generated through gravity wave breaking over a cold-air pool in the valley upwind of measurements. However, wave breaking was only observed when using a more sophisticated turbulence closure scheme known as the dynamic reconstruction model (Chow et al., 2005) was used. These insights are relevant to AWAKEN because, 25 years later, the region now consists of numerous wind farms and the effect of this intermittent turbulence on wind turbines and wind farms is potentially significant, yet still largely unknown, due to sparse observations and difficulty in simulating stable conditions.

In this study, we simulate idealized weak, moderate, and strong stability conditions to study the interaction between wind turbines and the SBL, to 1) determine how the presence of wind turbine wakes affects stable boundary layer evolution, and 2) examine the effect of intermittent turbulence on power production and wake recovery.

To answer these questions, we use LES to solve for the most energetic scales of turbulence while parameterizing the effects of the smaller turbulent length scales on the resolved-scale flow. LES of the SBL has typically been limited to weakly or moderately stable conditions due to the large computational expense required to resolve turbulence under strongly stable conditions. LES uses a spatial filter to separate the larger resolved scales from the subfilter-scale (SFS) motions. This filter can be implicit - based on the grid scale, or explicit. The effects of the SFS scales on the resolved scales are then parameterized using a turbulence model. As stability increases, the energetic turbulent motions become smaller and smaller, requiring a finer grid to resolve them. The most common LES schemes use an eddy-viscosity model with no explicit filter to relate SFS and resolved motions. These models are entirely dissipative with energy transfer from larger scales to smaller scales; however, energy transfer from small to large scales is important, especially in stably stratified environments (Sullivan et al., 2003). More sophisticated turbulence closures are able to account for this backscatter of energy using an explicit filtering approach. Here, we use the DRM model of Chow et al. (2005) to extend the working range of LES and to analyze turbine-airflow interactions in more stably stratified flows.

There have been a number of idealized LES studies that demonstrate the dependence of simulation results to the turbulence closure. Many of the first SBL LES simulations were done as part of the Global Energy and Water Cycle Experiment Atmospheric Boundary Layer Study (GABLS) (Beare et al., 2006). The GABLS setup is idealized with the lateral boundary conditions being periodic and stable stratification is realized using a prescribed surface cooling rate of 0.25 K h^{-1}. The initial conditions are a neutral potential temperature profile up to 100 m with an overlying inversion and a geostrophic wind speed of 8 m s^{-1}. In Beare et al. (2006), they found that at a moderate grid spacing (6.25 m), mean profiles were highly dependent on the turbulence closure; however, at fine resolutions of 2 m or less, there were only small changes in mean profiles. The GABLS study has provided the framework for many SBL studies even though the prescribed cooling rate is relatively weak. More recently, the work of Gadde and Stevens (2021b) has explored weak and moderate SBLs (cooling rates ranging from 0.125 to 0.5 K h^{-1}) with a very large finite wind farm. They found that wakes recover more quickly for less stable boundary layers but that wind veer can aid in wake recovery for stronger stratification. In their study, they used a scale-dependent model based on Lagrangian averaging to dynamically solve for the turbulent stresses. Zhou and Chow (2011) modeled a range of SBLs comparing the TKE-1.5 and the DRM closures at various grid resolutions in idealized conditions. They found that the DRM closure improves the representation of near-surface profiles under moderate and strong ($\sim$ 2.0 K h^{-1}) stability conditions. As a result, the DRM closure was able to sustain resolved turbulence and better represent mean shear and potential temperature profiles at coarser resolution.

In this study, we use LES and the DRM turbulence closure to simulate weak, moderate, and strong SBL conditions with a wind turbine parameterization (Sect. 4.2) to comprehensively explore the full range of SBL interactions with a wind farm. This builds on a number of previous studies in the literature, which have used idealized LES to examine certain SBL conditions for modeling wind turbine and wind farm flows (Lu and Porté-Agel, 2011; Marjanovic et al., 2017; Gadde and Stevens, 2021b; Sanchez Gomez et al., 2023). First, a grid sensitivity study is completed to verify that resolved turbulence is sustained in all stability regimes (Sect. 4.3). Then, because the strongly stable regime is intermittently turbulent, we quantify intermittency (Sect. 4.3). Lastly, we analyze the interaction between the wind farm and different SBL conditions focusing on wind farm power production (Secs. 4.3 and 4.3), followed by conclusions and recommendations for future work (Sect. 4.4).

4.2 Methods

WRF-LES-GAD

To study wind farm performance in a range of SBL conditions, we use the LES capability of the WRF model (Skamarock et al., 2021), version 4.4, with a generalized actuator disk (GAD) (Mirocha et al., 2014a), hereinafter referred to as WRF-LES-GAD. The GAD model implemented in WRF follows blade element momentum theory and requires specifications for the turbine's airfoil lift and drag coefficients. These coefficients come from a 1.6 megawatt (MW) wind turbine parameterization used in Arthur et al. (2020), which has a 80-m hub-height and 80-m rotor diameter (D). This GAD implementation typically requires a grid spacing of at least 10 m to capture the effect of the rotor drag on the resolved flow (Mirocha et al., 2014a; Mirocha et al., 2015; Arthur et al., 2020; Sanchez Gomez et al., 2022; Sanchez Gomez et al., 2023). WRF-LES-GAD also includes a modified surface layer implementation (Mirocha et al., 2015) which iteratively solves for velocities and temperature at the first grid point above the surface using Monin-Obukhov similarity theory (MOST) (Monin and Obukhov, 1954).

For turbulence, the main closure model used here is the dynamic reconstruction model (DRM) (Chow et al., 2005) implemented in WRF (Kirkil et al., 2012) as described further below. Comparisons are also made to the commonly-used turbulent kinetic energy order-1.5 model (TKE-1.5) (Deardorff, 1980), which solves a prognostic TKE equation with a grid-based length scale to define the eddy viscosity.

Dynamic reconstruction turbulence model

Note that the descriptions in the following two subsections are the same as described in Chapter 3, but are included for completeness and clarity.

The dynamic reconstruction model uses a 3D filter applied to the Navier-Stokes equations to separate large and small scales. This filter is twice the grid cell spacing and is applied explicitly in the model; it is thus distinct from the implicit effects of grid discretization. The effect of the implicit grid filter, as well as numerical truncation errors, is to prohibit motions smaller than the grid scale. There is thus a range of scales between the grid scale and the filter scale that can be partially reconstructed in the model.

The governing equations of LES on a discrete grid are:

$$\frac{\partial \overline{\tilde{u}}_i}{\partial t} + \frac{\partial \widetilde{\overline{\tilde{u}}_j \overline{\tilde{u}}_i}}{\partial x_j} = -\frac{1}{\rho}\frac{\partial \overline{\tilde{p}}}{\partial x_i} + \nu \frac{\partial^2 \overline{\tilde{u}}_i}{\partial x_i \partial x_j} - \frac{\partial \tilde{\tau}_{ij}}{\partial x_j} + \tilde{F}_i \tag{4.1}$$

where x_i represents the x, y, and z spatial dimensions, u_i are velocities, p is pressure, ρ is density, τ is the turbulent stress, and $\tilde{F}_i$ represents a body force (such as drag from a wind turbine rotor). The operators are: $\overline{u}_i$ is the filtered velocity field via a smooth spatial filter, $\tilde{u}_i$ is the resolved velocity field, and $\overline{\tilde{u}}_i$ is a resolved, filtered velocity. The larger implicit filter over the advection term represents the effect of the discretization ∂/∂_j which acts as an implicit filter cutting off higher wavenumbers.

The full turbulent stress term is referred to as the subfilter-scale stress (τ^{SFS}) which is made up of two components, a resolvable subfilter-stress (RSFS), τ^{RSFS}, and a subgrid-scale (SGS) stress, τ^{SGS}:

$$\tau^{SFS} = \tau_{ij} = \tau^{SGS} + \tau^{RSFS} = \left(\overline{u_i u_j} - \overline{\tilde{u}_i \tilde{u}_j}\right) + \left(\overline{\tilde{u}_i \tilde{u}_j} - \overline{\tilde{u}}_i \overline{\tilde{u}}_j\right) \tag{4.2}$$

The RSFS term represents the range of eddy motions between the implicitly defined grid filter (i.e., the Nyquist limit) and the explicit LES filter. When an explicit filter is defined, τ^{RSFS} is resolvable on the grid, but this term is generally ignored in conventional turbulence closures which only parameterize SGS stresses.

For the DRM, the subgrid scale stress, τ^{SGS} is parameterized using the Dynamic Wong-Lilly (DWL) (Wong and Lilly, 1994) eddy-viscosity model:

$$\tau^{SGS} = -2\nu_t \overline{\tilde{S}}_{ij} \tag{4.3}$$

where $\overline{\tilde{S}}_{ij}$ is the filtered and resolved strain rate tensor and $\nu_t = C_\epsilon \Delta^{4/3}$ is the dynamic eddy viscosity. In the dynamic eddy viscosity, Δ is the filter width chosen as 2 and C_ϵ is determined dynamically using the least-squares method of Lilly (1992).

The RSFS stress is determined by reconstructing the velocity field using the approximate deconvolution method (Stolz et al., 2001):

$$\tilde{u}_i \approx \overline{\tilde{u}}_i + (I - G) * \overline{\tilde{u}}_i + (I - G) * \left[(I - G) * \overline{\tilde{u}}_i\right] + \ldots \tag{4.4}$$

where I is the identity matrix, G is the explicit filter and $*$ represents the convolution operator. Each additional term in the series adds a level of reconstruction that more accurately represents the RSFS velocities. In this study, level-0 reconstruction is used which includes the first term in the series, and the velocity is approximated as the filtered velocity. This level-0 reconstruction is the same as the scale-similarity model of Bardina et al. (1983). Combined with the eddy viscosity SGS term, this level-0 reconstruction becomes a dynamic mixed model (Zang et al., 1993). We refer to the closure as DRM for simplicity and to indicate the more general implementation in WRF.

Lastly, near-wall stresses are usually under-predicted with dynamic SGS models applied in ABL flows. A near-wall stress model is used to account for this, following Brown et al. (2001), which has improved agreement with similarity theory in previous studies (Chow et al., 2005; Zhou and Chow, 2011; Zhou and Chow, 2012; Kirkil et al., 2012). The near-wall stress is defined for $i = 1, 2$ and is added only to the τ_{i3} terms, as follows:

$$\tau_{i3}^{\text{near-wall}}(z) = -\int_0^{H_c} C_c a(z) |\overline{\tilde{u}}| \overline{\tilde{u}}_i dz \tag{4.5}$$

where C_c is a strength factor, set to 0.5 due to the grid-aspect ratio in this study (Chow, 2004), and $a(z)$ is a shape function set to smoothly decay the effect of the canopy stress at a specific cutoff height H_c (Chow et al., 2005; Kirkil et al., 2012). H_c is chosen as $2\Delta x$ following Zhou and Chow (2011). The shape function is defined as:

$$a(z) = \cos\left(\frac{\pi z}{2H_c}\right)^2 \tag{4.6}$$

The DWL eddy-viscosity model and the scale-similar RSFS term are combined to create a mixed-model for turbulence. This mixed model along with the added canopy stress result in:

$$\tau_{ij} = \tau^{RSFS} + \tau^{SGS} = \overline{\tilde{u}_i\tilde{u}_j} - \overline{\tilde{u}_i}\,\overline{\tilde{u}_j} - 2C_\epsilon\Delta^{4/3}\overline{\tilde{S}}_{ij} + \tau_{i,\text{near-wall}} \tag{4.7}$$

With the DRM's formulation for RSFS motions, subfilter-scale turbulent dissipation $\epsilon = -\tau_{ij}\overline{\tilde{S}}_{ij}$ can vary both positively and negatively representing dissipation and backscatter. It is worth noting that in conventional closures, such as TKE-1.5, the eddy-viscosity form is purely dissipative. This is because the SFS stress does not represent RSFS motions and only encompasses SGS motions, resulting in ϵ being strictly positive.

The SFS scalar fluxes in the DRM follow a similar procedure to momentum. The SFS fluxes are comprised of two terms, the SGS, eddy-diffusivity contribution from the DWL model and the RSFS contribution from the approximate deconvolution method. The SFS potential temperature, θ, flux in the DRM model is:

$$\tau_{\theta j} = \underbrace{\overline{\tilde{\theta}\tilde{u}_j} - \overline{\tilde{\theta}}\,\overline{\tilde{u}}_j}_{\tau_{\theta j}^{RSFS}} \underbrace{-2\nu_{t,h}\frac{\partial\overline{\tilde{\theta}}}{\partial x_j}}_{\tau_{\theta j}^{SGS}} \tag{4.8}$$

where $\nu_{t,h}$ is the dynamic, scalar eddy diffusivity defined as $\nu_{t,h} = \frac{\nu_t}{\mathrm{Pr}}$ with $Pr = 1/3$ as defined in WRF (Skamarock et al., 2021).

Turbulent kinetic energy 1.5-order model

The TKE-1.5 model is an eddy-viscosity turbulence closure which solves a prognostic turbulent kinetic energy (TKE) equation to obtain a characteristic turbulent velocity scale and uses the grid spacing as the length scale to parameterize the SGS stresses (the RSFS term is not included) (Deardorff, 1980). The TKE equation describes the evolution of TKE and parameterizes sources and sinks from shear production, buoyancy production or suppression, turbulent mixing, and dissipation (Skamarock et al., 2021). The eddy-viscosity is defined as:

$$\nu_t = C_k l_{h,v} e^{1/2} \tag{4.9}$$

where e is the TKE and C_k is a constant (set to 0.15). The length scales are defined anisotropically with the horizontal length scale defined as $l_h = (\Delta x\Delta y)^{1/2}$ with $\Delta x, \Delta y$ representing the grid spacing in the corresponding direction. The vertical length scale depends on the Brunt-Väisälä frequency, N, and is given by:

$$l_v = \begin{cases} \min\left[\Delta z, 0.76\frac{e^{1/2}}{N}\right] & : N^2 > 0 \\ \Delta z & : N^2 \leq 0 \end{cases} \tag{4.10}$$

The scalar eddy diffusivity is defined for TKE-1.5 in the same way as the SGS component of the DRM model above:

$$\tau_{\theta j} = -2\nu_{t,h}\frac{\partial \bar{\tilde{\theta}}}{\partial x_j} \tag{4.11}$$

Simulation setup

WRF-LES-GAD is used in a one-way nested setup to study how a range of SBL conditions interact with a wind farm. The wind farm's inflow conditions are based on the parent domain, which is periodic and unaffected by the turbine wakes (due to one way nesting, wakes are confined to the child domain). The parent domain size is (Nx, Ny, Nz) = (750, 500, 120), which at a horizontal grid spacing of 8 m results in a physical domain size 6.0 km × 4.0 km × 1.0 km ($x \times y \times z$). The child domain has the same resolution as the parent domain, but has two fewer grid points in x and y to ensure that the child domain fits within the parent domain. The parent domain with periodic boundary conditions is spun up for 12 hours, then the child domain with a 3 × 3 array of wind turbines (see Fig. 4.1) is nested within the parent domain. The combined nested domains are then run for 2 hrs. The total simulation time is 14 hours for the parent domain and 2 hours for the child domain, with all analysis completed from hour 13 to 14. This is a computationally efficient approach which allows for turbulence to develop and for the surface fluxes to become pseudo-steady on the periodic parent domain while also accounting for a 1 hr spin-up period of the turbine wakes on the child domain. This minimal nesting setup has been previously used by Sanchez Gomez et al. (2023) to allow for the study of blockage in front of a wind farm in the child domain using turbulence developed from an outer domain with periodic boundary conditions.

Distinct wind farm configurations are used for each cooling rate to account for changes in wind direction at hub height. As discussed below, the wind direction varies significantly with height (wind veer) in the stable boundary layer and therefore produces very different wind directions at hub height for different stability conditions, even with the same geostrophic forcing. The 3 × 3 wind farm is therefore aligned with the hub-height wind direction (known a priori from the outer grid spinup) for each test case as shown in Fig. 4.1, to maximize efficiency in the computational domain. The turbines are spaced 320 m or $4D$ in the spanwise direction and $8D$ in the streamwise direction. The edge of each wind farm is located 800 m from the western and southern boundaries, i.e., the closest any turbine gets to a boundary is 800 m for the weakly and moderately stable configurations. For the the strongly stable configuration, the closest turbine is 1200 m from the southern boundary to account for the extreme wind veer. Figure 4.1 also shows points $5D$ upwind of the first row of turbines, as well as $5D$ and $10D$ downwind of the third row of turbines where u, v, w, and T are output

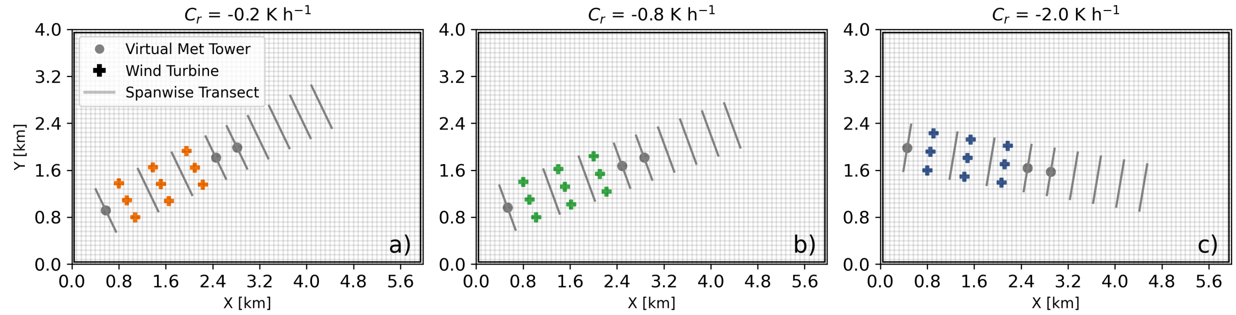

Figure 4.1: Simulation setup for the (a) weakly, (b) moderately, (c) and strongly (c) stable regimes denoted by the surface cooling rate C_r. The virtual meteorological tower is located $5D$ upwind of the wind farm and the lines represent $10D$-wide transects at various locations upwind, within, and downwind of the wind farm.

at all vertical levels at the model time-step meant to represent a virtual meteorological tower or vertical profiling lidar. Spanwise transects $10D$ or 800 m wide are also shown in Fig. 4.1 at various locations, which are used for analysis later in this work.

The simulations are forced with a geostrophic wind speed of $U = 10$ m s^{-1}, $V = 0$ m s^{-1}, which is typical in idealized studies (Kirkil et al., 2012; Zhou and Chow, 2011; Jiménez and Cuxart, 2005; Mirocha et al., 2014b). The three surface cooling rates used are -0.2, -0.8, and -2.0 K h^{-1} to represent weakly, moderately, and strongly stable conditions. These cooling rates fall within the range used by Zhou and Chow (2011) who also modeled weakly to strongly stable conditions. The grid has 8 m horizontal spacing and a vertical spacing of 2.5 m near the surface, with a gradual increase in spacing with height. These spacings are chosen because previous research has shown that the DRM is able to sustain resolved turbulence on this grid (Zhou and Chow, 2011). The 8 m grid spacing is also close to the moderate, 6.25 m spacing used in the SBL LES studies by Beare et al. (2006), which was shown to provide reasonable accuracy but with high dependence on the turbulence closure.

At the bottom boundary, surface cooling is prescribed using Monin-Obukhov similarity theory. The surface fluxes are determined using the constants and relationships from Businger et al. (1971) and the surface roughness, z_0, is set to 0.1 m. This surface roughness is appropriate for low crops with occasional large obstacles, which is characteristic of the AWAKEN site, especially during the summer season (Krishnamurthy et al., 2021). This configuration of the bottom boundary directly follows the methods of Zhou and Chow (2012). The potential temperature profile used for initialization is neutral at 300 K for the first 100 m with stable stratification of 4 K km^{-1} prescribed above, which follows the setups of Zhou and Chow (2011) and Peña et al. (2021).

When examining the effect of the turbulence closure model, only the parent domain is analyzed (i.e., wind turbine effects are not included). Additional runs at a horizontal grid spacing of 4 m are performed for both the DRM and TKE-1.5 closures (see Table 4.1) as a reference. Since turbulence in LES is strongly tied to the grid spacing, this sensitivity study allows us to assess model quality for both grid spacings and turbulence schemes. The same number of grid points is used for the 4 m configuration due to computational expense, as four times the number of grid points would be needed to keep the domain size consistent. The vertical resolution for the 8 m and 4 m configurations are identical (as defined previously). With varying the turbulence closure model, cooling rates, and horizontal grid spacing, this results in the 12 distinct simulations shown in Table 4.1.

4.3 Results and discussion

Effect of turbulence closure

Planar and time-averaged vertical profiles of wind speed, wind direction, and potential temperature are shown in Fig. 4.2 for the 8 m grid spacing setup. All simulations are run for fourteen hours, and outputs are set to every 30 s during the analysis period from hour 13 to 14 resulting in 120 time-instances in the time average. The simulations using 4 m resolution are very similar but with minor differences in the height of the LLJ (not shown). While 13 hours of surface cooling is not necessarily realistic, selecting an analysis window after this many hours is commonly done in idealized SBL studies (Beare et al., 2006; Gadde and Stevens, 2021a; Gadde and Stevens, 2021b; Peña et al., 2021). When the surface is cooled, in LES, it takes many hours until the Coriolis forcing and surface friction balance with super-geostrophic flow at the top of the stable layer. This super-geostrophic flow represents a low-level jet (see Fig. 4.2) and is commonly observed onshore at night (Vanderwende et al., 2015).

The effect of the different cooling rates is clearly observed in the differing LLJ heights. The wind speed profiles are very strongly sheared and become super-geostrophic at the top of the SBL. The maximum wind speed within the low-level jet is close to 12 m s^{-1} for all cases with this maximum occurring at 290 m, 130 m, and 70 m, for the weakly, moderately, and strongly stable regimes, respectively. While the LLJ wind speed is similar in all three cases, the 80-m hub-height wind speed varies greatly due to the shear. The hub-height wind speed is 7.5 m s^{-1}, 10 m s^{-1}, and 12 m s^{-1} for the weakly, moderately, and strongly stable regimes, respectively. The wide range of wind speeds across the rotor swept area leads to differing wake effects (see Sect. 4.3). Another contributing factor to wake behavior is the wind veer, which is nearly 40 degrees across the rotor swept area for the strongly stable regime, but only 5 degrees for the weakly stable regime. This difference has a strong effect on the lateral spreading of turbine wakes as discussed later, when the GAD is added on the inner nest to represent the turbines.

The thermally stable boundary layer develops as a strong potential temperature gradient

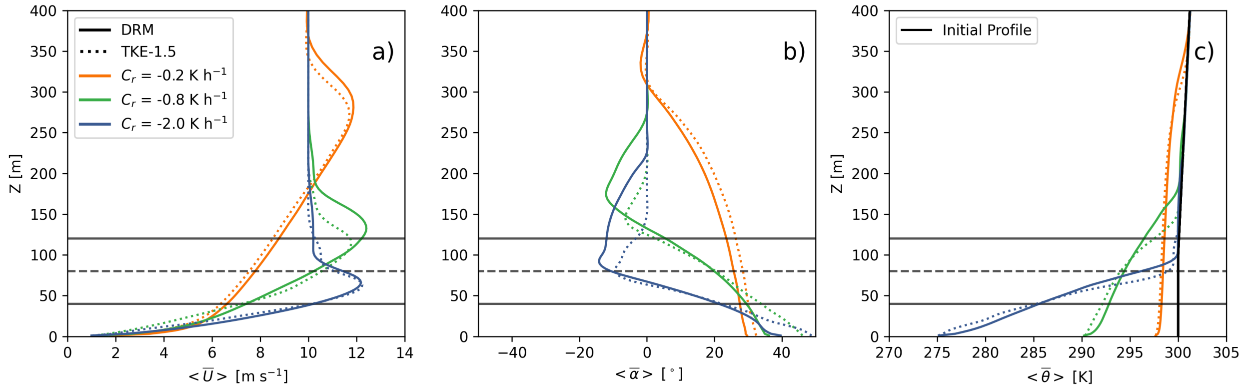

Figure 4.2: Planar- and time-averaged vertical profiles of (a) wind speed U, (b) wind direction α, and (c) potential temperature θ for the DRM and TKE-1.5 closures at 8 m resolution. Note that results shown are for the outer domain without wind turbines. The solid black lines represent the top and bottom of the rotor swept area and the dashed line represents the hub-height.

forms from the ground up to the free atmosphere. In the free atmosphere, the 4 K km^{-1} gradient initially imposed above 100 m persists due a lack of turbulent mixing in the upper atmosphere. The temperature profiles with the different cooling rates are shown in Fig. 4.3(c), with the surface cooling over 26 K for the strongly stable regime but less than 5 K for the weakly stable case. The height of the stable layer depends on the cooling rate and the choice of the turbulence model, with the stable layer being deeper for the DRM closure compared to the TKE-1.5 closure. This difference is consistent with previous comparisons of the TKE-1.5 and DRM closures in the SBL (Zhou and Chow, 2012). Additionally, the dependence of SBL height on turbulence closure is documented in the GABLS study (Beare et al., 2006).

Figure 4.3 shows the planar and time-averaged profiles of heat flux normalized by the heat flux value at the surface. (For the DRM, the surface heat flux values are -0.017, -0.030, and -0.040 K m s^{-1} for the weakly, moderately, and strongly stable regimes, respectively and for TKE-1.5, the values are -0.012, -0.030, and -0.041 K m s^{-1}.) The resolved fluxes are small near the surface and the turbulent fluxes are modeled by the turbulence closure. Above this region and within the SBL, the resolved fluxes reach a maximum and then decrease as buoyancy suppresses turbulence scales. The resolved and modeled heat fluxes can be used as a proxy to determine the percentage or fraction of resolved turbulence. This is done by calculating the vertically integrated resolved heat flux (q) divided by the vertically integrated total heat flux (Q). This quantity provides insight into whether the turbulence closure needs to model turbulence or if it can be resolved in the LES. For the DRM, the total heat flux includes the resolved component as well as the RSFS and SGS terms. For TKE-1.5, the

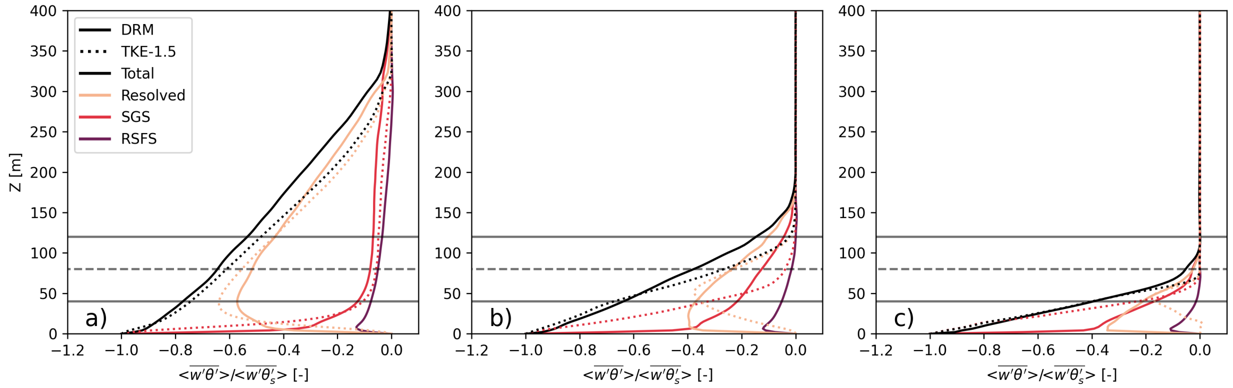

Figure 4.3: Planar- and time-averaged vertical profiles of normalized heat flux for the (a) weakly stable, (b) moderately stable, and (c) strongly stable regime for the DRM and TKE-1.5 closures at 8 m resolution. Note that results shown are for the outer domain without wind turbines.

total heat flux includes just the resolved component and SGS term. Table 4.1 shows the percentage of resolved heat flux for the three stability regimes and at grid spacings of 8 m and 4 m.

For all the resolutions and both turbulence closures, the percentage of resolved heat flux to total heat flux decreases with increasing stratification. This indicates that runaway cooling does not occur in any of the simulations (Jiménez and Cuxart, 2005; Zhou and Chow, 2011). At 8 m resolution and for the strongly stable case, the DRM closure resolves over 30% of the heat flux while the TKE-1.5 closure resolves just 11%. For the other stability regimes, the DRM and TKE-1.5 closures perform comparably. When the grid resolution is increased, both closures resolve more of the heat flux but with greater improvement for the TKE-1.5 closure versus the DRM closure. The TKE-1.5 closure is improved significantly for the strongly stable case when the grid spacing decreases to 4 m and resolves a similar but slightly lower percentage of the heat flux at 26% vs 32% for the DRM closure. Additionally, for the weakly and moderately stable cases (Figs. 4.3(a) and 4.3(b)), the TKE-1.5 resolves more heat flux. This is because, for the DRM, the effect of incorporating explicit filtering increases the total SFS modeled stress and thus the resolved stress must decrease accordingly. This is a known feature of the DRM which helps decrease numerical error near the filter cutoff. For the strongly stable regime (Fig. 4.3(c)), much of the heat flux is modeled so the effect of the RSFS term on the resolved field is less pronounced. Similar results to the q/Q ratios hold for other turbulence quantities such as turbulent kinetic energy (TKE) or momentum flux (not shown).

The computational cost factor in Table 4.1 is calculated by comparing the wall-clock time each simulation takes relative to the 8 m, weakly stable simulation using the TKE-1.5

closure. The cost factor inherently accounts for the decrease in time step required when the grid resolution is increased. The time steps used are 0.5 s and 0.2 s, for the 8 m and 4 m grid spacing simulations, respectively. This factor is also adjusted to compare a constant physical domain size when the grid resolution is increased, which results in a default factor of 4 in the cost calculation for the 4 m grid spacing simulations compared to the 8 m case. For example, on 400 processors, the 8 m grid spacing TKE-1.5 weakly stable simulation takes 4.13 hrs of real-time for every 1 hr of simulation time while the configuration with 4 m grid spacing takes 10.04 hrs with the same number of grid points. When the factor of 4 is included to compare a constant physical domain size, the 4 m grid spacing simulation would take 40.16 hrs, which results in a computational cost factor of 9.72. Using the DRM closure at the same resolution as the TKE-1.5 closure is 1.45 times the computational cost. With respect to q/Q, and at the same resolution, the TKE-1.5 closure therefore outperforms the DRM closure for weakly and moderately stable regimes at less computational cost. However, the DRM closure outperforms the TKE-1.5 closure for the strongly stable case even at the coarser 8 m grid spacing compared to the 4 m TKE-1.5 configuration. For the strongly stable case, the TKE-1.5 closure at 4 m resolution will resolve less turbulence at 7.3 times (10.67/1.46 from Table 4.1) the computational cost compared to the DRM closure at 8 m resolution. As a result, the DRM is better suited and more computationally efficient than the TKE-1.5 closure for simulating strongly stable boundary layers. Note that there are some differences in the computational cost factor for the same resolution and closure, but with different cooling rates because the cost can vary slightly in the MOST iterative procedure at the surface.

One of the benefits of the DRM is that it allows backscatter of energy from subfilter scales to resolved scales. This effect can be quantified by calculating the SFS dissipation rate $\epsilon = -\tau_{ij}\overline{\tilde{S}}_{ij}$. Figure 4.4 shows a histogram of the SFS dissipation rates for the TKE-1.5 and DRM closures at heights of 50 m and 80 m above the ground for the 8 m resolution strongly stable regime. As expected, the histograms of dissipation rate are entirely positive for the TKE-1.5 closure because it is an eddy-viscosity model. For the DRM closure, approximately 20% at z = 50 m and 40% at z = 80 m of the SFS dissipation rate values are negative, indicating backscatter. Traditional eddy-viscosity closures are known to be overly dissipative (Carper and Porté-Agel, 2004; Sullivan et al., 2003) and backscatter has been shown to be important, especially in stably stratified flows (Mason and Thomson, 1992; Kosović, 1997). Backscatter was also seen in Zhou and Chow (2011) and matches turbulence measurements in the atmospheric surface layer (Carper and Porté-Agel, 2004).

The ability of the DRM closure to physically represent backscatter leads to an improved representation of turbulence under strong stability compared to the TKE-1.5 closure, especially at the relatively coarse 8 m grid spacing. Using the DRM closure at 8 m grid spacing provides a computationally efficient framework for simulating a domain large enough to analyze wind turbine and farm wake effects under strongly stable conditions. Hereinafter, all results presented use the DRM closure.

Table 4.1: Vertically integrated resolved heat flux q over total (resolved + subfilter) heat flux Q and increase in computational cost for TKE-1.5. The computational cost factor is the increase in computation cost relative to the 8 m, weakly stable simulation using the TKE-1.5 closure.

Cooling Rate (K h^{-1})	Grid Spacing (m)	q/Q (%)	Computational Cost Factor
Closure: TKE-1.5			
-0.2	8	75.1	1.00
-0.8	8	51.3	1.01
-2.0	8	11.2	0.99
-0.2	4	85.0	9.72
-0.8	4	62.6	10.59
-2.0	4	26.1	10.67
Closure: DRM			
-0.2	8	66.7	1.45
-0.8	8	44.7	1.44
-2.0	8	32.4	1.46
-0.2	4	72.7	13.22
-0.8	4	50.1	11.80
-2.0	4	32.4	13.39

Quantifying intermittency

Given the ability of the DRM closure to represent the stable boundary layer with weak to strong stability conditions, the following analysis focuses on the SBL-wind turbine interactions. Hereinafter, all results shown are on the inner domain with the wind turbines. Time-height contours can provide insight into the qualitative behavior of turbulence during the hour of simulation analysis time. Figures 4.5(a), 4.5(b), and 4.5(c) show time-height contours of wind speed at 30 s intervals and at the location of the virtual met tower ($5D$ upwind of the wind farm). At this location, every vertical height is output at the model time step. Time-height contours of turbulent kinetic energy (TKE) are shown in Figs. 4.5(d), 4.5(e), and 4.5(f). The TKE is computed as TKE $= \frac{1}{2}\left(u'^2 + v'^2 + w'^2\right)$, where u', v', and w' are the fluctuating components of the velocities using running 30 s bins. The TKE values are also normalized by the vertically-averaged value during the hour-long analysis period so that the different stability regimes can be compared. The TKE signal in Figs. 4.5(d) and 4.5(e) is continuously variable while for the strongly stable regime in Fig. 4.5(f), there are periods of elevated turbulence and periods with more quiescent flow. In Fig. 4.5(f), the elevated periods of turbulence are most evident in the lower half of the rotor plane (z = 40-80 m).

To quantitatively describe the intermittent turbulence visible in the strongly stable cases in Fig. 4.5(f), we follow a similar approach to that used by Coulter and Doran (2002) who used heat flux measurements from sonic anemometer data during the CASES-99 field

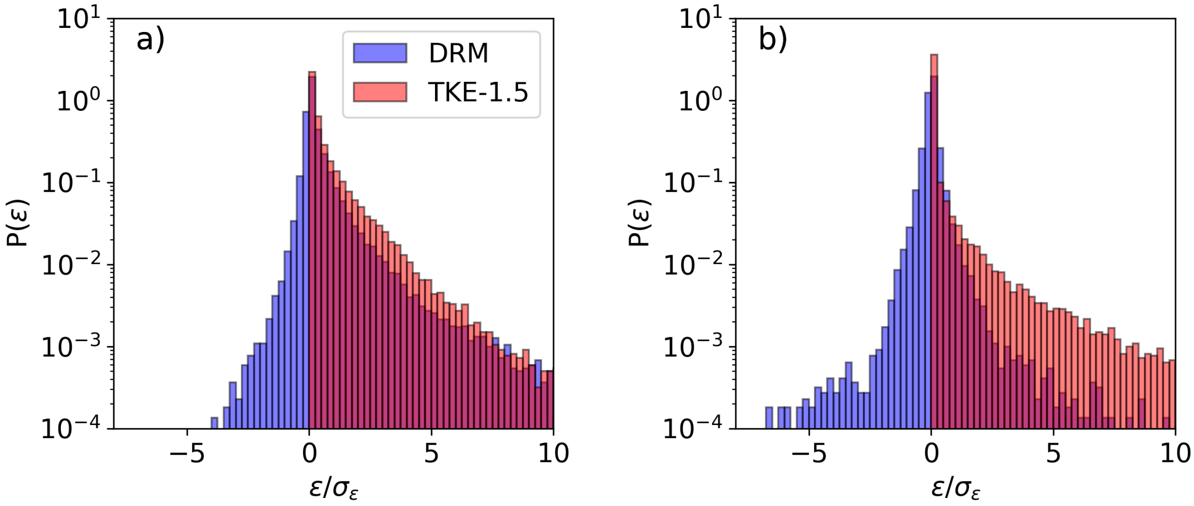

Figure 4.4: Distribution of subfilter scale turbulent dissipation rates for the TKE-1.5 and DRM closures at (a) z = 50 m and (b) hub-height (z = 80 m). The turbulence dissipation rate ϵ is normalized by its standard deviation σ_ϵ at the given height. Negative values represent the backscatter of turbulent energy from the subfilter scales to the resolved scales.

campaign. We apply their methodology but use TKE as the metric of interest as our goal is to identify turbulent periods. The TKE calculated for Fig. 4.5 is averaged again over a 1-min interval to further smooth the data (shown in Figure 4.6(a) at various heights). Then the values in the TKE time-series are sorted from largest to smallest to obtain a cumulative probability distribution.

The cumulative probability distribution of the sorted TKE at various heights within the rotor plane for the strongly stable regime is shown in Fig. 4.6(b). The black diagonal line represents the distribution if the TKE were distributed uniformly during the analysis period, i.e., 50% of the TKE would occur in 50% of the analysis period. We extend Coulter and Doran (2002)'s definition of "intermittency fraction" to TKE (from heat flux) such that it represents the first 50% of the sorted TKE signal. It should be noted that TKE cannot be uniformly distributed since it is defined itself by fluctuations, so there will always be some level of skewness and the intermittency fraction must be less than 50%. For the strongly stable regime, the intermittency fraction is 30% at hub-height and 29% at $z = 50$ m, meaning that 50% of the total TKE during the analysis period happens in just 30% of the analysis time. In the upper portion of the rotor plane, the intermittency fraction is closer to 40%. This is consistent with Fig. 4.5(f), where we can see the strongest bursts in TKE in the lower half of the rotor plane. An intermittency fraction of 29% is consistent with the <30% intermittency fractions observed during many of the strongly stable nights analyzed by Coulter and Doran (2002) during CASES99 (although they also saw nights with smaller

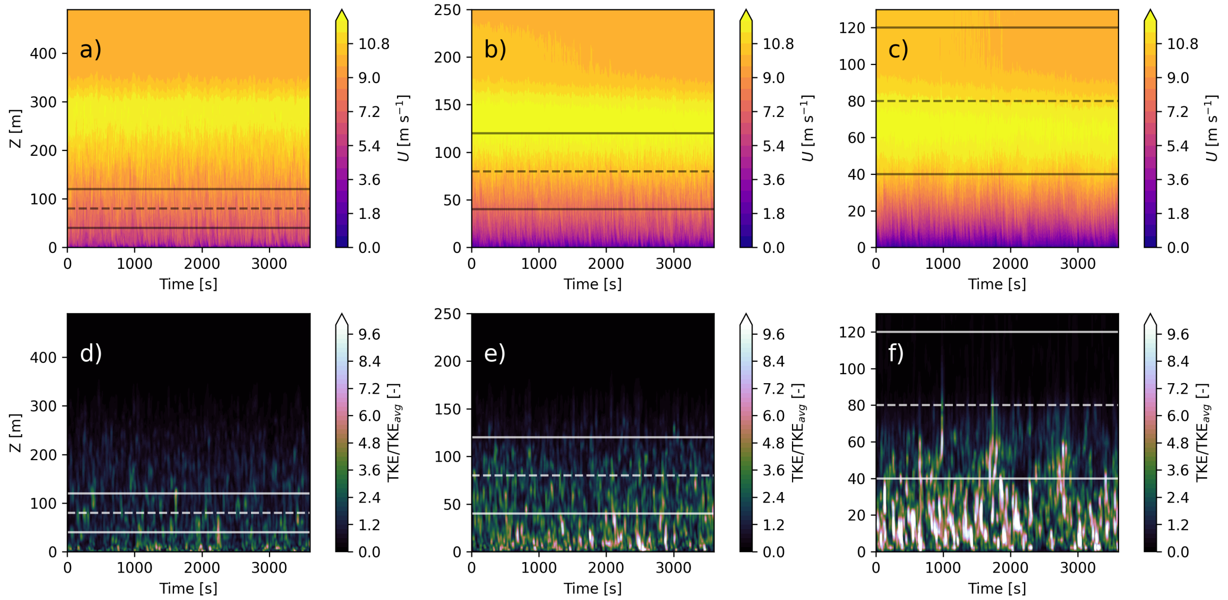

Figure 4.5: Time-height contours of wind speed and normalized TKE for the weak (a,d), moderate (b,e), and strong (c,f) stability regimes at the location of the virtual met tower ($5D$ upwind of the farm). The solid lines represent the top and bottom of the rotor swept area and the dashed line represents the hub-height. TKE is normalized by the vertically-averaged value during the hour-long analysis period for each case, which are 0.199, 0.084, and 0.033 m^2 s^{-2} for the weak, moderate, and strong stability regimes, respectively. Note that the velocities are output at 2 Hz, but are sub-sampled for visualization purposes.

intermittency fractions) and simulation results during strongly stable conditions from Zhou and Chow (2012). However, note that the results in this study do not provide a direct comparison since TKE is the metric used whereas the others used heat flux.

The analysis period is further subdivided into quiescent and turbulent periods. Figures 4.6(a) and 4.6(c) show time-series of the wind speed and TKE at $z = 50$ m, 80 m, and 110 m where periods with intermittency are highlighted in gray and denoted as "turbulent" periods while other periods are referred to as "quiescent" periods. The threshold between the periods is the TKE value at which 50% of the sorted TKE is achieved at a height of 50 m. Therefore, the gray periods in Figs. 4.6(a) and 4.6(c) are responsible for 50% of the TKE that occurs during the analysis period (at a height of 50 m). This threshold is the TKE value that corresponds to the intermittency fraction. We can qualitatively see large fluctuations in both the wind speed and TKE during the turbulent periods at 50 m. At 80 m (hub-height) and 110 m, the fluctuations are not as qualitatively evident. We extend our analysis of turbulence intermittency by quantifying the turbulence intensity, calculated as $\mathrm{TI} = \frac{\sigma_U}{U_{mean}}$, within the distinct turbulent and quiescent periods as determined by the

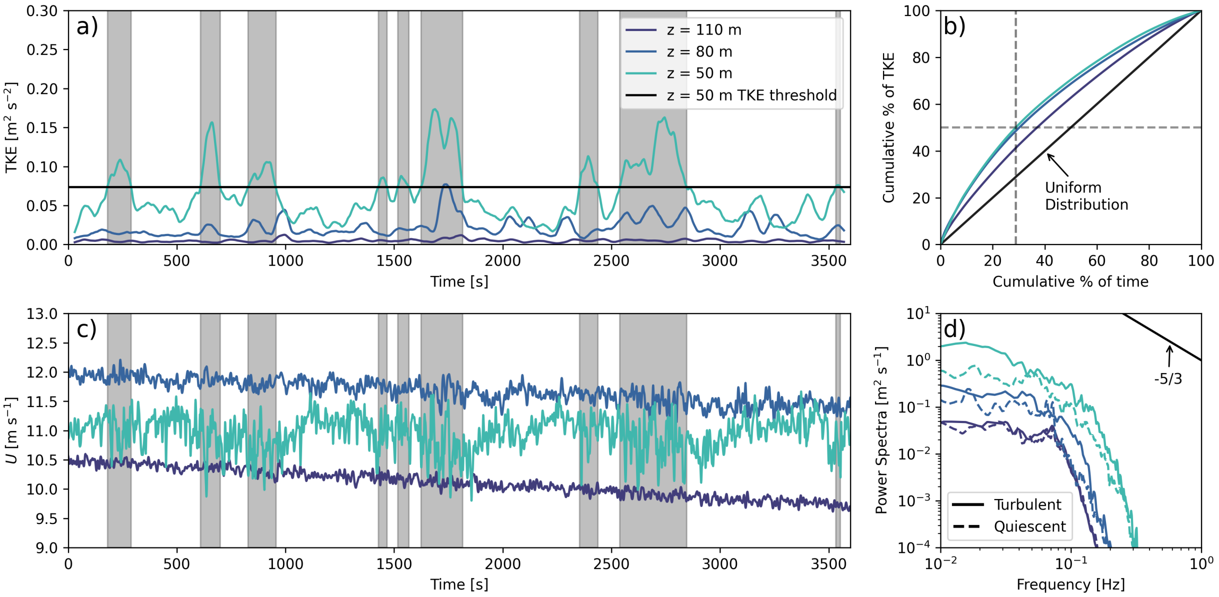

Figure 4.6: (a) Time-series and (b) CDF of TKE at various heights within the rotor disk for the strongly stable regime. (c) Time-series and (d) power spectra of wind speed at the same heights as in (a) and (b). The dashed lines in (b) pinpoint the the cumulative percentage of time it takes until 50% of the TKE occurs at a height of 50 m.

intermittency fraction analysis. At 50 m, the TI is 3.5% during the turbulent periods and only 2.2% during quiescent periods. Considering the relatively small TIs typical during SBL conditions, these differences in TI during quiescent and turbulent periods are significant, as discussed later. Note that at both 80 and 110 m, the wind speed slowly decreases in time due to multi-hour (∼18.7 hours at a latitude of 40 degrees) inertial oscillations at the Coriolis frequency.

Increased levels of turbulence during turbulent periods, as compared to quiescent periods, are also clear when plotting the power spectral density (PSD) of the wind speeds at the three heights as shown in Fig. 4.6(d). The wind speed signals have been separated by turbulent and quiescent periods as indicated by the gray shaded regions in panel (c). The PSDs are calculated for each distinct turbulent or quiescent period and then averaged. At 50 m, the energy content is increased across all frequencies during the turbulent periods compared with the quiescent periods. There is a much smaller difference in the energy content at the higher frequencies for heights of 80 m and 110 m. The additional energy content for only the lower-half of the rotor disk along with the intense vertical wind shear could lead to increased blade fatigue as described by Kelley et al. (2006).

Effect of wind farms on the stable boundary layer

The presence of a wind farm has different effects on the atmospheric boundary layer for each stability regime. Figure 4.7 shows plan views of hub-height instantaneous and time-averaged velocity deficits. The velocity deficit is calculated as the difference in the wind field from the velocity $5D$ upwind of the first row of turbines, with the reference value being averaged in the spanwise direction (from -$5D$ to $5D$) to account for the width of the farm. In the instantaneous slices in Figs. 4.7(a) and 4.7(c), turbulent structures are generally evenly distributed in the weakly and moderately stable regimes. For the strongly stable regime in Fig. 4.7(e), the hub-height is just above the nose of the LLJ and thus, much less turbulence is expected. For the instance shown in Fig. 4.7(e), there are no turbulent structures in the inflow other than some very faint wavy structures.

For all three regimes, the wind turbine wakes propagate over $30D$ downwind as seen in the time-averages in Figs. 4.7(b), 4.7(d), and 4.7(f). The considerable wind veer also results in the lateral spreading of the wakes, which depends on wind directions at heights where momentum is entrained from as discussed by Laan and Sørensen (2017). As expected, the velocity deficits are more pronounced downwind within the wind farm as the second and third rows are waked by upwind turbines. Wakes and velocity deficits depend on the operating turbine's thrust coefficient and are thus strongly dependent on the incoming hub-height wind speed. The velocity deficits for the first row of turbines are dependent on the incoming wind speeds, which are 7.8 m s^{-1}, 10.2 m s^{-1}, and 11.6 m s^{-1} for the weak, moderate, and strong stability regimes, respectively. In general, wind turbines (and specifically the turbine used in this study) have higher thrust coefficients at slower wind speeds, which then decrease as the wind speed increases. As a result, the velocity deficit for the first row of turbines in the farm is strongest for the weakly stable regime and weakest for the strongly stable regime. The downwind turbines within the farm have stronger wake deficits compared to the first row for all three stability regimes due to the lower wind speed, and thus higher thrust coefficients, that these turbines experience.

The vertical structure of the wake deficits persists for over $30D$ downwind and depends strongly on the height of the LLJ. Time-averaged vertical transects of wind speed aligned with the middle of the wind farm are shown in Figs. 4.8(a), 4.8(b), and 4.8(c) for all three stability regimes. The wakes of the turbines are a cumulative effect of individual wind turbine wakes morphing into a wind farm wake, which is consistent with observations of wind farm wakes during SBL conditions (Hirth and Schroeder, 2013). Additionally, these cumulative wakes can adversely affect downwind wind farms (Lundquist et al., 2019). The effect of the wind farm wake is most clear for the strongly stable regime where slower wind speeds above the LLJ nose persist downwind. At altitudes within and below the LLJ, the wake recovers relatively quickly because of the ambient turbulence; however, above the LLJ where turbulence levels are low, the wake recovers extremely slowly. Of course, the altitude of the LLJ, and therefore the wake recovery, is dictated by the stability. The average inflow TKE value at 50 m for the strongly stable regime is 0.086 m^2 s^{-2}, while it is 0.032 m^2 s^{-2} at 80 m and just 0.004 m^2 s^{-2} at 110 m.

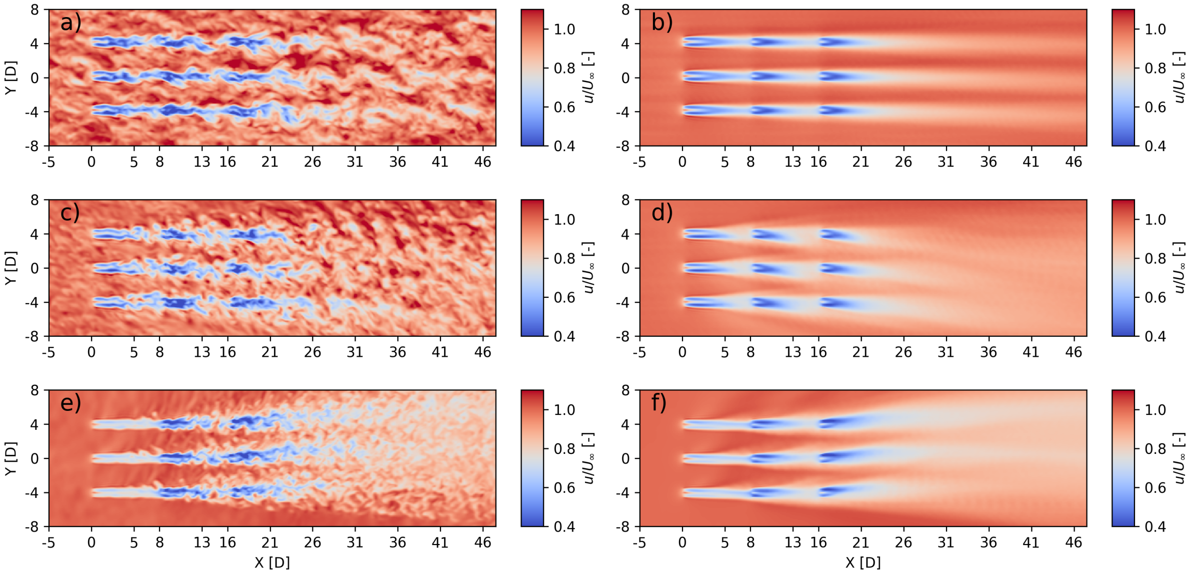

Figure 4.7: Instantaneous (a,c,e) and 1-hr time-averaged (b,d,f) plan view of velocity deficits at hub height for the weakly (a,b), moderately (c,d), and strongly (e,f) stable regimes. The wind turbines are spaced by $8D$ in the streamwise direction and $4D$ in the spanwise direction.

The slow recovery of velocities downwind of the farm in the moderately and strongly stable regimes is also evident in Fig. 4.8(d), which shows hub-height wind speed normalized by the wind speed at -5D, also with averaging in the spanwise direction to account for the width of the farm. The initial decrease in wind speed after the first row of turbines is greatest at 15% for the weakly stable regime; however, the greatest decrease in wind speed at the end of the farm is for the strongly stable regime where the deficit is 25% after the third row of turbines. These trends are similar to those observed by Gadde and Stevens (2021a) who saw that wake deficits for farms that interact with LLJs are greatest when the LLJ height is similar to the hub-height. For the strongly stable case, when the LLJ height is similar to a wind turbine's hub-height, momentum transfer (entrainment) is reduced because the LLJ structure is significantly impacted by the drag of the wind turbine rotors. Any entrainment for this case must come from the slower wind speeds above or below the LLJ. In contrast, for the weakly and moderately stable cases, entrainment from the faster wind speeds in the LLJ nose above the rotor disk aids in wake recovery.

Intermittent turbulence in the inflow for the strongly stable regime is overpowered by the wake-added turbulence from the wind farm. Figure 4.9 shows the CDFs of sorted TKE at locations of 5D upwind (x = -5D) and 10D downwind (x = 26D) of the wind farm for all three stability regimes at 50 m above the ground. As discussed in Sect. 4.3, the intermittency fraction for the strongly stable regime is 29%. While the term "intermittency

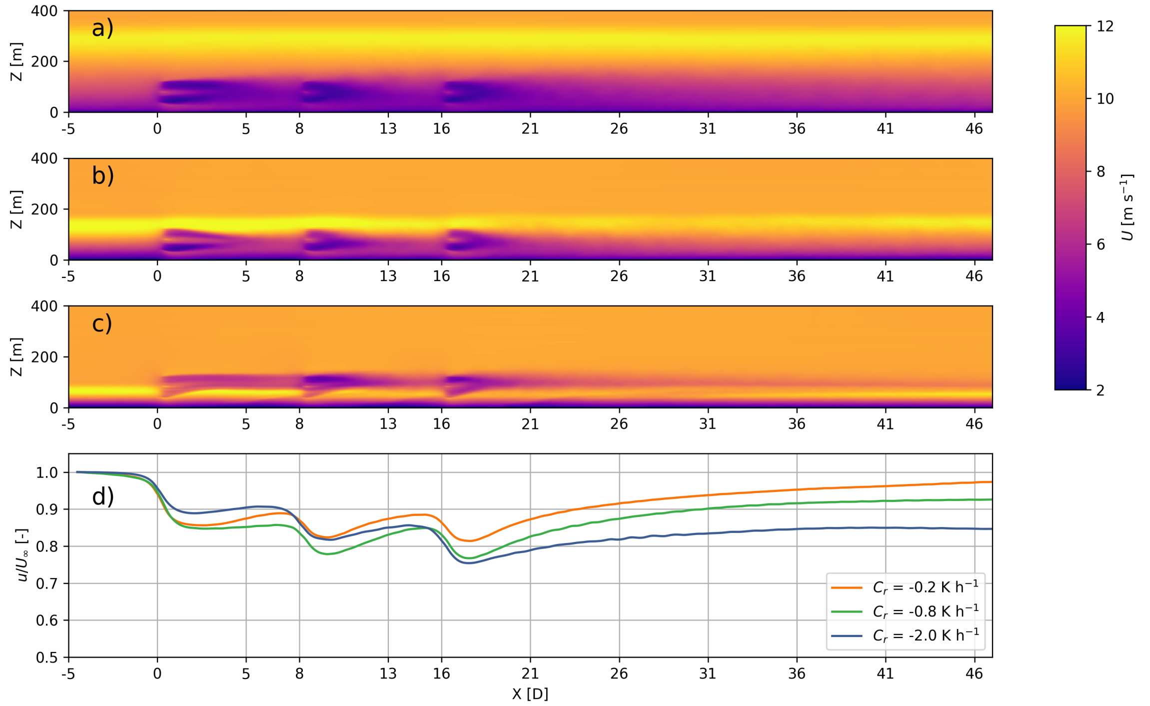

Figure 4.8: Time-averaged vertical transect of wind speed for the (a) weakly, (b) moderately, and (c) strongly stable regimes. (d) Hub-height wind speed as a streamwise distance normalized by the wind speed $5D$ upwind of the first row of turbines for each stability regime. For (d), the wind speed is averaged in the spanwise direction (-$5D$ to $5D$) to account for the three turbines in each row within the wind farm.

fraction" is not typically used to describe a continuously turbulent regime, we can calculate the intermittency fraction for weakly and moderately stable regimes as reference values for a continuously turbulent flow. We find intermittency fractions of approximately 40% for the weakly and moderately stable regimes. Downwind of the wind farm, all three stability regimes have similar distributions of turbulence indicating that wake-added turbulence now drives the turbulent structure. Wake-added turbulence is continuous throughout the hour-long period, i.e., without distinct periods of turbulence intermittency. The mean TKE value over the hour-long period at this height for the strongly stable case is 0.09 m^2 s^{-2} upwind of the farm, while it is 0.40 m^2 s^{-2} $10D$ downwind of the farm. Therefore, ambient turbulence is minimal compared to contributions from the wake in the strongly stable regime.

The added TKE from the farm impacts the SBL in a number of ways. Figures 4.10(a) and 4.10(b) show wind speed and momentum flux averaged across the spanwise transects in Fig. 4.1 at $5D$ upwind (x = -$5D$) and $5D$ downwind of the farm (x = $21D$) for all three stability regimes. The momentum flux is normalized by the value at the surface

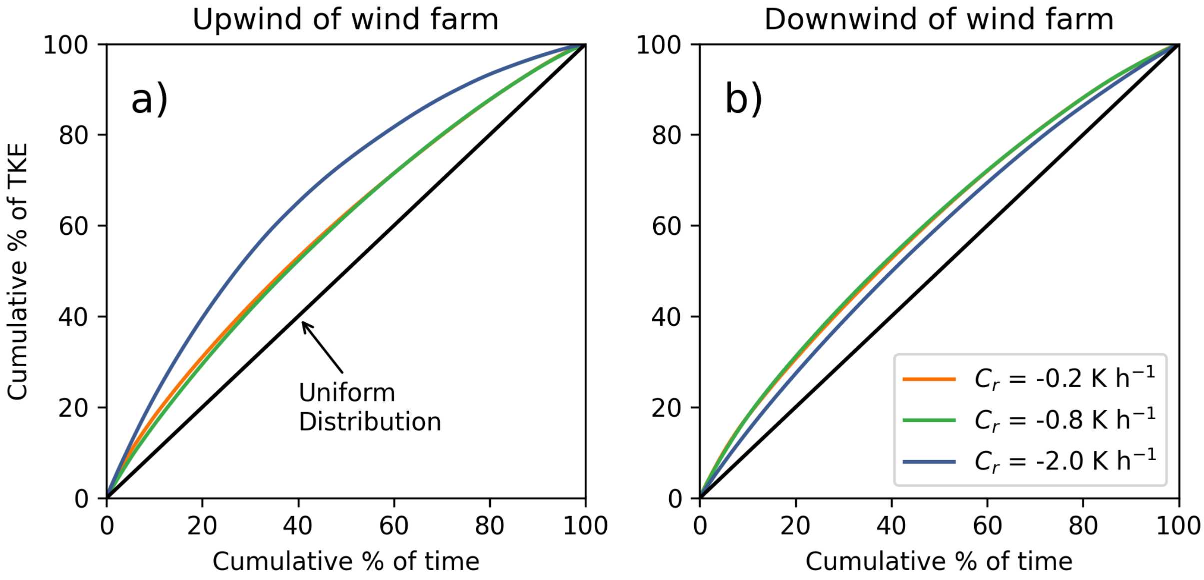

Figure 4.9: Cumulative distribution function of TKE (a) $5D$ upwind (x = -$5D$) and (b) $10D$ downwind (x = $26D$) of the wind farm for each stability regime at z = 50 m.

for each individual case. For all three regimes, the velocity deficit due to the wind farm wake is evident in reduced velocities within the rotor layer. The wind speeds are also decreased above the rotor layer because momentum is entrained into the wake from above, as indicated by negative momentum flux values in Fig. 4.10(b). For the strongly stable regime, the momentum flux is mostly positive in the bottom half of the rotor disk indicating that momentum is transferred from below, and this is because the nose of the LLJ is slightly below hub-height and the upper half of the rotor disk is in the negative shear region. This entrainment from below that aids in wake recovery agrees with modeling results from other work (Gadde and Stevens, 2021b).

The wakes also affect the thermodynamic characteristics of the stable layers. The spanwise averaged potential temperature and heat flux are shown in Figs. 4.10(c) and 4.10(d), respectively. The depth of the stable layer increases and the temperature gradient is reduced across the rotor disk most prominently for the moderately and strongly stable regimes. For all three stability regimes, the heat flux is negative indicating that warmer air is entrained from above. The wind farm induced change in stratification is also visible in Fig. 4.11, which show the spanwise averaged change in temperature (compared to -$5D$) as a function of height at various streamwise locations. For the strongly stable regime, the temperature decreases in the upper half of the rotor disk and increases in the lower half of the rotor disk. Similar trends hold for the weakly and moderately stable regimes but centered around the top of the rotor disk, although the changes in temperature are much smaller for the weakly stable

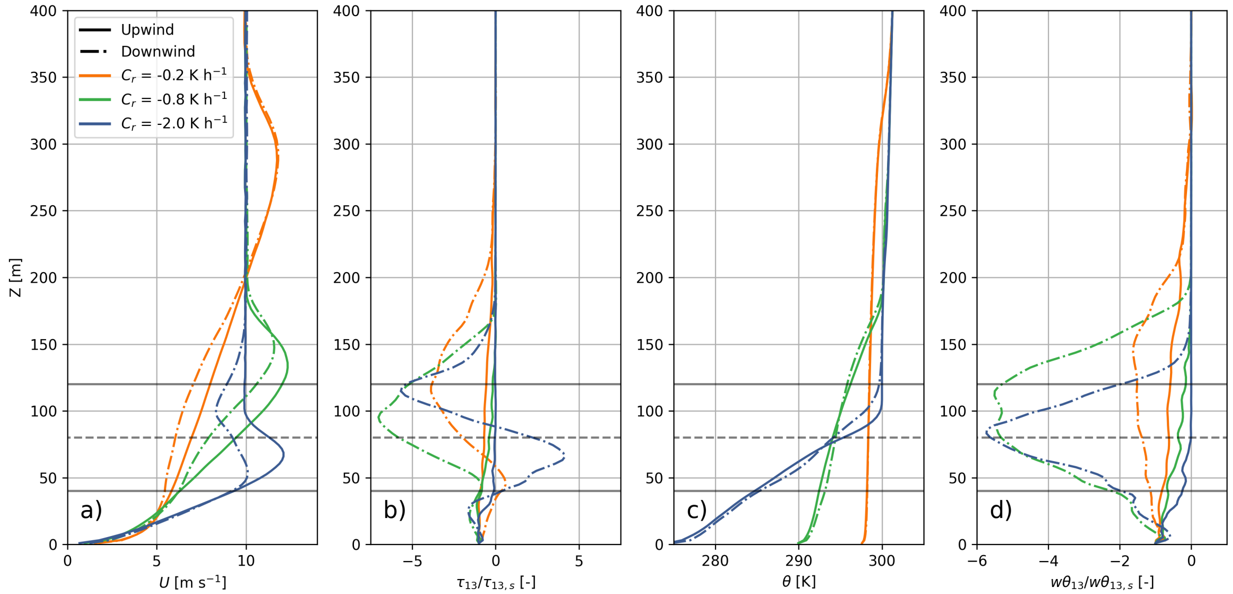

Figure 4.10: Vertical profiles of (a) wind speed, (b) streamwise vertical momentum flux, (c) potential temperature, and (d) vertical heat flux, $5D$ upwind (x = -$5D$) and $5D$ downwind (x = $21D$) of the farm for each stability regime. The solid horizontal lines represent the bottom and top of the rotor layer while the dashed line represents hub-height.

regime. The wind farm, in effect, creates a less stable layer from the ground to the top of the rotor disk and even up to 80 m above the rotor disk for the weakly and moderately stable regimes. These wind farm induced effects on the SBL persist over $30D$ downwind of the farm.

Effect of intermittent turbulence on farm performance

Considering the intermittent turbulence present in the strongly stable regime, the following work aims to to understand and quantify how intermittency affects wind turbine wake recovery as well as power production. To examine the flow structure during turbulent and quiescent periods for the strongly stable regime, we look at plan slices of the velocity deficit and TKE at 50 m above the ground. Figures 4.12(a) and 4.12(c) show a turbulent instance of velocity deficit and TKE while Figs. 4.12(b) and 4.12(d) show a quiescent instance. Note that the colorbar in Figs. 4.12(c) and 4.12(d) is truncated at a maximum value of 2.0 m^2 s^{-2} so that the inflow turbulence is more pronounced; there are higher values downwind due to wake-added turbulence which are not apparent with this colorbar. For the turbulent instance, smaller coherent structures are visible in the velocity deficits upwind of the first row of turbines as well as between the first and second row of turbines. These structures

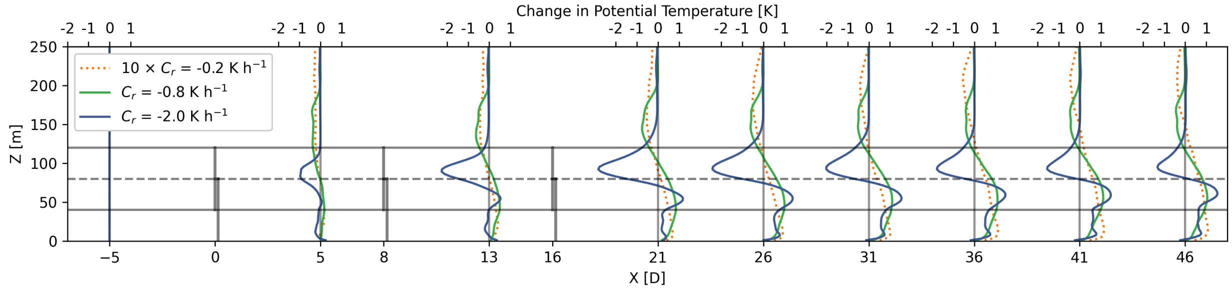

Figure 4.11: Spanwise averaged profiles for the change in potential temperature at various distances (relative to x = -5D) for each stability regime. Note that the profiles for the weakly stable regime have been amplified by a factor of 10 for visualization purposes. The solid horizontal lines represent the bottom and top of the rotor layer while the dashed line represents hub-height.

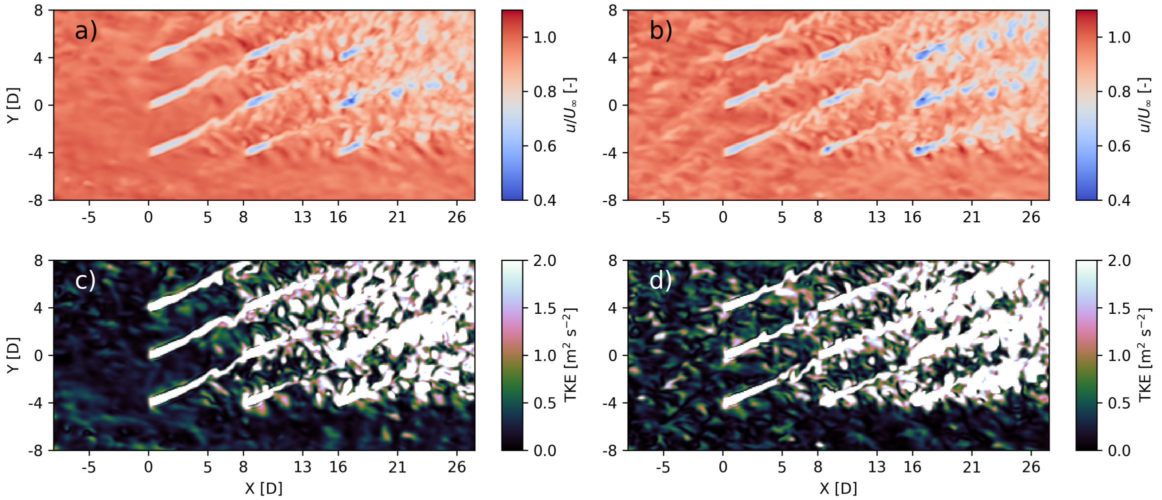

Figure 4.12: Example (a,c) quiescent and (b,d) turbulent instantaneous plan view of (a,b) velocity deficits and (c,d) TKE at 50 m above the ground for the strongly stable regime.

represent coherent turbulent eddies and are evident in the plan slice of TKE in Fig. 4.12(d).

The TKE is up to 10 times higher during turbulent periods compared to quiescent periods. However, the turbulent periods have little effect on wake recovery. Figure 4.13 shows the spanwise averaged (-5D to 5D) velocity deficit profiles within the wind farm and downwind of the wind farm. The velocity deficit profiles have been separated by whether the flow is more turbulent or quiescent using the procedure described in Section 4.3. The velocity

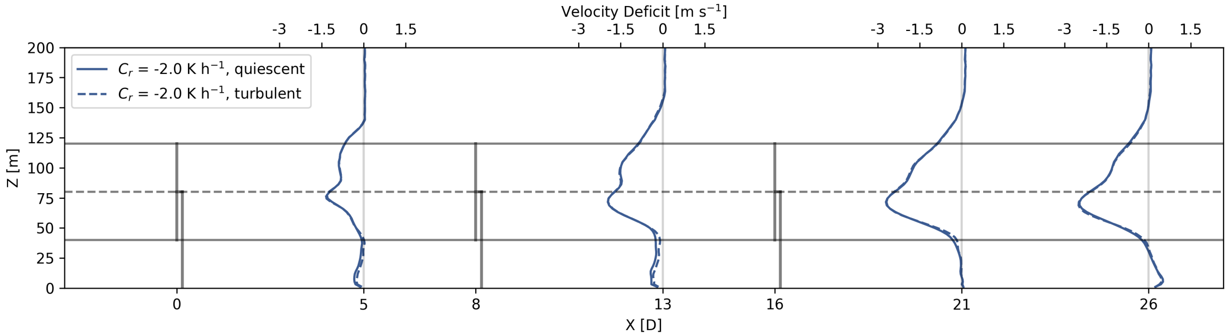

Figure 4.13: Velocity deficit profiles at various streamwise locations (relative to x = -5D) separated by quiescent and turbulent periods for the strongly stable regime. The solid horizontal lines represent the bottom and top of the rotor layer while the dashed line represents hub-height.

deficits are nearly identical regardless of the streamwise location. This is because, while the TKE is much larger during turbulent periods compared to quiescent periods, the TKE during the turbulent periods is still very small when compared to the other stability regimes or to the wake-added turbulence from the wind turbines. The larger turbulence during the intermittent turbulence does not aid in wake-mixing since turbulence levels are so small and thus, the velocity deficits are only marginally impacted as seen by the solid and dashed lines nearly overlapping in Fig. 4.13.

Intermittent turbulence has a small effect on the power variability of the wind farm during the strongly stable regime. Figure 4.14(a) shows the time-series of the average power production during the analysis period for each row of turbines within the farm, normalized by the rated power, with turbulent periods highlighted in gray. Figures 4.14(b), 4.14(c), and 4.14(d) show histograms of the power production to provide insight into the spread for each row. Note that the turbine used in this study can produce power greater than its rated power (greater than 1 in Fig. 4.14(a)) for wind speeds in the range of 10-13 m s^{-1} as discussed in Arthur et al. (2020), which impacts the distribution of the power signal. The first row sees the largest difference in variability with the standard deviation being 45.7 kW during turbulent periods and 40.8 kW during quiescent periods or a roughly 13% increase in the power variability. For the second and third rows, power variability is largely independent of intermittent turbulence since these turbines are just experiencing wake-added turbulence.

The intermittent turbulence resolved in this study does not significantly affect the average power production. Figure 4.15 shows the mean power production of each row, relative to other rows, for each stability regime. For the strongly stable regime, turbulent and quiescent periods have been separated as in previous figures. The power production of the three turbines within a single row are averaged and then normalized by the power for the first row of turbines. For the strongly stable regime, there is a negligible difference in the mean power

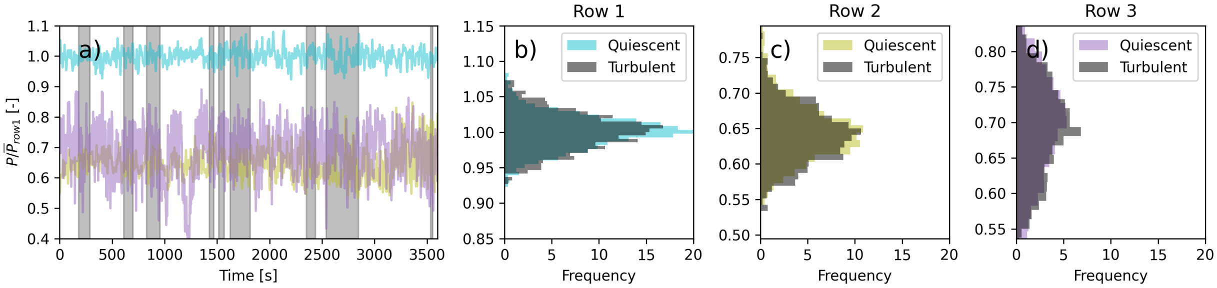

Figure 4.14: Time-series (a) and histograms by row (b,c,d) of detrended power normalized by the rated power of the turbine for the strongly stable regime. The periods highlighted in gray are turbulent while periods in white are quiescent, as determined by the method in Section 4.3.

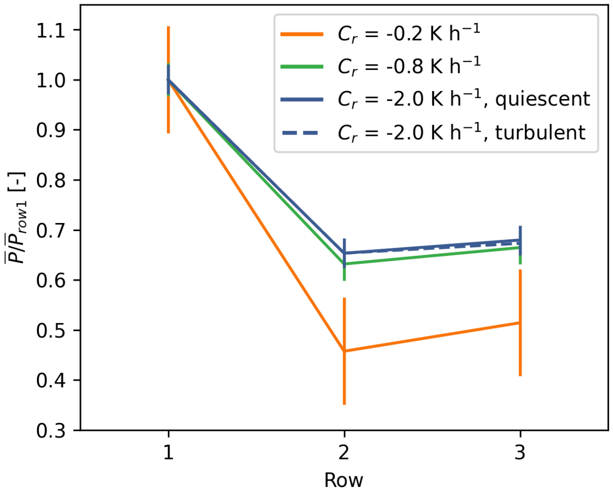

Figure 4.15: Wind farm power as a function of row normalized by the average power produced by the first row for each stability regime. The error bars represent ± 1 standard deviation.

output of the downwind turbines during turbulent and quiescent periods. The differences in average power output are within 1 standard deviation of variability, indicating that they are not statistically significant. However, the loss in power for downwind turbines for the strongly stable regime, regardless of whether the flow is more turbulent or quiescent, is not as large as the loss in power for the weakly and moderately stable regimes. This outcome is because the hub-height wind speeds are slower for the weakly and moderately stable regime, in region 2 of the turbine's power curve, where the wake velocity deficits have a more significant effect on the power production of downwind turbines.

4.4 Conclusions

In this study, the WRF-LES-GAD framework is used to provide insight into how wind farms interact with weakly, moderately, and strongly stable atmospheric boundary layer conditions. The primary focus is to determine 1) how the presence of wind turbine wakes affects stable boundary layer evolution, and 2) how the intermittent turbulence in strongly stable boundary layers affects power production and wake recovery. A one-way nested approach is used with idealized LES, where turbulence is spun-up on the outer domain using doubly periodic lateral boundary conditions. The outer domain provided forcing for the inner domain containing a 3 × 3 wind farm consisting of nine 1.6-MW turbines. The grid spacing was the same in each domain, meaning that the fully-developed turbulent structures from the periodic outer domain are passed directly into the inner domain.

The explicit filtering framework and dynamic reconstruction turbulence model of Chow et al. (2005) is used to extend the working range of LES in the stable boundary layer and, as a result, this is the first such LES study that represents a wind turbine parameterization in such strongly stable conditions. The development of turbulence and the resolved heat flux on the outer domain was first compared between the DRM closure and the commonly used TKE-1.5 closure. The percentage of vertically integrated resolved heat flux of the total heat flux was similar across both closures at a relatively coarse, 8 m horizontal resolution for the weakly and moderately stable regimes. However, for the strongly stable regime, the DRM closure resolved a larger fraction of the heat flux compared to the TKE-1.5 closure, indicating improved representation of heat flux (and, by extension, other turbulence quantities) in the resolved flow field. The TKE-1.5 closure is entirely dissipative by nature, while the DRM closure is able to physically represent the backscatter of turbulence from smaller scales to larger scales, which is especially important in strongly stable boundary layers.

For all three stability conditions, a low-level jet formed at the top of the stable layer with the height of the jet relative to the turbine having a major impact on the SBL evolution downwind. The height of this jet decreased with increasing stability, with the jet being above the rotor disk for the weakly and moderately stable regimes and just below hub-height for the strongly stable regime. Below the LLJ, continuous turbulence formed in the weakly and moderately stable regimes, but turbulence occurred intermittently for the strongly stable regime as shear-generated turbulence and buoyancy suppression compete. The wind farm in the strongly stable regime experienced intermittent turbulence below hub-height (50% of the turbulence occurs in just 29% of the simulation time) and very little turbulence along with a negative wind shear region in the upper half of the rotor disk. Downwind of the wind farm, turbulence was no longer intermittent as the flow structures were dominated by continuous, wake-added turbulence. Additionally, momentum transfer was dependent on the altitude of the LLJ. For the strongly stable regime, momentum was largely transferred upwards from the LLJ below hub-height to aid in wake recovery, whereas for the weakly and moderately stable regimes, momentum was entrained from higher wind speeds within the LLJ aloft. Heat was always transferred downward from above for all three stability regimes, resulting in a less stable layer downwind of the farm.

For the strongly stable regime, periods of elevated intermittent turbulence increased wind farm power variability but had little impact on the average power production. The standard deviation in the power output for the first row of turbines within the farm was 13% higher during turbulent periods compared to quiescent periods. However, downwind rows were not affected by this power variability because the turbulence the downwind turbines experience was wake-added and thus more continuous. The focus of this study was on turbine power production; the impact of intermittent turbulence on structural loading is an avenue for future work.

Both the numerical methods and analyses used in this idealized study can be extended to the conditions observed during AWAKEN or other future field campaigns. In particular, the DRM closure provides a less computationally expensive framework for modeling the SBL and interaction with wind farms. In ongoing work, the DRM closure is being used in multi-scale WRF-LES-GAD simulations for AWAKEN, with realistic time-varying inflow conditions downscaled from reanalysis data. The intermittent turbulence explored in this study is a result of the competition between shear production and buoyancy suppression. Other mechanisms for SBL intermittency that are common in the U.S. Southern Great Plains, the region for the AWAKEN field campaign, include breaking gravity waves, bores, Kelvin-Helmholtz billows, terrain-induced flows, and propagating density currents. Additionally, this study demonstrated a methodology for identifying and quantifying intermittent turbulence events from a time-series of TKE. These methods can be used in future work with observations from meteorological towers, vertical profiling lidars, and supervisory control and data acquisition (SCADA) data from AWAKEN to examine wind farm performance in various intermittent turbulence conditions.

Chapter 5

Gravity waves and wind farms[1]

5.1 Introduction

The United States (U.S.) Southern Great Plains, and more specifically, Oklahoma, is a region with significant wind turbine and wind farm development. Oklahoma currently has nearly 12 GW of installed wind capacity and the state has recently generated over 44% of its electricity demand from wind power, enough to power 3.3 million homes (U.S. Energy Information Administration, 2023). The region has abundant wind energy resources and is an area that will see continued wind farm development; it is critical to study atmospheric - wind farm interactions in this region further. In the Southern Great Plains, there are a number of relevant atmospheric science phenomena for which the effect on wind turbines and wind farms is not well understood. One such phenomenon, which is of particular interest to the wind energy community as part of the ongoing American Wake Experiment (AWAKEN) (Moriarty et al., 2020; Debnath et al., 2022; Moriarty et al., 2024), is intermittent or wavy turbulence.

In general, wavy turbulence in the atmosphere can either be shear-driven or buoyancy-driven. For shear-driven waves, competing shear and buoyancy driven effects result in an instability (Stull, 1988) thus inducing waves. Shear-driven waves commonly occur beneath low-level jets (LLJs), which exhibit a large amount of shear, and are dependent on local atmospheric conditions (Newsom and Banta, 2003). The occurrence of shear-driven waves in the U.S. Great Plains can depend on local topography, such as shallow river valleys, or land-use variability that affects wind shear profiles. Buoyancy-driven waves, also known as gravity waves, generally occur due to perturbations in a stably stratified atmosphere (Stull, 1988). Gravity wave generation mechanisms include frontal systems, thunderstorms, and mountains (Rottman and Simpson, 1989; Stull, 1988; Geerts et al., 2017), or even the wind farms themselves (Allaerts and Meyers, 2018; Lanzilao and Meyers, 2022; Stipa et al., 2024). Waves generated by mountains and wind farms are typically standing waves, while waves

---

[1] This chapter is being prepared for submission as "Large-eddy simulation of an atmospheric bore and associated gravity wave effects on wind farm performance in the Southern Great Plains" by Adam S. Wise (the principal author), Robert S. Arthur, Aliza Abraham, Sonia Wharton, Raghavendra Krishnamurthy, Rob Newsom, Brian Hirth, John Schroeder, Patrick Moriarty, and Fotini K. Chow to *Wind Energy Science*.

generated by frontal systems and thunderstorms propagate with a wave speed that depends on atmospheric conditions.

In this study, we focus on gravity waves associated with atmospheric bore events, which are commonly observed in the U.S. Great Plains. In the U.S. Great Plains, bores are often generated by a nocturnal mesoscale convective systems (MCS) (Haghi et al., 2019; Feng et al., 2019). In this case, a cold air pool created by the thunderstorm downdraft spreads radially as a density current resulting in a bore (Rottman and Simpson, 1989; Toms et al., 2017; Johnson et al., 2018; Haghi et al., 2019; Haghi and Durran, 2021) (although, note that density currents can also be generated by distant cold fronts, atmospheric mesoscale disturbances, or rapid surface cooling (Simpson, 1997; Sun et al., 2002; Lundquist, 2003)). Bores result in a temporary increase in the depth of the stable boundary layer (SBL), along with wavy oscillations and a shift in wind speed and wind direction associated with the propagation of the bore (Knupp, 2006).

Bore events were a major focus of the Plains Elevated Convection at Night (PECAN) Field Campaign, which took place during June and July 2015 (Geerts et al., 2017). PECAN set out to study nocturnal deep convection using a number of instruments, including mobile Doppler lidars, radars, atmospheric emitted radiance interferometers, radiosondes, and aircraft observations. Six intensive observational periods (IOPs) and two unofficial field operations were dedicated to bores, although bores were also observed during IOPs focused on other processes (Geerts et al., 2017; Weckwerth et al., 2019; Weckwerth and Romatschke, 2019).

In addition to the data gathered to characterize bores, forecasting and modeling of bores was also a critical component of the field campaign. Johnson et al. (2018) and Johnson and Wang (2019) conducted a number of Weather Research and Forecasting (WRF) model evaluations for predicting bores during PECAN. In their studies, they initialized simulations using the gridpoint statistical interpolation-based ensemble Kalman filter technique, where both in situ and convective-scale radar data are assimilated (Johnson and Wang, 2017; Johnson et al., 2017). They found that bore structure is especially sensitive to microphysics parameterizations, as microphysical low-level cooling within convection determines the strength of the cold pool. Other studies focused on deep convection have also found large modeling sensitivities to microphysics schemes (Pandey et al., 2023; Han et al., 2019). Johnson and Wang (2019) assessed the sensitivity of model predictions to the horizontal and vertical grid spacing, as well as the turbulence closure. They found that 250 m grid spacing offered improved results compared to 1-km grid spacing, with further improvement when using large-eddy simulation (LES). Additionally, enhanced low level vertical resolution improved simulation results.

In the present work, LES is used to examine how an atmospheric bore and its associated gravity waves affects wind farm performance. LES explicitly solves for the most energetic turbulent eddies in the atmospheric boundary layer (ABL) while parameterizing the effects of the smaller turbulent length scales on the resolved-scale flow. LES is especially well suited to capture transient and dynamic turbulent flow structures, such as bores, which are important features of the ABL that interact with wind farms. We use a nested multi-scale framework in the WRF model (Skamarock et al., 2021) v4.4, which allows us to explicitly resolve the convective-scales that generate the bore. The impact of the bore on the wind farm is simultaneously parameterized using a generalized actuator disk (GAD) to resolve the finer-scale turbulence associated with wind turbine wakes (Mirocha et al., 2014a; Aitken et al., 2014). The WRF-LES framework along with the GAD parameterization is hereinafter denoted as WRF-LES-GAD to describe the model in its entirety.

The goals of this study are to: (1) design a multi-scale framework to analyze bore-wind farm interactions, (2) analyze the sensitivity of the bore structure to modeling parameters, and (3) analyze how an intermittent turbulence event such as from a bore can modulate wind farm power production. To accomplish these goals, we use WRF-LES-GAD to model the King Plains wind farm in Oklahoma, which is a major focus of the AWAKEN field campaign (described in more detail in Sect. 5.2). The WRF-LES-GAD modeling setup is described in detail in Sects. 5.3 and 5.4, focusing on the microphysics schemes and LES turbulence closures which are known to affect model performance. Observations of the atmospheric bore and its characteristics at various times are compared with modeling results in Sect. 5.5. Lastly, the effect of the gravity waves on the simulated wind farm's power production is also quantified in Sect. 5.5 by analyzing time periods before, during, and after the gravity waves pass the Kings Plains wind farm.

5.2 Case study

Overview of the AWAKEN field campaign

The American WAKE experimeNt (AWAKEN) field campaign began in September 2022 with a scheduled end date of October 2024. AWAKEN is centered around five wind farms in northern Oklahoma near the town of Enid. While the AWAKEN domain covers a number of wind farms, the bulk of the instrumentation is located in the eastern half of the King Plains wind farm, which includes 50 wind turbines (see Fig. 5.1). The aim of the field campaign is to better understand wind farm-atmosphere interaction, and as part of AWAKEN, there are seven testable hypotheses (Moriarty et al., 2024). The focus of this study is on the hypothesis that intermittent turbulent bursting events related to Kelvin-Helmholtz instability, gravity waves, and bores lead to fluctuations in wind farm power production and structural loading of wind turbines. Specifically, this study is concerned with the effect of bores and associated gravity waves on wind farm power production.

The dominant wind direction in the region is southerly (Krishnamurthy et al., 2021; Debnath et al., 2023), which determined the design of a north-south instrument transect through the King Plains wind farm. In this study, we focus on data collected with remote sensing Doppler lidars at the A1 location (see Fig. 5.4). A scanning Doppler lidar (Halo Streamline XR+) deployed by the Atmospheric Radiation Measurement (ARM) (Newsom and Krishnamurthy, 2022) ran composite scans for 20 minutes of six-beam profiling (Sathe et al., 2015) and 10 minutes of vertical stares. The scanning Doppler lidar has a range

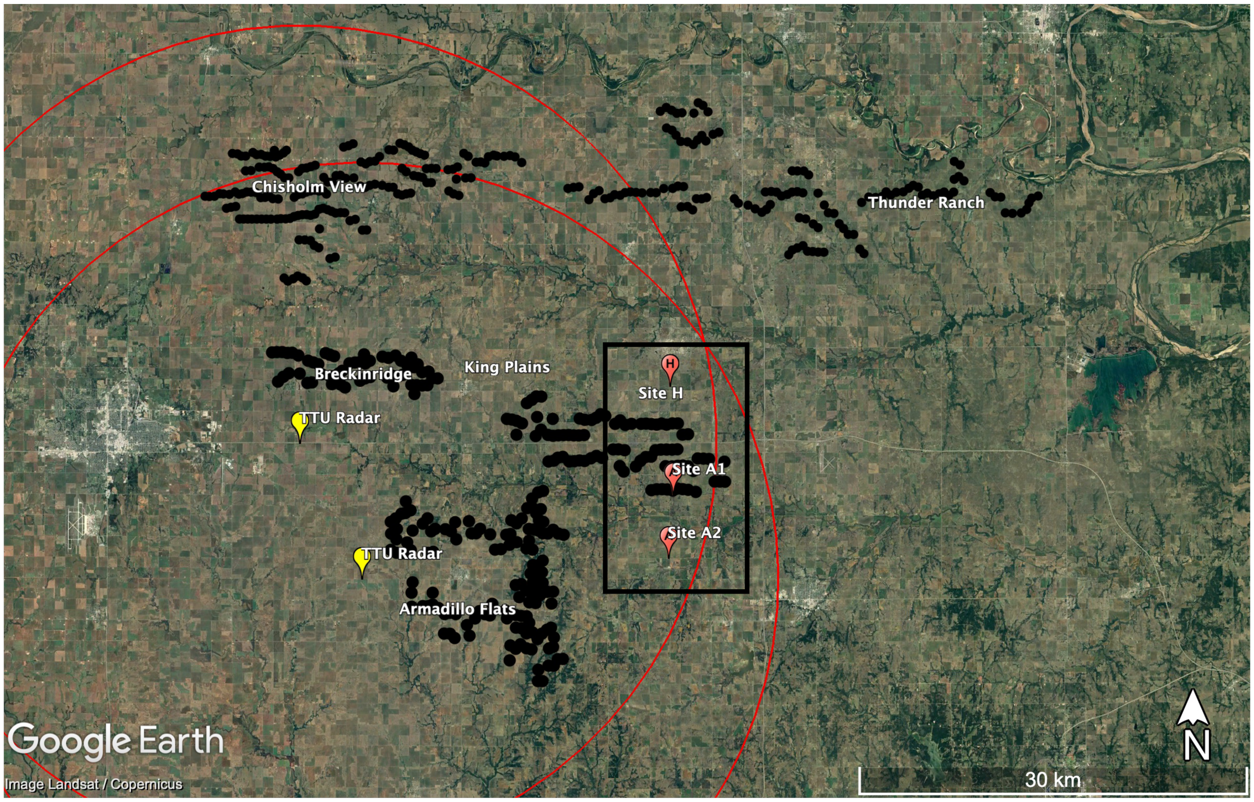

Figure 5.1: AWAKEN region with instrumented sites relevant to this site and black dots representing individual turbines. The X-band radars' ranges are highlighted with red circles. The area representing WRF domain d02 is outlined in black (see Fig. 5.4).

gate of 30 m and measured from 90 m to the top of the ABL with a temporal resolution of approximately 6 seconds per wind profile. The six-beam profiles are used for comparison in this study, with a least squares fit to the radial velocity measurement (Krishnamurthy et al., 2024). At Site A1, an additional short-range vertical profiling Doppler lidar was deployed by Lawrence Livermore National Laboratory (LLNL) to focus on the wind turbine rotor layer (40 m to 240 m). This higher-resolution lidar at A1 was a Windcube v2, which has a scan frequency of approximately 4 seconds.

This study also includes measurements generated by two X-Band radars from Texas Tech University (TTU) (Schroeder et al., 2017; Debnath et al., 2022). These radars provide wind measurements over a large portion of the study region (see Fig. 5.1), performing 145 degree scans over a vertical range of 2 degrees, resulting in observations over a three-dimensional volume roughly every two minutes. Dual-Doppler reconstruction is used to obtain the horizontal velocity vector field from the radial wind speeds recorded by the radars. In their near range, the radars provide observations with a grid spacing as fine as 25 m. However, the eastern half of the King Plains wind farm, which is the focus of this study, is on the edge of the radar range, resulting in 50 m spacing. Additionally, it is worth noting that there are areas without returns within the rotor swept area due to the lower elevation of the eastern half of the King Plains wind farm as the radar beam is blocked by terrain variations.

There are surface-based meteorological (met) stations scattered throughout the AWAKEN domain, which are used to characterize atmospheric surface layer stability. At Site A1, an eddy correlation flux measurement system (ECOR) was deployed by ARM from April until September 2024 (Cook, 2018). The ECOR system includes a sonic anemometer mounted 3 m above ground level (a.g.l.), measuring three-dimensional wind at 10 Hz. The data are post-processed in near-real-time into 30 minute fluxes. Fast-response wind and temperature measurements from the sonic anemometer are used to derive the Obukhov length.

Case study description

The phenomenon of interest in this work is an atmospheric bore with associated gravity waves. The historical weather radar imagery indicates that the weather consisted of localized precipitation on 06 June 2023. Figure 5.2 shows the weather radar reflectivity from the NEXRAD (NEXt generation of RADar) WSR-88D system at the Oklahoma City radar site (KTLX) operated by the National Weather Service. The radar images in Fig. 5.2 are from 03:30 to 05:00 UTC in 30 minute intervals. Localized precipitation caused by a cluster of thunderstorms is evident as increased reflectivity in Fig. 5.2. These storms form an organized nocturnal mesoscale convective system (MCS). At 03:30 UTC, the cold pool outflow from the MCS is evident as a fine line to the north and west of the MCS center. Similar outflow boundaries are commonly observed along with convective systems (Markowski and Richardson, 2010; Houze Jr., 2004). Over time, the outflow boundary propagates radially away from the MCS, approaching the AWAKEN region to the northwest.

The cold pool outflow visible as a fine line in Fig. 5.2 and as similarly seen for another MCS by Tomaszewski and Lundquist (2021). The fine line in this study represents the front of the atmospheric bore that ultimately reaches the King Plains wind farm. The TTU X-Band radars measure the wind speed over a region encompassing the AWAKEN site, with Fig. 5.3 showing wind speeds at various heights around 06:30 UTC. Starting at approximately 06:00 UTC on June 6, 2023, oscillations in the wind speed measurement were observed by the X-band radars . The oscillations passed through the entirety of the King Plains wind farm at approximately 06:30 UTC. The plan view shown in Fig. 5.3 has been post-processed to terrain-following heights of 95 m (which is close to the 88.5 m turbine hub-height), 145 m and 270 m a.g.l.

The radar observes bands of faster and slower wind speeds indicative of wavy turbulence (Fig. 5.3). In Fig. 5.3(a), at 95 m a.g.l. (near hub-height) the wave pattern is not clear, likely because the waves interact with the wind farm and ambient turbulence closer to the surface. However, at 270 m a.g.l. (the highest altitude measured by the radars), the oscillations, seen as alternating color bands stretching left-right across the image, are much more distinct (Fig. 5.3(c)). While the gravity waves become weaker closer to the surface, they are faintly

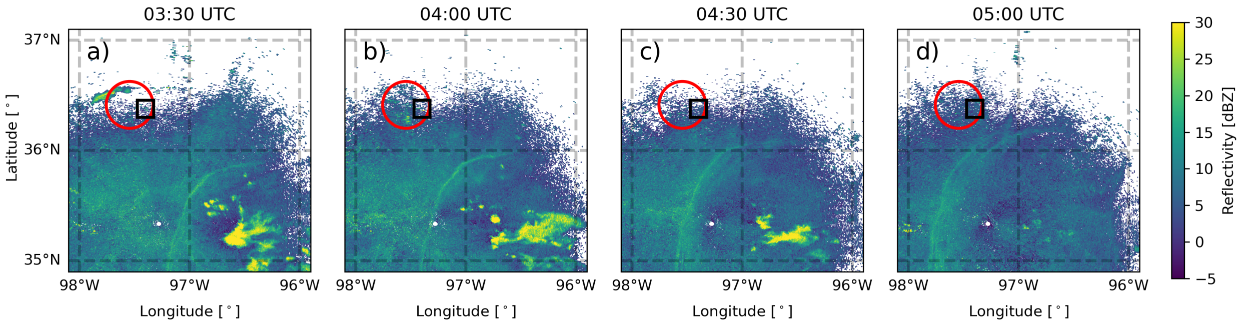

Figure 5.2: NEXRAD WSR-88D radar reflectivity over central Oklahoma at (a) 03:30, (b) 04:00, (c) 04:40, and (d) 05:00 UTC on June 6, 2023. The radar returns are from the Oklahoma City Site (KTLX). The area representing WRF domain d02 is outline in black (see Fig 5.4) and the approximate return from the TTU X-Band radars are outlined in red.

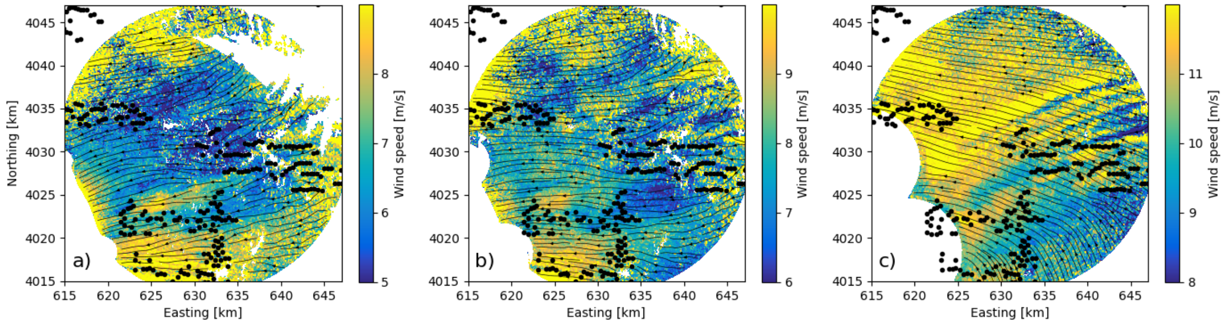

Figure 5.3: Plan view of dual-Doppler wind speed magnitude and streamlines from the TTU X-Band radars at 06:27:57 UTC on 06 June 2023 at heights of (a) 95 m, (b) 145 m, and (c) 270 m a.g.l. The time-stamp corresponds to the start of the scan routine completed by the radars which take approximately two minutes for a full return.

visible in Fig. 5.3(b), which represents a height close to the top of the wind turbine rotor layer.

Prior to the bore passage, the ambient atmosphere in the study region can be characterized as stable, as is typical for nighttime conditions in Oklahoma. 06:30 UTC corresponds to 01:30am central daylight time (CDT) with sunset occurring nearly five hours prior at 08:43pm CDT. The Obukhov length from the surface met station at A1 is 13.8, -27.9, -23.4 at 06:00, 06:30, 07:00 UTC, respectively, indicating very stable conditions prior to the bore followed by unstable conditions. The passage of the bore perturbs the stable boundary layer, inducing gravity waves that are eventually seen in the measured wind speed measurements in Fig 5.3. While the thermodynamic profiling instrumentation from AWAKEN was not online during this specific event, modeling results shown later in this study (see Fig. 5.6) suggest that the vertical structure of the atmosphere is stably stratified prior to the bore with additional discussion on how the bore affects the thermal structure in Sect. 5.5.

As denoted by the streamlines in Fig. 5.3, the ambient hub-height wind direction is easterly. This is a non-ideal wind direction for the King Plains wind farm as the layout was designed for the more dominant southerly wind direction. Interestingly, the gravity waves propagate from the south, which has a strong influence on the hub-height wind direction as discussed in later in this study. Additionally, the hub-height wind speeds are relatively low, on the order of 4-6 m s^{-1}, such that the power output of the farm is highly susceptible to wind speed fluctuations in this range (in region 2 of the power curve or in the operational mode of the wind turbines).

5.3 Methods

WRF-LES-GAD

The present work uses the large-eddy simulation capability of the WRF model, version 4.4, with modifications including the generalized actuator disk (GAD) (Mirocha et al., 2014a) with a turbine yawing capability (Arthur et al., 2020); a stochastic inflow perturbation method (the cell perturbation method; CPM) (Muñoz-Esparza et al., 2014; Muñoz-Esparza et al., 2015); and the implementation of a dynamic turbulence closure (Chow et al., 2005; Kirkil et al., 2012). The GAD requires specifications for the turbine's airfoil lift and drag coefficients. However, the required lift and drag parameters for the 2.8-MW General Electric turbines installed at King Plains are not publicly available. We therefore use the open source 2.8-MW turbine developed by the National Renewable Energy Laboratory (NREL) as a suitable representation in the model, with details available in Quon et al. (2024). The turbine has a hub-height of 88.5 m and rotor diameter of 126 m. Minor differences between the NREL turbine and the actual turbines at King Plains are not expected to be critical to the conclusions of this study.

Table 5.1: Description of various microphysics schemes used in WRF-LES-GAD. Variables are defined as follows: mixing ratio of water vapor (Qv); mixing ratio and number concentration of cloud water (Qc, Nc), rain (Qr, Nr), cloud ice (Qi, Ni), snow (Qs, Ns), and graupel (Qg, Ng); and number concentration of cloud condensation nuclei (Nn).

Parameterization	Sophistication	mp_physics	Variables
Thompson	1.5-moment	8	$Qc, Qr, Qi, Qs, Qg, Ni, Nr$
WDM6	Double-moment	16	$Qv, Qc, Qr, Qi, Qs, Qg, Nn, NcNr$
Morrison	Double-moment	10	$Qc, Qr, Qi, Qs, Qg, Nr, Ni, Ns, Ng$

Microphysics parameterizations

In modeling studies involving deep convection, simulation results show sensitivity to the microphysics parameterization (Pandey et al., 2023; Han et al., 2019). Microphysics schemes represent cloud and precipitation processes, describing the formation and growth of water particles (hydrometeors) for clouds, which are especially relevant to the MCS and bore formation in this study. The representation of microphysics in atmospheric models that are cloud-resolving is a major source of uncertainty and an active research area (Morrison et al., 2020; Tatsuya Seiki and Satoh, 2022). The microphysics schemes explored in this study in order of increasing sophistication are the Thompson (Thompson et al., 2008), WRF double-moment 6-class (WDM6) (Lim and Hong, 2010), and Morrison (Morrison et al., 2009) schemes, which are widely used by both operational models and in research. Microphysics schemes largely fall into two categories: single-moment schemes that predict the mixing ratios of hydrometeors and double-moment schemes (WDM6 and Morrison) that predict both the mixing ratio and the number concentration of hydrometeors. The schemes used in this study vary in what prognostic variables or species of particles they predict, which are detailed in Table 5.1. Note that some double-moment schemes may only be double-moment for a limited number particle species, as is the case for the Thompson model, which is why the Thompson model is denoted as 1.5-moment in Table 5.1. More detail on WRF microphysics schemes can be found in Skamarock et al. (2021).

Turbulence modeling

Extensive literature in LES turbulence closure modeling has shown that dynamic turbulence closures are able to perform better than standard eddy-viscosity approaches in SBL conditions (Zhou and Chow, 2011; Zhou and Chow, 2014; Wise et al., 2024). The standard approach to turbulence modeling relies on an implicit filter related to the grid resolution to parameterize the effect of the subgrid scale (SGS) motions on the resolved flow. In this study, we use an explicit filtering approach to separate large-scale from subfilter scale motions which provides a framework for using the dynamic procedure of Germano et al. (1991) to solve for coefficients of interest.

When an explicit filter is used, the presence of the numerical grid divides the subfilter scale (SFS) motions into resolved and unresolved portions. The unresolved SFS motions are the commonly referred to SGS motions. However, the effect of resolvable subfilter scale (RSFS) motions can be reconstructed using a scale-similarity approach (see Chow (2004) for derivations). The RFSF motions are neglected in standard closure schemes (i.e., those that do not use an explicit filter). In this study, we make use of the explicit filtering and reconstruction approach of the Dynamic Reconstruction Model (DRM) turbulence closure (Chow et al., 2005). The performance of the DRM closure with respect to ambient turbulence for this specific case study is compared with other closures in Appendix C.

5.4 Model configuration and description

The 2-domain nested setup for WRF-LES-GAD is shown in Figure 5.4 with details in Table 5.2. The setup is unique compared to other multi-scale WRF setups in that it uses only two domains. Mesoscale forcing is provided by the High-Resolution Rapid Refresh (HRRR) model v4 (Dowell et al., 2022) as the lateral boundary conditions (updated hourly) for domain d01 following the procedure of Blaylock et al. (2017). The HRRRv4 model was chosen because its horizontal grid spacing is 3 km, which is much finer than the grid resolution used by other regional or global models. In comparison, the Global Forecast System (GFS) (National Centers for Environmental Prediction, 2015) and the European Centre for Medium-Range Weather Forecasts Reanalysis v5 (ERA5) (Hersbach et al., 2020) have grid spacings of 0.25 degrees, which corresponds to roughly 27-28 km. The HRRRv4 3 km grid spacing is already a very fine-scale mesoscale simulation, and using a relatively large parent grid ratio of 10 from HRRRv4 to domain d01 is reasonable to intentionally skip across the convective gray zone where turbulence is only partially resolved (Wyngaard, 2004; Chow et al., 2019; Haupt et al., 2019; Muñoz-Esparza et al., 2017).

The HRRRv4 model was also chosen because of its high temporal update frequency and use of data assimilation (DA). The temporal update is hourly, which is important for modeling dynamic events. ERA5 has an hourly temporal update; the GFS has a temporal update of three hourly, with forecasts initialized every six hours. In HRRRv4, weather radar (NEXRAD) data is assimilated every 15 minutes during the first hour of simulation, which is referred to as the pre-forecast hour (Dowell et al., 2022). Preliminary simulations were also conducted using GFS and ERA5, which resulted in nocturnal MCSs but in the incorrect location (not shown). In this study, we use the HRRRv4 analysis product also known as the 0 hour forecast (which includes the hour of pre-forecast with NEXRAD data assimilated). Simulations showed that the DA in the HRRRv4 model constrains the initiation of the MCS to the correct location, which is critical to the present study.

Domain d01 is centered over the approximate midpoint between the AWAKEN region and the location where the MCS initiates. The 300 m horizontal grid spacing was chosen as a balance between computational cost and model resolution over a large geographic area. Note that preliminary simulations at 1 km grid spacing did not provide realistic bore structure (not shown). Additional preliminary simulations at 200 m grid spacing provided similar results as those with the 300 m grid spacing (not shown), which is consistent with the findings of Johnson and Wang (2019) who found little benefit to increasing the grid resolution beyond 250 m for their bore simulations. As previously mentioned, modeling studies that resolve deep convection show large sensitivities to cloud and precipitation processes. Therefore, three separate simulations for domain d01 are run with the microphysics schemes specified in Table 5.1 with results compared in Sect. 5.5.

Domain d02 has 20 m horizontal grid spacing, which is necessary to resolve the effects of individual wind turbines using the generalized actuator disk parameterization. The 20 m horizontal grid spacing is fine enough to include 6 grid points across each generalized actuator disk in the horizontal (and 16 in the vertical with the grid spacing described in Table 5.2). The GAD parameterization is typically used at 10 m resolution (Mirocha et al., 2014a; Arthur et al., 2020; Wise et al., 2022), but given the large domain size required here, preliminary simulations showed that 20 m provides reasonable results, with the bimodal distribution of the wind turbine velocity deficit in the near wake region still retained.

A parent grid ratio of 15 from d01 to d02 bridges the MCS-resolving domain (domain d01) to the turbine wake-resolving domain (domain d02). Intermediate nests with grid spacing between 300 and 20 m were explored but found to lessen the agreement with observations (not shown) as in Mazzaro et al. (2017). Because of the large parent grid ratio between domains d01 and d02, the development of small-scale turbulent structures on d02 is accelerated using the cell perturbation method (CPM), a stochastic inflow perturbation method (Muñoz-Esparza et al., 2014; Muñoz-Esparza et al., 2015). The CPM works by applying small temperature perturbations at the domain boundaries, fostering the development of a wider range of turbulent scales with negligible computational cost. CPM has been used successfully in a large number of WRF-LES studies (Arthur et al., 2020; Connolly et al., 2021; Wise et al., 2022; Sanchez Gomez et al., 2022; Sanchez Gomez et al., 2023).

At 20 m grid spacing, much of the ambient turbulence is resolved on d02; however, SBL conditions tend to reduce the turbulent length scale. Previous work has shown that dynamic turbulence closures can resolve more ambient turbulence compared to standard closures at coarser grid resolutions, especially in strongly stable conditions (Zhou and Chow, 2011; Zhou and Chow, 2014; Wise et al., 2024). Therefore, the DRM closure is especially well-suited for this case study and simulation setup. The sensitivity of resolved turbulence characteristics to the turbulence closure is explored in Appendix C.

Because of the computational expense of these simulations, the start time of domains d01 and d02 is staggered. Domain d01 begins on 06 June 2023 at 03:00 UTC, which is just over 3 hours prior to the gravity wave reaching the measurements at the AWAKEN site. A 3-hour lead time is chosen following the favorable results from the forecast start-time sensitivity conducted by Johnson and Wang (2017). Domain d02 begins at 05:00 UTC and is run until 07:30 UTC with the first hour (05:00-06:00 UTC) considered to be spin up, and therefore not used in the analysis. With both domains running concurrently, 30 minutes of simulation time takes approximately 24 hours of wall-clock time on 800 cores.

WRF-LES-GAD is run using a third-order Runge-Kutta time advancement scheme, with fifth-order horizontal and third-order vertical advection schemes. The physical parameter-

Table 5.2: Parameters used for the nested multi-scale WRF-LES-GAD setup. For the vertical resolution, Δz_{min} is for the first grid point above the surface and is approximate due to the nature of the terrain-following coordinate system in WRF.

Domain	Δx [m]	Grid ratio	$\sim \Delta z_{min}$ [m]	$N_x \times N_y$	Δt [s]	turb. closure
Forcing	3000	-	15	1800 × 1060	20	MYNN-EDMF
d01	300	10	8	1200 × 1200	1.5	TKE-1.5
d02	20	15	8	661 × 871	0.1	DRM

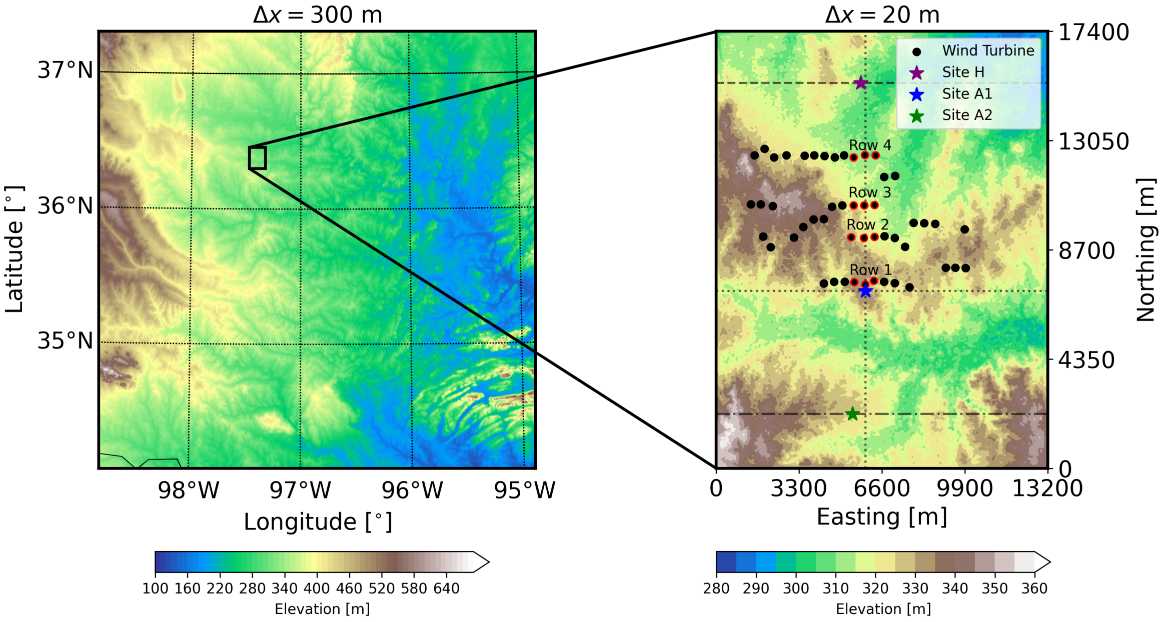

Figure 5.4: Topography of domains (a) d01 and (b) d02 used in the multi-scale simulation. Dimensions of each domain and other configuration information are included in Table 5.2.

izations are as follows: the Noah land surface model (Chen and Dudhia, 2001), the Rapid Radiative Transfer Model for longwave radiation (Mlawer et al., 1997), and the Dudhia shortwave radiation model (Dudhia, 1989). No cumulus parameterization option is used as convection is explicitly resolved using LES.

For the turbulence closure, on domain d01, we use the standard TKE-1.5 LES closure (Deardorff, 1980). On domain d02, where ambient turbulence is resolved and the wind turbines are parameterized, we use the DRM LES closure (with comparisons using other closures shown in Appendix C). All domains use the Eta similarity surface layer scheme (Janjić, 1994), which uses similarity theory (Monin and Obukhov, 1954) to determine the relevant surface fluxes. For topography, high-resolution terrain data (1-arc-second, approximately 30 m) are used from the Shuttle Radar Topography Mission (Farr et al., 2007). The landuse data similarly uses 30 m spacing and is a National Land Cover Database product converted into USGS categories (as in Chen et al. (2024)). The domain extends 20 km above the ground; at the upper-boundary condition, diffusive damping is applied with a coefficient of 0.01 following Johnson et al. (2018).

5.5 Results and discussion

Bore structure sensitivity to microphysics parameterizations

The case study examined in the present work is an atmospheric bore event with associated gravity waves that were observed to interact with the King Plains wind farm on 06 June 2023. The development of the bore is highly sensitive to the selected microphysics paramterization. Figure 5.5 shows the vertical velocity at 1 km a.g.l. and the potential temperature at 200 m a.g.l. for 04:00 UTC, which is an hour after the simulation/forecast start time. All three microphysics parameterizations resolve the deep convection and look qualitatively similar. Subtle differences in the strength of the cold pool, however, ultimately affect the development of the bore as it propagates roughly 100 km to the AWAKEN region.

The cold pool generated by the MCS is governed by latent cooling from the downdraft generated due to precipitation. The precipitation partially evaporates which produces the colder air downdraft, which forms the cold pool (Markowski and Richardson, 2010; Muller and Abramian, 2023). The cold pool then spreads horizontally as a density current when it reaches the surface. Planar-averaged vertical profiles of potential temperature and various hydrometeor species within the MCS are shown in Fig. 5.6. The subdomain that encompasses the MCS is shown in Fig. 5.5. The thermal structure of the MCS is similar for the three different microphysics parameterizations; however, results with the WDM6 microphysics are colder from the surface up to 3 km a.g.l. The stronger cold pool for the WDM6 microphysics scheme compared to the other schemes is because below the cloud base (approximately 2 km a.g.l., see Fig. 5.6(b)), the rain water mixing ratio decreases with decreasing altitude. The decrease in rain water mixing ratio indicates low-level rain evaporation as discussed by Johnson et al. (2018), which provides latent cooling. Both the Thompson and Morrison microphysics schemes have relatively constant rain water mixing ratios below the cloud base. Another contributing factor to the differences in the thermal structure of the MCS is the larger snow water mixing ratios in the upper atmosphere above the cloud base, which, in-turn, reduce the graupel and rain water mixing ratios. These trends are similar to those found by Johnson et al. (2018) in their microphysics sensitivity study.

In contrast with Johnson et al. (2018), only the WDM6 microphysics scheme provides realistic bore structure by the time it reaches the AWAKEN region. Time-height contours in Fig. 5.7 show vertical profiles of wind speed and vertical velocity for the three different microphysics parameterizations compared with the vertical profiling lidars at A1. Note that the observations in Figs. 5.7(a) and 5.7(b) include both the Halo XR+ lidar, which measures from 100 m a.g.l. to the top of the boundary layer but with an alternate scan schedule

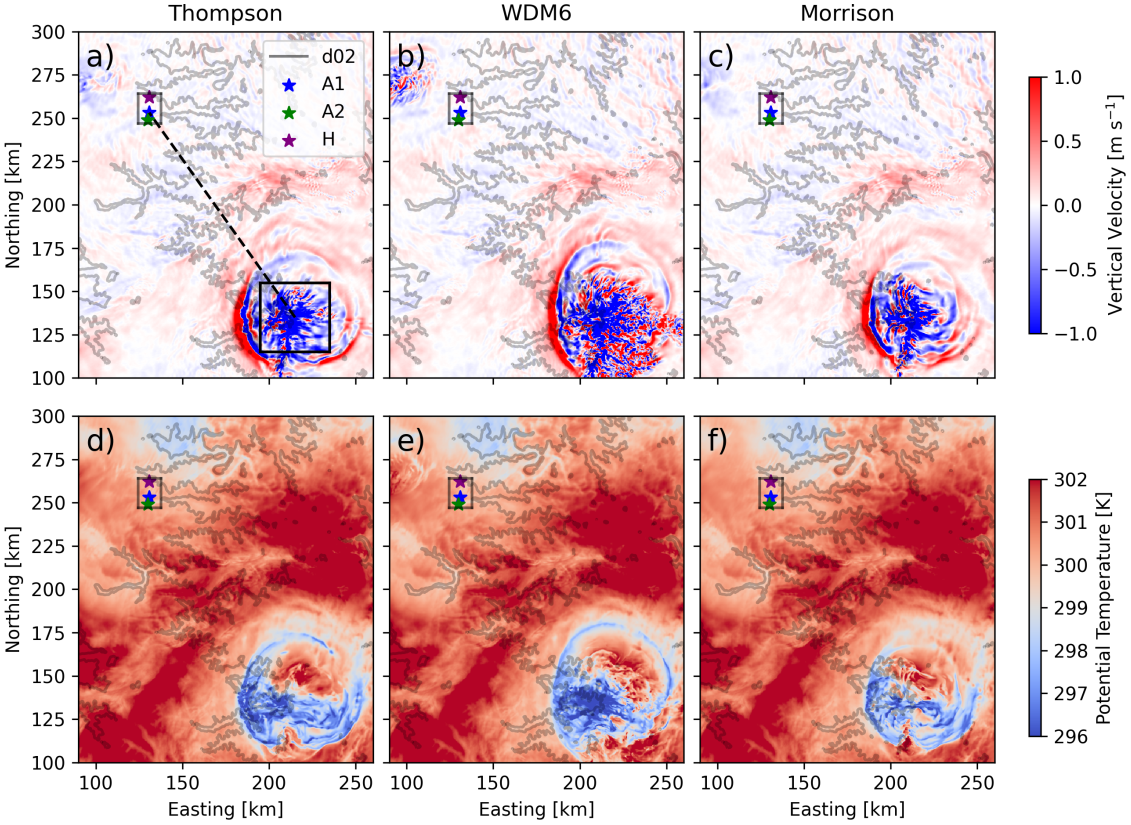

Figure 5.5: Instantaneous plan slice of (a-c) vertical velocity at 1 km a.g.l. and (d-f) potential temperature at 200 m a.g.l. on domain d01 for various microphysics schemes. Line contours represent 100 m changes in elevation. Note that the domain has been cropped for visualization purposes. A subdomain is denoted as the dashed box, which is used for analysis in Figure 5.6. The dotted line in (a) is a transect used for the visualization in Fig. 5.9.

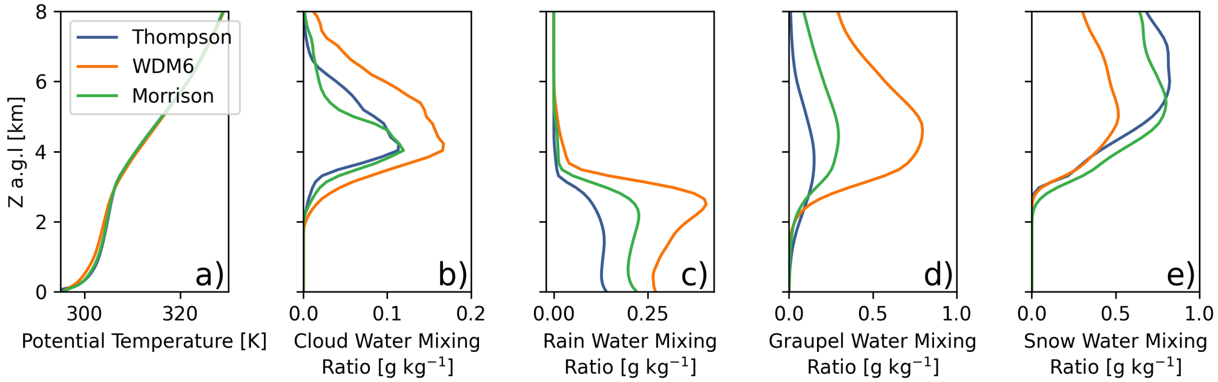

Figure 5.6: Vertical profiles averaged in the 20 m resolution subdomain from Fig. 5.5 for (a) potential temperature, (b) cloud water mixing ratio, (c) rain water mixing ratio, (d) graupel water mixing ratio, and (e) snow water mixing ratio for the various microphysics schemes.

every 20 minutes, as well as the Windcube v2, which focuses on lower altitudes measuring from 40 to 240 m a.g.l. While there are faint wavy structures in the simulation results using Thompson or Morrison, only WDM6 provides gravity waves that resemble observations and is therefore selected for further analysis. For example with WDM6, the period of the initial wave is ∼5 minutes in the model compared to ∼4.5 minutes for the observations as defined by the time between the first two wind speed peaks. There is a 16 minute delay in the timing of the bore for the results with WDM6 compared to observations, likely due to small differences in the bore speed with the gravity waves first appearing at 06:09 UTC in observations compared to 06:25 UTC in the model. Considering that the bore propagates over 100 km from the MCS to the AWAKEN region, for example, a difference in the bore speed of 1 m s^{-1} can result in a timing difference of nearly 20 minutes. Additionally, the bore propagation speed is not necessarily constant with time as it can be affected by the ambient environment (Johnson and Wang, 2017; Haghi et al., 2019).

The mesoscale environment is very similar regardless of microphysics scheme. Figure 5.7 shows that a low-level jet (LLJ) exists prior to the bore passage. The maximum wind speed in the LLJ is predicted accurately by the model at 270 m a.g.l. as was observed; however, there is a positive bias in the wind speeds predicted by the model. These differences can be quantified by time-averaging the flow prior to the gravity waves (05:30-05:50 for the observations and 05:46-06:06 for the model accounting for the time delay). Specifically, for results using WDM6, the model predicts a LLJ maximum wind speed of 10.2 m s^{-1} where as the observed maximum wind speed was 9.3 m s^{-1}. At the lowest altitude with consistent returns in the Halo XR+ lidar, 110 m a.g.l., the observed wind speeds were 4.8 m s^{-1} while the modeled wind speeds are 6.0 m s^{-1}. These errors in the wind speed are likely because of differences in the HRRR forcing used as the lateral boundary conditions. Importantly, the wind direction at 110 m a.g.l. is well-predicted by the model at 57.5 degrees whereas the observed wind direction was 59.0 degrees. Notably, the LLJ is weakened after the bore passage, which is discussed in more detail later.

The vertical velocity and wind speed signals in Fig. 5.7 are highly correlated during the gravity wave passage. During an updraft or downdraft of the wave, there is a corresponding convergence or divergence in the horizontal velocity. In Figs. 5.7(e) and 5.7(f), there are two strong peaks followed by residual wavy structures with less intensity. In the observations, there are at least three strong peaks which are followed by a 10 minute period of missing observations due to an alternate scan schedule for the Halo XR+ lidar. The observations are typical for bores where there are strong initial waves followed by elevated turbulence along with a lifting of the boundary layer (Haghi et al., 2019; Haghi and Durran, 2021), which is discussed in more detail in the following sections. It is also important to note that the gravity waves manifest most strongly in the wind speed signal at heights from 200-800 m a.g.l. The intensity of the gravity waves in the wind speed signal diminishes closer to the surface and towards the top of the rotor layer, which was also observed in the radar measurements (Fig. 5.3).

Gravity wave characteristics and evolution

The MCS-induced cold pool propagates outward, which perturbs the stably stratified atmosphere as a bore. The progression of a bore is well-described in Haghi et al. (2017) with the bore in the present study falling between a bore with undulations and one with solitary-like waves by the time the bore reaches the AWAKEN site. Note that all results presented in this manuscript hereinafter use the WDM6 microphysics scheme. Figure 5.8 shows instantaneous plan slices at 30 minute increments for the vertical velocity at 1 km a.g.l. and the potential temperature at 200 m a.g.l on domain d01. The height of 1 km a.g.l. is a standard for studies involving bores while 200 m a.g.l. represents a height closer to the surface and also where the cold pool is very strong. At 05:00 UTC, the bore forms a ring as it propagates outward and spreads radially from the parent MCS. As the bore moves closer to the AWAKEN region, it gradually mixes into the ambient environment. While the strength of the cold pool weakens the further it travels from its parent MCS, gravity waves continue to propagate in the thermally stratified atmosphere as evident in Fig. 5.8. At 05:00 UTC, there is a clear leading wave, and by 05:30 UTC, trailing waves are seen forming a wave train. The wave train reaches the AWAKEN region at 06:30 UTC with two large waves followed by a number of additional waves in the train. The waves then weaken in intensity at 07:00 UTC.

The vertical structure of the atmosphere is substantially impacted by the propagating bore and associated wave train. Figure 5.9 shows a vertical cross-section, along the transect illustrated in Fig. 5.5(a), of the wind speed and potential temperature at the same time increments as in Fig. 5.8. Note that the colorbar in Fig. 5.9 is specifically chosen to highlight the colder temperatures which form the SBL (but note that the entirety of the atmosphere in Fig. 5.9 is stably stratified). At 05:00 UTC (Figs. 5.9(a) and 5.9(b)), the bore is evident as an injection of faster wind speeds and colder temperatures into the transect with the

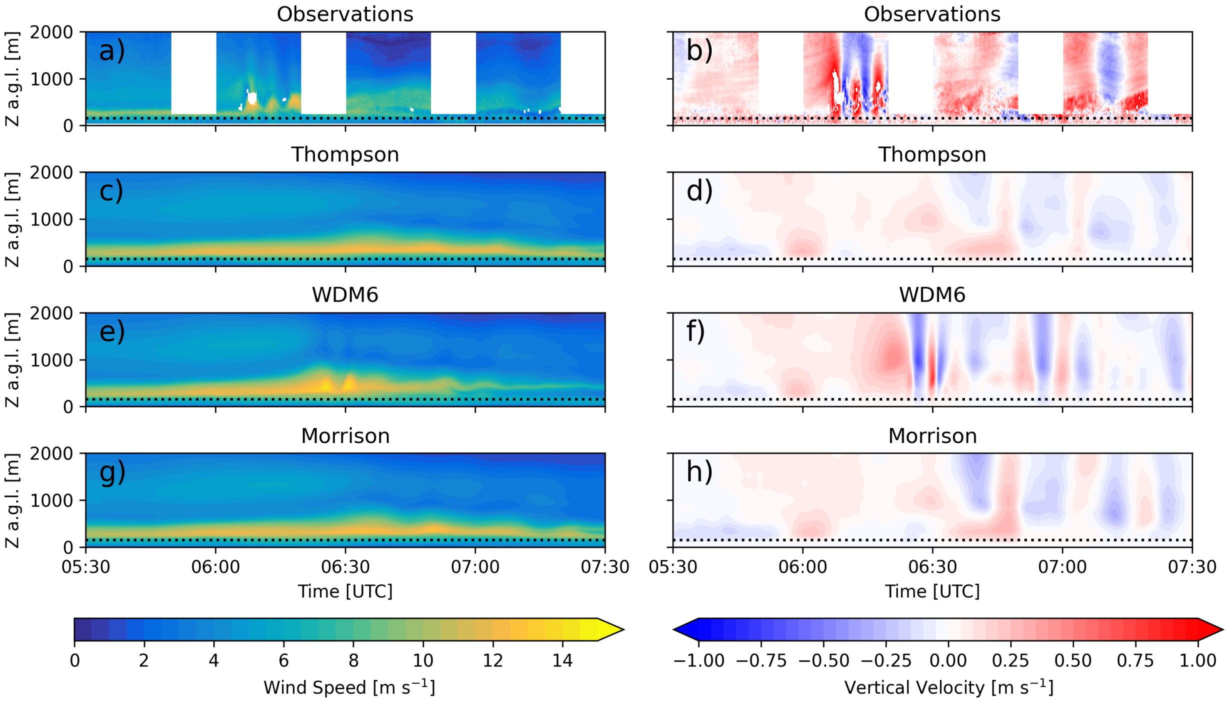

Figure 5.7: Time-height contours of wind speed and vertical velocity in (a,b) observations from the lidars and (c-g) the model for various microphysics schemes all at the Site A1 location. The dotted line corresponds to the top of the wind turbine rotor layer.

density current traveling in the positive direction. Initially, the colder temperatures in the bore appear most clearly as a singular front that perturbs the SBL. Over time, the front evolves into a number of wavy structures at the interface of the SBL and free atmosphere that form the wave train. Additionally, the bore itself increases the height of the SBL, which is discussed in more detail in the following section.

In the wind speed signal, the interaction between the bore and ambient environment is more complex. At 05:00 UTC (Fig. 5.9(a)) and upwind of the density current (distances $>$ 100 km) there is a pre-existing east-northeasterly LLJ with a height of 600 m a.s.l. and a maximum wind speed of 10 m s^{-1}. Also evident in Fig. 5.9(a) is the wind speed behind the bore front, which is greater than 14 m s^{-1}. Over time, the wind speeds within the bore weaken substantially from as high as 14 m s^{-1} to 6-8 m s^{-1}. However, the bore continues to propagate in the positive direction, which results in the advection of the pre-existing LLJ in the positive direction. By 06:30 UTC (Fig. 5.9(g)), the effect of the bore on the preexisting LLJ manifests itself as two well-defined waves in the wind speed signal (with a number of additional wavy structures behind the front). These two maxima result in the clear, distinct waves in the time-height contours at A1 (Fig. 5.7(e)) that occurred 5 minutes after each

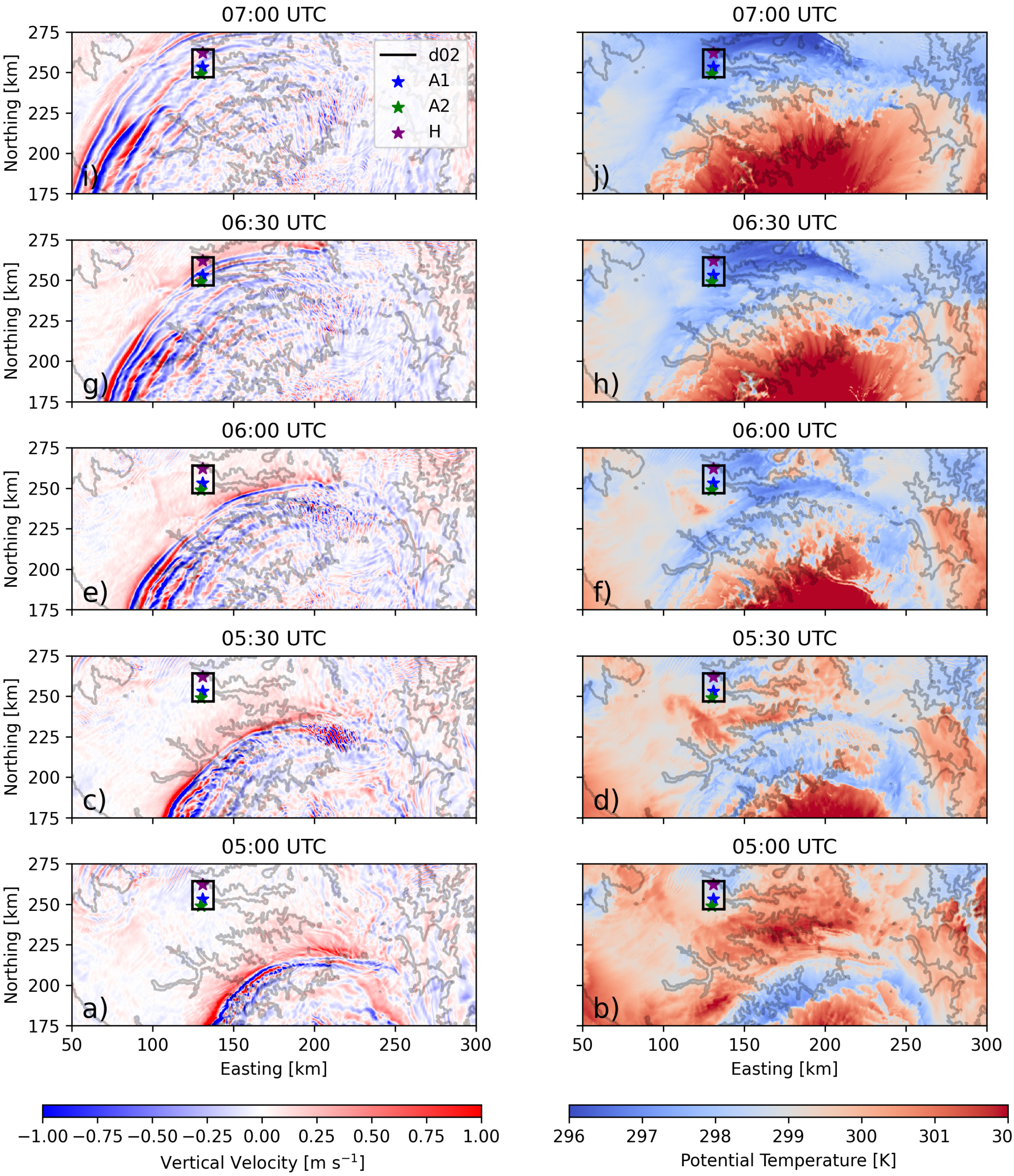

Figure 5.8: Plan slice of (a-e) vertical velocity at 1 km a.g.l. and (f-j) potential temperature at 200 m a.g.l. from 05:00 to 07:00 UTC in 30 minute increments on Domain d01. Line contours represent 100 m changes in elevation. Note that the domain has been cropped for visualization purposes, and that the panels progress in time from bottom to top to highlight the northward movement of the bore.

other. The distance between the well-defined maxima is 4.5 km. Trailing waves are also evident in Fig. 5.9(g) and 5.9(h) but are much slower in wind speed and also typically have larger distances between the waves. By 07:00 UTC (Fig. 5.9(i)), the effect of the bore is that the LLJ no longer extends into the AWAKEN region and, as a result, the wind turbines at King Plains experience much slower wind speeds. The effect of this modulation of the mesoscale environment by the bore is further quantified in the following section.

Bore and gravity wave effects on the boundary layer

The gravity waves associated with the bore are strongest higher in the atmosphere. Vertical slices of wind speed and vertical velocity for domain d02 are shown at various times during the gravity wave passage in Fig. 5.10. The vertical slices are taken along a north-south transect that intersect point A1 shown in Fig. 5.4. This transect intersects four rows of the King Plains wind farm but since the hub-height winds are more northeasterly, wakes are largely out-of-plane in Fig. 5.10. At 06:25 UTC, the first wave of the solitary-like wave train, which has a wave-to-wave time-interval of 5 minutes and physical distance of 4.5 km, is seen approaching the wind farm in Figs. 5.10(a) and 5.10(d). As time progresses, there are a number of additional waves that pass over the wind farm. While the gravity waves are the dominant feature above the wind turbines, there are other turbulent features related to wakes and ambient turbulence in the rotor layer and closer to the surface.

Vertical profiles provide a more quantitative understanding of how the structure of the atmosphere is modulated by gravity wave-wind farm interactions. Figure 5.11 shows vertical profiles of time-averaged wind speed, wind direction, potential temperature, and resolved heat flux at Site A1. At Site A1, model results are compared against both profiling (closer to the surface) and scanning (higher up in the atmosphere) Doppler lidar measurements of the wind speed. The vertical profiles are time-averaged for periods before, during, and after the gravity wave passage. The averaging windows used depend on the specific site due to the time it takes for the gravity waves to propagate northward. We assume that the gravity waves propagate at a speed equal to the wave-to-wave physical distance (4.5 km) divided by the time-interval (5 minutes), which is 15 m s^{-1}. Additionally, because there is some difference in when the wave arrives in the model compared to the measurements, there is a 16 minute shift used when defining these periods for the measurements compared to the model (as was done when similarly analyzing a MCS by Tomaszewski and Lundquist (2021)). For example, the averaging window used for "during" is 06:04-06:34 UTC at Site A1 for the measurements, while it is 06:20-06:50 UTC for the model. The averaging periods used to generate the vertical profiles are summarized in Table 5.3.

The measurements and modeling results demonstrate the weakening and eventual destruction of the LLJ due to the propagating gravity waves generated by the MCS. In the vertical profiles of wind speed (Fig. 5.11(a)), there is a well-defined maximum above the rotor layer (representing the LLJ nose) prior to the gravity waves. During the gravity wave passage, the vertical location of the LLJ nose increases in height and after the gravity waves, the LLJ maximum is significantly diminished. However, the wind speed maxima of the LLJ

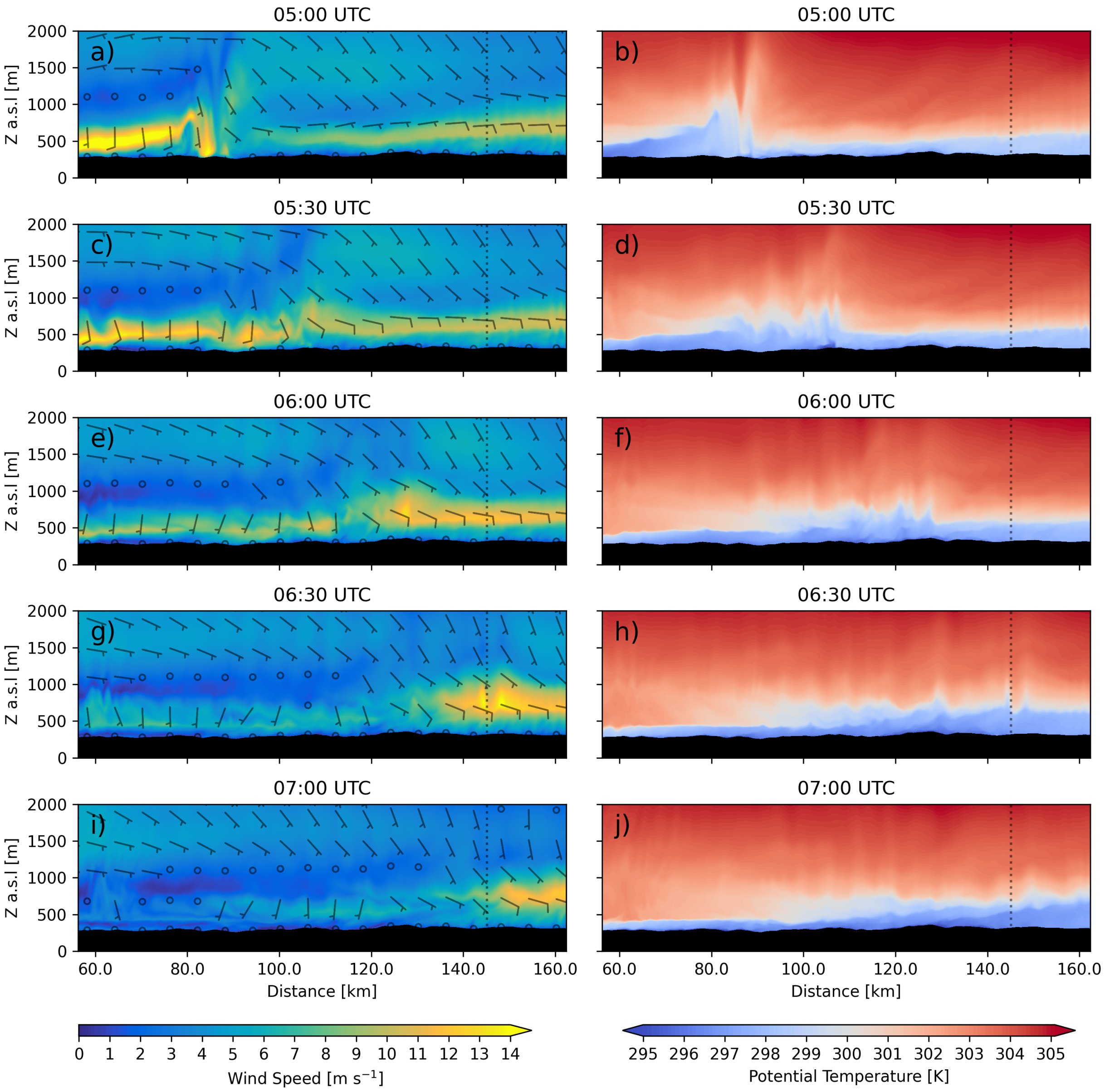

Figure 5.9: Vertical cross-section of wind speed (with wind barbs) and potential temperature from 05:00 to 07:00 UTC in 30 minute increments. The transects are along the dashed line shown in Fig. 5.5. The dotted line corresponds to the location for Site A1.

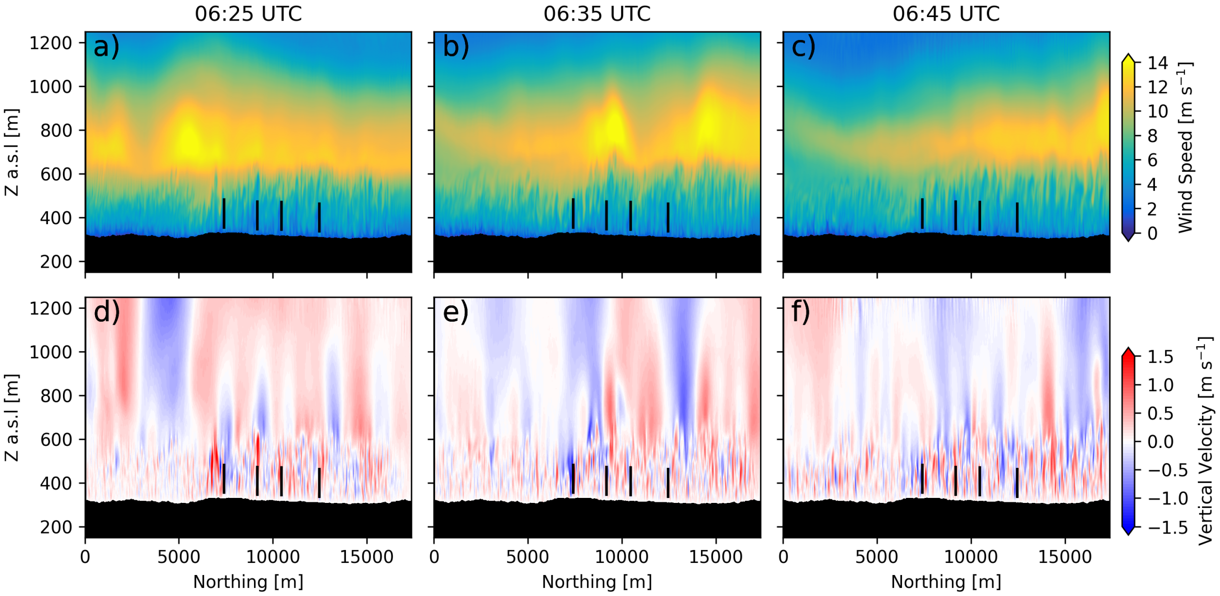

Figure 5.10: Instantaneous vertical cross-sections of (a-c) wind speed and (d-f) vertical velocity along the A1 north-south transect at various times during the gravity wave event.

Table 5.3: Time windows used for averaging vertical profiling results when comparing WRF-LES-GAD with observations at Site A1.

	Before	During	After
Measurements Averaging Window (UTC)	05:34-06:04	06:04-06:34	06:34-07:04
Model Averaging Window (UTC)	06:00-06:20	06:20-06:50	06:50-07:20

and the negative shear region above are both overestimated in the model. In addition to the decrease of wind speed due to the gravity waves, the wind direction also becomes more easterly as shown in Fig. 5.11(b). Before the gravity waves arrive, the wind direction is east-northeasterly (approximately 60 degrees) at hub-height, with substantial wind veer across the rotor layer. During and after the gravity wave passage, the wind direction is more easterly, which is suboptimal for the east-west rows of the King Plains wind farm, due to waking within the row. The bore and the associated gravity waves advect from the south-southeast, which forces the ambient northeasterly winds to become more easterly. The effect of the gravity waves on the wind direction is discussed further below.

The thermal structure of the atmosphere is also strongly impacted by the gravity wave passage. Prior to the gravity wave arrival, the boundary layer is stably stratified up to approximately 200 m, above which the atmosphere is more stable. In Fig. 5.11(c), the boundary layer height is increased during the gravity wave passage. The increased boundary

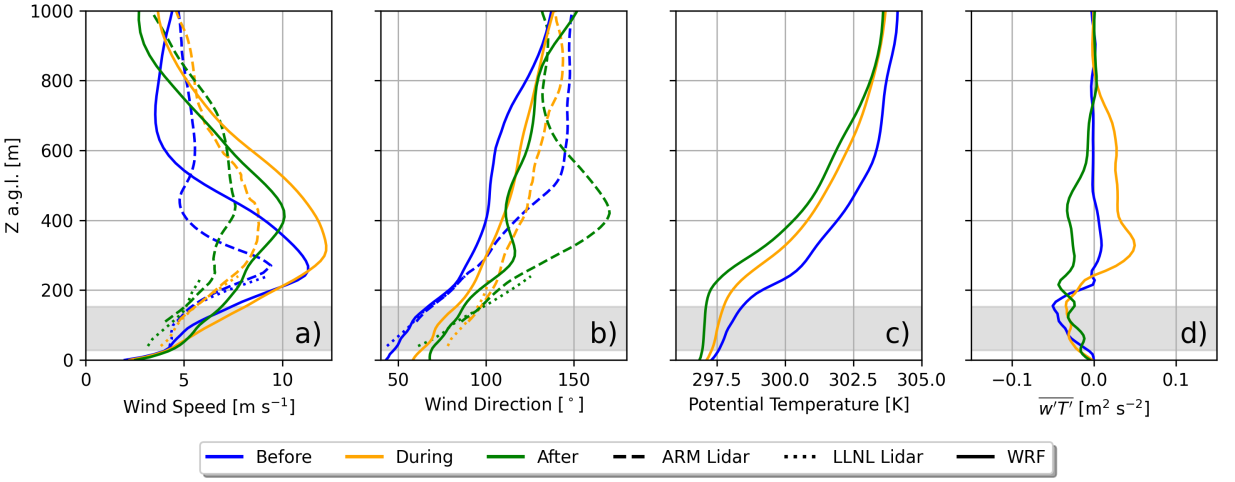

Figure 5.11: Time-averaged vertical profiles of (a) wind speed, (b) wind direction, (c) potential temperature, and (d) resolved heat flux for observations and simulation results at Site A1. See Table 5.3 for the averaging windows. The wind turbine rotor layer is highlighted in gray.

layer height persists even after the gravity wave passage, which is a common characteristic of bore events (Haghi et al., 2019; Haghi and Durran, 2021). In addition to the boundary layer height increasing, the boundary layer cools and the thermal stratification weakens during the gravity wave passage, and these changes also persist after the wave passage. The stability weakening was also observed by the sonic anemometers at the A1 surface met station as previously discussed in Sect. 5.2. The cooling and deepening of the boundary layer are driven in part by the advection of colder temperatures into the region by the bore itself. Additionally, as the gravity waves pass, there is a positive heat flux in the upper atmosphere (Fig. 5.11(d)), indicating that heat is transferred from lower altitudes to higher altitudes, thus weakening the thermal stratification.

Gravity wave - wind farm interaction

The effect of the gravity waves on the power production of the King Plains wind farm is two-fold. First, the destruction of the LLJ by the gravity waves results in a decrease in the average power production. Second, there is increased power variability during the gravity wave passage. Figure 5.12 shows a time-series of the power production of the wind farm by row with the power signal smoothed to reduce noise by applying a 1-minute running average. The King Plains wind farm layout is non-uniform and as a result, there are certain rows with more wind turbines than others. In an attempt to equalize this factor, three turbines in each row are selected as shown in Fig. 5.4. In Fig. 5.12, the period during which

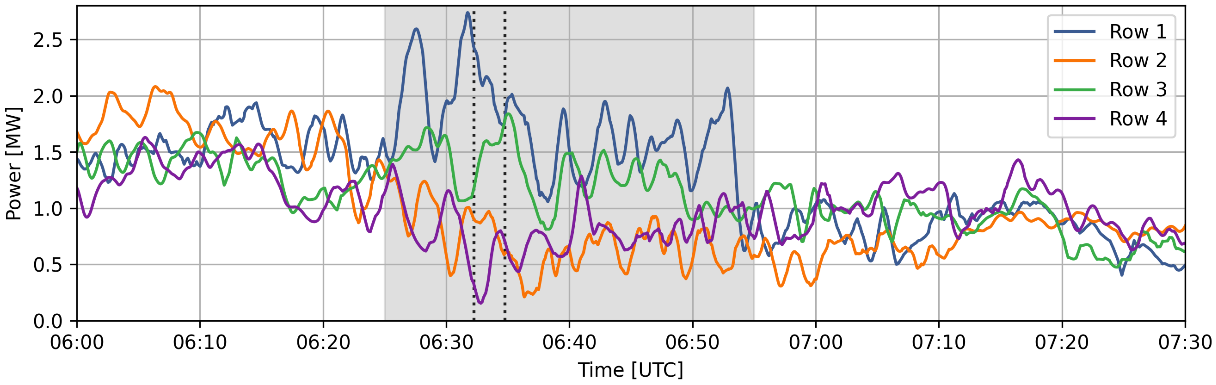

Figure 5.12: Time-series of row power for the eastern King Plains wind farm from 06:00 to 07:30 UTC. Figure 5.4 shows the turbines that represent each row. The dotted lines highlight the time-instants shown in Fig. 5.14.

the turbines are most significantly impacted by the gravity waves is highlighted in gray (06:25-06:55 UTC). Prior to the gravity waves, the first row of turbines averages 1.54 MW of power, whereas after the gravity waves have modulated the mesoscale environment, the first row of turbines averages 44% less power at 0.86 MW. All rows of turbines produce less power after the gravity waves pass, with row 2 producing 56% less power, row 3 producing 34% less power, and row 4 producing 15% less power on average. Row 1 has the largest increase in power variability during the gravity waves in terms of the standard deviation. The standard deviation increases by over 100% for row 1 from 0.18 MW prior and 0.16 MW after the gravity waves to 0.42 MW during the gravity waves. The power variability in the other rows is not as severely impacted.

The increased power variability during the gravity wave passage is an indirect effect, related to subtle shifts in the wind direction caused by the wave motion. Figure 5.13 shows the power signal in rows 1 and 2 along with the local perturbation pressure and wind direction signals. The perturbation pressure represents the total atmospheric pressure with the base pressure removed (Skamarock et al., 2021). The local hub-height perturbation pressure and wind direction signals are obtained by spatially averaging a 600 m × 600 m area centered over the middle turbine within each row. At the beginning of the period affected by the gravity waves, there are two peaks in the pressure signal which correlate to the waves in Fig. 5.7. The wind direction also correlates with the perturbation pressure signal, with higher perturbation pressure corresponding to more easterly wind and lower perturbation pressure corresponding to more east-northeasterly winds.

The correlation of the hub-height wind direction and perturbation pressure is qualitatively more clear in a plan view. Figure 5.14 shows the wind speed and perturbation pressure at hub-height along with streamlines at two different time instances. Closer to the surface,

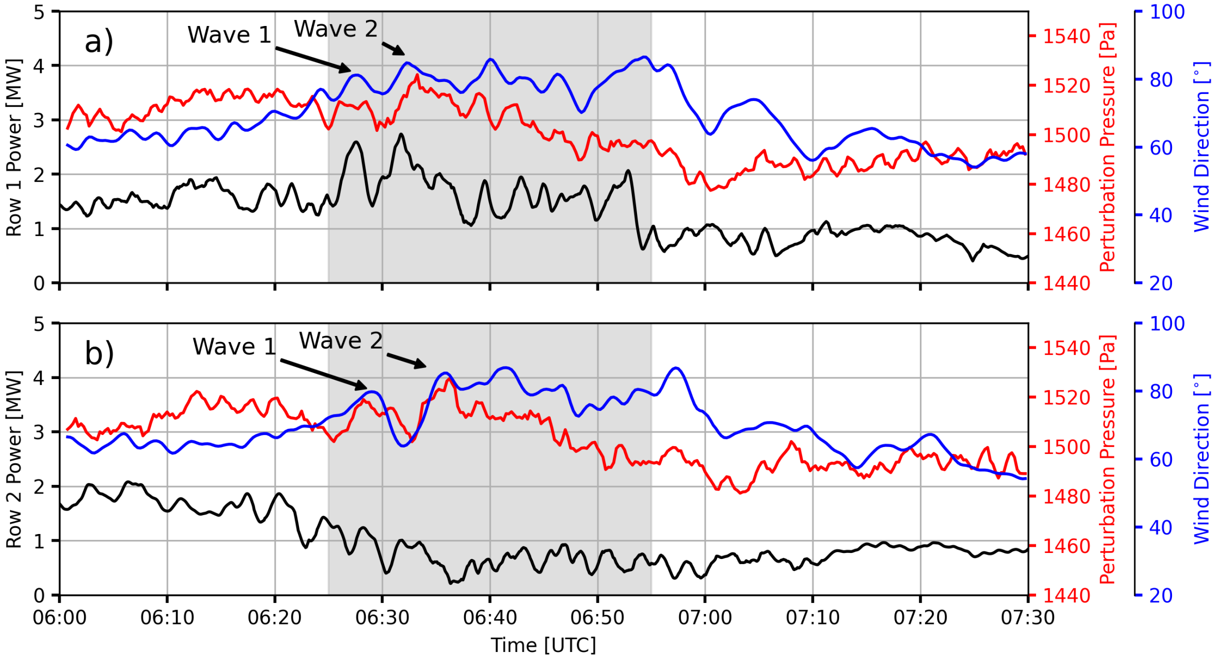

Figure 5.13: Time-series of the (a) Row 1 and (b) Row 2 local wind direction, perturbation pressure, and power for the eastern King Plains wind farm from 06:00 to 07:30 UTC.

the gravity waves manifest most clearly in the perturbation pressure signal. The two time instances were chosen to display the effect of high and low pressure regions beneath the gravity waves. During the first time-instance (06:32:15 UTC), the second row of turbines is in a low pressure region and is experiencing wind directions that are more east-northeasterly. During the second time-instance (06:34:45 UTC), the second row of turbines is in a high pressure region and the wind direction is easterly. The same relationship between pressure and wind direction is observed beneath the gravity waves. More easterly winds are less favorable for the King Plains layout and result in significant power losses due to wakes.

The second row of turbines produces more power during the first time-instance with the east-northeasterly winds at 0.90 MW while the same row produces 34% less power during the second time instance with easterly winds. A similar, but opposite, trend happens for row 4 related to the wave-to-wave distance of the waves. During the first time-instance, the majority of the turbines in row 4 are waked during the easterly wind directions and the row is producing just 0.32 MW of power. The turbines in row 4 experience more east-northeasterly wind directions during the second time-instance and are thus producing more power at 0.71 MW.

While the gravity waves induce wind direction shifts which modulate the produced power, it is important to remark that the power production in the farm is variable due to additional factors. Importantly, local turbulent structures have a strong impact on the wind speed experienced by turbines that increase or decrease power. Additionally, these local turbulent structures induce wake meandering and, given the non-optimal wind directions for the layout, can increase or decrease turbine power production depending on whether they are being waked or not.

5.6 Conclusions

In this study, WRF-LES-GAD is used to understand wind farm impacts from gravity waves observed during the American Wake Experiment (AWAKEN) field campaign. The gravity waves were associated with an atmospheric bore event, which was generated by nocturnal mesoscale convection near the AWAKEN site. A cold pool, which formed as a result of precipitation-induced latent cooling within the mesoscale convective system (MCS), began to spread radially as a density current or bore. A train of solitary waves formed at the front of the bore, interacting with the preexisting stable boundary layer in the study region and ultimately passing through the King Plains wind farm.

To model the bore and its associated gravity waves, we use a 2-domain nested setup in WRF-LES-GAD with grid spacings of 300 m and 20 m. Both domains use an LES closure. The nested grids are forced by the 3 km HRRRv4 model, which best captures the MCS by assimilating NEXRAD data. In this novel setup, the 300 m domain serves as the MCS-resolving grid, while the 20 m domain resolves ambient, small-scale turbulence as well as wake-generated turbulence. The effect of 50 wind turbines representing the eastern half of the King Plains wind farm are included on the 20 m domain using a generalized actuator disk approach.

The bore formation, propagation, and ultimately the structure of the gravity waves traveling through the AWAKEN region was found to be highly sensitive to the microphsyics parameterization, as found in previous work (Johnson et al., 2018). We investigated three different microphysics schemes: the Thompson parameterization (1.5-moment), the WRF 6-class (WDM6) parameterization (double-moment), and the Morrison parameterization (double-moment). Results with the WDM6 parameterization provided results with peaks separated by 5 minutes, which best matched observations from vertically profiling lidars. The WDM6 scheme produces a more realistic bore structure because the rain water mixing ratio profile shows a strong decrease below the cloud base, compared to relatively constant profiles for Thompson and Morrison. The decrease in rain water mixing ratio results in more latent cooling and thus a stronger cold pool and density current. Additionally, the Thompson and Morrison parameterizations result in more snow and less graupel and rain at higher altitudes. These results align with those of Johnson et al. (2018) who hypothesized that the increase in snow hydrometeors results in lower fall velocities in comparison to rain drops and thus less precipitation.

For the 20 m domain, the ambient turbulence was sensitive to the LES closure. Considering that 20 m is relatively coarse for a SBL simulation, resolving ambient turbulence

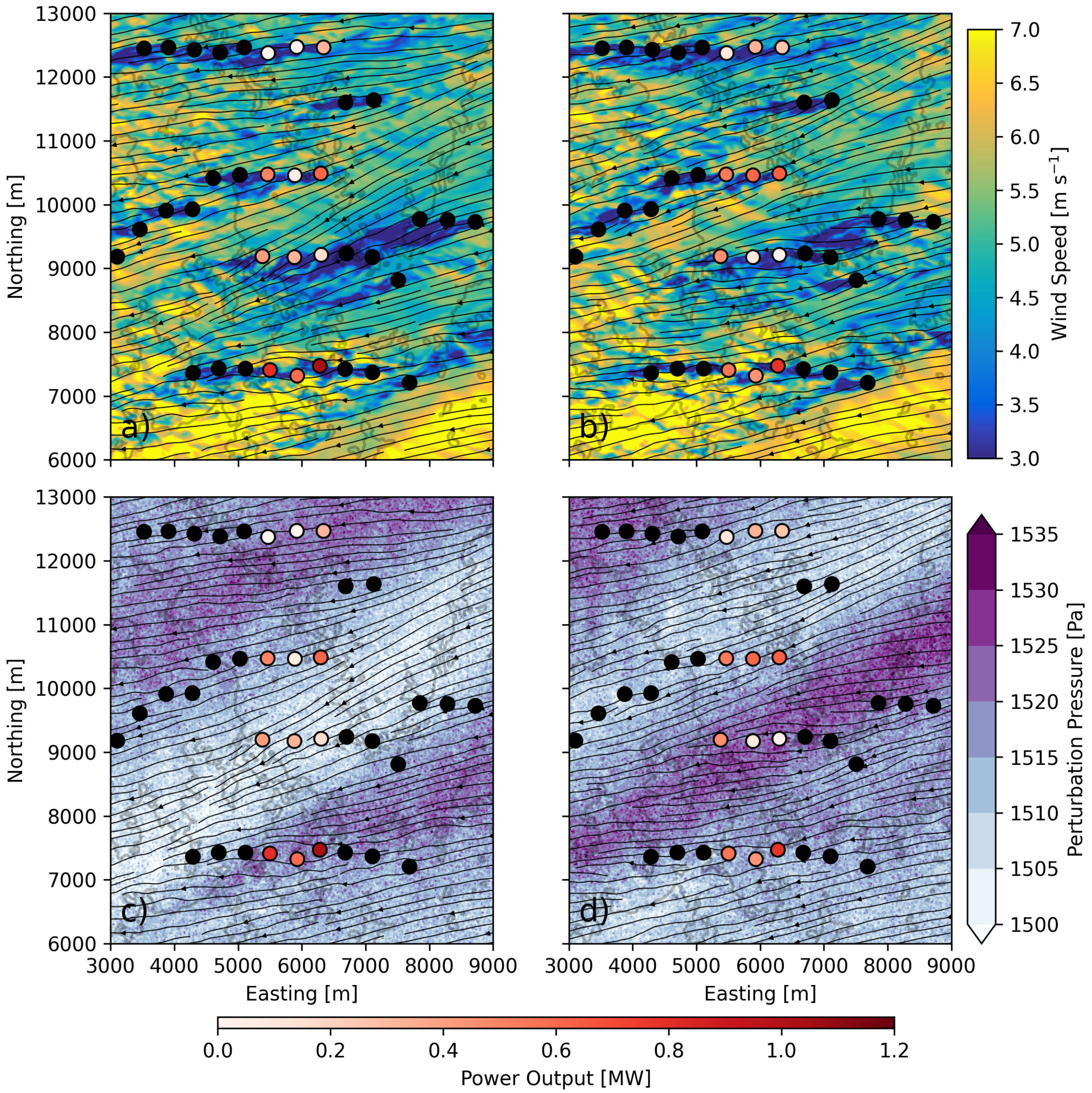

Figure 5.14: Instantaneous plan view of hub-height wind speed and perturbation pressure at (a,c) 06:32:15 UTC and (b,d) 06:34:45 UTC. The streamlines correspond to the hub-height wind speed; however, note that the gravity waves are advecting northward.

is a challenge for conventional closure schemes. While using finer grid resolution would be desirable, considering the large geographic extent of the region, 20 m grid spacing represented a compromise to reduce computational cost while still providing acceptable modeling results. For the given setup and case study, results with dynamic turbulence closures are more effective at capturing small-scale turbulence. This agrees with previous work that has shown that dynamic turbulence closures are more effective in SBL conditions and at coarser grid resolutions compared to conventional closures (Zhou and Chow, 2011; Zhou and Chow, 2012; Zhou and Chow, 2014; Wise et al., 2024).

The bore passage and associated gravity waves generated by the MCS affect both the average power production and the power variability during the study period. Prior to the bore event, the wind turbines experienced an easterly low-level jet, but the passage of the bore and gravity waves modulated the mesoscale environment substantially. After the gravity wave passage, the LLJ is effectively destroyed, with a much weaker jet nose resulting in reduced hub-height wind speeds, as was seen in both observations and modeling results. The LLJ is weakened because the gravity waves increase the SBL height, which is a common characteristic of bore events. As a result, the average power production decreases after the gravity wave passes, by up to 56% depending on the turbine row. During the gravity wave passage, the power variability is increased by over 100% for the most southern row of turbines. More northern rows of turbines less impacted in terms of power variability. The increase in power variability is shown to result from wind direction oscillations associated with the gravity wave passage with wind variability related to wave-induced turbulence also playing a role. The easterly wind direction is suboptimal for the King Plains wind farm since the east-west layout was designed for a predominantly southerly wind direction.

The WRF-LES-GAD modeling setup presented here provides a framework for simulating atmospheric bore and gravity wave effects on a wind farm. This case study shows good agreement between model results and available observations, demonstrating the efficacy of this approach for understanding the interaction between realistic gravity waves and wind farms. Gravity waves are a common feature in the Southern Great Plains, coming from many directions and with various amplitudes and periods. The modeling framework used here is well-suited for other gravity wave case studies from the AWAKEN field campaign. Future work will focus on characterizing the different types of gravity wave events observed during AWAKEN, to better understand their formation mechanisms and their effects on wind farm power production.

Chapter 6

Conclusion

Summary

The work in this dissertation advances high-fidelity large-eddy simulation (LES) for representing complex turbulence phenomena and their interactions with wind turbines. Wind turbines sit close to the Earth's surface in the atmospheric boundary layer (ABL) and thus experience ABL winds, which are highly influenced by local topography and thermal stratification. LES is used to capture the dynamic and turbulent behavior of ABL winds. Lower-fidelity wind turbine simulation methods fail to incorporate topography and struggle to account for dynamic flow behavior. While these lower-fidelity methods capture turbulence in a statistical sense, dynamic turbulent phenomena in the ABL can come from a wide range of physically-driven sources. The multi-scale modeling framework in the Weather Research and Forecasting (WRF) model, because of its ability to capture a broad range of scales, can incorporate larger-scale weather effects all the way down to ambient micro-scale turbulence resolved with LES.

The first study modeled as part of this dissertation was the Perdigão field campaign, which consisted of two parallel ridges with a wind turbine located on the southwest ridge (Chapter 2). The wind turbine wake was found to show strong dependence with atmospheric stability, with the wake deflecting upwards in a convective case study and downwards in stable case study. During the convective case study, flow recirculation occurred, which was observed to occur over 50% of the time when the flow was oriented perpendicular to the ridge. As a result of the recirculation zone, the wake was deflected upwards. During the stable case study, a mountain wave occurred, as was observed on 50% of the nights during the field campaign. The mountain wave forced the wake downwards following the terrain in the lee of the ridge. These findings on the vertical behavior of the wake are notable as the vertical deflection is not adequately accounted for in existing wind turbine wake models.

Next, in Chapter 3, the stable case study from Chapter 2 is investigated in more depth, specifically focusing on turbulence metrics, notably, the turbulent dissipation rate. The spatial structure of turbulence can be difficult to obtain in field campaigns; however, for Perdigão, the turbulent dissipation rate was derived from a scanning lidar in complex terrain for the first time in Wildmann et al. (2019) for this stable case study. Additionally, the turbulence dissipation rate was derived from sonic anemometers, a tethered lifting system, and a profiling lidar, thus providing a wide array of measurements to compare with modeling predictions. The DRM closure was used in an aim to better capture small-scale turbulence characteristics upwind of the major topographic features; further downwind, the differences between the TKE-1.5 and DRM closures was small. Additionally, while both closures predicted the turbulent dissipation rate accurately in the near-surface, the DRM closure showed better agreement higher up in the atmosphere, albeit where uncertainties in the observed turbulence dissipation rates are large. Negative turbulent dissipation rates are predicted by the DRM closure, which represent the backscatter of energy from smaller to large scales. The TKE-1.5 closure cannot predict backscatter due to its formulation as an eddy-viscosity model. While backscatter regions have been observed in other studies (Carper and Porté-Agel, 2004), limitations of the experimental setup and methods used for deriving turbulent dissipation rates at Perdigão meant that negative dissipation rates could not be validated in this case.

Next, the DRM closure is applied with a wind turbine parameterization in a range of idealized SBL conditions (Chapter 4). The range of conditions was designed to include weak SBL conditions where turbulence is continuously produced, as well as strong SBL conditions where turbulence is intermittent. This setup allowed investigation of research questions relevant to the AWAKEN field campaign, which included: (1) wind farm effects on SBL development and (2) intermittent turbulence effects on wind farm performance. The TKE-1.5 closure was unable to resolve turbulence intermittency. The DRM closure, however, captured the intermittency and resolved a greater fraction of turbulence compared to the TKE-1.5 closure in strong SBL conditions. Across all SBL conditions, the wind farm impacted the flow over 30 rotor diameters (2.4 km) downwind with wind speeds reduced and the thermal stratification weakened. Turbulence intermittency had no effect on the mean power production but did increase power variability.

Lastly, a case study of a gravity wave passage is simulated during the AWAKEN field campaign (Chapter 5). The generation mechanism for the gravity waves was a result of a cold pool generated by a nocturnal mesoscale convective system. The outward propagating cold pool formed a density current perturbing the SBL, thus inducing gravity waves. However, notably, the choice of the microphysics scheme, which represents cloud and precipitation processes, had a significant impact on the structure of the gravity waves. The signature of the simulated gravity waves was much stronger in the upper atmosphere compared to closer to the surface and in the wind turbine rotor layer. While the presence of the waves in the hub-height wind speed signal was weak, the waves induced significant local wind direction variation which affected wind farm power production due to waking given the layout of the farm. This study provides a modeling framework for simulating and analyzing gravity wave effects on wind farm performance as a result of nocturnal convection. Notably, this study demonstrates, for the first time, the interaction between observed gravity waves and a wind farm.

Future work

Research avenues

Complex terrain cases are very sensitive to meteorological conditions; therefore, further study is needed to explore the range of turbulent flows in the boundary layer. The convective and stable case studies for the Perdigão field campaign were representative of flow conditions at the site, but mountain waves during SBL conditions can come in a wide variety of forms. The dependence of the wind turbine wake on the Froude number in complex terrain needs further exploration, perhaps following the work of Sauer et al. (2016), but with a wind turbine rotor parameterization. Developing an analytical relationship between the Froude number and vertical wake deflection would be useful as it could be easily implemented into tools used in designing wind farms. Results from the DRM closure can also be analyzed in a wider variety of flow regimes. Chapter 3 demonstrated that there were improvements in the turbulence representation in certain regions when using the DRM closure, but downwind of the most impactful topographic features, the difference between the TKE-1.5 and DRM closures was small. The role of topographically-induced turbulence as the main driver of the type of turbulence can be assessed compared to other conditions where the closure may make more of an impact.

The most important next step for studies involving the AWAKEN field campaign is to systematically classify the various types of wavy turbulent structures that are observed in the region. There are a wide variety of wavy turbulent structures that may or may not impact wind farm performance. The focus in Chapter 5 was on a large-scale buoyancy-driven gravity wave that affected the entire farm; however, smaller-scale shear-driven waves have a more heterogeneous effect (as seen in Appendix D). Shear-driven waves could also potentially occur more frequently compared to buoyancy-driven waves and thus represent a larger impact on wind farm design and operation. While the modeling framework used in this dissertation helped better understand the dynamics of a few types of waves, there is much to be learned about various waves by analyzing the large amounts of data gathered from the AWAKEN site.

The modeling setups used in this dissertation rely on high-performance computing (HPC) and are computationally intensive. Dynamic LES closures aim to extend the ability of the modeling setups without drastically increasing the computational cost. In this work, we took advantage of this increased efficiency by analyzing specific types of turbulent events at the AWAKEN site. Wind farm wakes, the merging of many individual wind turbine wakes within a wind farm into a singular deficit, are another major focus of the AWAKEN field campaign (Moriarty et al., 2024) where dynamic LES closures could be helpful. Wind farm wakes span very large geographic regions and are thus very computationally expensive to simulate realistically with LES. The findings in this dissertation demonstrate the efficacy of dynamic closures at relatively coarse resolutions. Simulating wind farm wakes (by resolving individual wind turbines using generalized actuator disks) with the dynamic closures in canonical conditions and validating modeling results with the data available from AWAKEN, especially the wide-ranging radar data, is a useful next step.

In addition to using dynamic closures to reduce computational cost when simulating large geographic areas, another research direction to pursue are LES codes developed to run native on graphical-processing units (GPUs). The next-generation HPC machines are all being built on GPU architectures, as GPU LES codes are much more computationally efficient compared to conventional methods (Sauer and Muñoz-Esparza, 2020; Almgren et al., 2023). The author's next steps include model development for GPU LES methods with the hope that this suite of tools can be used for real-time forecasting with LES or other applications that demand computational efficiency.

With respect to wind energy applications, coupling of LES model outputs with a wind turbine structural design tool can provide an alternative to the existing methods and standards (International Electrotechnical Commission (IEC), 2019) for designing individual wind turbines. Currently, design standards use synthetic turbulence generators (Mann, 1994; Mann, 1998; Jonkman and Buhl, 2005) that are very computationally efficient to simulate a broad range of environmental conditions that a wind turbine may experience. These synthetic turbulence generators were designed nearly 20 years ago, and only capture basic turbulence statistics. The models struggle to capture more complex statistics, such as coherence, which has been shown to significantly impact wind turbine performance (Kelley et al., 2006; Bachynski and Eliassen, 2018; Robertson et al., 2019; Wise and Bachynski, 2020). As LES becomes increasingly efficient, it can be used to to more realistically account for coherent turbulence (from canonical conditions or specific wavy events, for example) in the wind turbine design process, thus increasing wind turbine reliability.

Practical implications for wind farm design and operation

There are a number of practical implications of this work for future wind farm design and operation. Most importantly, thermal stability and topography should be primary design drivers of siting future wind turbines within a wind farm.

For wind turbines, especially those onshore, thermal stability drives turbulence. This includes both the turbulence a wind turbine will experience (relevant for design and operation) as well as the turbulence that interacts with wind turbine wakes. The work in this dissertation adds to the large body of literature demonstrating that larger eddies in convective conditions increase wake mixing with the ambient environment while the smaller eddies in stable conditions struggle to dissipate wakes with these wakes then persisting for a number of kilometers. Wind farm designers should include atmospheric stability (along with wind speed and wind direction) when determining spacing within wind farms when logistically feasible.

Wind farm design generally accounts for the topographic acceleration or flow speedup over hills and elevated topography to increase the average power output. This dissertation, however, demonstrates that the impacts of terrain and stability on turbulence are intertwined, with wake effects being important even in highly complex terrain. In certain stable conditions, likely depending on the Froude number, wakes can persist for many kilometers even with the presence of terrain-induced turbulence. Additionally, wakes deflect upwards or downwards depending on stability and this is not currently accounted for in wind farm design tools. Even in more simple terrain, such as the U.S. Southern Great Plains, the placement of individual wind turbines is critical to power output.

This body of work goes to show that there is likely not a one-size-fits-all approach to wind farm design and operation. Individual sites have their own characteristics that need to be studied in detail. It is a hope that the findings in this dissertation can be implemented in more computationally efficient approaches that wind farm designers and operators use. We have also demonstrated the importance of conducting site-specific high-resolution simulations to better understand the spatial heterogeneity of flow conditions and turbulence as implementing an array of site-specific measurement devices is impractical and costly.

Bibliography

Aagaard Madsen, H. (1997). "A CFD analysis of the actuator disc flow compared with momentum theory results". English. In: *IEA Joint action. Aerodynamics of wind turbines.* Ed. by B. Maribo Pedersen. 10th IEA Meeting on Aerodynamics, IEA ; Conference date: 16-12-1996 Through 17-12-1996. Technical University of Denmark. Department of Fluid Mechanics, pp. 109–124.

Abkar, Mahdi and Fernando Porté-Agel (Mar. 2015). "Influence of atmospheric stability on wind-turbine wakes: A large-eddy simulation study". In: *Physics of Fluids* 27.3, p. 035104. ISSN: 1070-6631. DOI: `10.1063/1.4913695`. eprint: `https://pubs.aip.org/aip/pof/article-pdf/doi/10.1063/1.4913695/15919392/035104\_1\_online.pdf`. URL: `https://doi.org/10.1063/1.4913695`.

Abkar, Mahdi, Ahmad Sharifi, and Fernando Porté-Agel (Apr. 2016). "Wake flow in a wind farm during a diurnal cycle". en. In: *Journal of Turbulence* 17.4, pp. 420–441. ISSN: 1468-5248. DOI: `10.1080/14685248.2015.1127379`. URL: `http://www.tandfonline.com/doi/full/10.1080/14685248.2015.1127379` (visited on 01/08/2021).

Aitken, Matthew L. et al. (May 2014). "Large eddy simulation of wind turbine wake dynamics in the stable boundary layer using the Weather Research and Forecasting Model". en. In: *Journal of Renewable and Sustainable Energy* 6.3, p. 033137. ISSN: 1941-7012. DOI: `10.1063/1.4885111`. URL: `http://aip.scitation.org/doi/10.1063/1.4885111` (visited on 09/23/2020).

Allaerts, Dries and Johan Meyers (Feb. 2018). "Gravity Waves and Wind-Farm Efficiency in Neutral and Stable Conditions". en. In: *Boundary-Layer Meteorology* 166.2, pp. 269–299. ISSN: 0006-8314, 1573-1472. DOI: `10.1007/s10546-017-0307-5`. URL: `http://link.springer.com/10.1007/s10546-017-0307-5` (visited on 04/29/2024).

Almgren, Ann et al. (July 2023). "ERF: Energy Research and Forecasting". en. In: *Journal of Open Source Software* 8.87, p. 5202. ISSN: 2475-9066. DOI: `10.21105/joss.05202`. URL: `https://joss.theoj.org/papers/10.21105/joss.05202` (visited on 06/11/2024).

Arthur, Robert S. et al. (Feb. 2020). "Multi-Scale Simulation of Wind Farm Performance during a Frontal Passage". en. In: *Atmosphere* 11.3, p. 245. ISSN: 2073-4433. DOI: `10.3390/atmos11030245`. URL: `https://www.mdpi.com/2073-4433/11/3/245` (visited on 09/23/2020).

Bachynski, Erin E. and Lene Eliassen (2018). "The effects of coherent structures on the global response of floating offshore wind turbines". In: *Wind Energy* 0.0, pp. 1–20. DOI:

`10.1002/we.2280`. URL: `https://onlinelibrary.wiley.com/doi/abs/10.1002/we.2280`.

Baines, Peter G (1998). "Topographic effects in stratified flows: Chapter 6 Stratified flow past three-dimensional topography". In: Cambridge University Press, pp. 344–443.

Balsley, Ben B. (Mar. 2008). "The CIRES Tethered Lifting System: a survey of the system, past results and future capabilities". In: *Acta Geophysica* 56.1, pp. 21–57. ISSN: 1895-7455. DOI: `10.2478/s11600-007-0045-z`. URL: `https://doi.org/10.2478/s11600-007-0045-z`.

Banta, Robert M. (Mar. 2008). "Stable-boundary-layer regimes from the perspective of the low-level jet". en. In: *Acta Geophysica* 56.1, pp. 58–87. ISSN: 1895-6572, 1895-7455. DOI: `10.2478/s11600-007-0049-8`. URL: `http://link.springer.com/10.2478/s11600-007-0049-8` (visited on 03/12/2024).

Bardina, J., J.H. Ferziger, and W. Reynolds (1983). *Improved Turbulence Models Based on Large Eddy Simulation of Homgeneous, Imcompressible, Turbulent Flows.* Tech. rep. Stanford University.

Barthelmie, R. J. et al. (2010). "Quantifying the Impact of Wind Turbine Wakes on Power Output at Offshore Wind Farms". In: *Journal of Atmospheric and Oceanic Technology* 27.8, pp. 1302–1317. DOI: `10.1175/2010JTECHA1398.1`. URL: `https://journals.ametsoc.org/view/journals/atot/27/8/2010jtecha1398_1.xml`.

Barthelmie, Rebecca J. and Sara C. Pryor (June 2019). "Automated wind turbine wake characterization in complex terrain". en. In: *Atmospheric Measurement Techniques* 12.6, pp. 3463–3484. ISSN: 1867-8548. DOI: `10.5194/amt-12-3463-2019`. URL: `https://amt.copernicus.org/articles/12/3463/2019/` (visited on 09/23/2020).

Beare, Robert J. et al. (Feb. 2006). "An Intercomparison of Large-Eddy Simulations of the Stable Boundary Layer". In: *Boundary-Layer Meteorology* 118.2, pp. 247–272. ISSN: 1573-1472. DOI: `10.1007/s10546-004-2820-6`. URL: `https://doi.org/10.1007/s10546-004-2820-6`.

Berg, J. et al. (May 2017). "Large-Eddy Simulation of turbine wake in complex terrain". en. In: *Journal of Physics: Conference Series* 854, p. 012003. ISSN: 1742-6588, 1742-6596. DOI: `10.1088/1742-6596/854/1/012003`. URL: `https://iopscience.iop.org/article/10.1088/1742-6596/854/1/012003` (visited on 09/23/2020).

Blaylock, Brian K., John D. Horel, and Erik T. Crosman (2017). "Impact of Lake Breezes on Summer Ozone Concentrations in the Salt Lake Valley". In: *Journal of Applied Meteorology and Climatology* 56.2, pp. 353–370. DOI: `10.1175/JAMC-D-16-0216.1`. URL: `https://journals.ametsoc.org/view/journals/apme/56/2/jamc-d-16-0216.1.xml`.

Bodini, N., J. K. Lundquist, and M. Optis (2020). "Can machine learning improve the model representation of turbulent kinetic energy dissipation rate in the boundary layer for complex terrain?" In: *Geoscientific Model Development* 13.9, pp. 4271–4285. DOI: `10.5194/gmd-13-4271-2020`. URL: `https://gmd.copernicus.org/articles/13/4271/2020/`.

Bodini, Nicola, Julie K. Lundquist, and Rob K. Newsom (July 2018). "Estimation of turbulence dissipation rate and its variability from sonic anemometer and wind Doppler lidar during the XPIA field campaign". en. In: *Atmospheric Measurement Techniques* 11.7, pp. 4291–4308. ISSN: 1867-8548. DOI: `10.5194/amt-11-4291-2018`. URL: `https://amt.copernicus.org/articles/11/4291/2018/` (visited on 05/01/2024).

Bodini, Nicola, Dino Zardi, and Julie K. Lundquist (Aug. 2017). "Three-dimensional structure of wind turbine wakes as measured by scanning lidar". en. In: *Atmospheric Measurement Techniques* 10.8, pp. 2881–2896. ISSN: 1867-8548. DOI: `10.5194/amt-10-2881-2017`. URL: `https://amt.copernicus.org/articles/10/2881/2017/` (visited on 01/08/2021).

Bossard, M, Jan Feranec, J Otahel, et al. (2000). *CORINE land cover technical guide: Addendum 2000*. Tech. rep.

Bougeault, P. and P. Lacarrere (1989). "Parameterization of Orography-Induced Turbulence in a Mesobeta–Scale Model". In: *Monthly Weather Review* 117.8, pp. 1872–1890. DOI: `10.1175/1520-0493(1989)117<1872:POOITI>2.0.CO;2`. URL: `https://journals.ametsoc.org/view/journals/mwre/117/8/1520-0493_1989_117_1872_pooiti_2_0_co_2.xml`.

Bromm, Marc, Lukas Vollmer, and Martin Kühn (2017). "Numerical investigation of wind turbine wake development in directionally sheared inflow". In: *Wind Energy* 20.3, pp. 381–395. DOI: `https://doi.org/10.1002/we.2010`. eprint: `https://onlinelibrary.wiley.com/doi/pdf/10.1002/we.2010`. URL: `https://onlinelibrary.wiley.com/doi/abs/10.1002/we.2010`.

Brown, A. R., J. M. Hobson, and N. Wood (Mar. 2001). "Large-Eddy Simulation Of Neutral Turbulent Flow Over Rough Sinusoidal Ridges". In: *Boundary-Layer Meteorology* 98.3, pp. 411–441. ISSN: 1573-1472. DOI: `10.1023/A:1018703209408`. URL: `https://doi.org/10.1023/A:1018703209408`.

Businger, J. A. et al. (1971). "Flux-Profile Relationships in the Atmospheric Surface Layer". In: *Journal of Atmospheric Sciences* 28.2, pp. 181–189. DOI: `10.1175/1520-0469(1971)028<0181:FPRITA>2.0.CO;2`. URL: `https://journals.ametsoc.org/view/journals/atsc/28/2/1520-0469_1971_028_0181_fprita_2_0_co_2.xml`.

Carper, Matthew and Fernando Porte-Agel (Nov. 2004). "The role of coherent structures in subfilter-scale dissipation of turbulence measured in the atmospheric surface layer". en. In: *Journal of Turbulence* 5, N40. ISSN: 1468-5248. DOI: `10.1088/1468-5248/5/1/040`. URL: `http://www.informaworld.com/openurl?genre=article&doi=10.1088/1468-5248/5/1/040&magic=crossref%7C%7CD404A21C5BB053405B1A640AFFD44AE3` (visited on 05/01/2024).

Carper, Matthew A and Fernando Porté-Agel (2004). "The role of coherent structures in subfilter-scale dissipation of turbulence measured in the atmospheric surface layer". In: *Journal of Turbulence* 5, N40. DOI: `10.1088/1468-5248/5/1/040`.

Champagne, F. H. (1978). "The fine-scale structure of the turbulent velocity field". In: *Journal of Fluid Mechanics* 86.1, pp. 67–108. DOI: `10.1017/S0022112078001019`.

Chen, Bicheng, Tammy Thompson, and Fotini Katopodes Chow (2024). "Hyper-local source strength retrieval and apportionment of black carbon in an urban area". In: *Atmospheric Environment: X* 22, p. 100252. ISSN: 2590-1621. DOI: `https://doi.org/10.1016/j.`

aeaoa.2024.100252. URL: `https://www.sciencedirect.com/science/article/pii/S2590162124000194`.

Chen, Fei and Jimy Dudhia (2001). "Coupling an advanced land surface-hydrology model with the Penn State-NCAR MM5 modeling system. Part I: Model implementation and sensitivity". In: *Monthly Weather Review* 129.4, pp. 569–585.

Chow, Fotini et al. (May 2019). "Crossing Multiple Gray Zones in the Transition from Mesoscale to Microscale Simulation over Complex Terrain". en. In: *Atmosphere* 10.5, p. 274. ISSN: 2073-4433. DOI: `10.3390/atmos10050274`. URL: `https://www.mdpi.com/2073-4433/10/5/274` (visited on 10/14/2020).

Chow, Fotini Katopodes (2004). "Subfilter-scale turbulence modeling for large-eddy simulation of the atmospheric boundary layer over complex terrain". en. Ph.D dissertation. Stanford University.

Chow, Fotini Katopodes et al. (July 2005). "Explicit Filtering and Reconstruction Turbulence Modeling for Large-Eddy Simulation of Neutral Boundary Layer Flow". en. In: *Journal of the Atmospheric Sciences* 62.7, pp. 2058–2077. ISSN: 1520-0469, 0022-4928. DOI: `10.1175/JAS3456.1`. URL: `https://journals.ametsoc.org/doi/10.1175/JAS3456.1` (visited on 04/14/2021).

Churchfield, Matthew J. and Senu Sirnivas (2018). "On the Effects of Wind Turbine Wake Skew Caused by Wind Veer". In: *2018 Wind Energy Symposium*. DOI: `10.2514/6.2018-0755`. eprint: `https://arc.aiaa.org/doi/pdf/10.2514/6.2018-0755`. URL: `https://arc.aiaa.org/doi/abs/10.2514/6.2018-0755`.

Clyne, John et al. (2007). "Interactive desktop analysis of high resolution simulations: application to turbulent plume dynamics and current sheet formation". In: *New Journal of Physics* 9.8, p. 301.

Connolly, Alex et al. (2021). "Efficacy of the Cell Perturbation Method in Large-Eddy Simulations of Boundary Layer Flow over Complex Terrain". In: *Atmosphere* 12.1. ISSN: 2073-4433. DOI: `10.3390/atmos12010055`. URL: `https://www.mdpi.com/2073-4433/12/1/55`.

Cook, David R. (Aug. 2018). "Eddy Correlation Flux Measurement System (ECOR) Instrument Handbook". In: DOI: `10.2172/1467448`. URL: `https://www.osti.gov/biblio/1467448`.

Coulter, R. and J. Doran (Nov. 2002). "Spatial and Temporal Occurrences of Intermittent Turbulence During CASES-99". In: *Boundary layer Meteorology* 105, pp. 329–349. DOI: `10.1023/A:1019993703820`.

Crespo, A. and J. Hernández (June 1996). "Turbulence characteristics in wind-turbine wakes". en. In: *Journal of Wind Engineering and Industrial Aerodynamics* 61.1, pp. 71–85. ISSN: 01676105. DOI: `10.1016/0167-6105(95)00033-X`. URL: `https://linkinghub.elsevier.com/retrieve/pii/016761059500033X` (visited on 05/01/2024).

Dahlberg, J.Å., M. Poppen, and S.E. Thor (1992). "Load/fatigue effects on a wind turbine generator in a wind farm". In: *Journal of Wind Engineering and Industrial Aerodynamics* 39.1, pp. 199–209. ISSN: 0167-6105. DOI: `https://doi.org/10.1016/0167-`

6105(92)90546-M. URL: `http://www.sciencedirect.com/science/article/pii/016761059290546M`.

Daniels, Megan H. et al. (Oct. 2016). "A New Vertical Grid Nesting Capability in the Weather Research and Forecasting (WRF) Model". en. In: *Monthly Weather Review* 144.10, pp. 3725–3747. ISSN: 0027-0644, 1520-0493. DOI: `10.1175/MWR-D-16-0049.1`. URL: `https://journals.ametsoc.org/doi/10.1175/MWR-D-16-0049.1` (visited on 01/08/2021).

Dar, Arslan Salim et al. (Nov. 2019). "On the self-similarity of wind turbine wakes in a complex terrain using large eddy simulation". en. In: *Wind Energy Science* 4.4, pp. 633–644. ISSN: 2366-7451. DOI: `10.5194/wes-4-633-2019`. URL: `https://wes.copernicus.org/articles/4/633/2019/` (visited on 09/23/2020).

Deardorff, James W (1980). "Stratocumulus-capped mixed layers derived from a three-dimensional model". In: *Boundary-Layer Meteorology* 18.4, pp. 495–527.

— (1970). "A numerical study of three-dimensional turbulent channel flow at large Reynolds numbers". In: *Journal of Fluid Mechanics* 41.2, pp. 453–480. DOI: `10.1017/S0022112070000691`.

Debnath, Mithu et al. (May 2022). "Design of the American Wake Experiment (AWAKEN) field campaign". en. In: *Journal of Physics: Conference Series* 2265.2, p. 022058. ISSN: 1742-6588, 1742-6596. DOI: `10.1088/1742-6596/2265/2/022058`. URL: `https://iopscience.iop.org/article/10.1088/1742-6596/2265/2/022058` (visited on 04/29/2024).

Debnath, Mithu et al. (June 2023). "Characterization of wind speed and directional shear at the AWAKEN field campaign site". In: *Journal of Renewable and Sustainable Energy* 15.3, p. 033308. ISSN: 1941-7012. DOI: `10.1063/5.0139737`. eprint: `https://pubs.aip.org/aip/jrse/article-pdf/doi/10.1063/5.0139737/18007552/033308\_1\_5.0139737.pdf`. URL: `https://doi.org/10.1063/5.0139737`.

Devesse, K. et al. (2022). "Including realistic upper atmospheres in a wind-farm gravity-wave model". In: *Wind Energy Science* 7.4, pp. 1367–1382. DOI: `10.5194/wes-7-1367-2022`. URL: `https://wes.copernicus.org/articles/7/1367/2022/`.

Dowell, David C. et al. (2022). "The High-Resolution Rapid Refresh (HRRR): An Hourly Updating Convection-Allowing Forecast Model. Part I: Motivation and System Description". In: *Weather and Forecasting* 37.8, pp. 1371–1395. DOI: `10.1175/WAF-D-21-0151.1`. URL: `https://journals.ametsoc.org/view/journals/wefo/37/8/WAF-D-21-0151.1.xml`.

Draxl, C. et al. (2021). "Mountain waves can impact wind power generation". In: *Wind Energy Science* 6.1, pp. 45–60. DOI: `10.5194/wes-6-45-2021`. URL: `https://wes.copernicus.org/articles/6/45/2021/`.

Dudhia, Jimy (1989). "Numerical study of convection observed during the winter monsoon experiment using a mesoscale two-dimensional model". In: *Journal of the Atmospheric Sciences* 46.20, pp. 3077–3107.

Durran, Dale, Jonathan A Weyn, and Maximo Q Menchaca (2017). "Practical considerations for computing dimensional spectra from gridded data". In: *Monthly Weather Review* 145.9, pp. 3901–3910.

Englberger, Antonia and Andreas Dörnbrack (June 2018). “Wind-turbine wakes responding to stably stratified flow over complex terrain”. en. In: *Journal of Physics: Conference Series* 1037, p. 072014. ISSN: 1742-6588, 1742-6596. DOI: `10.1088/1742-6596/1037/7/072014`. URL: `https://iopscience.iop.org/article/10.1088/1742-6596/1037/7/072014` (visited on 01/08/2021).

Englberger, Antonia and Julie K Lundquist (2020). “How does inflow veer affect the veer of a wind-turbine wake?” en. In: *Journal of Physics* 1452, p. 012068. DOI: `doi:10.1088/1742-6596/1452/1/012068`. URL: `https://iopscience.iop.org/article/10.1088/1742-6596/1452/1/012068/pdf`.

Fairall, C. W. et al. (1990). “Inertial-Dissipation Air-Sea Flux Measurements: A Prototype System Using Realtime Spectral Computations”. In: *Journal of Atmospheric and Oceanic Technology* 7.3, pp. 425–453. DOI: `10.1175/1520-0426(1990)007<0425:IDASFM>2.0.CO;2`. URL: `https://journals.ametsoc.org/view/journals/atot/7/3/1520-0426_1990_007_0425_idasfm_2_0_co_2.xml`.

Farr, Tom G et al. (2007). “The shuttle radar topography mission”. In: *Reviews of Geophysics* 45.2.

Feng, Zhe et al. (2019). “Spatiotemporal Characteristics and Large-Scale Environments of Mesoscale Convective Systems East of the Rocky Mountains”. In: *Journal of Climate* 32.21, pp. 7303–7328. DOI: `10.1175/JCLI-D-19-0137.1`. URL: `https://journals.ametsoc.org/view/journals/clim/32/21/jcli-d-19-0137.1.xml`.

Fernando, H. J. S. et al. (May 2019). “The Perdigão: Peering into Microscale Details of Mountain Winds”. en. In: *Bulletin of the American Meteorological Society* 100.5, pp. 799–819. ISSN: 0003-0007, 1520-0477. DOI: `10.1175/BAMS-D-17-0227.1`. URL: `https://journals.ametsoc.org/bams/article/100/5/799/344800/The-Perdig%C3%A3o-Peering-into-Microscale-Details-of` (visited on 09/23/2020).

Fitch, Anna C., Joseph B. Olson, and Julie K. Lundquist (2013). “Parameterization of Wind Farms in Climate Models”. In: *Journal of Climate* 26.17, pp. 6439–6458. DOI: `10.1175/JCLI-D-12-00376.1`. URL: `https://journals.ametsoc.org/view/journals/clim/26/17/jcli-d-12-00376.1.xml`.

Frandsen, S. and C.J. Christensen (1994). “Structural loads in large wind farm arrays”. English. In: European Wind Energy Conference and Exhibition, EWEC ’94. Conference date: 09-10-1994 Through 13-10-1994.

Frandsen, Sten and Kenneth Thomsen (1997). “Change in Fatigue and Extreme Loading when Moving Wind Farms Offshore”. In: *Wind Engineering* 21.3, pp. 197–214. ISSN: 0309524X, 2048402X. URL: `http://www.jstor.org/stable/43749643`.

Frehlich, Rod, Yannick Meillier, and Michael L. Jensen (2008). “Measurements of Boundary Layer Profiles with In Situ Sensors and Doppler Lidar”. In: *Journal of Atmospheric and Oceanic Technology* 25.8, pp. 1328–1340. DOI: `10.1175/2007JTECHA963.1`. URL: `https://journals.ametsoc.org/view/journals/atot/25/8/2007jtecha963_1.xml`.

Gadde, Srinidhi N. and Richard J. A. M. Stevens (Jan. 2021a). “Effect of low-level jet height on wind farm performance”. en. In: *Journal of Renewable and Sustainable Energy* 13.1,

p. 013305. ISSN: 1941-7012. DOI: `10.1063/5.0026232`. URL: `https://aip.scitation.org/doi/10.1063/5.0026232` (visited on 01/17/2023).

Gadde, Srinidhi N. and Richard J. A. M. Stevens (Jan. 2021b). “Interaction between low-level jets and wind farms in a stable atmospheric boundary layer”. en. In: *Physical Review Fluids* 6.1, p. 014603. ISSN: 2469-990X. DOI: `10.1103/PhysRevFluids.6.014603`. URL: `https://link.aps.org/doi/10.1103/PhysRevFluids.6.014603` (visited on 01/17/2023).

Geerts, Bart et al. (Apr. 2017). “The 2015 Plains Elevated Convection at Night Field Project”. en. In: *Bulletin of the American Meteorological Society* 98.4, pp. 767–786. ISSN: 0003-0007, 1520-0477. DOI: `10.1175/BAMS-D-15-00257.1`. URL: `https://journals.ametsoc.org/doi/10.1175/BAMS-D-15-00257.1` (visited on 03/12/2024).

Germano, Massimo et al. (July 1991). “A dynamic subgrid-scale eddy viscosity model”. In: *Physics of Fluids A: Fluid Dynamics* 3.7, pp. 1760–1765. ISSN: 0899-8213. DOI: `10.1063/1.857955`. eprint: `https://pubs.aip.org/aip/pof/article-pdf/3/7/1760/12459782/1760\_1\_online.pdf`. URL: `https://doi.org/10.1063/1.857955`.

Glauert, H. (1963). “Aerodynamic Theory”. In: *Aerodynamic Theory.* Ed. by W. F. Durand. Springer, New York, 1935.

Haghi, Kevin R. and Dale R. Durran (Jan. 2021). “On the Dynamics of Atmospheric Bores”. en. In: *Journal of the Atmospheric Sciences* 78.1, pp. 313–327. ISSN: 0022-4928, 1520-0469. DOI: `10.1175/JAS-D-20-0181.1`. URL: `https://journals.ametsoc.org/view/journals/atsc/78/1/jas-d-20-0181.1.xml` (visited on 03/12/2024).

Haghi, Kevin R., David B. Parsons, and Alan Shapiro (Oct. 2017). “Bores Observed during IHOP_2002: The Relationship of Bores to the Nocturnal Environment”. en. In: *Monthly Weather Review* 145.10, pp. 3929–3946. ISSN: 0027-0644, 1520-0493. DOI: `10.1175/MWR-D-16-0415.1`. URL: `https://journals.ametsoc.org/doi/10.1175/MWR-D-16-0415.1` (visited on 03/12/2024).

Haghi, Kevin R. et al. (June 2019). “Bore-ing into Nocturnal Convection”. en. In: *Bulletin of the American Meteorological Society* 100.6, pp. 1103–1121. ISSN: 0003-0007, 1520-0477. DOI: `10.1175/BAMS-D-17-0250.1`. URL: `https://journals.ametsoc.org/view/journals/bams/100/6/bams-d-17-0250.1.xml` (visited on 03/12/2024).

Han, Bin et al. (2019). “Cloud-Resolving Model Intercomparison of an MC3E Squall Line Case: Part II. Stratiform Precipitation Properties”. In: *Journal of Geophysical Research: Atmospheres* 124.2, pp. 1090–1117. DOI: `https://doi.org/10.1029/2018JD029596`. eprint: `https://agupubs.onlinelibrary.wiley.com/doi/pdf/10.1029/2018JD029596`. URL: `https://agupubs.onlinelibrary.wiley.com/doi/abs/10.1029/2018JD029596`.

Haupt, Sue Ellen et al. (Dec. 2019). “On Bridging A Modeling Scale Gap: Mesoscale to Microscale Coupling for Wind Energy”. en. In: *Bulletin of the American Meteorological Society* 100.12, pp. 2533–2550. ISSN: 0003-0007, 1520-0477. DOI: `10.1175/BAMS-D-18-0033.1`. URL: `https://journals.ametsoc.org/bams/article/100/12/2533/344473/On-Bridging-A-Modeling-Scale-Gap-Mesoscale-to` (visited on 10/14/2020).

Hersbach, Hans et al. (2020). “The ERA5 global reanalysis”. In: *Quarterly Journal of the Royal Meteorological Society* 146.730, pp. 1999–2049. DOI: `https://doi.org/10.1002/qj.3803`. eprint: `https://rmets.onlinelibrary.wiley.com/doi/pdf/10.1002/qj.3803`. URL: `https://rmets.onlinelibrary.wiley.com/doi/abs/10.1002/qj.3803`.

Hirth, Brian and John Schroeder (Jan. 2013). “Documenting Wind Speed and Power Deficits behind a Utility-Scale Wind Turbine”. In: *Journal of Applied Meteorology and Climatology* 52, pp. 39–46. DOI: `10.1175/JAMC-D-12-0145.1`.

Hong, Song-You, Yign Noh, and Jimy Dudhia (2006). “A New Vertical Diffusion Package with an Explicit Treatment of Entrainment Processes”. In: *Monthly Weather Review* 134.9, pp. 2318–2341. DOI: `10.1175/MWR3199.1`. URL: `https://journals.ametsoc.org/view/journals/mwre/134/9/mwr3199.1.xml`.

Honnert, Rachel et al. (2020). “The Atmospheric Boundary Layer and the “Gray Zone” of Turbulence: A Critical Review”. In: *Journal of Geophysical Research: Atmospheres* 125.13. e2019JD030317 10.1029/2019JD030317, e2019JD030317. DOI: `https://doi.org/10.1029/2019JD030317`. eprint: `https://agupubs.onlinelibrary.wiley.com/doi/pdf/10.1029/2019JD030317`. URL: `https://agupubs.onlinelibrary.wiley.com/doi/abs/10.1029/2019JD030317`.

Houze Jr., Robert A. (2004). “Mesoscale convective systems”. In: *Reviews of Geophysics* 42.4. DOI: `https://doi.org/10.1029/2004RG000150`. eprint: `https://agupubs.onlinelibrary.wiley.com/doi/pdf/10.1029/2004RG000150`. URL: `https://agupubs.onlinelibrary.wiley.com/doi/abs/10.1029/2004RG000150`.

International Electrotechnical Commission (IEC) (2019). *Wind turbines: Part 1: Design Requirements*. Tech. rep. IEC61400-1.

Jackson, Peter L, Georg Mayr, and Simon Vosper (2013). “Mountain weather research and forecasting - recent progress and current challenges: Chapter 3 Dynamically-Driven Winds”. In: New York: Springer, pp. 121–218. ISBN: 978-94-007-4097-6.

Janjić, Zaviša I (1994). “The step-mountain eta coordinate model: Further developments of the convection, viscous sublayer, and turbulence closure schemes”. In: *Monthly Weather Review* 122.5, pp. 927–945.

Jiménez, M. A. and J. Cuxart (May 2005). “Large-Eddy Simulations of the Stable Boundary Layer Using the Standard Kolmogorov Theory: Range of Applicability”. en. In: *Boundary-Layer Meteorology* 115.2, pp. 241–261. ISSN: 0006-8314, 1573-1472. DOI: `10.1007/s10546-004-3470-4`. URL: `http://link.springer.com/10.1007/s10546-004-3470-4` (visited on 01/18/2023).

Johnson, Aaron and Xuguang Wang (Feb. 2017). “Design and Implementation of a GSI-Based Convection-Allowing Ensemble Data Assimilation and Forecast System for the PECAN Field Experiment. Part I: Optimal Configurations for Nocturnal Convection Prediction Using Retrospective Cases”. en. In: *Weather and Forecasting* 32.1, pp. 289–315. ISSN: 0882-8156, 1520-0434. DOI: `10.1175/WAF-D-16-0102.1`. URL: `https://journals.ametsoc.org/doi/10.1175/WAF-D-16-0102.1` (visited on 03/12/2024).

— (May 2019). “Multicase Assessment of the Impacts of Horizontal and Vertical Grid Spacing, and Turbulence Closure Model, on Subkilometer-Scale Simulations of Atmospheric

Bores during PECAN". en. In: *Monthly Weather Review* 147.5, pp. 1533–1555. ISSN: 0027-0644, 1520-0493. DOI: `10.1175/MWR-D-18-0322.1`. URL: `http://journals.ametsoc.org/doi/10.1175/MWR-D-18-0322.1` (visited on 03/12/2024).

Johnson, Aaron, Xuguang Wang, and Samuel Degelia (June 2017). "Design and Implementation of a GSI-Based Convection-Allowing Ensemble-Based Data Assimilation and Forecast System for the PECAN Field Experiment. Part II: Overview and Evaluation of a Real-Time System". en. In: *Weather and Forecasting* 32.3, pp. 1227–1251. ISSN: 0882-8156, 1520-0434. DOI: `10.1175/WAF-D-16-0201.1`. URL: `https://journals.ametsoc.org/doi/10.1175/WAF-D-16-0201.1` (visited on 04/29/2024).

Johnson, Aaron et al. (Sept. 2018). "Evaluation of Forecasts of a Convectively Generated Bore Using an Intensively Observed Case Study from PECAN". en. In: *Monthly Weather Review* 146.9, pp. 3097–3122. ISSN: 0027-0644, 1520-0493. DOI: `10.1175/MWR-D-18-0059.1`. URL: `http://journals.ametsoc.org/doi/10.1175/MWR-D-18-0059.1` (visited on 03/12/2024).

Jonkman, B J and M L Buhl (2005). "TurbSim User's Guide". en. In: *Technical Report*, p. 18.

Kaimal, J C and J J Finnigan (Mar. 1994). "Atmospheric Boundary Layer Flows: Their Structure and Measurement". In: Oxford University Press. ISBN: 9780195062397. DOI: `10.1093/oso/9780195062397.001.0001`. URL: `https://doi.org/10.1093/oso/9780195062397.001.0001`.

Kelley, Neil, B. Jonkman, and G. Scott (Jan. 2006). "Great Plains Turbulence Environment: Its Origins, Impact, and Simulation". In.

Kirkil, Gokhan et al. (Jan. 2012). "Implementation and Evaluation of Dynamic Subfilter-Scale Stress Models for Large-Eddy Simulation Using WRF*". en. In: *Monthly Weather Review* 140.1, pp. 266–284. ISSN: 0027-0644, 1520-0493. DOI: `10.1175/MWR-D-11-00037.1`. URL: `http://journals.ametsoc.org/doi/10.1175/MWR-D-11-00037.1` (visited on 04/14/2021).

Knupp, Kevin (Aug. 2006). "Observational Analysis of a Gust Front to Bore to Solitary Wave Transition within an Evolving Nocturnal Boundary Layer". en. In: *Journal of the Atmospheric Sciences* 63.8, pp. 2016–2035. ISSN: 1520-0469, 0022-4928. DOI: `10.1175/JAS3731.1`. URL: `https://journals.ametsoc.org/doi/10.1175/JAS3731.1` (visited on 03/12/2024).

Kolmogorov, A. N. (1941). "The Local Structure of Turbulence in Incompressible Viscous Fluid for Very Large Reynolds' Numbers". In: *Dokl. Akad. Nauk SSSR*. Vol. 30, pp. 301–305.

Kosović, Branko (1997). "Subgrid-scale modelling for the large-eddy simulation of high-Reynolds-number boundary layers". In: *Journal of Fluid Mechanics* 336, pp. 151–182. DOI: `10.1017/S0022112096004697`.

Krishnamurthy, R. et al. (2024). "Observations of wind farm wake recovery at an operating wind farm". In: *Wind Energy Science Discussions* 2024, pp. 1–37. DOI: `10.5194/wes-2024-29`. URL: `https://wes.copernicus.org/preprints/wes-2024-29/`.

Krishnamurthy, Raghavendra et al. (Jan. 2021). “Boundary Layer Climatology at ARM Southern Great Plains”. In: DOI: `10.2172/1779279`. URL: `https://www.osti.gov/biblio/1779279`.

Laan, M. P. van der and N. N. Sørensen (2017). “Why the Coriolis force turns a wind farm wake clockwise in the Northern Hemisphere”. In: *Wind Energy Science* 2.1, pp. 285–294. DOI: `10.5194/wes-2-285-2017`. URL: `https://wes.copernicus.org/articles/2/285/2017/`.

Lanzilao, Luca and Johan Meyers (May 2022). “Effects of self-induced gravity waves on finite wind-farm operations using a large-eddy simulation framework”. en. In: *Journal of Physics: Conference Series* 2265.2, p. 022043. ISSN: 1742-6588, 1742-6596. DOI: `10.1088/1742-6596/2265/2/022043`. URL: `https://iopscience.iop.org/article/10.1088/1742-6596/2265/2/022043` (visited on 05/04/2024).

Lilly, D. K. (1992). “A proposed modification of the Germano subgrid-scale closure method”. In: *Physics of Fluids A: Fluid Dynamics* 4.3, pp. 633–635. DOI: `10.1063/1.858280`.

Lim, Kyo-Sun Sunny and Song-You Hong (2010). “Development of an Effective Double-Moment Cloud Microphysics Scheme with Prognostic Cloud Condensation Nuclei (CCN) for Weather and Climate Models”. In: *Monthly Weather Review* 138.5, pp. 1587–1612. DOI: `10.1175/2009MWR2968.1`. URL: `https://journals.ametsoc.org/view/journals/mwre/138/5/2009mwr2968.1.xml`.

Lissaman, P. B. S. (Nov. 1979). “Energy Effectiveness of Arbitrary Arrays of Wind Turbines”. en. In: *Journal of Energy* 3.6, pp. 323–328. ISSN: 0146-0412, 1555-5917. DOI: `10.2514/3.62441`. URL: `http://arc.aiaa.org/doi/10.2514/3.62441` (visited on 07/19/2019).

Lu, Hao and Fernando Porté-Agel (June 2011). “Large-eddy simulation of a very large wind farm in a stable atmospheric boundary layer”. en. In: *Physics of Fluids* 23.6, p. 065101. ISSN: 1070-6631, 1089-7666. DOI: `10.1063/1.3589857`. URL: `https://pubs.aip.org/pof/article/23/6/065101/838842/Large-eddy-simulation-of-a-very-large-wind-farm-in` (visited on 03/12/2024).

Lundquist, J. K. and L. Bariteau (Feb. 2015). “Dissipation of Turbulence in the Wake of a Wind Turbine”. In: *Boundary-Layer Meteorology* 154.2, pp. 229–241. ISSN: 1573-1472. DOI: `10.1007/s10546-014-9978-3`. URL: `https://doi.org/10.1007/s10546-014-9978-3`.

Lundquist, J. K. et al. (Feb. 2015). “Quantifying error of lidar and sodar Doppler beam swinging measurements of wind turbine wakes using computational fluid dynamics”. In: *Atmos. Meas. Tech.* 8.2, pp. 907–920. ISSN: 1867-8548. DOI: `10.5194/amt-8-907-2015`. URL: `https://www.atmos-meas-tech.net/8/907/2015/`.

Lundquist, J. K. et al. (Jan. 2019). “Costs and consequences of wind turbine wake effects arising from uncoordinated wind energy development”. en. In: *Nature Energy* 4.1, pp. 26–34. ISSN: 2058-7546. DOI: `10.1038/s41560-018-0281-2`. URL: `http://www.nature.com/articles/s41560-018-0281-2` (visited on 03/05/2019).

Lundquist, Julie K. (2003). “Intermittent and Elliptical Inertial Oscillations in the Atmospheric Boundary Layer”. In: *Journal of the Atmospheric Sciences* 60.21, pp. 2661–2673. DOI: `10.1175/1520-0469(2003)060<2661:IAEIOI>2.0.CO;2`. URL: `https:`

//journals.ametsoc.org/view/journals/atsc/60/21/1520-0469_2003_060_2661_iaeioi_2.0.co_2.xml.

Magnusson, Mikael and Ann-Sofi Smedman (1994). "Influence of Atmospheric Stability on Wind Turbine Wakes". In: *Wind Engineering* 18.3, pp. 139–152. ISSN: 0309524X, 2048402X. URL: http://www.jstor.org/stable/43749538 (visited on 05/03/2024).

Mahrt, L. (Mar. 1999). "Stratified Atmospheric Boundary Layers". In: *Boundary-Layer Meteorology* 90.3, pp. 375–396. ISSN: 1573-1472. DOI: 10.1023/A:1001765727956. URL: https://doi.org/10.1023/A:1001765727956.

— (2014). "Stably Stratified Atmospheric Boundary Layers". In: *Annual Review of Fluid Mechanics* 46.Volume 46, 2014, pp. 23–45. ISSN: 1545-4479. DOI: https://doi.org/10.1146/annurev-fluid-010313-141354. URL: https://www.annualreviews.org/content/journals/10.1146/annurev-fluid-010313-141354.

Mann, J (1998). "Wind field simulation". In: *Probabilistic Engineering Mechanics* 13.4, pp. 269–282.

Mann, Jakob (1994). "The spatial structure of neutral atmospheric surface-layer turbulence". In: *Journal of fluid mechanics* 273, pp. 141–168.

Marjanovic, Nikola et al. (Nov. 2017). "Implementation of a generalized actuator line model for wind turbine parameterization in the Weather Research and Forecasting model". en. In: *Journal of Renewable and Sustainable Energy* 9.6, p. 063308. ISSN: 1941-7012. DOI: 10.1063/1.4989443. URL: http://aip.scitation.org/doi/10.1063/1.4989443 (visited on 09/23/2020).

Markowski, Paul and Yvette Richardson (2010). "Mesoscale Convective Systems". In: *Mesoscale Meteorology in Midlatitudes*. John Wiley Sons, Ltd. Chap. 9, pp. 245–272. ISBN: 9780470682104. DOI: https://doi.org/10.1002/9780470682104.ch9. eprint: https://onlinelibrary.wiley.com/doi/pdf/10.1002/9780470682104.ch9. URL: https://onlinelibrary.wiley.com/doi/abs/10.1002/9780470682104.ch9.

Mason, P. J. and D. J. Thomson (1992). "Stochastic backscatter in large-eddy simulations of boundary layers". In: *Journal of Fluid Mechanics* 242, pp. 51–78. DOI: 10.1017/S0022112092002271.

Mazzaro, L. J. et al. (2017). "Nested mesoscale-to-LES modeling of the atmospheric boundary layer in the presence of under-resolved convective structures". In: *Journal of Advances in Modeling Earth Systems* 9.4, pp. 1795–1810. DOI: https://doi.org/10.1002/2017MS000912. eprint: https://agupubs.onlinelibrary.wiley.com/doi/pdf/10.1002/2017MS000912. URL: https://agupubs.onlinelibrary.wiley.com/doi/abs/10.1002/2017MS000912.

Menke, Robert et al. (Oct. 2018). "Does the wind turbine wake follow the topography? A multi-lidar study in complex terrain". en. In: *Wind Energy Science* 3.2, pp. 681–691. ISSN: 2366-7451. DOI: 10.5194/wes-3-681-2018. URL: https://wes.copernicus.org/articles/3/681/2018/ (visited on 09/23/2020).

Menke, Robert et al. (Mar. 2019). "Characterization of flow recirculation zones at the Perdigão site using multi-lidar measurements". en. In: *Atmospheric Chemistry and*

Physics 19.4, pp. 2713–2723. ISSN: 1680-7324. DOI: `10.5194/acp-19-2713-2019`. URL: `https://acp.copernicus.org/articles/19/2713/2019/` (visited on 09/23/2020).

Menke, Robert et al. (Aug. 2020). “Multi-lidar wind resource mapping in complex terrain”. en. In: *Wind Energy Science* 5.3, pp. 1059–1073. ISSN: 2366-7451. DOI: `10.5194/wes-5-1059-2020`. URL: `https://wes.copernicus.org/articles/5/1059/2020/` (visited on 10/18/2020).

Mikkelsen, R (2003). “Actuator disk methods applied to wind turbines”. PhD thesis. Technical University of Denmark.

Mirocha, J. D. et al. (Jan. 2014a). “Implementation of a generalized actuator disk wind turbine model into the weather research and forecasting model for large-eddy simulation applications”. en. In: *Journal of Renewable and Sustainable Energy* 6.1, p. 013104. ISSN: 1941-7012. DOI: `10.1063/1.4861061`. URL: `http://aip.scitation.org/doi/10.1063/1.4861061` (visited on 09/23/2020).

Mirocha, Jeff, Branko Kosović, and Gokhan Kirkil (Feb. 2014b). “Resolved Turbulence Characteristics in Large-Eddy Simulations Nested within Mesoscale Simulations Using the Weather Research and Forecasting Model”. en. In: *Monthly Weather Review* 142.2, pp. 806–831. ISSN: 0027-0644, 1520-0493. DOI: `10.1175/MWR-D-13-00064.1`. URL: `http://journals.ametsoc.org/doi/10.1175/MWR-D-13-00064.1` (visited on 01/18/2023).

Mirocha, Jeffrey D. et al. (July 2015). “Investigating wind turbine impacts on near-wake flow using profiling lidar data and large-eddy simulations with an actuator disk model”. en. In: *Journal of Renewable and Sustainable Energy* 7.4, p. 043143. ISSN: 1941-7012. DOI: `10.1063/1.4928873`. URL: `http://aip.scitation.org/doi/10.1063/1.4928873` (visited on 09/23/2020).

Mlawer, Eli J et al. (1997). “Radiative transfer for inhomogeneous atmospheres: RRTM, a validated correlated-k model for the longwave”. In: *Journal of Geophysical Research: Atmospheres* 102.D14, pp. 16663–16682.

Monin, Andrei Sergeevich and Alexander Mikhailovich Obukhov (1954). “Basic laws of turbulent mixing in the surface layer of the atmosphere”. In: *Contrib. Geophys. Inst. Acad. Sci. USSR* 151.163, e187.

Moriarty, Patrick et al. (May 2020). *American WAKE experimeNt (AWAKEN)*. en. Tech. rep. NREL/TP-5000-75789, 1659798, MainId:5894, NREL/TP–5000–75789, 1659798, MainId:5894. DOI: `10.2172/1659798`. URL: `https://www.osti.gov/servlets/purl/1659798/` (visited on 01/17/2023).

Moriarty et al. (2024). “Design of Wind Turbine Models for the American WAKE ExperimeNt (AWAKEN)”. en. In: *accepted for publication in Journal of Renewable and Sustainable Energy.*

Morrison, H., G. Thompson, and V. Tatarskii (2009). “Impact of Cloud Microphysics on the Development of Trailing Stratiform Precipitation in a Simulated Squall Line: Comparison of One- and Two-Moment Schemes”. In: *Monthly Weather Review* 137.3, pp. 991–1007. DOI: `10.1175/2008MWR2556.1`. URL: `https://journals.ametsoc.org/view/journals/mwre/137/3/2008mwr2556.1.xml`.

Morrison, Hugh et al. (2020). "Confronting the Challenge of Modeling Cloud and Precipitation Microphysics". In: *Journal of Advances in Modeling Earth Systems* 12.8. e2019MS001689 2019MS001689, e2019MS001689. DOI: `https://doi.org/10.1029/2019MS001689`. eprint: `https://agupubs.onlinelibrary.wiley.com/doi/pdf/10.1029/2019MS001689`. URL: `https://agupubs.onlinelibrary.wiley.com/doi/abs/10.1029/2019MS001689`.

Muller, Caroline and Sophie Abramian (May 2023). "The cloud dynamics of convective storm systems". In: *Physics Today* 76.5, pp. 28–28. ISSN: 0031-9228. DOI: `10.1063/PT.3.5234`. eprint: `https://pubs.aip.org/physicstoday/article-pdf/76/5/28/17242588/28\_1\_pt.3.5234.pdf`.

Muñoz-Esparza, D et al. (2015). "A stochastic perturbation method to generate inflow turbulence in large-eddy simulation models: Application to neutrally stratified atmospheric boundary layers". In: *Physics of Fluids* 27.3, p. 035102.

Muñoz-Esparza, Domingo and Branko Kosović (June 2018). "Generation of Inflow Turbulence in Large-Eddy Simulations of Nonneutral Atmospheric Boundary Layers with the Cell Perturbation Method". en. In: *Monthly Weather Review* 146.6, pp. 1889–1909. ISSN: 0027-0644, 1520-0493. DOI: `10.1175/MWR-D-18-0077.1`. URL: `http://journals.ametsoc.org/doi/10.1175/MWR-D-18-0077.1` (visited on 11/29/2018).

Muñoz-Esparza, Domingo et al. (2014). "Bridging the transition from mesoscale to microscale turbulence in numerical weather prediction models". In: *Boundary-Layer Meteorology* 153.3, pp. 409–440.

Muñoz-Esparza, Domingo et al. (2017). "Coupled mesoscale-LES modeling of a diurnal cycle during the CWEX-13 field campaign: From weather to boundary-layer eddies". In: *Journal of Advances in Modeling Earth Systems* 9.3, pp. 1572–1594. DOI: `https://doi.org/10.1002/2017MS000960`. eprint: `https://agupubs.onlinelibrary.wiley.com/doi/pdf/10.1002/2017MS000960`. URL: `https://agupubs.onlinelibrary.wiley.com/doi/abs/10.1002/2017MS000960`.

Nakanishi, Mikio and Hiroshi Niino (2006). "An improved Mellor–Yamada level-3 model: Its numerical stability and application to a regional prediction of advection fog". In: *Boundary-Layer Meteorology* 119.2, pp. 397–407.

— (2009). "Development of an Improved Turbulence Closure Model for the Atmospheric Boundary Layer". In: *Journal of the Meteorological Society of Japan. Ser. II* 87.5, pp. 895–912. DOI: `10.2151/jmsj.87.895`.

National Centers for Environmental Prediction (2015). *NCEP GFS 0.25 Degree Global Forecast Grids Historical Archive*. Boulder CO. URL: `https://doi.org/10.5065/D65D8PWK`.

Newsom, RK and Raglavendra Krishnamurthy (Dec. 2022). "Doppler Lidar (DL) Instrument Handbook". In: DOI: `10.2172/1034640`. URL: `https://www.osti.gov/biblio/1034640`.

Newsom, Rob K. and Robert M. Banta (2003). "Shear-Flow Instability in the Stable Nocturnal Boundary Layer as Observed by Doppler Lidar during CASES-99". In: *Journal of the Atmospheric Sciences* 60.1, pp. 16–33. DOI: `10.1175/1520-0469(2003)060<0016:SFIITS>2.0.CO;2`. URL: `https://journals.ametsoc.org/view/journals/atsc/60/1/1520-0469_2003_060_0016_sfiits_2.0.co_2.xml`.

Oncley, Steven P. et al. (1996). “Surface-Layer Fluxes, Profiles, and Turbulence Measurements over Uniform Terrain under Near-Neutral Conditions”. In: *Journal of Atmospheric Sciences* 53.7, pp. 1029–1044. DOI: `10.1175/1520-0469(1996)053<1029:SLFPAT>2.0.CO;2`. URL: `https://journals.ametsoc.org/view/journals/atsc/53/7/1520-0469_1996_053_1029_slfpat_2_0_co_2.xml`.

Palma, José M. L. M. et al. (Mar. 2020). *The digital terrain model in the computational modelling of the flow over the Perdigão site: the appropriate grid size*. en. preprint. Wind and turbulence. DOI: `10.5194/wes-2019-96`. URL: `https://wes.copernicus.org/preprints/wes-2019-96/` (visited on 10/14/2020).

Pandey, Apoorva et al. (2023). “Sensitivity of Deep Convection and Cross-Tropopause Water Transport to Microphysical Parameterizations in WRF”. In: *Journal of Geophysical Research: Atmospheres* 128.14. e2022JD037053 2022JD037053, e2022JD037053. DOI: `https://doi.org/10.1029/2022JD037053`. eprint: `https://agupubs.onlinelibrary.wiley.com/doi/pdf/10.1029/2022JD037053`. URL: `https://agupubs.onlinelibrary.wiley.com/doi/abs/10.1029/2022JD037053`.

Peña, A., B. Kosović, and J. D. Mirocha (2021). “Evaluation of idealized large-eddy simulations performed with the Weather Research and Forecasting model using turbulence measurements from a 250 m meteorological mast”. In: *Wind Energy Science* 6.3, pp. 645–661. DOI: `10.5194/wes-6-645-2021`. URL: `https://wes.copernicus.org/articles/6/645/2021/`.

Pineda, N et al. (2004). “Using NOAA AVHRR and SPOT VGT data to estimate surface parameters: application to a mesoscale meteorological model”. In: *International Journal of Remote Sensing* 25.1, pp. 129–143.

Porté-Agel, Fernando, Majid Bastankhah, and Sina Shamsoddin (Jan. 2020). “Wind-Turbine and Wind-Farm Flows: A Review”. en. In: *Boundary-Layer Meteorology* 174.1, pp. 1–59. ISSN: 0006-8314, 1573-1472. DOI: `10.1007/s10546-019-00473-0`. URL: `http://link.springer.com/10.1007/s10546-019-00473-0` (visited on 10/18/2020).

Porté-Agel, Fernando et al. (Apr. 2011). “Large-eddy simulation of atmospheric boundary layer flow through wind turbines and wind farms”. en. In: *Journal of Wind Engineering and Industrial Aerodynamics* 99.4, pp. 154–168. ISSN: 01676105. DOI: `10.1016/j.jweia.2011.01.011`. URL: `https://linkinghub.elsevier.com/retrieve/pii/S0167610511000134` (visited on 01/08/2021).

Poulos, Gregory S. et al. (Apr. 2002). “CASES-99: A Comprehensive Investigation of the Stable Nocturnal Boundary Layer”. en. In: *Bulletin of the American Meteorological Society* 83.4, pp. 555–581. ISSN: 0003-0007, 1520-0477. DOI: `10.1175/1520-0477(2002)083<0555:CACIOT>2.3.CO;2`. URL: `http://journals.ametsoc.org/doi/10.1175/1520-0477(2002)083%3C0555:CACIOT%3E2.3.CO;2` (visited on 01/17/2023).

Powers, Jordan G. et al. (2017). “The Weather Research and Forecasting Model: Overview, System Efforts, and Future Directions”. In: *Bulletin of the American Meteorological Society* 98.8, pp. 1717–1737. DOI: `10.1175/BAMS-D-15-00308.1`. URL: `https://journals.ametsoc.org/view/journals/bams/98/8/bams-d-15-00308.1.xml`.

Quon, E. et al. (2024). "Design of Wind Turbine Models for the American WAKE ExperimeNt (AWAKEN)". en. In: *Submitted to Journal of Renewable and Sustainable Energy.*

Rivera-Arreba, Irene et al. (2022). "Effects of atmospheric stability on the structural response of a 12 MW semisubmersible floating wind turbine". In: *Wind Energy* 25.11, pp. 1917–1937. DOI: `https://doi.org/10.1002/we.2775`. eprint: `https://onlinelibrary.wiley.com/doi/pdf/10.1002/we.2775`. URL: `https://onlinelibrary.wiley.com/doi/abs/10.1002/we.2775`.

Rivera-Arreba, Irene et al. (2023). "Effect of atmospheric stability on the dynamic wake meandering model applied to two 12 MW floating wind turbines". In: *Wind Energy* 26.12, pp. 1235–1253. DOI: `https://doi.org/10.1002/we.2867`. eprint: `https://onlinelibrary.wiley.com/doi/pdf/10.1002/we.2867`. URL: `https://onlinelibrary.wiley.com/doi/abs/10.1002/we.2867`.

Robertson, A. N. et al. (2019). "Sensitivity analysis of the effect of wind characteristics and turbine properties on wind turbine loads". In: *Wind Energy Science* 4.3, pp. 479–513. DOI: `10.5194/wes-4-479-2019`. URL: `https://wes.copernicus.org/articles/4/479/2019/`.

Robey, R. and J. K. Lundquist (2024). "Influences of lidar scanning parameters on wind turbine wake retrievals in complex terrain". In: *Wind Energy Science Discussions* 2024, pp. 1–27. DOI: `10.5194/wes-2024-18`. URL: `https://wes.copernicus.org/preprints/wes-2024-18/`.

Rogers, E. et al. (2001). *National Oceanic and Atmospheric Administration Changes to the NCEP Meso Eta Analysis and Forecast System: Increase in resolution, new cloud microphysics, modified precipitation assimilation, modified 3DVAR analysis.* Tech. rep. NOAA).

Rottman, James W. and John E. Simpson (July 1989). "The formation of internal bores in the atmosphere: A laboratory model". en. In: *Quarterly Journal of the Royal Meteorological Society* 115.488, pp. 941–963. ISSN: 0035-9009, 1477-870X. DOI: `10.1002/qj.49711548809`. URL: `https://rmets.onlinelibrary.wiley.com/doi/10.1002/qj.49711548809` (visited on 03/12/2024).

Sanchez Gomez, M. et al. (2021). "Turbulence dissipation rate estimated from lidar observations during the LAPSE-RATE field campaign". In: *Earth System Science Data* 13.7, pp. 3539–3549. DOI: `10.5194/essd-13-3539-2021`. URL: `https://essd.copernicus.org/articles/13/3539/2021/`.

Sanchez Gomez, M. et al. (2023). "Investigating the physical mechanisms that modify wind plant blockage in stable boundary layers". In: *Wind Energy Science* 8.7, pp. 1049–1069. DOI: `10.5194/wes-8-1049-2023`. URL: `https://wes.copernicus.org/articles/8/1049/2023/`.

Sanchez Gomez, Miguel et al. (Nov. 2022). "Can lidars assess wind plant blockage in simple terrain? A WRF-LES study". In: *Journal of Renewable and Sustainable Energy* 14.6, p. 063303. ISSN: 1941-7012. DOI: `10.1063/5.0103668`. URL: `https://doi.org/10.1063/5.0103668`.

Sarlak, H., C. Meneveau, and J.N. Sørensen (May 2015). “Role of subgrid-scale modeling in large eddy simulation of wind turbine wake interactions”. en. In: *Renewable Energy* 77, pp. 386–399. ISSN: 09601481. DOI: `10.1016/j.renene.2014.12.036`. URL: `https://linkinghub.elsevier.com/retrieve/pii/S0960148114008635` (visited on 05/01/2024).

Sathe, A. et al. (2013). “Influence of atmospheric stability on wind turbineloads”. In: *Wind Energy* 16.7, pp. 1013–1032. ISSN: 1099-1824. DOI: `10.1002/we.1528`. URL: `http://dx.doi.org/10.1002/we.1528`.

Sathe, A. et al. (2015). “A six-beam method to measure turbulence statistics using ground-based wind lidars”. In: *Atmospheric Measurement Techniques* 8.2, pp. 729–740. DOI: `10.5194/amt-8-729-2015`. URL: `https://amt.copernicus.org/articles/8/729/2015/`.

Sauer, Jeremy A. and Domingo Muñoz-Esparza (2020). “The FastEddy® Resident-GPU Accelerated Large-Eddy Simulation Framework: Model Formulation, Dynamical-Core Validation and Performance Benchmarks”. In: *Journal of Advances in Modeling Earth Systems* 12.11. e2020MS002100 10.1029/2020MS002100, e2020MS002100. DOI: `https://doi.org/10.1029/2020MS002100`. eprint: `https://agupubs.onlinelibrary.wiley.com/doi/pdf/10.1029/2020MS002100`. URL: `https://agupubs.onlinelibrary.wiley.com/doi/abs/10.1029/2020MS002100`.

Sauer, Jeremy A. et al. (2016). “A Large-Eddy Simulation Study of Atmospheric Boundary Layer Influence on Stratified Flows over Terrain”. In: *Journal of the Atmospheric Sciences* 73.7, pp. 2615–2632. DOI: `10.1175/JAS-D-15-0282.1`. URL: `https://journals.ametsoc.org/view/journals/atsc/73/7/jas-d-15-0282.1.xml`.

Schroeder, John, Brian Hirth, and Jerry Guynes (Mar. 2017). “Final Technical Report: The Incubation of Next-Generation Radar Technologies to Lower the Cost of Wind Energy”. In: DOI: `10.2172/1364776`. URL: `https://www.osti.gov/biblio/1364776`.

Shin, Hyeyum Hailey and Song-You Hong (2015). “Representation of the Subgrid-Scale Turbulent Transport in Convective Boundary Layers at Gray-Zone Resolutions”. In: *Monthly Weather Review* 143.1, pp. 250–271. DOI: `10.1175/MWR-D-14-00116.1`. URL: `https://journals.ametsoc.org/view/journals/mwre/143/1/mwr-d-14-00116.1.xml`.

Sim, Chungwook, Lance Manuel, and Sukanta Basu (2010). “A Comparison of Wind Turbine Load Statistics for Inflow Turbulence Fields Based on Conventional Spectral Methods and Large Eddy Simulation”. In: *48th AIAA Aerospace Sciences Meeting Including the New Horizons Forum and Aerospace Exposition*. DOI: `10.2514/6.2010-829`. eprint: `https://arc.aiaa.org/doi/pdf/10.2514/6.2010-829`. URL: `https://arc.aiaa.org/doi/abs/10.2514/6.2010-829`.

Simpson, J.E. (1997). *Gravity Currents in the Environment and the Laboratory*. Cambridge University Press, p. 244.

Sisterson, D. L. and P. Frenzen (1978). “Nocturnal boundary-layer wind maxima and the problem of wind power assessment.” In: *Environmental Science & Technology* 12.2, pp. 218–221. DOI: `10.1021/es60138a014`.

Skamarock, William C (2004). “Evaluating mesoscale NWP models using kinetic energy spectra”. In: *Monthly weather review* 132.12, pp. 3019–3032.

Skamarock, William C et al. (2008). *A description of the advanced research WRF version 3*. Tech. rep. NCAR.

Skamarock, William C et al. (2021). "A Description of the Advanced Research WRF Model Version 4". en. In.

Smagorinsky, J. (1963). "GENERAL CIRCULATION EXPERIMENTS WITH THE PRIMITIVE EQUATIONS: I. THE BASIC EXPERIMENT". In: *Monthly Weather Review* 91.3, pp. 99–164. DOI: `10.1175/1520-0493(1963)091<0099:GCEWTP>2.3.CO;2`. URL: `https://journals.ametsoc.org/view/journals/mwre/91/3/1520-0493_1963_091_0099_gcewtp_2_3_co_2.xml`.

Smalikho, I. N. et al. (Nov. 2013). "Lidar Investigation of Atmosphere Effect on a Wind Turbine Wake". en. In: *Journal of Atmospheric and Oceanic Technology* 30.11, pp. 2554–2570. ISSN: 0739-0572, 1520-0426. DOI: `10.1175/JTECH-D-12-00108.1`. URL: `http://journals.ametsoc.org/doi/10.1175/JTECH-D-12-00108.1` (visited on 05/01/2024).

Sørensen, J. N., W. Z. Shen, and X. Munduate (1998). "Analysis of wake states by a full-field actuator disc model". In: *Wind Energy* 1.2, pp. 73–88. DOI: `https://doi.org/10.1002/(SICI)1099-1824(199812)1:2<73::AID-WE12>3.0.CO;2-L`. eprint: `https://onlinelibrary.wiley.com/doi/pdf/10.1002/%28SICI%291099-1824%28199812%291%3A2%3C73%3A%3AAID-WE12%3E3.0.CO%3B2-L`. URL: `https://onlinelibrary.wiley.com/doi/abs/10.1002/%28SICI%291099-1824%28199812%291%3A2%3C73%3A%3AAID-WE12%3E3.0.CO%3B2-L`.

Sørensen, Jens Nørkær and Robert Flemming Mikkelsen (2001). "On the validity of the blade element momentum theory". English. In: *Proceedings of the 2001 European Wind Energy Conference and Exhibition*. 2001 European Wind Energy Conference and Exhibition (EWEC '01), EWEC'01 ; Conference date: 02-07-2001 Through 07-07-2001. WIP - Renewable Energies. URL: `http://www.ewea.org/index.php?id=146`.

Stevens, Richard J.A.M. and Charles Meneveau (2017). "Flow Structure and Turbulence in Wind Farms". In: *Annual Review of Fluid Mechanics* 49.1, pp. 311–339. DOI: `10.1146/annurev-fluid-010816-060206`. eprint: `https://doi.org/10.1146/annurev-fluid-010816-060206`. URL: `https://doi.org/10.1146/annurev-fluid-010816-060206`.

Stipa, S. et al. (2024). "An LES Model for Wind Farm-Induced Atmospheric Gravity Wave Effects Inside Conventionally Neutral Boundary Layers". In: *Wind Energy Science Discussions* 2024, pp. 1–22. DOI: `10.5194/wes-2023-171`. URL: `https://wes.copernicus.org/preprints/wes-2023-171/`.

Stoll, Rob et al. (Dec. 2020). "Large-Eddy Simulation of the Atmospheric Boundary Layer". In: *Boundary-Layer Meteorology* 177.2, pp. 541–581. ISSN: 1573-1472. DOI: `10.1007/s10546-020-00556-3`. URL: `https://doi.org/10.1007/s10546-020-00556-3`.

Stolz, S., N. A. Adams, and L. Kleiser (2001). "The approximate deconvolution model for large-eddy simulations of compressible flows and its application to shock-turbulent-boundary-layer interaction". In: *Physics of Fluids* 13.10, pp. 2985–3001. DOI: `10.1063/1.1397277`. eprint: `https://doi.org/10.1063/1.1397277`. URL: `https://doi.org/10.1063/1.1397277`.

Stull, Roland B (1988). *An introduction to boundary layer meteorology.* Springer Science & Business Media.

— (2005). *Meteorology For Scientists And Engineers.* Brooks/Cole.

— (2017). *Practical Meteorology: An Algebra-based Survey of Atmospheric Science.*

Sullivan, P. et al. (Feb. 2003). "Structure of Subfilter-Scale Fluxes in the Atmospheric Surface Layer with Application to Large-Eddy Simulation Modelling". In: *Journal of Fluid Mechanics* 482. DOI: `10.1017/S0022112003004099`.

Sun, Jielun et al. (Nov. 2002). "Intermittent Turbulence Associated with a Density Current Passage in the Stable Boundary Layer". In: *Boundary-Layer Meteorology* 105.2, pp. 199–219. ISSN: 1573-1472. DOI: `10.1023/A:1019969131774`. URL: `https://doi.org/10.1023/A:1019969131774`.

Sun, Jielun et al. (2015). "Review of wave-turbulence interactions in the stable atmospheric boundary layer". In: *Reviews of Geophysics* 53.3, pp. 956–993. DOI: `https://doi.org/10.1002/2015RG000487`. eprint: `https://agupubs.onlinelibrary.wiley.com/doi/pdf/10.1002/2015RG000487`. URL: `https://agupubs.onlinelibrary.wiley.com/doi/abs/10.1002/2015RG000487`.

Tatsuya Seiki, Woosub Roh and Masaki Satoh (2022). "Cloud Microphysics in Global Cloud Resolving Models". In: *Atmosphere-Ocean* 60.3-4, pp. 477–505. DOI: `10.1080/07055900.2022.2075310`.

Taylor, G J (Jan. 1990). *Wake measurements on the Nibe wind turbines in Denmark.* Tech. rep. CEC Contract EN3W.0039.UK(H1).

Thompson, Gregory et al. (2008). "Explicit Forecasts of Winter Precipitation Using an Improved Bulk Microphysics Scheme. Part II: Implementation of a New Snow Parameterization". In: *Monthly Weather Review* 136.12, pp. 5095–5115. DOI: `10.1175/2008MWR2387.1`. URL: `https://journals.ametsoc.org/view/journals/mwre/136/12/2008mwr2387.1.xml`.

Thomsen, Kenneth and Poul Sørensen (Mar. 1999). "Fatigue loads for wind turbines operating in wakes". en. In: *Journal of Wind Engineering and Industrial Aerodynamics* 80.1-2, pp. 121–136. ISSN: 01676105. DOI: `10.1016/S0167-6105(98)00194-9`. URL: `https://linkinghub.elsevier.com/retrieve/pii/S0167610598001949` (visited on 07/19/2019).

Tomaszewski, J. M. and J. K. Lundquist (2021). "Observations and simulations of a wind farm modifying a thunderstorm outflow boundary". In: *Wind Energy Science* 6.1, pp. 1–13. DOI: `10.5194/wes-6-1-2021`. URL: `https://wes.copernicus.org/articles/6/1/2021/`.

Toms, Benjamin A. et al. (2017). "Analysis of a Lower-Tropospheric Gravity Wave Train Using Direct and Remote Sensing Measurement Systems". In: *Monthly Weather Review* 145.7, pp. 2791–2812. DOI: `10.1175/MWR-D-16-0216.1`. URL: `https://journals.ametsoc.org/view/journals/mwre/145/7/mwr-d-16-0216.1.xml`.

U.S. Energy Information Administration (2022). *Levelized Costs of New Generation Resources in the Annual Energy Outlook 2022.* en. Tech. rep. U.S. Energy Information Administration, p. 26.

U.S. Energy Information Administration (June 2023). *Oklahoma State Energy Profile*. Tech. rep. Washington, D.C. URL: `https://www.eia.gov/state/print.php?sid=OK` (visited on 04/29/2024).

— (Feb. 2024). *What is U.S. electricity generation by energy source?* Tech. rep. Washington, D.C. URL: `https://www.eia.gov/tools/faqs/faq.php?id=427&t=3` (visited on 04/29/2024).

Vanderwende, Brian J. et al. (June 2015). "Observing and Simulating the Summertime Low-Level Jet in Central Iowa". en. In: *Monthly Weather Review* 143.6, pp. 2319–2336. ISSN: 0027-0644, 1520-0493. DOI: `10.1175/MWR-D-14-00325.1`. URL: `http://journals.ametsoc.org/doi/10.1175/MWR-D-14-00325.1` (visited on 03/14/2024).

Vanderwende, Brian J. et al. (2016). "Simulating effects of a wind-turbine array using LES and RANS". In: *Journal of Advances in Modeling Earth Systems* 8.3, pp. 1376–1390. DOI: `https://doi.org/10.1002/2016MS000652`. eprint: `https://agupubs.onlinelibrary.wiley.com/doi/pdf/10.1002/2016MS000652`. URL: `https://agupubs.onlinelibrary.wiley.com/doi/abs/10.1002/2016MS000652`.

Veers, Paul et al. (2019). "Grand challenges in the science of wind energy". In: *Science* 366.6464, eaau2027. DOI: `10.1126/science.aau2027`. eprint: `https://www.science.org/doi/pdf/10.1126/science.aau2027`. URL: `https://www.science.org/doi/abs/10.1126/science.aau2027`.

Wagner, Johannes et al. (Jan. 2019a). "Long-term simulation of the boundary layer flow over the double-ridge site during the Perdigão 2017 field campaign". en. In: *Atmospheric Chemistry and Physics* 19.2, pp. 1129–1146. ISSN: 1680-7324. DOI: `10.5194/acp-19-1129-2019`. URL: `https://acp.copernicus.org/articles/19/1129/2019/` (visited on 10/14/2020).

Wagner, Timothy J., Petra M. Klein, and David D. Turner (2019b). "A New Generation of Ground-Based Mobile Platforms for Active and Passive Profiling of the Boundary Layer". In: *Bulletin of the American Meteorological Society* 100.1, pp. 137–153. DOI: `10.1175/BAMS-D-17-0165.1`. URL: `https://journals.ametsoc.org/view/journals/bams/100/1/bams-d-17-0165.1.xml`.

Weckwerth, Tammy M. and Ulrike Romatschke (2019). "Where, When, and Why Did It Rain during PECAN?" In: *Monthly Weather Review* 147.10, pp. 3557–3573. DOI: `10.1175/MWR-D-18-0458.1`. URL: `https://journals.ametsoc.org/view/journals/mwre/147/10/mwr-d-18-0458.1.xml`.

Weckwerth, Tammy M. et al. (2019). "Nocturnal Convection Initiation during PECAN 2015". In: *Bulletin of the American Meteorological Society* 100.11, pp. 2223–2239. DOI: `10.1175/BAMS-D-18-0299.1`. URL: `https://journals.ametsoc.org/view/journals/bams/100/11/bams-d-18-0299.1.xml`.

Welch, Peter (1967). "The use of fast Fourier transform for the estimation of power spectra: a method based on time averaging over short, modified periodograms". In: *IEEE Transactions on audio and electroacoustics* 15.2, pp. 70–73. DOI: `10.1109/TAU.1967.1161901`.

Wendels, W.H.M. (Aug. 2019). "Investigation of a nested large eddy simulation of the atmospheric boundary layer over the Perdigão field campaign site". PhD thesis. University of Twente.

Wiersema, David J. et al. (2022). "Evaluation of Turbulence and Dispersion in Multiscale Atmospheric Simulations over Complex Urban Terrain during the Joint Urban 2003 Field Campaign". In: *Monthly Weather Review* 150.12, pp. 3195–3209. DOI: `10.1175/MWR-D-22-0056.1`. URL: `https://journals.ametsoc.org/view/journals/mwre/150/12/MWR-D-22-0056.1.xml`.

Wildmann, Norman, Stephan Kigle, and Thomas Gerz (June 2018). "Coplanar lidar measurement of a single wind energy converter wake in distinct atmospheric stability regimes at the Perdigão 2017 experiment". en. In: *Journal of Physics: Conference Series* 1037, p. 052006. ISSN: 1742-6588, 1742-6596. DOI: `10.1088/1742-6596/1037/5/052006`. URL: `https://iopscience.iop.org/article/10.1088/1742-6596/1037/5/052006` (visited on 09/23/2020).

Wildmann, Norman et al. (Dec. 2019). "Estimation of turbulence dissipation rate from Doppler wind lidars and in situ instrumentation for the Perdigão 2017 campaign". en. In: *Atmospheric Measurement Techniques* 12.12, pp. 6401–6423. ISSN: 1867-8548. DOI: `10.5194/amt-12-6401-2019`. URL: `https://amt.copernicus.org/articles/12/6401/2019/` (visited on 09/23/2020).

Wise, A. S. et al. (2022). "Meso- to microscale modeling of atmospheric stability effects on wind turbine wake behavior in complex terrain". In: *Wind Energy Science* 7.1, pp. 367–386. DOI: `10.5194/wes-7-367-2022`. URL: `https://wes.copernicus.org/articles/7/367/2022/`.

Wise, A. S. et al. (2024). "Two-way interactions between wind turbines and atmospheric turbulence under weak to strong stability conditions". en. In: *Submitted to Journal of Renewable and Sustainable Energy*.

Wise, Adam S. and Erin E. Bachynski (2020). "Wake meandering effects on floating wind turbines". In: *Wind Energy* 23.5, pp. 1266–1285. DOI: `https://doi.org/10.1002/we.2485`. eprint: `https://onlinelibrary.wiley.com/doi/pdf/10.1002/we.2485`. URL: `https://onlinelibrary.wiley.com/doi/abs/10.1002/we.2485`.

Wise, Adam S. et al. (2020). "Multi-Scale Modeling of a Wind Turbine Wake Over Complex Terrain in Different Atmospheric Stability Regimes". In: *19th Conference of Mountain Meteorology*. `https://ams.confex.com/ams/19Mountain/meetingapp.cgi/Session/54552`, p. 8.2.

Wong, V. C. and D. K. Lilly (Feb. 1994). "A comparison of two dynamic subgrid closure methods for turbulent thermal convection". en. In: *Physics of Fluids* 6.2, pp. 1016–1023. ISSN: 1070-6631, 1089-7666. DOI: `10.1063/1.868335`. URL: `http://aip.scitation.org/doi/10.1063/1.868335` (visited on 04/28/2022).

Wu, Yu-Ting and Fernando Porté-Agel (Mar. 2011). "Large-Eddy Simulation of Wind-Turbine Wakes: Evaluation of Turbine Parametrisations". In: *Boundary-Layer Meteorology* 138.3, pp. 345–366. ISSN: 1573-1472. DOI: `10.1007/s10546-010-9569-x`. URL: `https://doi.org/10.1007/s10546-010-9569-x`.

Wyngaard, John C (2004). “Toward numerical modeling in the ”Terra Incognita””. In: *Journal of the Atmospheric Sciences* 61.14, pp. 1816–1826.

Xia, Geng et al. (2021). “Validating simulated mountain wave impacts on hub-height wind speed using SoDAR observations”. In: *Renewable Energy* 163, pp. 2220–2230. ISSN: 0960-1481. DOI: `https://doi.org/10.1016/j.renene.2020.10.127`. URL: `https://www.sciencedirect.com/science/article/pii/S0960148120316992`.

Zang, Yuqi, Robert Street, and Jeffrey Koseff (Dec. 1993). “A Dynamic Mixed Subgrid-Scale Model and Its Application to Turbulent Recirculating Flows”. In: *Physics of Fluids A: Fluid Dynamics* 5, p. 3186. DOI: `10.1063/1.858675`.

Zhang, Xu et al. (2018). “A Three-Dimensional Scale-Adaptive Turbulent Kinetic Energy Scheme in the WRF-ARW Model”. In: *Monthly Weather Review* 146.7, pp. 2023–2045. DOI: `10.1175/MWR-D-17-0356.1`. URL: `https://journals.ametsoc.org/view/journals/mwre/146/7/mwr-d-17-0356.1.xml`.

Zhou, Bowen and Fotini Katopodes Chow (Sept. 2011). “Large-Eddy Simulation of the Stable Boundary Layer with Explicit Filtering and Reconstruction Turbulence Modeling”. en. In: *Journal of the Atmospheric Sciences* 68.9, pp. 2142–2155. ISSN: 0022-4928, 1520-0469. DOI: `10.1175/2011JAS3693.1`. URL: `https://journals.ametsoc.org/doi/10.1175/2011JAS3693.1` (visited on 01/17/2023).

— (Mar. 2012). “Turbulence Modeling for the Stable Atmospheric Boundary Layer and Implications for Wind Energy”. In: *Flow, Turbulence and Combustion* 88.1, pp. 255–277. ISSN: 1573-1987. DOI: `10.1007/s10494-011-9359-7`. URL: `https://doi.org/10.1007/s10494-011-9359-7`.

— (2014). “Nested Large-Eddy Simulations of the Intermittently Turbulent Stable Atmospheric Boundary Layer over Real Terrain”. In: *Journal of the Atmospheric Sciences* 71.3, pp. 1021–1039. DOI: `10.1175/JAS-D-13-0168.1`. URL: `https://journals.ametsoc.org/view/journals/atsc/71/3/jas-d-13-0168.1.xml`.

Appendix A

Perdigão: Sensitivity of model results to grid resolution

Nested WRF-LES-GAD simulations provide increasingly detailed flow predictions according to the resolution of both the terrain and land-use data, and the ability to resolve turbulent flow structures. Further, nesting from 6750 m to 10 m resolution allows the finest 10 m grid to represent the turbine using the generalized actuator disk model and still be influenced by mesoscale forcing from the larger domains. This appendix quantifies some of the differences between results on different grid nesting levels.

The power spectral density of the 80 m wind speed signals shown in Fig. A.1(a) illustrate that higher-frequency turbulence is captured as the grid resolution increases. The spectra are computed using Welch's method Welch, 1967. The spectra from the measurements at SW_TSE04 roughly follow an inertial subrange slope of -5/3 following Kolmogorov, 1941. The spectra for d05 also have an inertial subrange slope of -5/3 and similar energy content to the measurements. Domains d04 and d03 contain a drop-off in the wind speed spectra as is typical of models with finite-difference discretization schemes. The effective resolution for WRF is $\approx 7\Delta x$ Skamarock, 2004. For wind speeds in the range of 6-8 m s^{-1}, the grid cut-off frequency at the effective resolution is 0.1 Hz, 0.02 Hz, and 0.007 Hz for d05, d04, and d03, respectively. Therefore, only d05 can resolve small-scale features like those observed at SW_TSE04 and that affect wind turbine wake dissipation.

Figure A.1(b) shows the 80 m wind speed for d05 (Δx = 10 m), d04 (Δx = 50 m), and d03 (Δx = 150 m) as well as the measurements at SW_TSE04 with error metrics in Table A.1. The bias and RMSE values for all three domains are similar indicating that there is no significant reduction in mean wind speed errors at this particular location when nesting to finer grid resolution. The errors are driven more by the background flow, which will not change very much between the domains.

In addition to the smaller-scale turbulence resolved on d05, steeper terrain slopes are also resolved on d05 compared to domains d04 and d03. This directly affects whether the flow recirculates in the lee of the first ridge as illustrated in Fig. A.2, which shows 1 h time-averaged transects of wind speeds across the wind turbine rotor plane (note that the turbine is

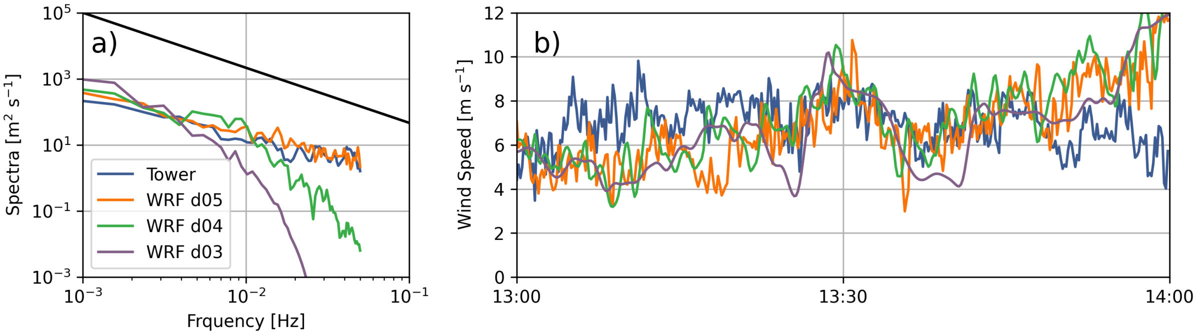

Figure A.1: Comparison of (a) time-series and (b) spectra between SW_TSE04 tower data and WRF-LES-GAD d05 ($\Delta x = 10$ m), d04 ($\Delta x = 50$ m) and d03 ($\Delta x = 150$ m) for 80 m wind speed at SW_TSE04 for the convective case study. The -5/3 inertial subrange power law is provided in black for reference. Note that the model wind speed is output at 10 s intervals; therefore, the highest resolvable frequency with this time-series is 0.05 Hz.

Table A.1: 80 m wind speed bias and RMSE between WRF-LES-GAD on domains d03, d04, and d05 and SW_TSE04 tower measurements for the convective case study from 13:00 - 14:00 UTC.

	80 m Wind Speed (m s^{-1})	
Domain	Bias	RMSE
WRF d05 (Δx =10 m)	-0.20	2.17
WRF d04 (Δx =50 m)	0.20	2.28
WRF d03 (Δx =150 m)	-0.33	2.20

only parameterized on d05). While the recirculation zone is resolved on d05 (Fig. A.2(a)), the gentler resolved slopes d04 and d03 do not induce recirculation on those domains (Fig. A.2(b and c)). Recall that lidar observations in Fig. 2.9 showed recirculation in the lee of the first ridge. Put together, the effects of increased grid resolution and terrain resolution on d05 provide more accurate representation of the observed flow features including the turbine wake.

Figure A.3 shows wind speed and energy spectra for the stable case study. It is clear in Figure A.3(b) that d03 and d04 show wind speeds much smoother than those observed by the tower. The finest domain, d05, is able to capture some fine-scale turbulent variability in the first and last parts of the 2-hr time period, but not in between. We see this in the spectra in Figure A.3(a), where high-frequency turbulence is underestimated in the model compared to the meteorological tower. The energy is shifted to lower-frequencies, thus overestimating the energy content at larger scales compared to the observations. Note that overall the energy content is lower for the stable compared to the convective case. This, in part, explains why

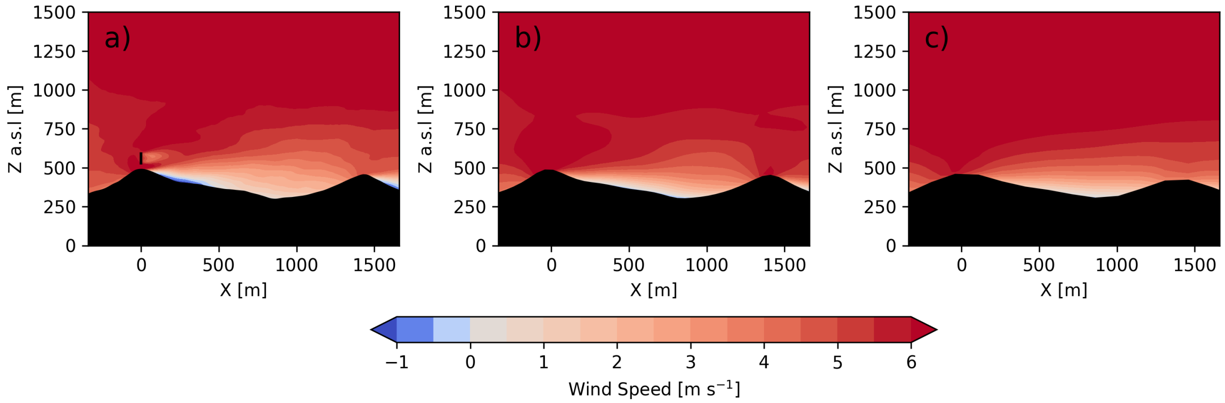

Figure A.2: Transect of 1 h time-averaged wind speed for (a) d05 (Δx = 10 m), (b) d04 (Δx = 50 m) and (c) d03 (Δx = 150 m) during the convective case study.

the effect of the grid cut-off frequency is less pronounced compared to Fig A.1. Despite the expected limitations of the model to fully capture turbulence in the stable case, we note that the wind turbine wake behavior is largely determined by the mountain wave, which is governed by the internal Froude number and shows limited sensitivity to small-scale turbulence and increasing grid resolution (Figure A.4). The bias and RMSE values in Table A.2 for all three domains are similar, but do indicate slightly higher bias and RMSE on d05 due to the greater turbulent variability (whereas d03 and d04 are closer to the observed mean velocities but cannot capture the turbulence at all). In conclusion, for the stable case study, large-scale dynamics (the mountain wave) do not require a 10 m grid, but wake and turbulence dynamics do.

Table A.2: 80 m wind speed bias and RMSE between WRF-LES-GAD on domains d03, d04, and d05 and SW_TSE04 tower measurements for the stable case study from 4:00 - 6:00 UTC.

	80 m Wind Speed (m s^{-1})	
Domain	Bias	RMSE
WRF d05 (Δx =10 m)	-0.22	0.83
WRF d04 (Δx =50 m)	0.07	0.63
WRF d03 (Δx =150 m)	0.04	0.46

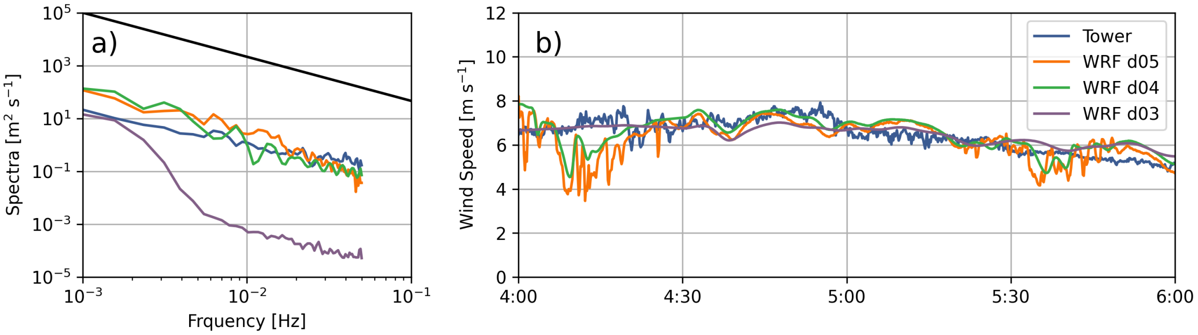

Figure A.3: Comparison of (a) time-series and (b) spectra between SW_TSE04 tower data and WRF-LES-GAD d05 ($\Delta x = 10$ m), d04 ($\Delta x = 50$ m) and d03 ($\Delta x = 150$ m) for 80 m wind speed at SW_TSE04 for the stable case study. The -5/3 inertial subrange power law is provided in black for reference. Note that the model wind speed is output at 10 s intervals; therefore, the highest resolvable frequency with this time-series is 0.05 Hz.

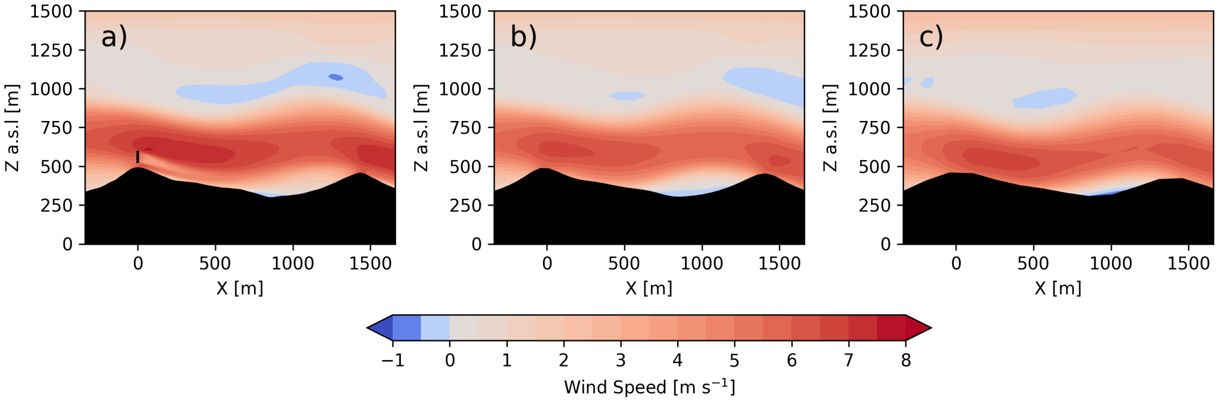

Figure A.4: Transect of 1 h time-averaged wind speed for (a) d05 ($\Delta x = 10$ m), (b) d04 ($\Delta x = 50$ m) and (c) d03 ($\Delta x = 150$ m) during the stable case study.

Appendix B

Perdigão: Sensitivity to PBL scheme on domain d03

A sensitivity study was conducted for modeling results on domain d03 with various turbulence closures in an effort to best represent the mountain wave or low-level jet structure. Domain d03 is high enough resolution (Δx =150 m) to resolve the double-ridge topography of the Perdigão site (domains d01 and d02 are too coarse). On domain d03, we expect to resolve the mountain wave structure that was observed by the DTU multi-Doppler lidar scans in Chapter 2 (Wise et al., 2022). In Chapter 2, domain d03 used the TKE-1.5 turbulence closure (Deardorff, 1980); however, in Chapter 3, the choice of closure is reexamined as a newer version of WRF is used (v4.4 compared to v3.7). We examine the mountain wave structure sensitivity to five popular closures available in WRF: the Melor-Yamada-Nakanishi-Niino (MYNN) level-2.5 planetary boundary layer (PBL) scheme (Nakanishi and Niino, 2006; Nakanishi and Niino, 2009), the 3DTKE scheme (which extends the TKE-1.5 large-eddy simulation model to the mesoscale limit) (Zhang et al., 2018), the Mellor-Yamada-Janjić (MYJ) PBL scheme (Janjić, 1994), the Shin-Hong PBL scheme (Shin and Hong, 2015), and the Bougeault–Lacarrere (BouLac) PBL scheme (Bougeault and Lacarrere, 1989).

All five closures resolve the mountain wave with reasonable accuracy except for the Shin-Hong scheme. Figure B.1 shows an instantaneous vertical cross-section of along-transect velocity at 04:30 UTC. The specific transect in Fig. B.1 intersects the location of the wind turbine (which is only included on domain d05) and represents flow conditions that are passed as boundary conditions to higher-resolution domains (domains d04 and d05). The Shin-Hong scheme predicts slightly slower wind speeds resulting in a shorter mountain wave wavelength, which gets distorted as the wave interacts with the second ridge. All other schemes look similar qualitatively with minor differences largely downwind of the parallel ridges. The mountain wave in the MYJ scheme stays elevated above the terrain downwind of the second ridge compared to MYNN, 3DTKE, and BouLac. The 3DTKE scheme also predicts a sharper hydraulic jump downwind of the second ridge. The MYNN and and BouLac schemes predict negative flow velocities near the surface downwind of the second ridge, resembling a rotor, which are common underneath mountain waves. Lastly, the mountain wave extends vertically to the highest elevation for the BouLac scheme.

Two soundings were launched at the Perdigõ site during the period of interest from the Orange Grove site near the location of the TLS and CLAMPS devices in Fig. 3.1. Figure B.2 compares vertical profiles of wind speed, wind direction, and potential temperature between the modeling results with various closures and the sounding launched at 03:55 UTC. Figure B.3 does the same but for 05:16 UTC. Errors for the vertical profiles in terms of biases and root mean square error (RMSE) for the modeling results and the two different soundings can be found in Tables B.1 and B.2, respectively. Overall, all five schemes under-predict the maximum wind speed in the low-level jet, but with better agreement higher in the atmosphere where all closures perform similarly. Note that any smaller-scale variability or turbulence is only captured on domains d04 and d05 and not on domain d03 as the grid resolution is too coarse.

At 03:55 UTC, there are only minor differences in the model predicted wind speed and thermal structure of the mountain wave between the closures. For the wind direction, there is a lot of variability between the closures closer to the surface; however, wind speeds are much slower in this region and measurements from soundings tend to be more uncertain. With respect to wind speed and potential temperature, the outlier is the Shin-Hong scheme, which most drastically under-predicts wind speeds within the low-level jet. The BouLac scheme has the lowest wind speed bias and RMSE at 0.61 m s^{-1} and 2.17 m s^{-1}, respectively, compared to the vertically averaged observed wind speed of 13.31 m s^{-1} . The BouLac scheme again has the lowest wind speed bias and RMSE for the profile at 05:16 UTC. From Fig. B.3, the extension of the low-level jet higher into the atmosphere for the BouLac scheme compared to other schemes (especially as compared to Shin-Hong and MYNN) is evident. While the differences between the closures may be small, we select the BouLac scheme for further analysis as it qualitatively captures the structure of the mountain wave best and because the BouLac scheme has the smallest wind speed errors compared to observations.

Table B.1: Biases and errors of wind speed, wind direction, and potential temperature on domain d03 for various closures compared to an observed sounding launched at 03:55 UTC.

	Wind Speed (m s^{-1})		Wind Direction (°)		θ (K)	
Closure	Bias	RMSE	Bias	RMSE	Bias	RMSE
MYNN	0.69	2.38	-4.6	26.1	-0.31	1.19
3DTKE	0.70	2.32	-5.0	26.0	-0.25	1.10
MYJ	0.75	2.31	-7.2	28.7	-0.32	1.11
Shin-Hong	0.57	2.52	-5.8	29.6	-0.17	1.15
BouLac	0.61	2.17	-5.1	27.1	-0.26	1.15

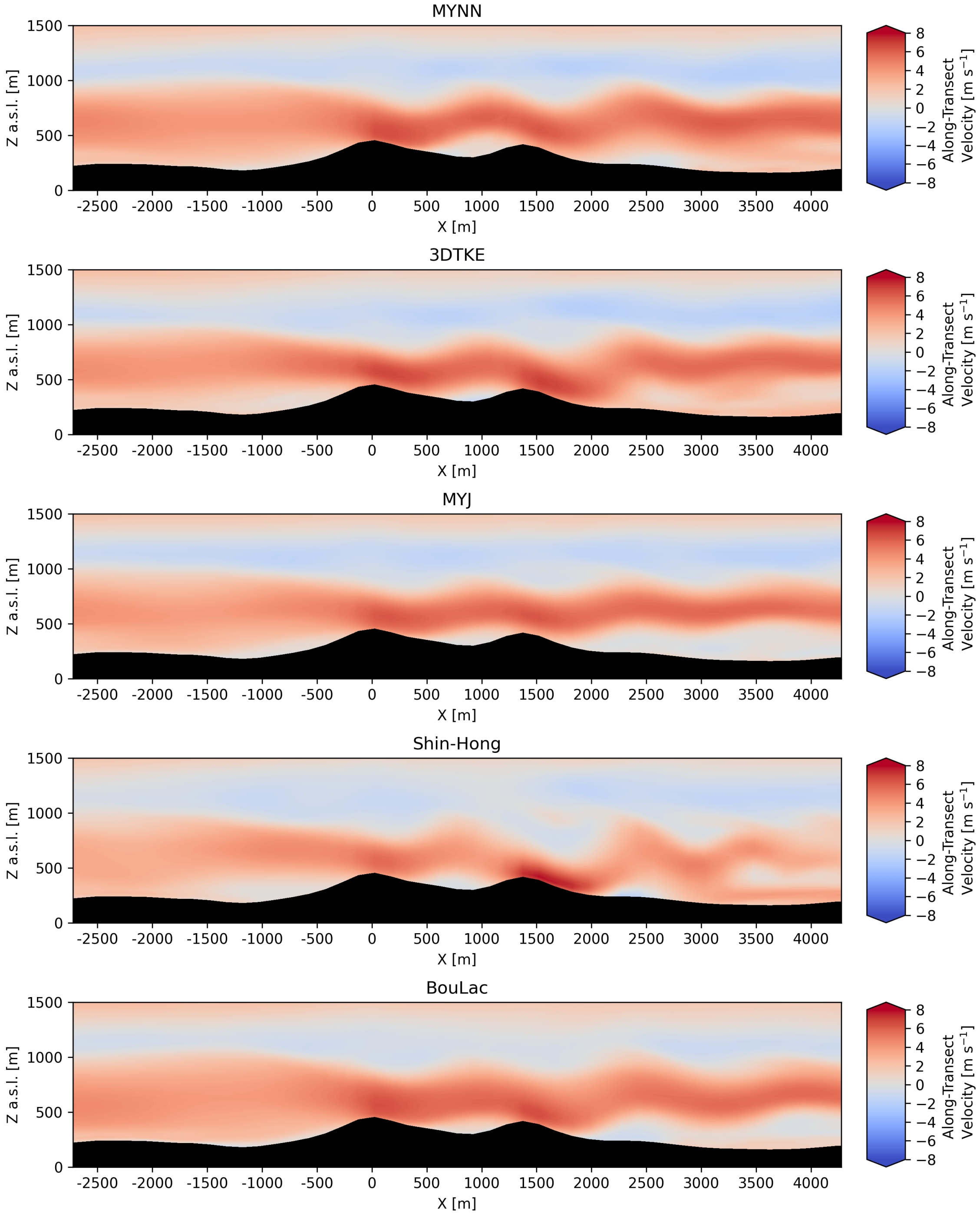

Figure B.1: Vertical slice of along-transect velocity for various closure schemes on domain d03 at 04:30 UTC. The transects are aligned with the lidar transect from Fig. 3.1.

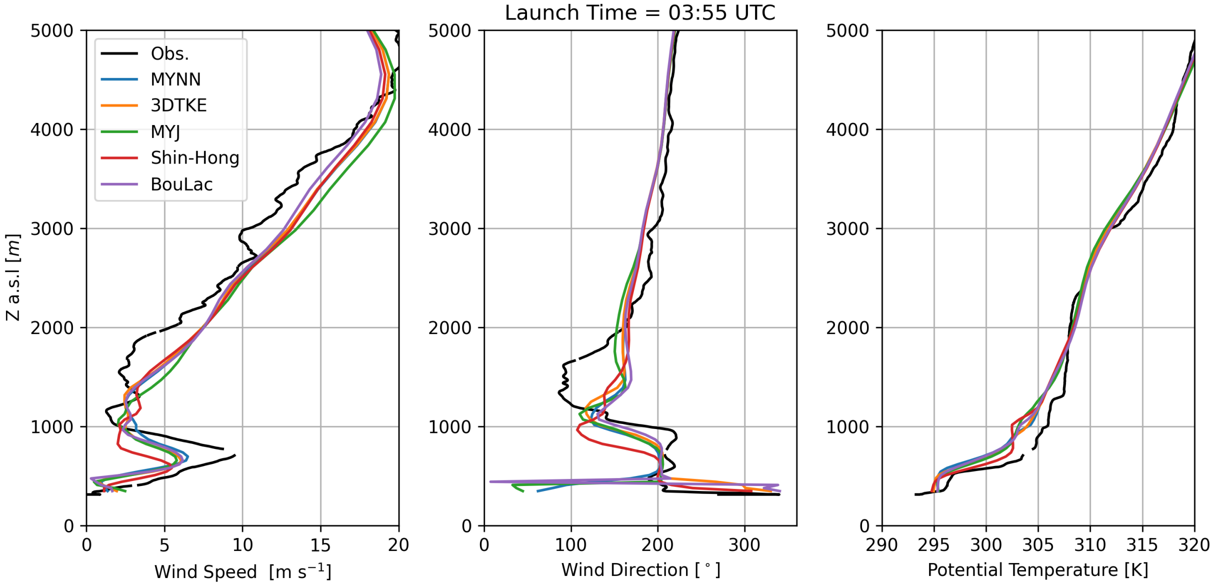

Figure B.2: Vertical profiles of (a) wind speed, (b) wind direction, and (c) potential temperature from the model with various closures and from a sounding at 03:55 UTC.

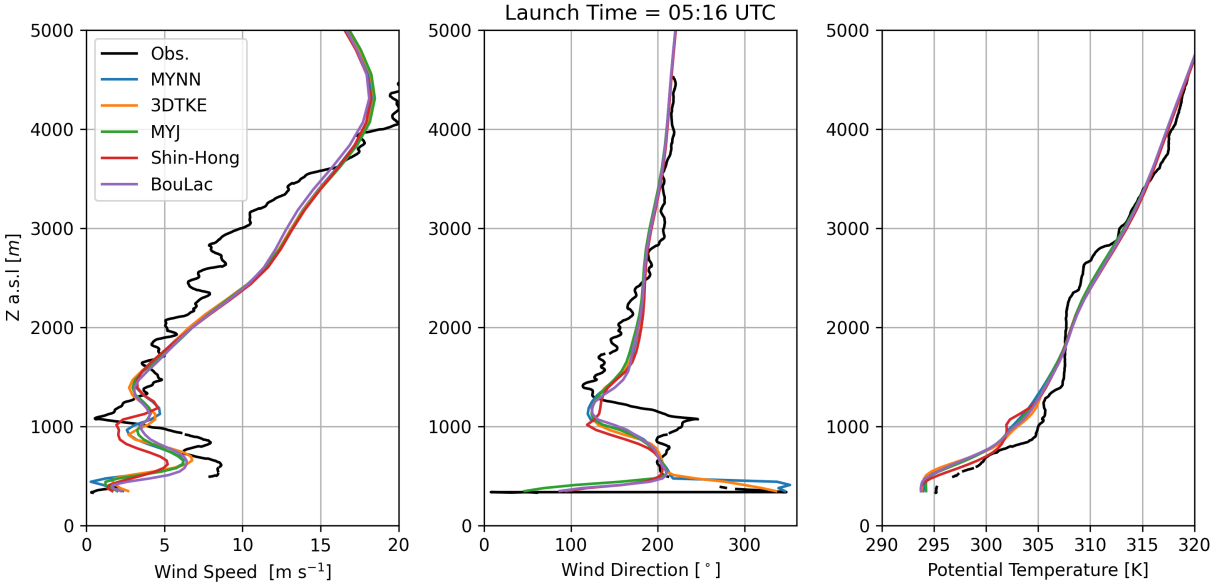

Figure B.3: Vertical profiles of (a) wind speed, (b) wind direction, and (c) potential temperature from the model with various closures and from a sounding at 05:16 UTC.

Table B.2: Biases and errors of wind speed, wind direction, and potential temperature on domain d03 for various closures compared to an observed sounding launched at 05:16 UTC.

	Wind Speed (m s^{-1})		Wind Direction (°)		θ (K)	
Closure	Bias	RMSE	Bias	RMSE	Bias	RMSE
MYNN	0.73	1.67	-4.8	29.7	0.59	1.14
3DTKE	0.64	1.64	-1.1	26.9	-0.59	1.06
MYJ	1.08	2.03	-5.9	31.3	-0.60	1.11
Shin-Hong	0.60	1.81	-3.8	29.8	-0.50	1.01
BouLac	-0.39	1.58	0.2	30.8	-0.55	1.11

Appendix C

AWAKEN: Ambient turbulence sensitivity to closure scheme

For the AWAKEN model setup in the region surrounding the King Plains wind farm, d01 resolves the mesoscale bore and gravity waves, and the nested domain d02 additionally resolves smaller-scale ambient turbulence. At 20 m grid spacing and in stably stratified conditions, the role of the turbulence closure in representing ambient turbulence is critical, especially to accurately represent the dissipation of individual wind turbine wakes. While results using the DRM closure are used in the body of this study, domain d02 is also run with the Turbulent kinetic energy 1.5-order model (TKE-1.5) (Deardorff, 1980) and the Dynamic Wong-Lilly (DWL) model (Wong and Lilly, 1994) for comparison. The TKE-1.5 model (Deardorff, 1980) is one of the standard turbulence closures used in WRF (and many other LES modeling tools). This model solves a prognostic turbulent kinetic energy (TKE) equation, which describes the evolution of TKE and parameterizes sources and sinks from shear production, buoyancy production or suppression, turbulent mixing, and dissipation. The Dynamic Wong-Lilly (DWL) model is the subgrid scale component of the DRM model (the DRM model uses a combination of the DWL eddy-viscosity model and and the scale-similar RSFS term to create a mixed-model for turbulence) with the DWL model using the explicit filter to dynamically solve for the eddy viscosity coefficients of interest (Lilly, 1992).

Figure C.1 shows an instantaneous plan slice of hub-height wind speed at 06:00 UTC (prior to the gravity wave and after 1 h of spin up). Qualitatively, the wind speeds are very similar across all three closures; however, the fine-scale structure of turbulence is different. The wind direction is east-northeasterly and wakes are seen as the slower wind speeds downwind of each individual turbine. For the TKE-1.5 closure, there are patches in the flow where there is very little turbulence, especially in the inflow regions upwind of the farm. For the DWL and DRM closures, the small-scale wind speed variability is more uniform, which is more realistic for ambient turbulence.

High quality hub-height turbulence observations are limited in the AWAKEN region; however, wind speeds in the rotor layer were measured at relatively high temporal frequency (∼0.25 Hz) by the profiling Doppler lidar at A1. The lidar at A1 was a pulsed lidar, which

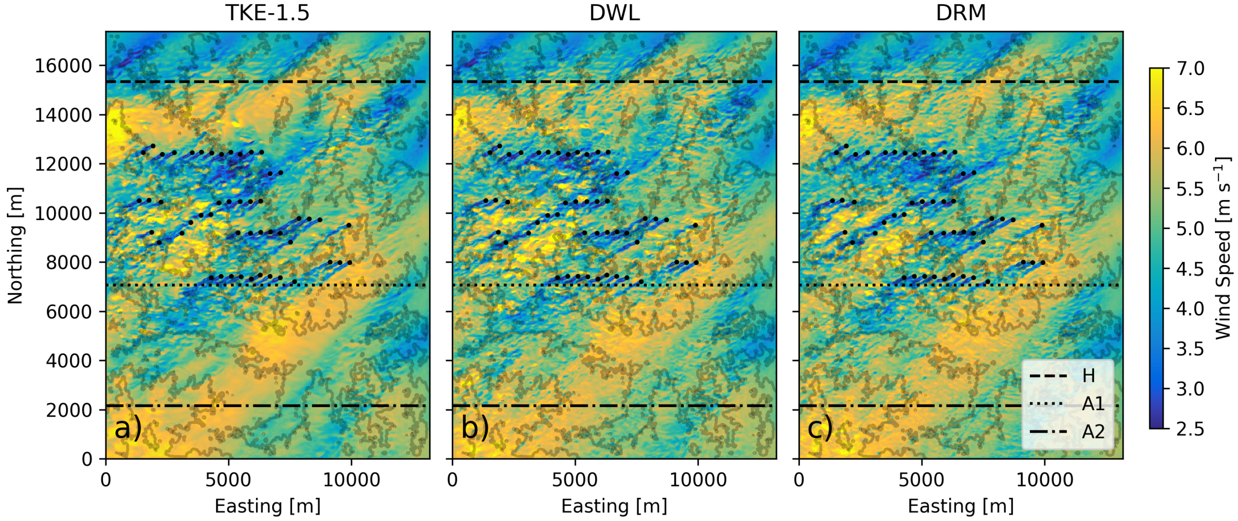

Figure C.1: Plan slice of hub-height wind speed at 06:00 UTC in domain d02 for simulations results using the (a) TKE-1.5, (b) DWL, and (c) DRM turbulence closures. Line contours represent 15 m changes in elevation.

allowed for this faster scan frequency. Using these measurements, the power spectra for the hub-height wind speed can be generated in time from 06:00 to 06:25 UTC (prior to the gravity waves) shown in Fig. C.2, which can be directly compared with simulation results at A1. Note that the 16 minute delay in which the gravity waves arrive in the model has been accounted for with the time period for the lidar in Fig. C.2(a) and C.2(b) being shifted to 05:44 - 06:09 UTC. The spectra are computed using Welch's method (Welch, 1967). Overall, there is reasonable agreement between the modeling results and measurements with limitations related to the relatively coarse grid resolution. The modeling results and measurements agree well in the inertial subrange and follow a slope of -5/3 for part of the spectrum (Kolmogorov, 1941); however, the larger-scale or lower-frequency structures are overestimated and the smaller-scale or higher-frequency structures are underestimated by the model.

The dynamic closures contain more energy at higher frequencies compared to TKE-1.5, as expected, with the DRM simulation containing the most energy in a frequency range of 0.012 - 0.016 Hz (∼60-80 s) compared to the other closures. At higher frequencies (above ∼0.02 Hz), the reduction in energy due to the effect of the grid-cutoff is apparent, as is typical for finite difference schemes Skamarock, 2004. Additionally, because the high-frequency turbulence is underestimated, the energy content is shifted to lower frequencies, which results in an overestimation of larger-scale turbulence in the model compared to observations. A similar shift occurred in SBL conditions for Wise et al. (2022) and in neutral boundary layer conditions for Wiersema et al. (2022), and is indicative of large-scale structures not cascading into smaller-scale motions limited by the grid resolution. Importantly, the hub-height wind

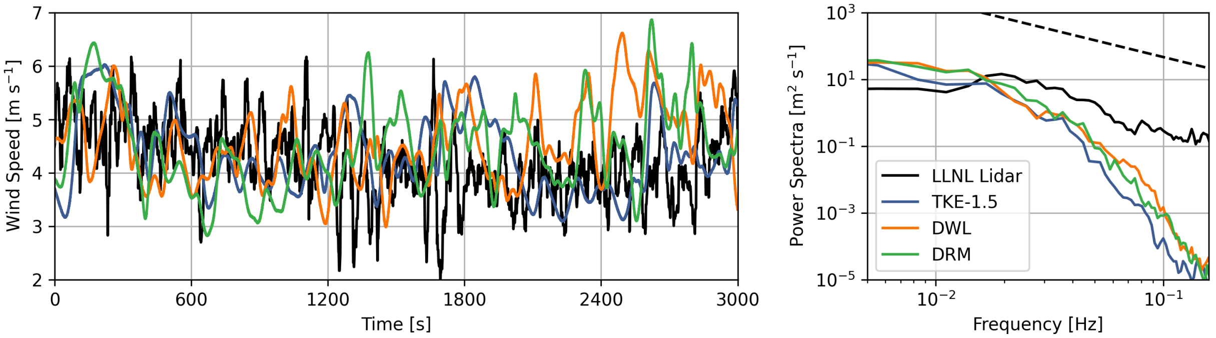

Figure C.2: Time-series (a) and power spectral density (b) of wind speed at Site A1 for the observations and simulation results with the various closures prior to the gravity waves. The analysis period for the modeling results is 06:00 - 06:25 UTC and 05:44 - 06:09 UTC to account for the delay in which the gravity waves occur in the model. The dashed black line in (b) represents the -5/3 energy cascade range in the inertial subrange.

speed and turbulence intensity are well-predicted by the model during the analysis period. For all three closures, the hub-height wind speed biases are under 0.4 m s^{-1} and the mean absolute errors are less than 1.0 m s^{-1}. For the DRM closure, which we conclude to perform best in the spectral analysis, the model predicted mean hub-height wind speed is 4.50 m s^{-1} compared to an observed wind speed of 4.24 m s^{-1} (the low values are because Site A1 is waked during the analysis period). Additionally, the mean model-predicted turbulence intensity is 17.9% compared to an observed 16.5% during 06:00 to 06:25 UTC.

To quantify the spatial variation in turbulence between the three closures, we use energy spectra in the vertical velocity signal along various east-west transects in domain d02. Figure C.3 shows spectra in wave-space of the vertical velocity for the three different closures taken along east-west transects that intersect Sites H, A1, and A2. Hereinafter, these transects will be denoted as Transect H, Transect A1, and Transect A2. The spectra are obtained following the methods of Durran et al. (2017) and Connolly et al. (2021) and consist of 650 points along the transect (excluding 5 points near the eastern and western boundaries). The spectra shown in Fig. C.3 are an average of the individual spectra calculated at each output time step (every 15 s) from 06:00 UTC to 06:25 UTC, prior to the gravity wave interaction. Transect H can be considered as purely inflow, while the flow at other transects is affected by wind turbine wakes. Along Transect H (Fig . C.3(a)), there is increased energy for larger wavenumbers (smaller wavelengths) when using the DWL and DRM closure compared to TKE-1.5, indicating that turbulence is more evenly distributed for the DWL and DRM closures. A similar trend holds true for Transects A1 and A2 (Figs. C.3(b) and C.3(c)) but to a much smaller degree. Additionally, transects A1 and A2 contain more energy in the smaller scales, as these locations are downstream of the wind farm and therefore contain

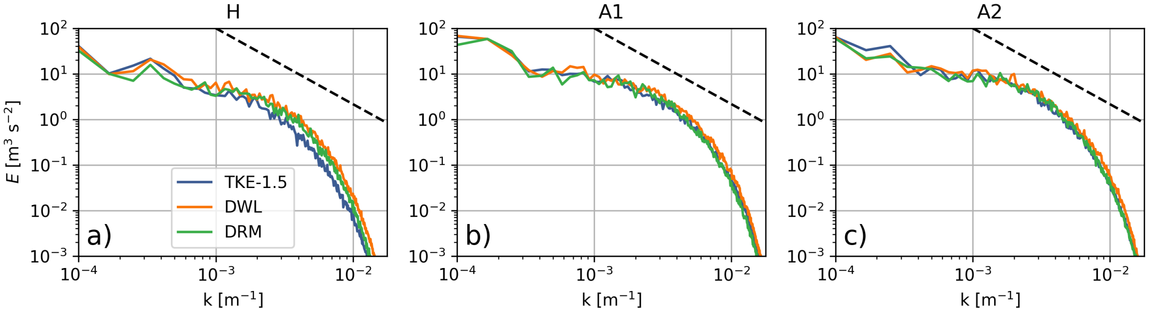

Figure C.3: Wave-space spectra of vertical velocity for the various closures along the (a) H , (b) E, and (c) A1 east-west transects. Spectra are calculated every 15 s from 06:00 to 06:25 UTC and then averaged. The dashed black line represents the -5/3 energy cascade range in the inertial subrange.

added energy from wind turbine wake turbulence.

Ultimately, the DRM closure was used for further analysis as it best represents the ambient turbulent structures and provides good agreement in the hub-height wind speed and turbulence intensity. There has been significant research on the sensitivity of LES modeling results in SBL conditions to the turbulence closure, and the present work agrees with previous findings in that dynamic turbulence models are able to resolve more turbulence in stably stratified conditions (Zhou and Chow, 2011; Zhou and Chow, 2012; Zhou and Chow, 2014; Wise et al., 2024). Interestingly, other simulations of the same site at the same grid resolution but focused on shear-driven instabilities in strong SBL conditions showed dramatic differences in the quality of ambient turbulence to the closure (Appendix E). In contrast with the study of Appendix E, the current setup takes advantage of HRRRv4 forcing and the CPM, which is one reason why there are smaller differences in the representation of turbulence when using the different closures in this study. Another likely reason is that the strength of stratification is weaker in the present study compared to Appendix E.

Appendix D

AWAKEN: Vertical profiles of lidar data and modeling results at Sites H and A2 for the atmospheric bore

Vertical profiles comparing observations with WRF-LES-GAD modeling results at Sites H and A2 for the AWAKEN campaign (Figs. D.1 and D.2) similarly demonstrate the impact of the gravity waves on the mesoscale environment as in Fig. 5.11. The averaging windows used to generate the profiles in Figs. D.1 and D.2 can be found in Table D.1. Similar conclusions include a destruction, weakening, and raising of the LLJ due to the gravity waves. Additionally, the gravity waves results in more easterly flow.

The thermal structure of the boundary layer at Sites H and A2 (Figs. D.1 and D.2) exhibits similar trends to Site A1 (Fig. 5.11). The boundary layer height increases and heat is transferred from lower in the atmosphere to higher in the atmosphere during the gravity waves. The magnitude of the resolved heat flux profiles is, in general, weaker compared to those at Site A1 as Sites H and A2 are closer to the domain boundaries. However, while Site H is close to the northern boundary, the effect of the gravity waves is still resolved at Site H (Fig. D.1(d)) because the gravity waves are advecting from the south.

Table D.1: Time windows used for averaging vertical profiling results when comparing WRF-LES-GAD with observations.

	Measurements Averaging Window (UTC)			Model Averaging Window (UTC)		
Site	Before	During	After	Before	During	After
H	05:44-06:14	06:14-06:44	06:44-07:14	06:00-06:30	06:30-07:00	07:00-07:30
A2	05:29-05:59	05:59-06:29	06:29-06:59	06:00-06:15	06:15-06:45	06:45-07:15

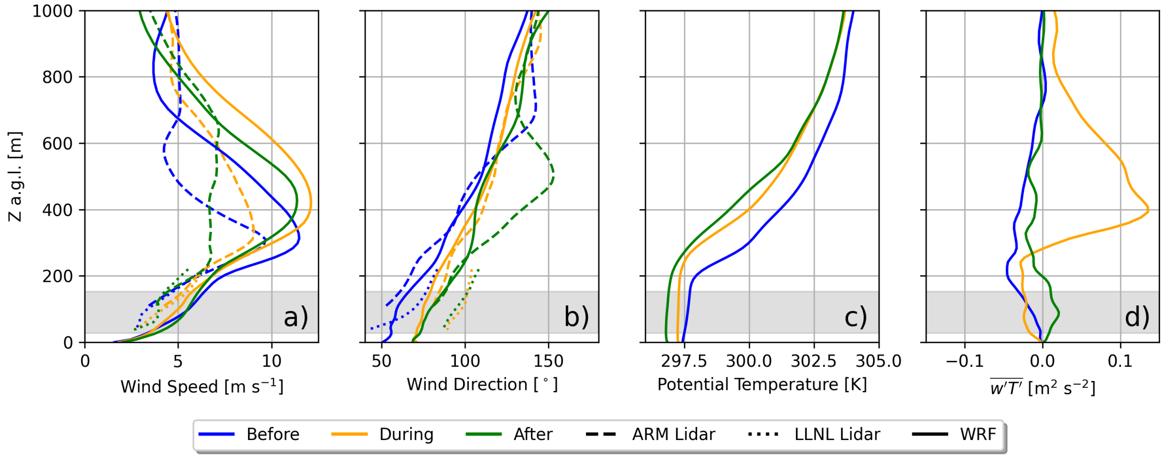

Figure D.1: Time-averaged vertical profiles of (a) wind speed, (b) wind direction, (c) potential temperature, and (d) resolved heat flux for observations and simulation results at Site H. See Table 5.3 for the averaging windows. The wind turbine rotor layer is highlighted in gray.

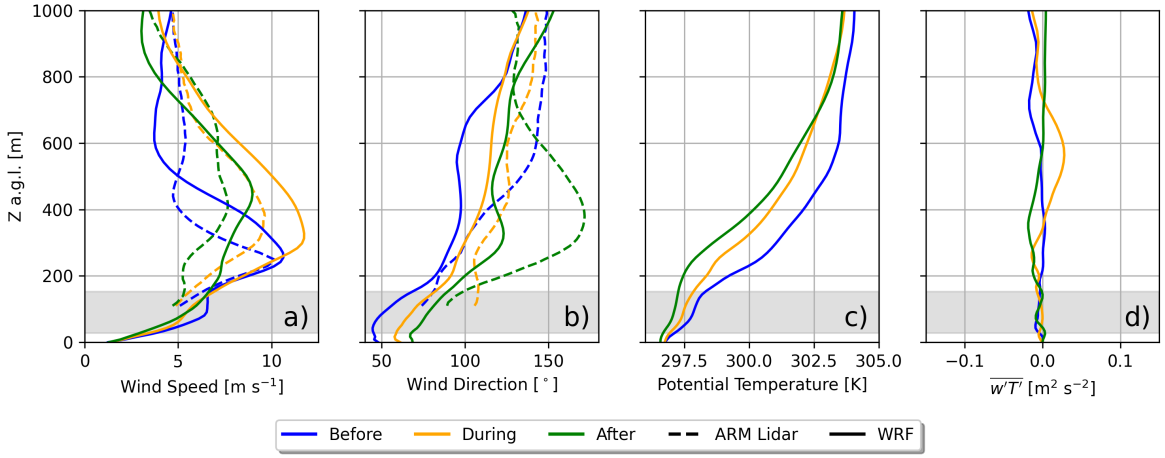

Figure D.2: As in Fig. D.1 but for Site A2.

Appendix E

AWAKEN: Shear-driven instabilities in the U.S. Southern Great Plains

E.1 Introduction

The American Wake Experiment (AWAKEN) is an ongoing (as of May 2024) field campaign located in central Oklahoma focused on wind farm atmosphere interactions (Moriarty et al., 2020). Specifically, a research question of interest is how intermittent, wavy turbulent bursting events affect wind farms. As mentioned in Chapter 5, wavy turbulence can largely be categorized into shear-driven and buoyancy-driven waves. While a buoyancy-driven wave is the focus of Chapter 5, this appendix focuses on a shear-driven wavy event.

The U.S. Southern Great Plains has previously hosted a number of field campaigns. The Cooperative Atmospheric Surface Exchange Study 1999 (CASES-99) field campaign is notable as a number of shear-driven wavy events were observed. Additionally, the CASES-99 field campaign occurred in topography with numerous east-west running river valleys, similar to the topography in AWAKEN. Newsom and Banta (2003) observed a shear-driven wavy event (which they refer to as a shear-flow instability event) in Doppler lidar measurements at CASES-99. They found that a shear-flow instability, which occurred elevated above the ground and beneath a low-level jet (LLJ), was triggered by the flow slowing thus increasing shear and decreasing the gradient Richardson number. While the characteristics of the LLJ were similar before and after the shear-flow instability, Newsom and Banta (2003) also showed that there was an increase in downward momentum flux. Coulter and Doran (2002) characterized a number of intermittent turbulence events during strongly stable atmospheric conditions potentially related to shear-driven wavy turbulence. They found that while some intermittent turbulent events spanned many kilometers, many were local and likely influenced by topography. Given the observations of intermittent, wavy turbulence events in the region that occurred before a number of wind turbines and wind farms were installed in the area, how these events affect wind farms is an open question. Note that, hereinafter, these turbulent events will be referred to in their entirety as wavy turbulence.

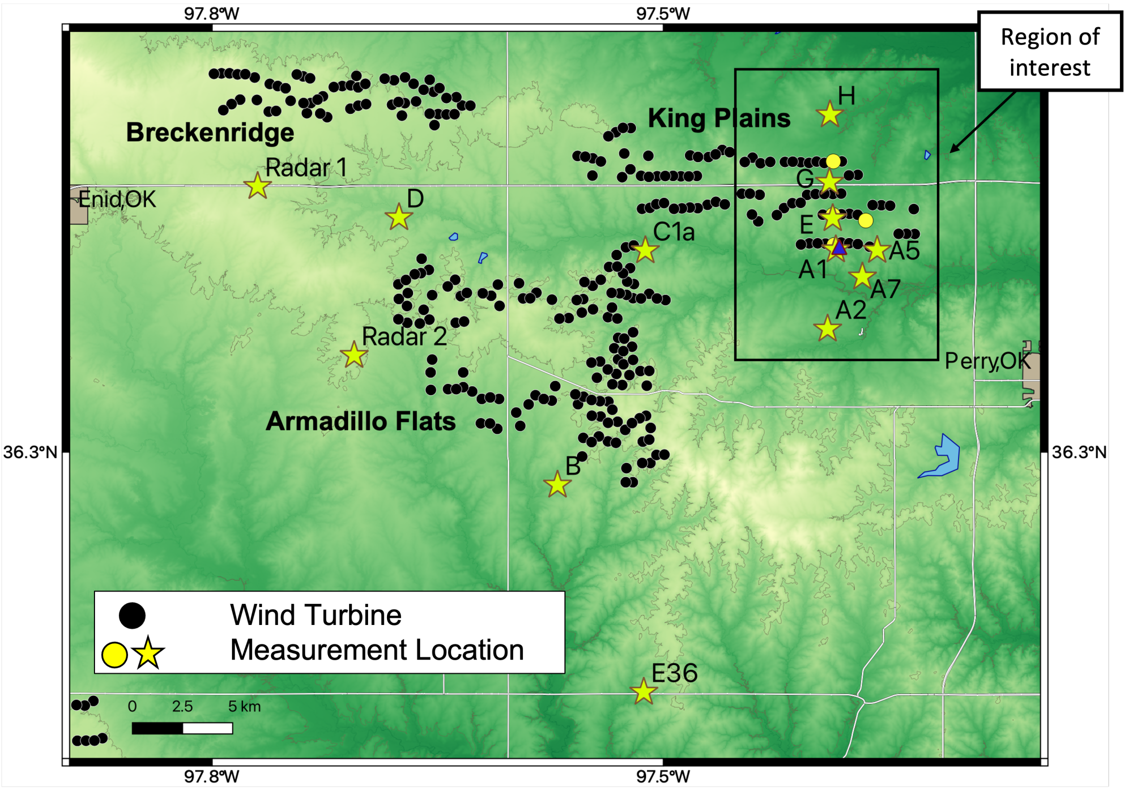

Figure E.1: Layout of the AWAKEN region including the Breckenridge, Armadillo Flats, and King Plains wind farms along with a number of measurement device locations. Image from Debnath et al. (2022).

E.2 Case study description

The layout of the AWAKEN region along with three major wind farms is shown in Fig. E.1. At sites A1, E36, and near C1a at the Rolling Meadow Golf Course (RMGC), vertical profiling (VP) lidars were installed by the Lawrence Livermore National Laboratory. At these locations, the lidars were focused on heights relevant to the wind turbine rotor layer which enabled a faster scan frequency compared to the other lidars at AWAKEN focused on the upper atmosphere.

On 02 Nov 2022, wavy turbulence was observed by all three lidars from 06:00 to 07:00 UTC. Figure E.2 shows time-height contours of wind speed gathered by the lidars at the three sites. In addition to the wavy turbulence, a southerly low-level jet was observed with very high wind shear. The wavy turbulence event is most clear in the returns at the A1 site, which is located just upwind (south) of the eastern half of the King Plains wind farm.

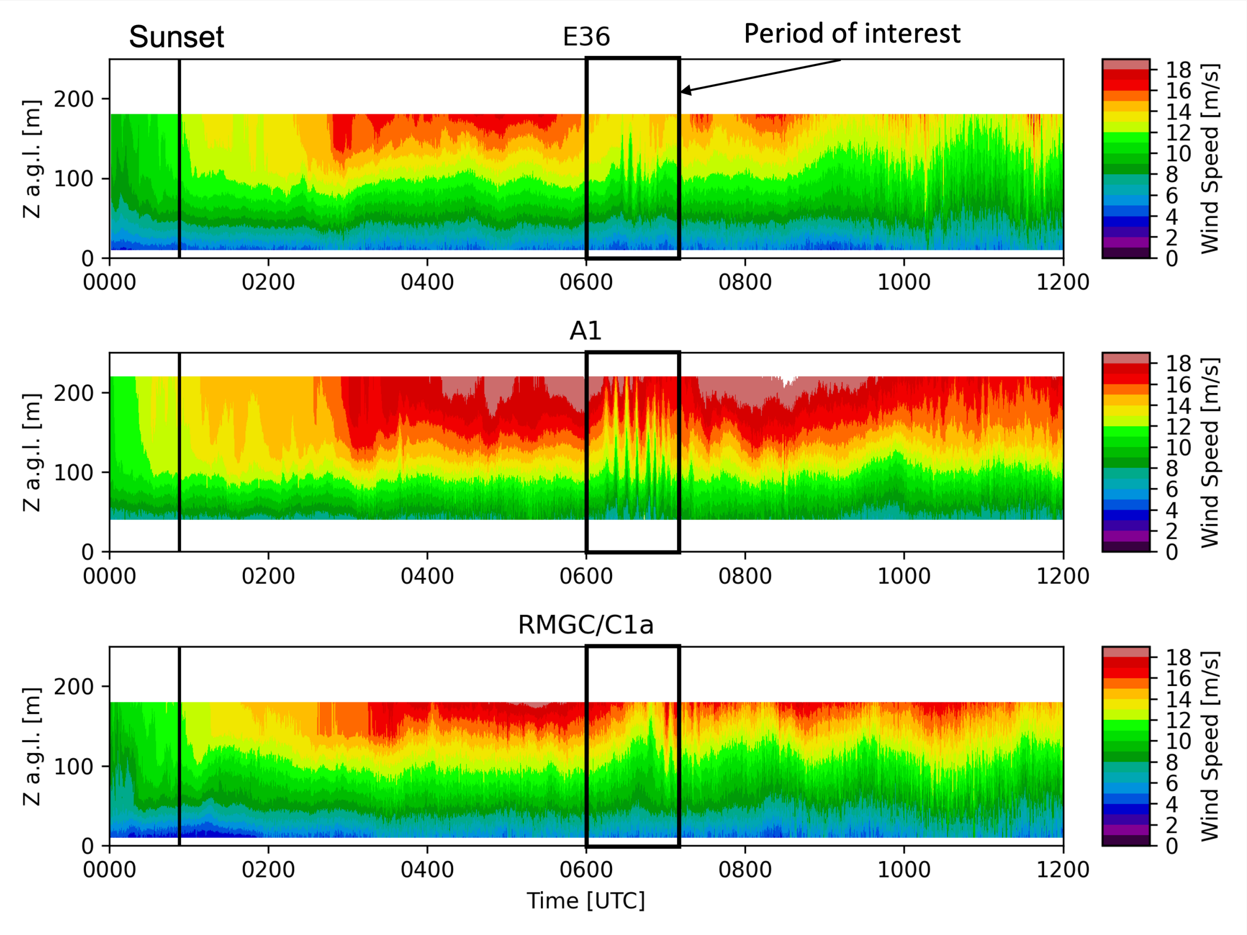

Figure E.2: Time-height contours from vertical profiling lidars at various sites in the AWAKEN region. The period of interest with the wavy turbulence is outlined in black (06:00-07:00 UTC).

Table E.1: Parameters used for the nested multi-scale WRF-LES-GAD setup. For the vertical resolution, Δz_{min} is for the first grid point above the surface and is approximate due to the nature of the terrain-following coordinate system in WRF.

Domain	Δx [m]	Nest ratio	$\sim\Delta z_{min}$ [m]	$N_x \times N_y$	Δt [s]	turb. closure
d01	5000	-	60	360 × 360	30	MYJ (Janjić, 1994)
d02	500	10	30	361 × 401	3	TKE 1.5
d03	100	5	20	361 × 501	0.5	TKE 1.5/DWL/DRM
d04	20	5	8	541 × 701	0.1	TKE 1.5/DWL/DRM

E.3 Methods

To model the wavy event, we use a multi-scale nested setup Weather Research and Forecasting model v4.4 (Skamarock et al., 2021). Figure E.3 shows the terrain used for the four domains with other relevant details for each domain in Table E.1. The nested setup is designed to mimic Zhou and Chow (2014) as their study is the only successful modeling study of shear-driven wavy turbulence in the U.S. Southern Great Plains. Importantly, Zhou and Chow (2014) showed that the shear-driven wavy turbulence event was only resolved when using a dynamic turbulence closure. Therefore, in this study, we utilize the Dynamic Wong-Lilly (DWL) (Wong and Lilly, 1994) and Dynamic Reconstruction Model (DRM) (Chow et al., 2005) turbulence closures on domains d03 and d04 in an aim to capture both the shear-driven wavy turbulence event as well as ambient turbulence, which is important for wind turbine wake dynamics. We also conduct simulations with the TKE-1.5 closure (Deardorff, 1980) as a reference. On domain d04, wind turbines are parameterized using a generalized actuator disk (GAD) (Mirocha et al., 2014a) for the 50 wind turbines that represent the eastern half of the King Plains wind farm. The King Plains turbines are General Electric 2.8 megawatt (MW) wind turbines with a hub-height of 88.5 m and a rotor diameter of 127 m with details available in Quon et al. (2024). The physics parameterizations are the same as those used in Arthur et al. (2020) who simulated a portion of the Chisholm View wind farm, which is located roughly 40 km to the northwest. We follow their setup as they found good agreement with observations and considering their domain is in the same region. Lastly, forcing for domain d01 is provided by the North American Mesoscale Forecast System (NAM).

E.4 Results and discussion

Generation of shear-driven wavy turbulence

All three turbulence closures capture the low-level jet on 02 Nov 2022; however, only the dynamic closures (DWL and DRM) resolve wavy turbulence during the period of interest. Figure E.4 shows time-height contours of wind speed from the observations and modeling

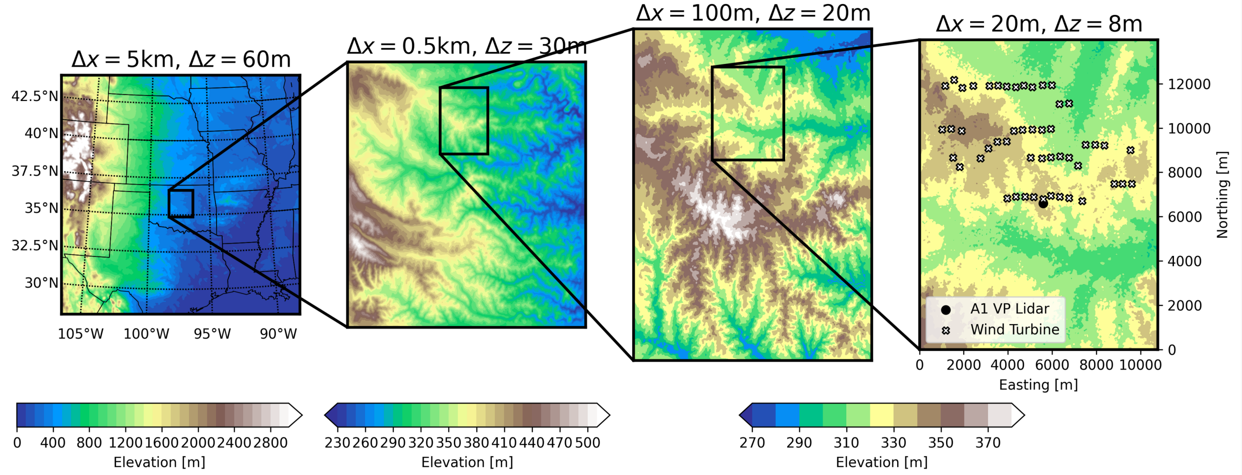

Figure E.3: Terrain in the multi-scale nested setup in WRF-LES-GAD with the horizontal and near-surface vertical grid resolution stated at the top of each domain.

results at the A1 site on domain d03. The shear layer close to the surface is well-predicted by the model regardless of closure after sunset. The results with the TKE-1.5 closure become very quiescent (less variable) later in the night whereas the dynamic closures resolve some variability.

The generation mechanism of the wavy turbulence is similar to that observed by Newsom and Banta (2003) where the Richardson number decreases and approaches a critical value of ∼0.2 when the flow goes from being both dynamically and statically stable to being dynamically unstable but statically stable. Figure E.5 shows the vertical wind shear ($S = dU/dz$), the potential temperature gradient ($d\theta/dz$), and the bulk Richardson number between heights of 100 m and 300 m a.g.l. The bulk Richardson number is defined as $Ri = N^2/S^2$ where N is the Brunt-Väisälä frequency, $\sqrt{g/\theta \, d\theta/dz}$, with g being gravitational acceleration. While shear does increase in the modeling results, importantly, the strength in the stratification also weakens significantly. It is difficult to identify exact reasons for the increase in shear and decrease in stratification, but the most likely reasons are due to changes in the mesoscale environment.

Note that the frequency of the resolved wavy turbulence is high compared to the observations. The waves predicted by the model have a period of approximately 1 minute while the waves in the observations have a period of nearly 10 minutes. The waves in the model oscillate at the Brunt-Väisälä frequency. No measurements are available to estimate the Brunt-Väisälä frequency in the observations. Considering that the observed waves are longer in period and cover a relatively large geographic region, it is possible that the generation mechanism of the observed waves is an atmospheric bore as in Chapter 5. Even though the generation mechanism in the model does not provide insight into the generation

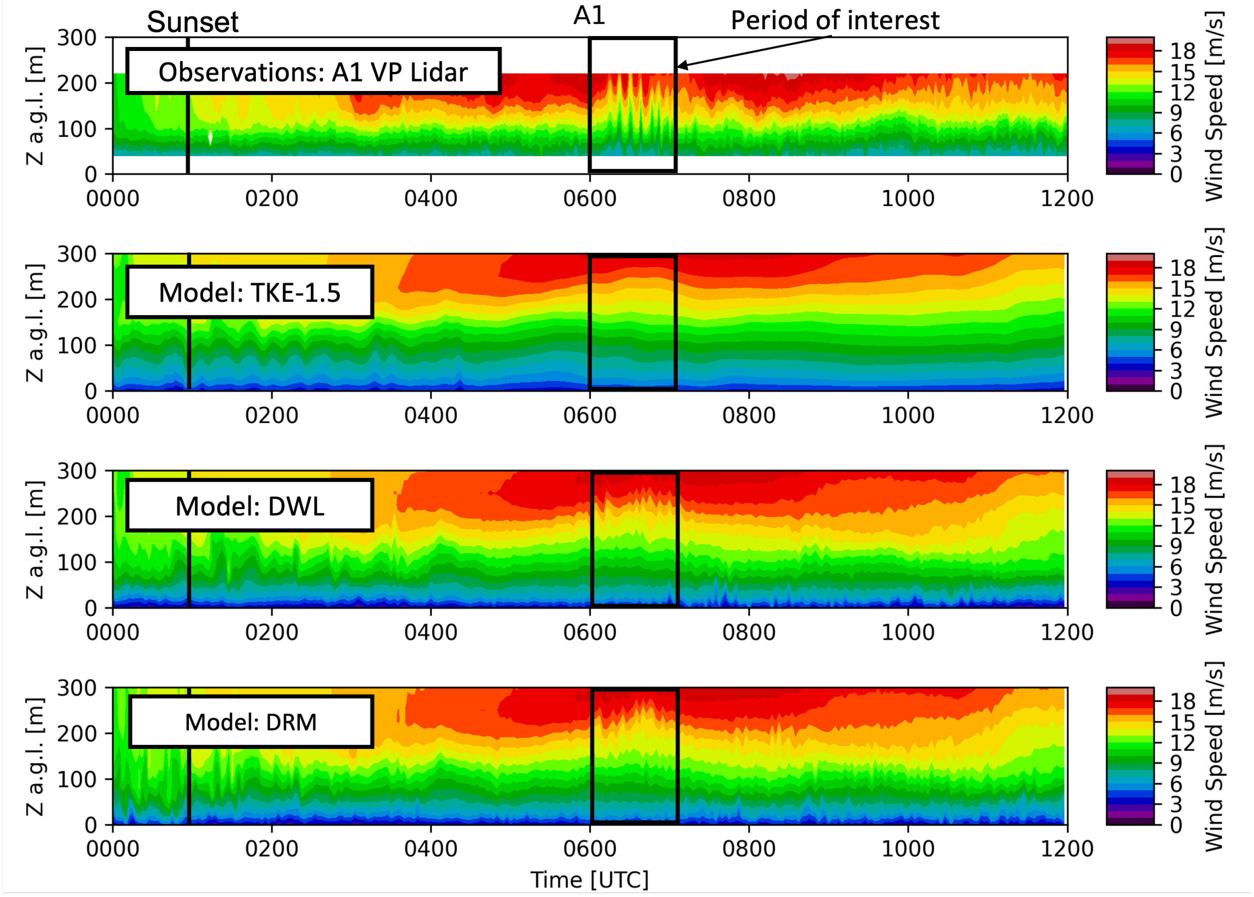

Figure E.4: Time-height contours of wind speed for the observations and modeling results on the domain with 100 m horizontal grid spacing.

mechanism for the observed waves, we move forward with analysis using purely modeling results, as the results demonstrate how shear-driven wavy turbulence may affect wind farm performance. Additionally, while the generation mechanism for this specific case study of observed waves is not clear, wavy turbulence events of all varieties occur commonly in the Southern Great Plains.

Closure sensitivity to resolving ambient turbulence

On domain d04, ambient turbulence is expected to be resolved with the given simulation setup. The shear-driven wavy turbulence is resolved on domain d03 and passed as the lateral boundary conditions for domain d04. As a result, domain d04 contains both shear-driven wavy turbulence as well as ambient or background turbulence. Figure E.6 shows

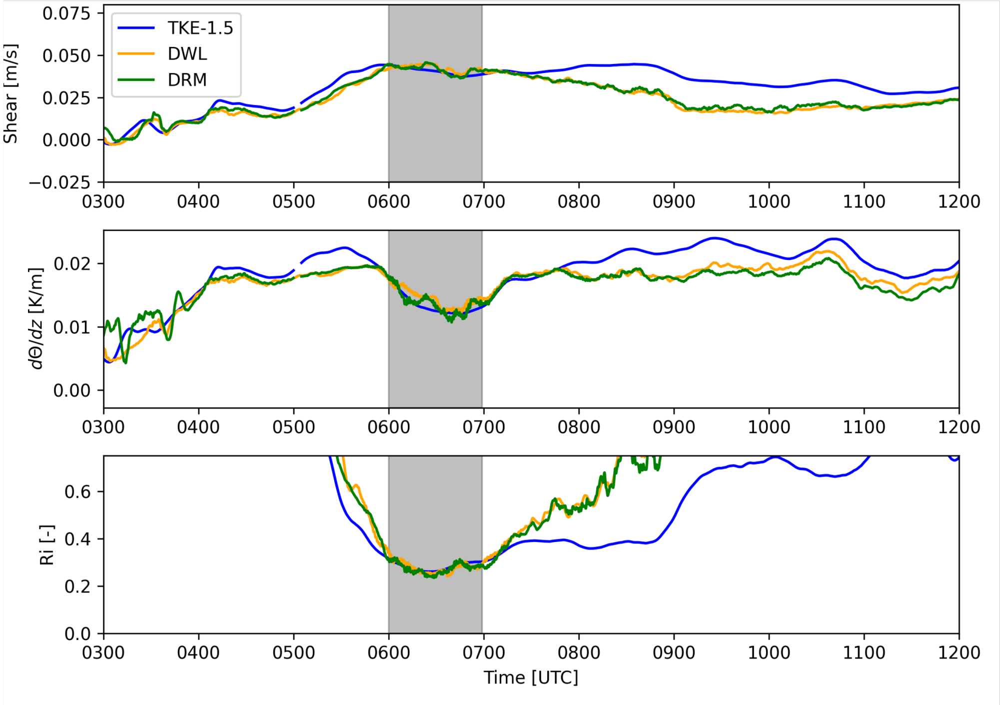

Figure E.5: Time-series of the vertical wind shear, potential temperature gradient, and Richardson number at the A1 site for the various closures on the domain with 100 m horizontal grid spacing.

instantaneous plan views of hub-height wind speed for the three different closures after 1 hour of simulation time. Very little ambient turbulence is resolved and the flow is essentially laminar when using the TKE-1.5 closure, which results in wind turbine wakes not dissipating realistically. For both of the dynamic closures, qualitatively, there is variability in the wind speed signal that represents ambient turbulence. These turbulent structures interact with the wind turbine wakes in addition to any shear-driven wavy structures. We move forward with results from the DRM closure to analyze wind farm performance during the analysis period as the DRM has the added benefit of capturing backscatter, which is an important mechanism in SBL flows.

Effect of shear-driven instabilities on wind farm performance

At hub height, the shear-driven wavy turbulence largely affects only the western half of the domain (from an Easting of 2000 to 6000 m). Figure E.7 shows an instantaneous plan view of the hub-height wind speed and vertical velocity at 06:00:15 UTC for results with the DRM closure. In addition to the background variability and wind turbine wake turbulence, patterns of upward and downward motion in the vertical velocity signal in Fig. E.7 are indicative of

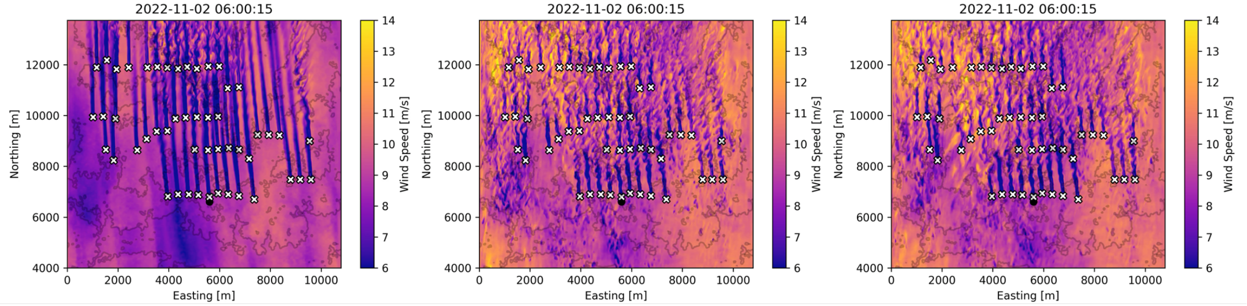

Figure E.6: Instantaneous plan view of hub-height wind speed at 06:00:15 UTC for the (left) TKE-1.5, (middle) DWL, and (right) DRM closures.

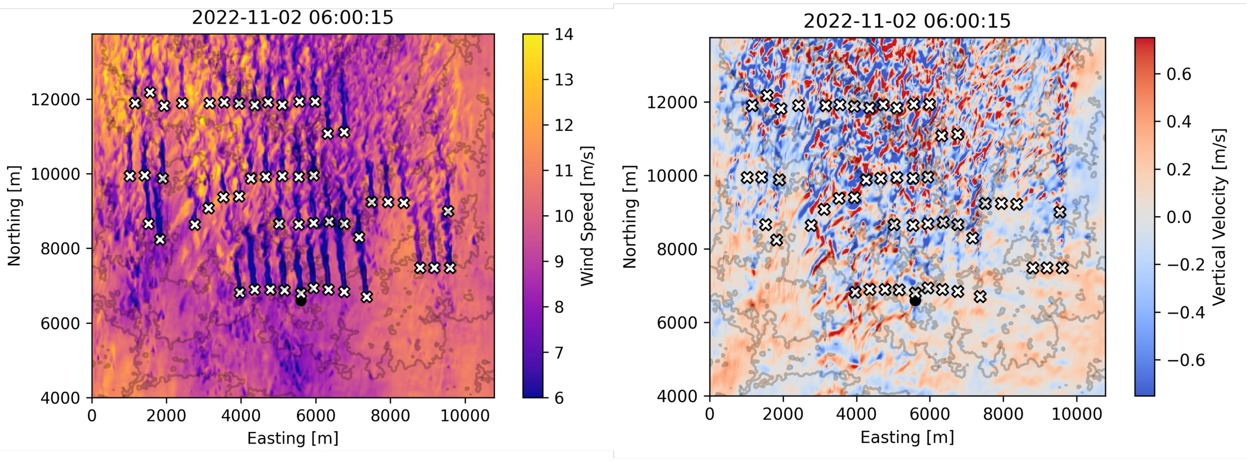

Figure E.7: Instantaneous plan view of (left) hub-height wind speed and (right) hub-height vertical velocity at 06:00:15 UTC for the DRM closure.

wavy turbulence. While the wavy turbulence is very clear in the vertical velocity signal, it is less clear in the wind speed signal.

By averaging quantities over the entire analysis period (06:00-07:00 UTC), we can attempt to differentiate the various factors affecting wind farm performance. The southerly flow as it affects the King Plains wind farm is actually quite heterogeneous as shown in Fig. E.8. There are three major factors that determine the average turbine power output during the analysis period and these include terrain, wavy turbulence, and wake effects. Wake effects result in a reduction of wind speed thus lowering power output. Wake effects are most apparent in the center of the domain where there are four rows of turbines. There are also subtle terrain affects; for example, in Fig. E.8, a narrow gulch is pointed out that results in slower wind speeds thus reducing average power for a few turbines. Additionally, the northwestern

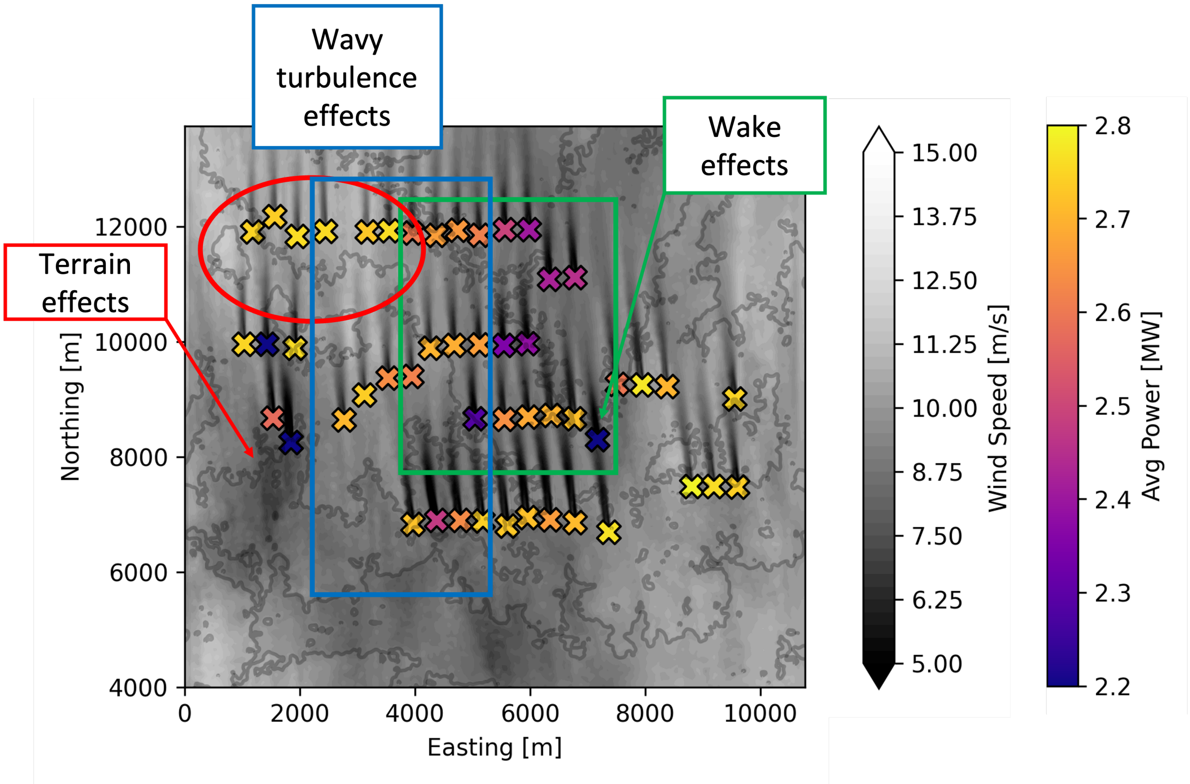

Figure E.8: Time-averaged hub-height wind speed and individual turbine power. Annotations of various factors that affect average power production are included to highlight regions with specific contributions.

region of the domain is at a higher elevation, which results in topographic acceleration and flow speed up. The most northern row of turbines in the western region of the domain is actually producing rated power as these turbines see very fast wind speeds even though they are also experiencing wake effects. Lastly, between an Easting of 2000 and 6000 m, the farm is affected by wavy turbulence. The wavy turbulence results in faster wind speeds from aloft being transferred down to hub height. Turbines that are affected by wavy turbulence produce very high power as they experience the faster wind speeds entrained from aloft.

Lastly, both wakes and wavy turbulence strongly affect power variability during the analysis period (06:00-07:00 UTC). Figure E.9 shows the average turbulence intensity, $TI = \sigma_U/U_{avg}$, and standard deviation of power output for individual turbines. Time-series of normalized power are shown for four individual turbines to highlight the effect of wakes and wavy turbulence. The first turbine in the southeast of the domain is considered the baseline turbine as it experiences purely ambient turbulence. The average power from this turbine is the dotted line in all of the other time-series shown. The turbine in the southwest is experiencing wavy turbulence, which increases variability significantly, but the average

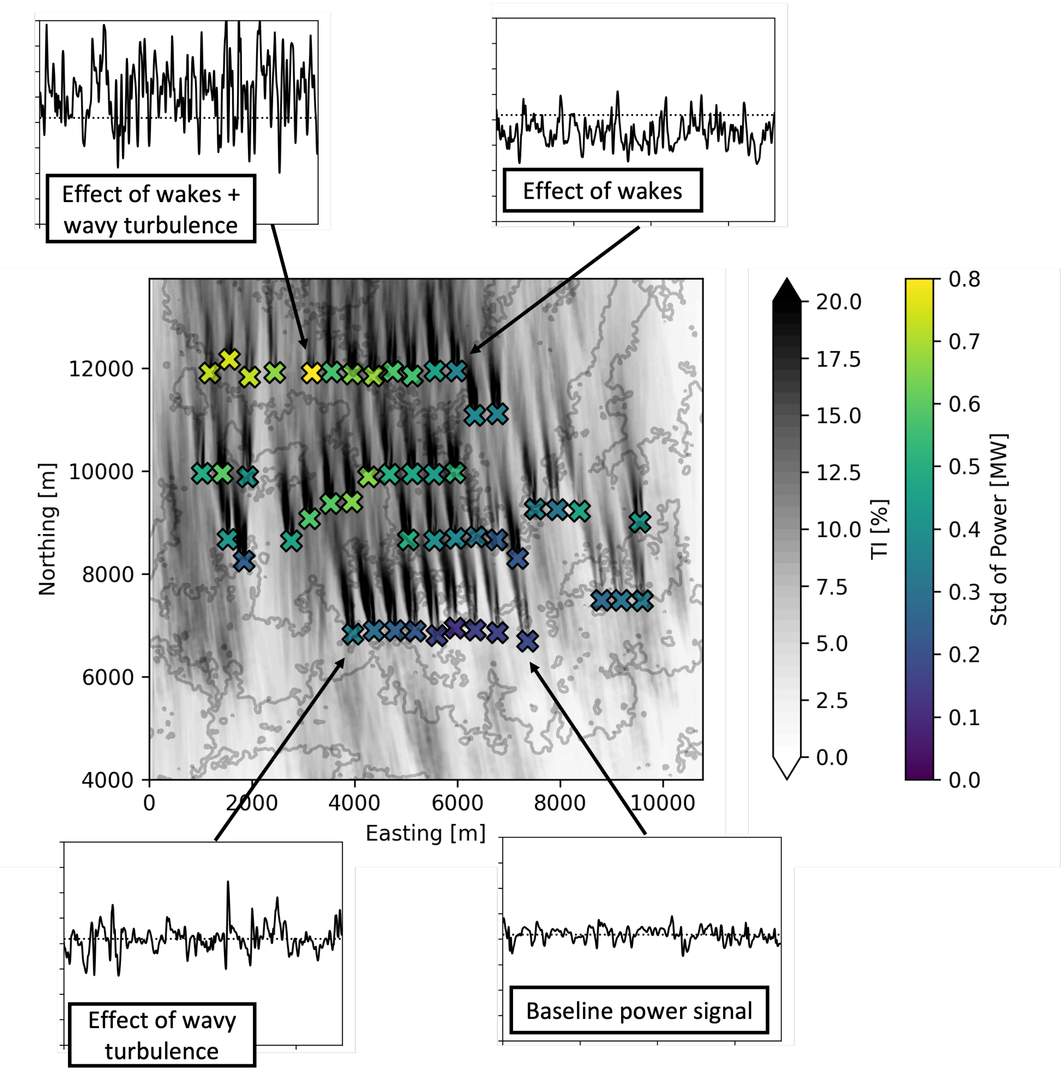

Figure E.9: Time-averaged hub-height turbulence intensity and standard deviation of individual turbine power. Time-series of the power signal from four different turbines are also included to demonstrate the effect of intermittent turbulence and wakes. Note that the time-period for the time-series is 30 minutes and all four subplots have the same y-axis range.

power is not greatly affected. The turbine in the northeast is experiencing the wakes of three rows of turbines in front of it and thus has more power variability as well as lower average power output. In the northwest part of the domain, the turbine highlighted experiences the combined effect of wakes and wavy turbulence. This turbine has the most power variability but also produces the most amount of power on average as the faster wind speeds entrained by wavy turbulence overpower any wake effects.

E.5 Conclusions

In this study, WRF-LES-GAD is used to understand wind farm impacts from wavy turbulence observed during the American Wake Experiment (AWAKEN) field campaign. We use a multi-scale nested setup to capture turbulence across a broad range of scales with grid spacings ranging from 5 km to 20 m. On the domain with the finest grid resolution, we represent 50 wind turbines from the King Plains wind farm using a generalized actuator disk rotor parameterization. In-line with previous work by Zhou and Chow (2014), we find that wavy turbulence is only resolved when using a dynamic turbulence closure (Wong and Lilly, 1994; Chow et al., 2005) and not when using the TKE-1.5 closure. Additionally, when using the TKE-1.5 closure, no background or ambient turbulence is resolved and the flow is laminar. We find that the most realistic representation of turbulence on the finest grid is achieved when using the Dynamic Reconstruction Model (DRM) turbulence closure.

There are three major contributors to how wind farm power production varies during this specific case study. Wake effects, which decrease available wind resource and increase turbulence for downwind turbines, decrease power and increase power variability as expected. While the terrain is considered simple and not nearly as complex as many other regions where wind turbines are sited, there are important variations in the terrain that affect power output. For example, a narrow gulch is found to decrease power for two turbines within the farm. Importantly, the northwest region of the farm is more elevated compared to the rest of the farm and thus experiences faster wind speeds. The subtle increase in elevation results in topographic acceleration increasing wind speeds and overcoming any wake effects for turbines in the northwest region of the farm. Lastly, wavy turbulence affects only a small subset of the farm. The intermittent turbulence brings down faster, more elevated wind speeds aloft similarly overpowering any wake power losses. However, the increased power comes at a cost in that the power variability during the analysis period is significantly higher for turbines experiencing wavy turbulence.